Aaron Marshall

Electrocatalysts for the Oxygen Evolution Electrode in Water Electrolysers using Proton Exchange Membranes: Synthesis and Characterisation

Doctoral thesis
for the degree of philosophiae doctor

Trondheim, June 2005

Norwegian University of Science and Technology
Faculty of Natural Sciences and Technology
Department of Materials Technology

NTNU
Innovation and Creativity

IMT-report 2005:71

NTNU
Norwegian University of Science and Technology
Doctoral thesis
for the degree of philosophiae doctor
Norwegian University of Science and Technology
Faculty of Natural Sciences and Technology
Department of Materials Technology

ISBN 82-471-7069-8 (printed vers.)
ISBN 82-471-7067-1 (electronic vers.)
ISSN 1503-8181

Doctoral theses at NTNU, 2005:96
Printed by NTNU-trykk

Acknowledgments

The work for the following thesis was conducted at the Department of Materials Technology, NTNU, from April 2002 to April 2005. The late Professor Georg Hagen was my main supervisor during the first 2.5 years, and I am very appreciative of the chance Georg gave me to study in Norway at NTNU, as well as the help and encouragement he gave me during this time. Georg always supported this project, and activitely worked to promote and propergate new ideas for PEM and electrochemical energy technology. My co-supervisors, Professor Reidar Tunold and Associate Professor Børre Børresen, also gave me considerable support during my work and I thank them for many very useful discussions, which I hope will continue beyond this work. I would also like to thank Professor Svein Sunde for taking responsibility of my project in the last few months and showing an interest in my work. Dr Mikhail Tsypkin helped with many of the experimental aspects of this work, and his cooperation is thanked. Associate Professor Magnus Rønning of the Department of Chemical Engineering, NTNU, is also acknowledged for his role in my work using X-ray absorption spectroscopy at the European Synchrotron Radiation Facility in Grenoble, France. Magnus was very open to trying a range of measurements and helped a lot with the practical issues involved with these measurements. Dr Sten Egil Johnsen and Dr Mikhail Tsypkin also contributed to the X-ray absorption spectroscopy work, and I thank them for many nice discussions during my entire project.

I also would like to thank everyone at the Department of Materials Technology, for making my stay in Norway very interesting and rewarding. Martha Bjerknes and Kjell Røkke are acknowledged for their support and help they give to everyone at our department. Tusen Takk !

This work was financially supported by the Norwegian Research Council and Norsk Hydro ASA, without which, my project would not have been possible.

Lastly, I would like to thank my family, who gave considerable support during the three years spent in Norway. My wife Sonia was always supportive and understanding, and this time would not have been nearly as much fun without her.

Thanks

Aaron Marshall

Summary

Electrocatalysts based on IrO_2 have been synthesised and characterised using a wide range of techniques. These oxide materials were primarily developed as oxygen evolution electrocatalysts for proton exchange membrane (PEM) water electrolysis. This development has enabled high performances to be achieved in a PEM water electrolysis cell. Overall the best result was obtained with an $Ir_{0.6}Ru_{0.4}O_2$ anode and 20 wt% Pt/C cathode, with a cell voltage of 1.567 V at 1 A cm^{-2} and 80 °C when using Nafion 115 as the electrolyte membrane. This represents a cell efficiency of 76 % ($\varepsilon_{\Delta G}$) and an energy consumption of 3.75 kWhr Nm^{-3} H_2 at 1 A cm^{-2}.

Initial results showed that previous synthesis methods used for PEM water electrolysis electrocatalysts, were not suitable for multi element oxides, due to the formation of multiple oxide phases, and general controllability problems. This lead to the development of a new method, based on the thermal oxidation of metallic colloids. This method (modified polyol method) was then used to prepare $Ir_xSn_{1-x}O_2$ and $Ir_xRu_{0.5-x}Sn_{0.5}O_2$.

The effect of annealing temperature on $Ir_xSn_{1-x}O_2$ was examined and showed that the crystallinity increases, and the active area decreases, with increasing annealing temperature. The specific activity of this material however was seen to be constant over the entire temperature range, with the performance losses only due to the reduction of active surface area. At high temperatures, the solid solution of $Ir_xSn_{1-x}O_2$ was seen to become unstable, with segregation of SnO_2 from the oxide lattice, and formation of metallic iridium.

The electrochemical properties of the oxides prepared at 500 °C, showed that the addition of SnO_2 to IrO_2 particles had no beneficial effect. Cyclic voltammetry showed that the active area decreases as the tin content increases, with this related to the crystallinity increase and dilution of the active iridium oxide sites. Additions of up to 20 mol% tin may be acceptable as little change in the active area occurs at low tin contents, however there was still a 40 mV increase in cell voltage at 1 A cm^{-2} and 80 °C in a PEM water electrolyser. The specific activity of the oxides prepared by the polyol method remains constant until 50–60 mol% tin whereafter the activity decreases. Overall, the electrocatalytic properties in 0.5 M H_2SO_4 and a PEM cell are similar, however there is evidence to suggest that there are extra resistance issues in the PEM cell due to the poor conductivity of some

of the prepared oxides. The effect of anode composition on the PEM cell ohmic resistance confirmed that high tin contents causes high performance losses due to poor layer conductivity.

$Ir_xRu_{0.5-x}Sn_{0.5}O_2$ electrocatalysts showed that additions of 15–25 mol% ruthenium improved the overall oxygen evolution performance at low current densities. However due to agglomeration of metallic ruthenium during the colloid synthesis stage, the electrochemically active area of this oxide, decreased with ruthenium content. XPS revealed that the reduction in active area was directly related to the concentration of noble metals at the surface of the powders. The specific activity of the iridium species at the electrode surface was seen to increase as the ruthenium content of the bulk increased. This finding maybe due to a "support" affect, in which the underlying ruthenium influences the structure and electronic properties of the surface iridium. This reduced active surface area and the increase specific electrocatalytic activity resulted in an optimum in the electrocatalytic performance towards the oxygen evolution reaction at 15–25 mol% Ru.

$Ir_xRu_yTa_zO_2$ nanocrystalline and amorphous powders were prepared by a hydrolysis method. These oxides exhibited high active surface areas and supercapacitor like properties with the electrode capacitance typically around 200-300 F g^{-1}. No evidence was found to suggest that tantalum oxide forms solid solutions with iridium or ruthenium oxides. It was found however, that the lattice parameters of the rutile oxide in $Ir_xRu_yTa_zO_2$ samples, can be explained by a solid solution between IrO_2 and RuO_2. Electrochemical measurements showed that additions of tantalum decreased the electrochemically active surface area, as did high levels of ruthenium. At intermediate ruthenium contents, it was shown that both the low current and high current performance in a PEM water electrolysis cell was very high. Additions of up to 20 mol% Ta are possible without significantly decreasing the performance.

X-ray absorption spectroscopy was used to examine a range of oxide electrocatalysts using both ex-situ and in-situ measurements. The in-situ measurements were performed on oxide electrodes polarised in aqueous 0.5 M H_2SO_4 electrolyte. The ex-situ measurements on $Ir_xSn_{1-x}O_2$ showed that it is unlikely that Ir and Sn are atomically mixed as there was no evidence to suggest that Sn is within the first few coordination shells of the Ir. In contrast, for $Ir_xRu_{1-x}O_2$, Ru was found in the first few Ir–metal coordination shells. Electrochemical measurements showed that for amorphous IrO_2,

increasing the electrode potential from 0.5 to 1.4 V causes there to be more d-orbital vacancies in the iridium atoms. A valence change (probably $Ir^{3+} \rightarrow Ir^{4+}$) also occurred between 0.9 and 1.0 V vs RHE and there was no evidence to suggest that the iridium was present in any higher oxidation state. From the EXAFS analysis, it was found that the Ir–O bond length decreased by 0.05 Å as the potential increased from 0.5 to 1.4 V vs RHE. This is in good agreement with the expected bond length change due to valence change.

Contents

List of Figures

List of Tables

Chapter 1

Introduction

1.1 Hydrogen as an energy carrier

The need for a new energy carrier is well established and there is no doubt that the worlds current use of hydrocarbons as a primary energy source is not sustainable [1]. The increasing world energy demand, the current reliance on non renewable energy sources, and the environmental pressures caused from the use of these non renewable energy sources, all indicate that alternative energy sources need to be investigated and implemented. There is however large debate on how and when the "new energy age" will begin.

Hydrogen as an energy carrier is by far the most attractive option, with many ways to produce and utilise hydrogen. When hydrogen is combusted, either electrochemically in a fuel cell or conventionally in an internal combustion engine, there is no carbon emissions with pure water as the product.

An idealised "energy cycle" incorporating hydrogen as the energy carrier is shown in Figure 1.1. In this cycle, electricity from renewable energy sources, is used to electrochemically split water into hydrogen and oxygen. The hydrogen may then be stored, before being electrochemically oxidised in a fuel cell to form electric power and water. The only input to this cycle is the clean renewable energy and the only output is electric power.

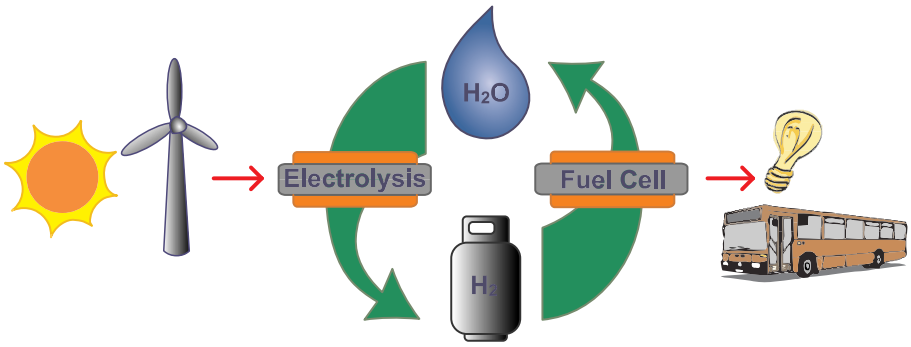

Figure 1.1: Ideal energy cycle involving hydrogen

1.2 Hydrogen production

Hydrogen can be produced in many ways, for example via the processing of hydrocarbons (e.g. steam reforming), by water electrolysis, photochemical reactions, or by biological processes. When water electrolysis is carried out using renewable energy (e.g. Hydro, Wind, Solar) the hydrogen can be considered as a completely renewable and clean energy carrier. It is important to remember that hydrogen is only the energy carrier and therefore electrochemically produced hydrogen is only as clean as the primary energy source.

Water electrolysis offers several advantages over other production methods such as steam reforming (Table 1.1). There are of course some challenges as well (Table 1.2).

Table 1.1: Advantages of water electrolysis for hydrogen production

No carbon emissions
Very pure hydrogen (no CO poisoning of fuel cell catalysts)
No dependence on hydrocarbon sources
Small scale / real time hydrogen supply is simple
Utilises renewable primary energy sources
Storage solution for renewable primary energy
Pure oxygen as a by-product

Water electrolysis is a well studied process, and as with fuel cells, the different

Table 1.2: Challenges of water electrolysis for hydrogen production

Need inexpensive renewable energy sources
Need hydrogen storage for fluctuating primary energy supplies
Technologies can be expensive

technologies can be grouped either by operating temperature or electrolyte, e.g. high temperature (Solid oxide electrolytes), and low temperature (Liquid Alkali or Solid polymer electrolytes). Recently solid polymer electrolyte (SPE) or more specifically proton exchange membrane (PEM) electrolyser systems have become interesting as a production method for carbon free hydrogen [2]. These PEM systems offer several advantages compared to the traditional alkali based systems (Table 1.3).

Table 1.3: Advantages of PEM electrolysis for hydrogen production

Higher performance / efficiency
Much higher current densities (up to 13 A cm^{-2} reported [3])
Wide range of current densities = flexible production rate
Very pure H_2 and O_2
Greater safety (no circulating caustic electrolyte) [4]
High differential pressure across membrane is possible [4]
Inherent gas separation by membrane electrolyte [4]
Possibility of combined fuel cell / electrolyser [5]

1.3 PEM water electrolysis

A schematic of a PEM water electrolysis cell is shown in Figure 1.2. The PEM water electrolysis cell consists primarily of a proton exchange membrane on which the anode and cathode are bonded. These electrodes are normally a composite of electrocatalytic particles and electrolyte polymer. Normally different electrocatalysts are utilised for the anode (eg. IrO_2) and cathode (eg. Pt). When the electrode layers are bonded to membrane, it is known as the membrane electrode assembly (MEA). The electrical contact and mechanical support is established with porous backings like metallic meshes or sinters.

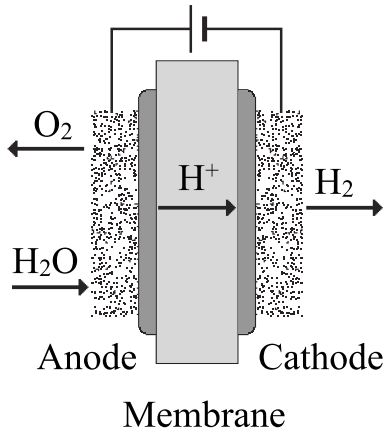

Figure 1.2: PEM water electrolyser schematic

Presently there is no large scale use of PEM water electrolysis systems, with only a very few commercial systems available [6]. The restricting aspects of these systems is the high cost of the materials such as the electrolyte membrane and noble metal based electrocatalysts, as well as the complex system components to ensure safe and reliable operation.

Recent work at the Department of Materials Technology, NTNU, has clearly showed that the oxygen evolution overpotential is much larger than the hydrogen evolution overpotential [7]. For this reason this work has concentrated on the anode electrocatalyst development.

1.4 Present work description

As stated above, the anode electrocatalyst is the focus of this work. As there is very few commercial PEM water electrolysis systems available, there are no commercial electrocatalysts suitable for high performance anodes. Therefore the majority of this work is dedicated to the synthesis and characterisation of suitable anode materials. Based on the findings of Rasten [7], IrO_2 was chosen as the base material for the electrocatalyst particles. In addition to the development of materials suitable for the oxygen evolution reaction, considerable work has been carried out to explore various physico-chemical characterisation methods. These methods have been used to help develop

the electrocatalysts and synthesis methods, as well as understanding the overall electrocatalysis process of mixed oxides during oxygen evolution.

The main objectives of the work is as follows:

- Review of possible synthesis methods
- Preparation of mixed oxides based on iridium oxide
- Characterisation of mixed oxides by electrochemical methods
- Characterisation of mixed oxides by physico-chemical methods
- Performance analysis of developed electrocatalysts in a PEM water electrolyser

1.5 Thesis outline

The majority of the following chapters are or will be published in relevant international journals and are included in an "article" format. Therefore some introduction and experimental details is unavoidably repeated. The first chapters are present in order to give a larger overview of the necessary theory and literature, than which is found in the result chapters.

Chapter 2

Theory and Background

2.1 Principles of water electrolysis

The principles behind any water electrolysis system are simple: water is electrochemically split into hydrogen at the cathode and oxygen at the anode. In PEM water electrolysis this is achieved by supplying water to the anode where it is decomposed into oxygen (or firstly oxygen intermediates), protons, and electrons. The protons are transported through the proton conductive membrane to the cathode. The electrons exit the cell via the external circuit, which supplies the driving force (i.e. cell potential) for the reaction. At the cathode the electrons and protons re-combine to give hydrogen gas. This is visually shown in Figure 1.2 with the electrode and cell reactions given by equations 2.1–2.3.

$$H_2O \rightarrow \frac{1}{2}O_2 + 2H^+ + 2e^- \qquad (Anode) \tag{2.1}$$

$$2H^+ + 2e^- \rightarrow H_2 \qquad (Cathode) \tag{2.2}$$

$$H_2O \rightarrow \frac{1}{2}O_2 + H_2 \qquad (Cell) \tag{2.3}$$

2.2 Thermodynamics and kinetics

Both thermodynamics and reaction kinetics should be considered when electrochemically splitting water into hydrogen and oxygen.

The Gibbs free energy (ΔG) for the net reaction for producing hydrogen and oxygen by water electrolysis is given by:

$$\begin{aligned} \Delta G &= \mu_{H_{2(g)}} + \frac{1}{2}\mu_{O_{2(g)}} - \mu_{H_2O_{(l)}} \\ &= \Delta G^\circ + RT\ln(p_{H_2} p_{O_2}^{\frac{1}{2}}) \end{aligned} \tag{2.4}$$

where $\mu_{H_{2(g)}}$, $\mu_{O_{2(g)}}$, and $\mu_{H_2O_{(l)}}$ are the chemical potentials of hydrogen, oxygen and water respectively, p_{H_2} and p_{O_2} are the partial pressures of hydrogen and oxygen respectively and ΔG° is the Gibbs free energy at standard conditions (1 atm, 25°).

The reversible potential to electrochemically split water can be found using the Nernst equation:

$$\begin{aligned} E^{rev} &= -\frac{\Delta G}{nF} \\ &= -\frac{\Delta G^\circ}{nF} - \frac{RT}{nF}\ln(p_{H_2} p_{O_2}^{\frac{1}{2}}) \\ &= E^\circ - \frac{RT}{nF}\ln(p_{H_2} p_{O_2}^{\frac{1}{2}}) \end{aligned} \tag{2.5}$$

where n is the number of electrons involved, R is the gas constant, T is temperature (K), F is the Faraday constant, and E° is the standard potential. At standard conditions (298 K, 1 atm) $E^{rev} = 1.23V$ which constitutes the lowest possible applied potential between any two electrodes in order to split water.

The energy balance for the cell reaction may also be written, with the energy required to break and form molecular bonds and to bring the reactants to their reference states being the enthalpy (ΔH) [8]:

$$\Delta G = \Delta H - T\Delta S \tag{2.6}$$

giving (at standard conditions):

$$U_{tn} = -\frac{\Delta H}{nF} \tag{2.7}$$

where U_{tn} is the thermoneutral potential difference. When the cell potential $E_{cell} < U_{tn}$ the cell absorbs heat from the environment, whereas if $E_{cell} > U_{tn}$, heat is lost from the cell.

Efficiencies for the overall reaction can also be written with the thermal energy efficiency defined as:

$$\epsilon_{\Delta H} = \frac{U_{tn}}{E_{cell}} \tag{2.8}$$

and the energy efficiency based on Gibbs free energy defined as:

$$\epsilon_{\Delta G} = \frac{E^{rev}}{E_{cell}} \tag{2.9}$$

Although thermodynamics gives the minimum potential required to split water, due to the kinetics of the electrochemical reactions there will always be overpotentials decreasing the efficiency.

$$E_{cell} = E^{rev} + \eta_{anode} - \eta_{cathode} + IR \tag{2.10}$$

where E_{cell}, η_{anode}, $\eta_{cathode}$, and IR represent the actual cell potential, the anodic overpotential, the cathodic overpotential, and the voltage gain due to the cell ohmic resistance.

Both the overpotentials and the ohmic resistance vary with current density. The resistance is given by Ohm's law, whereas the overpotentials can be given by the Tafel equation (which is a simplification of the Butler-Volmer equation):

$$\eta_{\text{anode}} = \frac{\mathrm{RT}}{\alpha_{\mathrm{a}}\mathrm{nF}} \ln \frac{\mathrm{i}}{\mathrm{i}_0} \tag{2.11}$$

$$\eta_{\text{cathode}} = -\frac{\mathrm{RT}}{\alpha_{\mathrm{c}}\mathrm{nF}} \ln \frac{|\,\mathrm{i}\,|}{\mathrm{i}_0} \tag{2.12}$$

The terms $\frac{\mathrm{RT}}{\alpha \mathrm{nF}}$ is defined as the Tafel slope, which can be used to determine the reaction mechanism. Both the Tafel slope and the exchange current (i_0) are material dependent, and are the principle measures of specific electrocatalytic activity.

2.3 Reaction mechanisms

Of the two electrode reactions, only the anode or oxygen evolution reaction will be discussed. An overview of the cathode or hydrogen evolution reaction is available elsewhere [7].

2.3.1 The oxygen evolution reaction

The oxygen evolution reaction (as well as the oxygen reduction reaction as in a fuel cell) is one of the most studied electrochemical processes. Even so, this reaction and the mechanism is still not widely understood and very difficult to interpret, with Trasatti [9] suggesting that this is due to three main reasons.

- High energy reaction intermediates and complex pathways of high activation energy making the reaction very sensitive to the electrode surface properties
- At the potential ranges required, the electrode surface can go through dramatic changes
- As the electrodes change, the kinetics may also be time dependent

There have been many oxygen evolution reaction mechanisms proposed, however few actually take into consideration the nature of the electrode surface [9], which is critical for understanding the real reaction mechanism

(see point 2 above). Of course only oxide covered electrodes should be discussed in any mechanism as all metals will be covered by a thin oxide layer at the potentials required for oxygen evolution. As the metal-oxygen (M-O) bond is always stronger than the O–O dissolution energy, the reaction will always occur on an oxide surface [7]. Also the oxygen evolution reaction involves the formation and breakage of bonds between the metal and oxygen species [10], indicating that the electrocatalysis process includes some material transformation processes as well. This complex combination of reactions involving surface species and material transformations, has lead to the formation of a so-called Volcano plot (Figure 2.1) in which the electrocatalytic activity (measured as the anodic overpotential) is related to the enthalpy for the oxide to form a higher oxidation state from a lower oxidation state (ΔH_t°) [10]. It is seen that materials with intermediate values of ΔH_t° show the best overall activity, whereas materials whose ΔH_t° is high are too easily oxidised and therefore the intermediates bind too strongly. Likewise those with low ΔH_t° are difficult or impossible to oxidise (eg. TiO_2 and PbO_2) and therefore the intermediates are adsorbed too weakly [9].

Rasiyah and Tseung have also correlated the electrocatalytic activity of electrodes towards the oxygen evolution reaction with the redox potential of the metal present in the active oxide phase [11]. The ability of the oxide to undergo solid state redox transitions, is clearly important in respect to the materials electrocatalytic activity. Matsumoto and Sato suggest that the strength of the M–O bond in the various intermediates is critical in determining the rate of desorption and/or adsorption steps in the oxygen evolution mechanism [12]. They also suggest that rate of electron transfer follows the Franck-Condon principle, in which the electron transfer is controlled by the density of electron states at the Fermi level and the degree of orbital overlapping of the active sites and adsorbed intermediates [12]. Although the reaction occurs on a quite different surface [13], studies of the oxygen reduction reaction have shown a dependence of the electrocatalytic activity (measured as the overpotential at a given current) on the Pt–Pt bond length and d-orbital vacancy [14], both of which can be directly measured by X-ray absorption spectroscopy.

There are many proposed reaction mechanisms for the oxygen evolution reaction, and Bockris has described a way to express the kinetics of an electrochemical reaction involving multiple steps, and applied this method to five mechanisms fro the oxygen evolution reaction [15]. Matsumoto and Sato

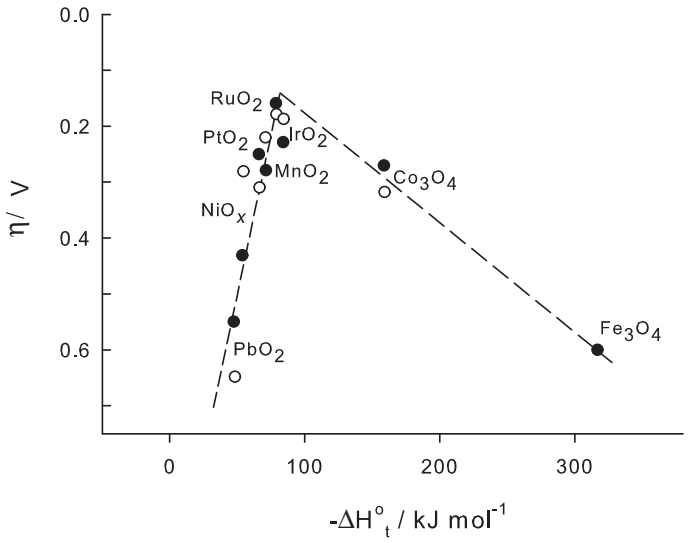

Figure 2.1: Electrocatalytic activity towards the oxygen evolution reaction of various oxides as a function of the enthalpy of the lower → higher oxide transition, in acid (○) and alkaline (●) solutions, (Reproduced with permission from [10])

also reviewed four popular oxygen evolution mechanisms [12]. The oxygen evolution mechanism is also discussed in a number of other publications [9, 16, 17, 18, 19]. Here three common mechanisms are shown:

The Electrochemical Oxide path:

$$S + H_2O \rightleftharpoons S - OH_{ads} + H^+ + e^- \tag{2.13}$$

$$S - OH_{ads} \rightleftharpoons S - O + H^+ + e^- \tag{2.14}$$

$$2S - O \rightarrow 2S + O_{2_{(g)}} \tag{2.15}$$

The Oxide path:

$$S + H_2O \rightleftharpoons S - OH_{ads} + H^+ + e^- \tag{2.16}$$
$$2S - OH_{ads} \rightleftharpoons S - O + S + H_2O \tag{2.17}$$
$$2S - O \rightarrow 2S + O_{2_{(g)}} \tag{2.18}$$

The Krasil'shchikov path:

$$S + H_2O \rightleftharpoons S - OH_{ads} + H^+ + e^- \tag{2.19}$$
$$S - OH_{ads} \rightleftharpoons S - O^- + H^+ \tag{2.20}$$
$$S - O^- \rightleftharpoons S - O + e^- \tag{2.21}$$
$$2S - O \rightarrow 2S + O_{2_{(g)}} \tag{2.22}$$

As previously mentioned, the reaction mechanism and rate determining step can be determined from analysis of the Tafel slope found from steady state polarisation measurements [15], although as pointed out by Matsumoto and Sato, this relies various assumptions being correct, including the assumption that the potential drop only occurs in the Helmholtz layer, which may be questioned if the oxides have semi-conducting properties [12]. The symmetry factor, β, which is often assumed to be 0.5, should also be treated carefully as several authors have shown that β may not always be 0.5 [17, 20].

2.4 Electrocatalysis and electrocatalysts

As pointed out in section 2.2, at standard conditions, thermodynamically only 1.23 V, are required to split water. Unfortunately due to the kinetics of the reactions, some extra energy (i.e. the overpotentials) is required in order to have the reaction proceed at a reasonable rate. The overpotentials are strongly dependent on the material used for the electrodes (i.e. the electrocatalysts). Therefore the electrocatalysts are chosen in order to decrease the overpotentials as well as to improve other important aspects of the process. Trasatti gives a comprehensive list of requirements for technological applications of electrodes or electrocatalysts (Table 2.1) [10]. An additional requirement for the electrocatalysts used in this work, is that they must be

easily formed in a electrocatalytic layer or MEA without losing their electrocatalytic performance. Factors influencing electrocatalysis at oxide surfaces has been discussed by Trasatti [10] as well as Matsumoto and Sato [12] (Table 2.2).

Table 2.1: Requirements of electrocatalysts [10]

High surface area
High electrical conduction
Good electrocatalytic properties
Long-term mechanical and chemical stability
Minimised gas bubble problems
Enhanced selectivity
Availability and low cost
Health safety

Table 2.2: Factors influencing electrocatalysis [10, 12]

Chemical nature of the catalyst
Morphology (dispersion, crystal size, crystallinity, lattice distortion etc.)
Non-stoichiometry (ionic defects, electronic defects, solid-state redox etc.)
Magnetic properties
Band structure of the oxide
Bond strength of M–O
Number of d-electrons
Effective Bohr magneton
Surface electronic structure
Geometric factors
Crystal-field stabilization energy
Synergetic effects (mixed and doped oxides)

As well as the composition and structure at the atomic level, another important catalyst structure is the particle structure. This will be especially important in systems where the catalyst is used in a catalytic layer consisting of catalytic particles (e.g. fuel cell or PEM water electrolysis catalytic layers). These particle structures will influence the dispersion or utilisation of active material, the total available surface area, layer morphology, product and reactant transport phenomena, layer and particle electronic conductivity, and layer mechanical stability. The particle structure may also influence atomic

behavior, with nano-sized size structures often having different properties to bulk materials [21], and supported catalysts showing different catalysis properties due to metal-support interactions [22]. Several possible catalyst structures are illustrated in Figure 2.2

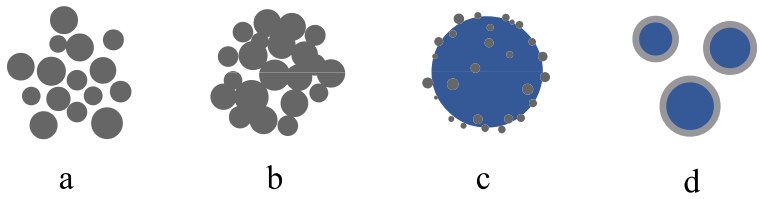

Figure 2.2: Possible catalyst structures

The structure in Figure 2.2a is simply mono dispersed particles (preferably sub micron or nano sized) with homogenous composition. These particles could be polycrystalline, single crystals, or amorphous. If these mono dispersed particles sinter or form agglomerates they could be illustrated by Figure 2.2b. These agglomerates should be porous to allow for good reactant and product transport as well as high surface areas. Agglomerates may be preferred over the mono dispersed particles if they impart improved layer properties such as higher electronic conductivity due to a more continuous electrical pathway through the electrocatalytic layer. Structure 2.2c is a classical supported catalyst structure, with very small active nano particles decorating a larger support particle or cluster. This enables a very high active area to be obtained as well as good layer properties due to the size of the support (i.e. larger macro pores between the larger support particles). If the support has high electrical conductivity this will also improve the overall layer conductivity. A good example of such a structure in the standard Pt/C fuel cell electrocatalysts [23]. The last structure (2.2d) is a so-called core-shell structure with a very thin layer of active material coating a inert or low activity core particle. This structure might also arise from strong surface segregation of the active species from structures “a” and “b” if these particles contained multiple species. As most materials used in this work contain expensive noble metals, by designing and synthesising oxides with the “supported catalyst” or “core-shell structure”, could greatly improve the utilisation of the expensive component, thus decreasing the noble metal loading and cost of the catalytic layers. Structures involving inert support

materials could also improve the properties of the electrocatalyst through interactions (either geometric or chemical) between the support material and the active phase.

2.4.1 Structure of rutile type oxides

Crystal structure of rutile type oxides

The materials of interest in this work are based on noble metal oxides such as IrO_2 which exhibit a tetragonal symmetry, commonly referred to as the rutile structure (Figure 2.3). In this oxide structure each metal atom is coordinated to 6 oxygen atoms. Each of these oxygen atoms is approximately located at the centre of an equilateral triangle of metal atoms. The "a" and "c" lattice parameters define the dimensions of the crystal unit cell. The "c" axis of the unit cell has the shortest M–M distance.

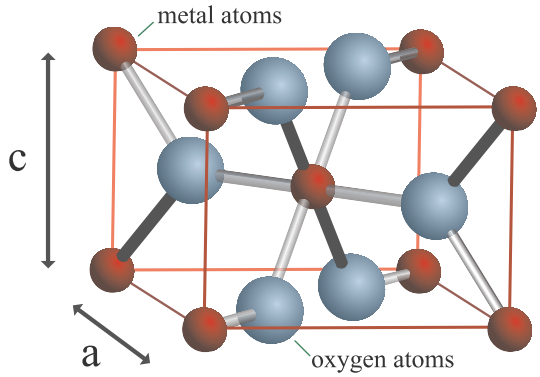

Figure 2.3: Unit cell of a Rutile oxide

Electronic structure of rutile type oxides

As mentioned above, a vital property of the electrocatalyst material is the electronic conductivity of the material. Naturally without this property no electrocatalytic activity will occur. For the conductive rutile oxides it is suggested that the electron orbitals are quite spread out and that the Fermi level falls near the middle of t-type energy band, which explains the metallic

conductivities found [24]. Several reviews have tabulated the electrical properties of many of the important electrocatalytic oxides [25, 12] and Rogers *et al* has reviewed the important crystal chemistry of the rutile-related structures [26]. Goodenough has also reviewed in detail the electronic structure of metallic oxides [27]. As many technological electrodes incorporate non conductive oxides such as TiO_2 as dispersing or stabilising agents, these may lead to the formation of semiconducting properties. This could lead to poor performance due to the formation of the space charge layer, even if overall the conductivity is suitable [12]. The potential drop in the space charge layer will be small for a p-type semiconductor under anodic polarisation due to the accumulation of holes at the oxide-electrolyte interface, and therefore p-type semiconductors are thought to be more useful than n-type semiconductors [12].

Acid-base properties of rutile type oxides

When an oxide is placed in contact with water, the surface will become covered in OH groups. The water (and dissociated water species) which is adjacent to the oxide surface will undergo some ordering following a model such as the Gouy-Chapman model of the electrical double layer. In this model, the ions, which balance the charge on the oxide, are non-uniformly distributed close to the electrode, with the ion concentration largest at the surface of the electrode, and then decreasing non-linearly away from the surface towards the bulk concentration [1]. This model may be acceptable as the OH groups are present in both phases and therefore physical separation of the oxide and water phases is practically impossible when considering the system on the scale of the double layer [28]. The structure of oxide–water interface therefore creates a potential difference between the oxide bulk and the water (or electrolyte) bulk.

The metal ions in oxide surfaces can be generally classed as Lewis acids (i.e.

[1]The Gouy-Chapman model results in a very large surface concentration of ions, due to the assumption that the ions are infinitely small and can get infinitely close to the surface of the electrode. In the Gouy-Chapman-Stern model, the Stern modification takes this inconsistency into account by combining the Helmholtz and Gouy-Chapman models. Thus the Gouy-Chapman-Stern model assumes a "plane of closest approach" (from the Helmholtz model) where some of excess ions reside and followed by a "diffuse layer" (from the Gouy-Chapman model).

an electron pair acceptor), however they will also act as Brønsted acids or bases (i.e. proton acceptors or donors) when in contact with water etc:

$$IrO_xO^- + 2H^+ \rightleftharpoons IrO_xOH + H^+ \rightleftharpoons IrO_xOH_2^+ \tag{2.23}$$

This proton transfer gives rise to surface charge, which is normally controlled by the pH of the electrolyte. Trasatti and co-workers have reviewed the acid-base properties of electrocatalytic oxides several times [9, 28, 29], and it is clear that this is an important area of electrocatalysis especially for the oxygen reactions. The surface charge of the oxide can be conveniently measured using a potentiometric titration or electrophoretic measurements. The quantity which is used to define the acid-base properties of the oxide is the point of zero charge (pzc) or isoelectric point (iep). The pzc is defined as the pH at which the net charge of the surface is zero. This also indicates that there will be no net charge in the diffuse or double layer, if no specific adsorption occurs (i.e. iep = pzc). Metal ions with high electronegativity withdraw electrons from the bonded OH groups and therefore cause protons to be more easily released. This implies that the acidity of metal oxide increases (pzc decreases) as the electronegativity of the metal increases. For mixed oxides the total pzc or acidity will lie somewhere between that for the pure oxides [30, 31]. The pzc of some important oxides is given in several reviews [28, 29] and the reader should consult these reviews for a more comprehensive overview.

2.5 Electrochemical analysis methods

2.5.1 Steady state polarisation

Steady state polarisation is a straight forward analysis method, in which the potential-current (E-I) relationship is measured either potentiometrically or galvanometrically. In order for the relationship to be at steady state, normally either a very slow scan or staircase type profile is used. Analysis of the polarisation curve, can be either to find the kinetic and mechanism parameters as given by equations 2.11 and 2.12 or the overall performance by comparing electrodes at a given overpotential or current density.

2.5.2 Cyclic voltammetry

Cyclic voltammetry (CV) is one of the most useful analysis tools used during this work. The voltammogram is a current response to a potential sweep and gives an electrochemical spectrum of the electrode surface, with information regarding the solid-state redox transitions, active area and the electrode capacitance being found.

Normally cyclic voltammetry is performed by sweeping the potential between two potential limits at a constant sweep rate (linear cyclic voltammetry). Often cyclic voltammetry is used to study electrode reactions involving electroactive species present in the electrolyte but also is extremely useful for following the adsorption of species on to the electrode (e.g. H_{ads} on Pt).

Reversible adsorption processes are characterised by the anodic and cathodic peaks being sharp and symmetrical with no significant difference in the peak potentials. For irreversible adsorption processes, the forward peak (i.e. adsorption of soluble species onto the electrode) becomes non-symmetric and the reverse desorption peak does not occur. For quasi-reversible reactions, there will be both peaks, however they will not be symmetric and there will be some difference between the peak potentials [32].

Cyclic voltammetry on platinum electrodes in acid are a classic example of adsorption processes. A typical voltammogram[2] of Pt in 0.5 M H_2SO_4 is shown in Figure 2.4. The voltammogram can be divided into two distinct regions: the hydrogen region (0-0.35 V) and the oxide region (starting at 0.8 V during the anodic scan, and ending at 0.6 V during the cathodic scan). The peaks in the hydrogen region are attributed to the adsorption of hydrogen. Typically there are two of peak pairs, with the peaks around 0.12 V and 0.25 corresponding to weakly and strongly adsorbed hydrogen respectively. As the potential is swept anodically, a thin oxide layer begins to form on the platinum surface. During the scan in the cathodic direction, this oxide thin is reduced back to platinum metal giving rise to the strong cathodic peak around 0.7 V.

The active surface area of a platinum electrode can be estimated by calculating the charge associated with the hydrogen adsorption. This charge is found by integrating the voltammogram over the hydrogen adsorption po-

[2]Thanks to Frode Seland for this voltammogram

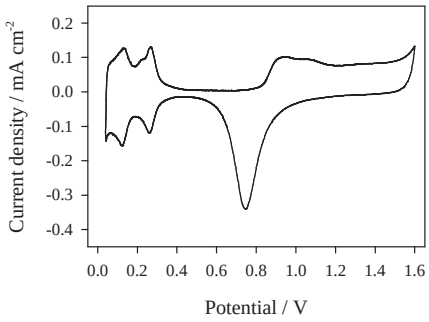

Figure 2.4: Voltammogram of polycrystalline Pt in 0.5 M H_2SO_4

tential range. This charge is then used to find the electrochemically active area by assuming that 1 cm^2 of Pt area has a hydrogen adsorption charge of 210 μC [33].

Noble metal oxides such as IrO_2 and RuO_2 have quite characteristics voltammograms[3] in acid as shown by Figures 2.5 and 2.6. In particular the voltammograms show the solid state redox transitions as peaks or broad waves. These redox transitions occur due to the adsorption and oxidation of oxygenated species from the electrolyte. These processes can be described as a pseudo capacitance, as the adsorbed species effectively store charge on the electrode surface. This differs from the double layer capacitance as this pseudo capacitance is a Faradaic process in which electrons can cross the double layer region.

The charging / adsorption process for iridium oxide is given by the following equation [34]:

$$IrO_a(OH)_b \rightleftharpoons IrO_{a+\delta}(OH)_{b-\delta} + \delta H^+ + \delta e^- \tag{2.24}$$

Normally the peaks found on a voltammogram of iridium oxide in acid are located around 0.8-0.9 and 1.25-1.35 V and correspond to the redox transitions of Ir^{3+}/Ir^{4+} and Ir^{4+}/Ir^{6+} respectively.

[3]These voltammograms were obtained with DSA type electrodes prepared by thermal decomposition of chloride precursors at 450 °C.

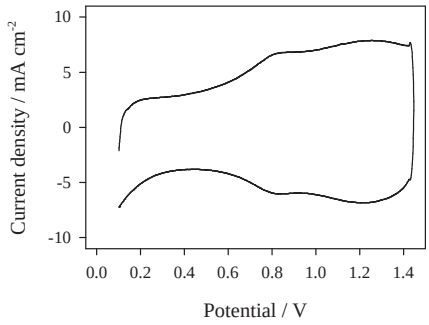

Figure 2.5: Voltammogram of an IrO_2 DSA electrode in 0.5 M H_2SO_4

Similarly to IrO_2, the charging process for RuO_2 is given by [34]:

$$RuO_a(H_20)_b \rightleftharpoons RuO_{a+\delta}(H_20)_{b-\sigma} + 2\delta H^+ + 2\delta e^- \tag{2.25}$$

This charging process is associated with three redox transitions, Ru^{2+}/Ru^{3+}, $Ru^{3+}/Ru^{4+}$and Ru^{4+}/Ru^{6+} resulting in three broad peaks in the oxide region of the voltammogram (Figure 2.6). At higher potentials ruthenium oxide electrodes can be further oxidised to Ru^{8+}, which can result in formation of volatile RuO_4.

IrO_2 and RuO_2 both are covered in a hydroxide layer when placed in an electrolyte. This hydroxide and lattice oxy groups enable the oxides to conduct protons via a "hopping" type mechanism. This implies that under some circumstances, protons can penetrate into the bulk of the oxide along crystal grain boundaries, pores, and defects, with the transport limited by the diffusion at these interfaces [35]. This observation gives rise to the "inner" and "outer" surface area of the oxides (see section 3.5.6).

2.5.3 Electrochemical impedance spectroscopy

During electrochemical impedance spectroscopy (EIS) or AC impedance, a small sinusoidal potential or current is applied to an electrode. Normally this small sinusoidal perturbation is superimposed over a fixed DC potential

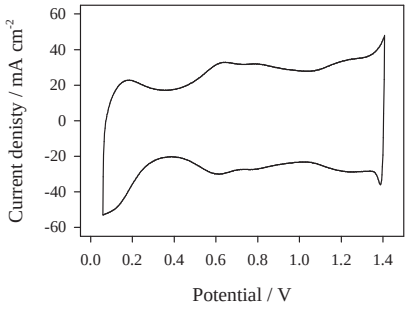

Figure 2.6: Voltammogram of a RuO_2 DSA electrode in 0.5 M H_2SO_4

or current. The frequency of this sinusoidal perturbation is then varied over a range of frequencies (typically kHz to mHz range) and the AC response of the electrode is recorded. The wide range of frequencies employed gives an impedance spectrum which includes a range of electrode processes, which normally cannot be singularly observed with DC measurements.

As the rates of electrochemical reaction steps have a exponential relationship with the electrode potential (i.e. the Butler-Volmer equation), the sinusoidal perturbation must be kept small, so that the system can be assumed to be linear. This limits the maximum AC amplitude to around 10 mV at room temperature [36].

The following discussion deals with a potential perturbation although the discussion is just as valid if a current perturbation is used. The potential, E(t) at a time t, can be written as:

$$\mathrm{E(t)} = \mathrm{E_{amp}} \sin(\omega \mathrm{t}) \tag{2.26}$$

where $\mathrm{E_{amp}}$ is the sinusoidal amplitude and ω is the angular frequency, with ω related to the frequency (f) by ω=2πf.

The current response, I(t), of the electrode is then given by:

$$\mathrm{I(t)} = \mathrm{I_{amp}} \sin(\omega \mathrm{t} + \phi) \tag{2.27}$$

where I_{amp} is the current sinusoidal amplitude and ϕ is the phase shift of the current sine wave in relation to the potential sine wave. This is illustrated in Figure 2.7, along with the phasor diagram showing the potential and current phasors rotating at a frequency given by ω and separated by the phase angle ϕ.

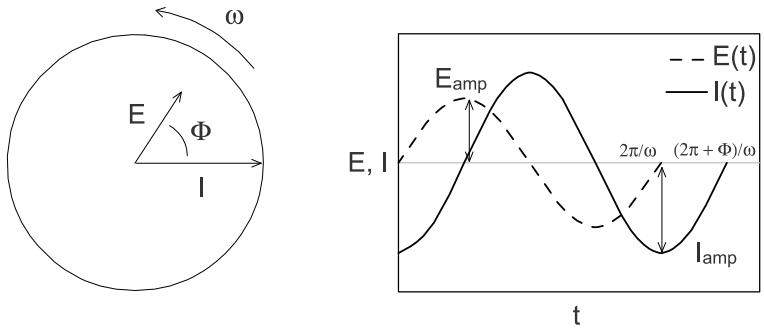

Figure 2.7: Illustration of E(t) and I(t) during a EIS measurement

The impedance of the electrode response is then given by the simple relationship:

$$| Z(\omega) | = \frac{E(\omega)}{I(\omega)} \tag{2.28}$$

Once solved, for easy data comparison the impedance is often written in complex notation, by separating the impedance into the real (Z_{real}) and imaginary (Z_{imag}) parts:

$$| Z(\omega) | = Z_{real} + jZ_{imag} \tag{2.29}$$

where $j = \sqrt{-1}$.

This relationship gives rise to the complex or Nyquist diagram where Z_{imag} is plotted against Z_{real}. Any point on the Nyquist diagram can be converted from the Z_{real} and Z_{imag} coordinates to the impedance modulus $| Z|$ and a phase angle using:

$$\phi = \arctan \frac{Z_{imag}}{Z_{real}} \tag{2.30}$$

$$| \, Z \, | = \sqrt{(Z_{real}^2 + Z_{imag}^2)} \tag{2.31}$$

To interpret electrochemical impedance spectrums, the electrochemical system are often represented by a electrical circuit, which has an equivalent impedance to the system under investigation. These circuits typically contain resistors (R), capacitors (C), and inductors (L). Other more complex elements are also used to better fit both theoretical and experimental data, like Warburg (W) elements which normally describe diffusion processes and constant phase elements (CPE) which can be used to help describe porous or rough electrodes [37].

The impedance of a resistor (Z_R) is simply taken from Ohm's Law:

$$I = \frac{E}{R} = \frac{E_{amp} \sin(\omega t)}{R} \tag{2.32}$$

therefore

$$Z_R = \frac{E}{I} = \frac{E_{amp} \sin(\omega t)}{\frac{E_{amp} \sin(\omega t)}{R}} = R \tag{2.33}$$

Therefore the impedance modules, $|Z| = R$ and ϕ=0. The impedance of a capacitor (Z_C) is a little more complicated to derive (see [36]) and is given by:

$$Z_C = \frac{1}{j\omega C} \tag{2.34}$$

It should be noted that the Z_C only has an imaginary part and then using equation 2.30 we see that the phase angle is constant at 90 degrees. Similarly the impedance of an inductor (Z_L) has only an imaginary part and is given by:

$$Z_L = j\omega L \tag{2.35}$$

The impedance of the CPE (Z_{CPE}) is given by:

$$Z_{CPE} = \frac{1}{B(j\omega)^{\alpha}} \tag{2.36}$$

where B is a frequency independent term, and α is a constant between 0 and 1. If $\alpha = 0$, Z_{CPE}=Z_R, if $\alpha = 1$, Z_{CPE}=Z_C and if $\alpha = 0.5$, Z_{CPE}=Z_W. For porous or rough electrodes normally $0.5 < \alpha < 1$.

For any equivalent circuit the total impedance is given by the addition of impedance terms for elements in series and for parallel elements the addition of the reciprocal impedance for each element.

$$Z_{Total} = \sum_{i=1}^{n} Z_{s_i} \tag{2.37}$$

$$\frac{1}{Z_{Total}} = \sum_{i=1}^{n} \frac{1}{Z_{p_i}} \tag{2.38}$$

where Z_s is the impedance of elements in series and Z_p is the impedance of elements which are in parallel.

The most common equivalent circuit is known as Randles circuit and is shown in Figure 2.8 along with the corresponding Nyquist diagram. In this circuit the resistor R_s, is ascribed to the ohmic resistance between the working electrode and the reference electrode. The capacitance, C, refers to the double layer capacitance and the resistance R_{ct} refers to the charge transfer resistance for the electrode reaction. This charge transfer resistance decreases with increasing overpotential, and also decreases with increased exchange current density.

R_s is found from the high frequency measurements, by letting $f \to \infty$ and using the equation for $Z_{Randles}$ which is found by using equations 2.33, 2.34, 2.37, and 2.38.

$$Z_{Randles} = Z_{R_s} + (\frac{1}{Z_C} + \frac{1}{Z_{R_{ct}}})^{-1} \tag{2.39}$$

$$= R_s + ((j\omega C) + \frac{1}{R_{ct}})^{-1} \tag{2.40}$$

In figure 2.8, R_s is seen to be the high frequency intercept with the real axis. At low frequencies, $Z_C \rightarrow \infty$ so that the total impedance, $Z_{Randles} \rightarrow R_s + R_{ct}$ which is found on the Nyquist diagram as the low frequency intercept with the real axis.

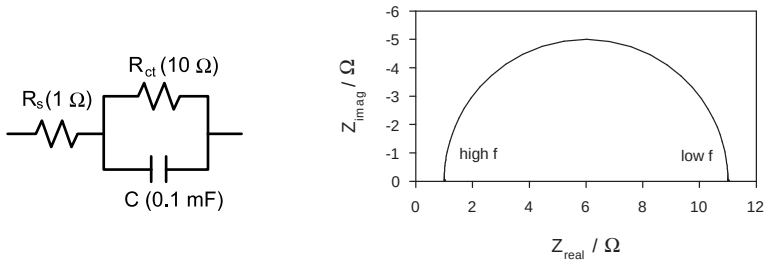

Figure 2.8: Randles circuit and corresponding Nyquist diagram

Any further EIS theory will be reserved for later chapters when necessary.

2.6 Physicochemical analysis techniques

2.6.1 Electron microscopy

Scanning electron microscopy

Scanning electron microscopy (SEM), is a convenient method to assess the morphology and element distribution of electrodes. Electron microscopy is based on using an electron beam to probe the surface (or bulk as in TEM). The processes which occur in electron microscopy can be illustrated by Figure 2.9. In SEM the primary electron beam is scanned across the surface of a sample and either the secondary or backscattered electrons emitted from the sample are measured. Secondary electrons arise due to non-elastic collisions between the primary electron beam and the outer electrons of the sample, with these outer electrons ejected from the sample as secondary electrons. These electrons have low energy < 50eV and therefore must be close to the surface of the sample in order to overcome the surface energy barrier and escape to the detector. This means that the secondary electrons are normally

used to give the surface morphology of the sample. Backscattered electrons are the primary electrons which have entered the sample, and through interactions with atomic nuclei (elastic spreading) are reflected back out of the sample. As this backscattering effect is proportional to the square of the atomic number, backscattered electrons give a image weighted by element composition. These images can be used to inspect element distribution in a sample. For a full discussion of scanning electron microscopy one may refer to Goldstein *et al* [38].

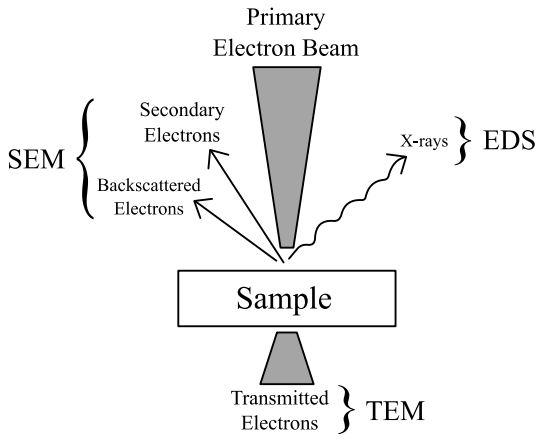

Figure 2.9: Principles of electron microscopy

Transmission electron microscopy

Transmission electron microscopy (TEM) utilises only the electrons transmitted through the sample (Figure 2.9). As the electron beam passes completely through the very thin sample, both an image and diffraction pattern can be observed. The diffraction pattern arises through the diffraction of the electron beam off the crystal lattice planes. For further TEM reading refer to Williams and Carter [39].

Energy dispersive spectroscopy

Energy dispersive spectroscopy (EDS) or Energy Dispersive X-ray analysis (EDX) is a method which uses the emitted X-rays from the sample for com-

position analysis. When the incoming electron beam penetrates the sample, the holes left by the ejected secondary electrons cause the atom to be unstable. In order to stabilise the atom, electrons from higher energy orbitals relax, filling the hole and emitting their excess energy in the form of X-rays. The X-rays emitted have a characteristic energy and wavelength from both the element from which the X-rays are emitted and also the orbital of the ejected secondary electron and the orbital of the electron which fills the hole. Thus the X-rays provides quantitative elemental analysis and can give spacial resolution down to a few micrometers at high acceleration voltages (>15kV) or much smaller analysis areas at low acceleration voltages [40].

2.6.2 X-ray diffraction

X-ray diffraction (XRD) is one of the oldest and most frequently used techniques for catalyst characterisation. The method allows both qualitative and quantitative crystal structure analysis as well as crystallite size and distribution analysis. The method is relatively simple and can be used to investigate a range of materials such as single crystals, polycrystalline solids, powders, and electrode layers.

X-rays have wavelengths in the angstrom range (Cu K_α=1.54 Å) and can penetrate into solids to probe internal structure (XRD information is mostly derived from the bulk and not the surface). X-ray diffraction occurs from the elastic scattering of the incoming X-rays by atoms in a periodic lattice (crystal). The scattered monochromatic X-rays interfere constructively when in phase, giving rise to intensity peaks. The Bragg relationship defines the diffraction angle as a function of the lattice spacing and wavelength (Equation 2.41) and is illustrated by Figure 2.10

$$\mathrm{n}\lambda = 2\mathrm{d}\sin\theta \quad ;\mathrm{n} = 1, 2, \mathrm{etc} \tag{2.41}$$

where d is the distance between crystal planes, λ is the wavelength of incoming X-rays, and θ is the angle between the sample and incoming X-rays.

Constructive interference of scattered X-rays occurs when the crystal lattice planes (with interplaner distance of d) are oriented at the angle θ to the incoming X-rays, which means only some particles in a powder sample contribute to the diffraction pattern. Polycrystalline samples have diffraction

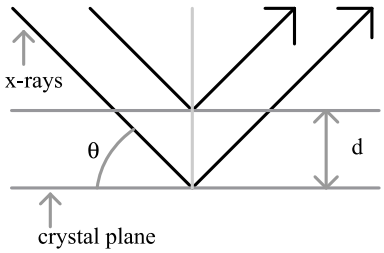

Figure 2.10: Diffraction in crystalline material

patterns with peaks given by the Bragg relationship for each crystal orientation, and therefore XRD provides a method to identify crystallographic phases in a catalyst sample. However it is important to remember that XRD only provides information from the bulk crystals present in the sample (not amorphous or surface structure). Sharp XRD peaks are only clear for long range lattice orders (>20nm) (Amorphous materials or very small crystals show very broad peaks or none at all). This fact however can be used to extract crystal dimension information from peak widths and shapes. It is seen that as peaks broaden as crystal size decreases, with this broadening due to incomplete destructive interference. The Scherrer formula relates crystal size to peak width (equation 2.42).

$$< \mathrm{L} >= \mathrm{K}\lambda/\beta\cos\theta \tag{2.42}$$

where K is a constant (often close to 1), <L> is the crystal size perpendicular to the reflection plane, and β is the peak width at half the maximum peak height (FWHM).

Although the Scherrer formula provides a simple and fast way of determining average crystal sizes, by profiling the peaks and using Fourier line-broadening analysis, more information can be obtained. Normally Gaussian profiles can be used to explain crystal strain and Cauchy (Lorentzian) profiles to explain crystal size. These can be combined into functions like Pseudo-Voigt (a linear combination of Gaussian and Cauchian profiles). From these profiling techniques the Warren-Averbach method can then be used to obtain crystal sizes and distributions as well as any possible lattice distortions. The Warren-Averbach method has been fully described previously by Warren [41]. The method is based on expressing the distribution of diffracted power

(P'$_2\theta$) per unit length on a Debye-Scherrer cone as a Fourier series. To use this analysis a standard which exhibits no broadening due to strain or size must be available, so that instrument broadening can be removed from the samples.

It is important to note that this method often gives different values in comparison to the Scherrer formula. This is because Warren-Averbach method gives the average crystal size as the average column length (which is averaged over all columns in each crystal and averaged over all crystals), whereas using the Scherrer formula gives a volumetric average.

The majority of the materials used in this work are based on the rutile oxide structure (Figure 2.3). A critical aspect of the structure of these materials is the mixing of multiple elements within the oxide matrix. It is believed to achieve the highest stability and to have electronic interactions between the elements, a solid solution should be formed. Solid solutions between the oxides means that the metals must occur within the same crystal matrix without preferential arrangement within this matrix. This implies that the elements which form solutions should have similar lattice parameters and form the same crystal structures. The elements also should have similar atomic radii (within 15 %) as suggested by the Hume-Rothery rule for solid solutions [42]. It is also possible that the crystal structures can be doped with foreign metal atoms which could be situated at metal or interstitial sites. By including metals within a certain metal oxide crystal, the crystal lattice parameters will change, and some crystal strain may also occur.

2.6.3 X-ray photoelectron spectroscopy

X-ray photoelectron spectroscopy (XPS) is based on the photoelectric effect. X-ray radiation is directed at the sample in ultra high vacuum (UHV) conditions. The photoelectric effect occurs when a X-ray with energy hν is absorbed by elements in the sample and a photoelectron is emitted with a kinetic energy of E_k (Figure 2.11). The kinetic energy of the emitted photoelectron is measured allowing the binding energy (E_b) of the electron in its core state just after the X-ray excitation to be calculated (equation 2.43). Binding energies are characteristic for an element as well as the electronic state and environment that the element is in.

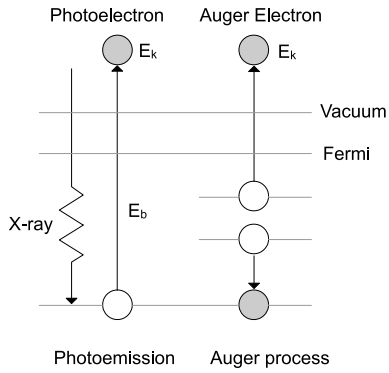

Figure 2.11: Processes during XPS

$$E_k = h\nu - E_b - \varphi \tag{2.43}$$

where φ is the work function of the spectrometer.

As shown in Figure 2.11, a second process also occurs during the photoemission process. This Auger process occurs due to the relaxation of the excited element. This relaxation occurs by an electron from a higher shell filling the core hole left by the photoelectron. The energy released during this transition is absorbed by another electron which is emitted from the sample with element specific kinetic energy. The Auger electrons on a typical XPS spectrum can easily be resolved by running the same spectrum with a different X-ray source energy (the photoelectron kinetic energy depends on the X-ray energy whereas the auger electron kinetic energies do not).

A significant reason that XPS is used to study catalysts, is the surface sensitivity of this method. Most useful photoelectrons have kinetic energies in the range of 0.2 to 15 keV, and due to scattering in the sample, only photoelectrons from the very top atomic layers have enough energy to escape the sample and reach the detector. Typically the depth which XPS probes is between 1.5 and 6 nm depending on the kinetic energy of the photoelectron. By comparing the intensity (or area) of photoelectron lines and correcting these by appropriate sensitivity factors, it is possible to calculate the surface composition of the sample. This measurement is very important for catalyst development, as catalysis is almost solely a surface specific process.

As mentioned above the binding energy of the photoelectron is not only element specific but also affected by the environment and oxidation state that the element is in. It is found that the binding energies increase with oxidation state and for a constant valence, binding energy increases with electronegativity of ligands (chemical shift). Chemical shifts are typically around 0-3 eV. The reason for these observed changes in binding energy are relatively straight forward. As a metal atom loses electrons (i.e. increases oxidation state), the remaining number of electrons feel a larger attractive force (per electron) from the nucleus, thus increasing the binding energy of these electrons. Similarly as the electronegativity of the ligand increases, the electron withdrawing effect of the ligand increases, and thus the electrons are harder to eject from the central atom.

2.6.4 X-ray absorption spectroscopy

X-ray Absorption spectroscopy (XAS) can be used to determine structural information of a sample. The benefit of XAS is that nearly all materials can be investigated as the method is not limited by things such as crystallinity or electronic conductivity. The absorption spectra contain absorption edges which are element specific and contain the fine structures called XANES (X-ray Absorption Near Edge Structure) and EXAFS (Extended X-ray Absorption Fine Structure). XANES is typically within approximately 30–50 eV from the main absorption edge and the EXAFS extends up to 1000 eV above the edge. As the absorption edges for elements are known with some accuracy, the element of interest can be probed by tuning the incoming X-rays to the appropriate energy and sweeping the energy from just below the edge to around 1000 eV above the edge. This implies that a synchrotron radiation source is normally required for XAS measurements.

Both XANES and EXAFS arise from the same physical processes, and the distinction is convenient for interpretation of the measurements. Whereas EXAFS gives information regarding the atomic distances, coordination number and types of nearest neighboring elements, XANES is useful for analysis of the oxidation state and coordination chemistry of the element of interest.

The principle concern of XAS measurements is how the absorption coefficient, μ varies with the X-ray energy. This absorption coefficient gives the probability of the absorption of X-rays and is related to the X-ray intensity

by Beer's Law:

$$I_t = I_0 e^{-\mu t} \tag{2.44}$$

where I_0 is the incoming X-ray intensity to the sample, I_t is the X-ray intensity transmitted through the sample and t is the sample thickness. The actual experimental setup and data acquisition required to perform XAS experiments is quite simple as shown in Figure 2.12, and involves basic X-ray intensity measurements before and after the sample (plus measurements after a reference if necessary). The X-ray fluorescence from the sample can also be measured using a suitable detector.

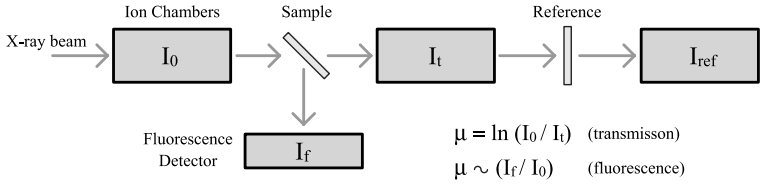

Figure 2.12: Schematic of basic experimental setup for XAS measurements

The XAS process involves the excitation of electrons from core levels to unoccupied states due to the absorption of an X-ray with an energy E. If E is equal to the binding energy of the core electron, E_0, a rapid rise in the probability for X-ray absorption occurs (this is the absorption edge). The absorption process coincides with the release of a photoelectron with wave number k, via the photoelectric effect. At higher X-ray energies, the transitions to continuum states occur [43]. For an isolated atom, the emitted photoelectron propagates away from the atom in a spherical wave, and gives rise to an smooth Absorption-Energy profile. If there is a neighboring atom, the photoelectron can be backscattered from this atom back towards the first central atom. As the absorption coefficient (or probability for absorption) depends on the availability of electronic states with the correct energy and momentum, this backscattered photoelectron alters the absorption coefficient or probability of absorption of the central atom. This gives rise to the X-ray absorption fine structure. This process can be illustrated by Figure 2.13, with (a) showing the incoming X-ray, (b) showing the photoelectron wave from the central atom, and (c) showing the backscattered waves interfering with the outgoing wave. The net result is a series of oscillations in

the absorption above the absorption edge. These oscillations can be used to determine the atomic number, distance and coordination number of the atoms surrounding the element whose absorption edge is being examined.

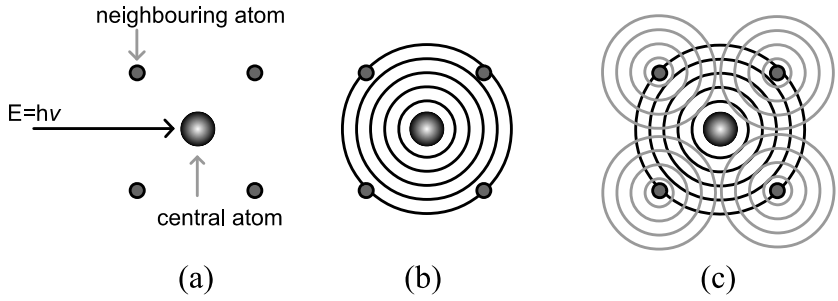

Figure 2.13: Schematic of processes occuring in EXAFS

Electrochemical cells for in-situ XAS studies

XAS experiments can be often performed on materials in-situ under real conditions, making this one major advantage over other analysis techniques. In-situ XAS during electrochemical processes are relatively straight forward provided a suitable spectroscopic cell can be developed. The main requirements of such cells is that the X-ray beam is not too affected (i.e. absorbed) by the electrolyte and other cell components and that the analysed area is homogenous. This implies the use of thin electrolytes and careful placement or choice of reference and counter electrodes. For transmission measurements, homogenous sample (working electrodes) must be used. For composite electrodes made from particles (e.g. fuel cell and PEM water electrolysis electrodes) the electrode layers must be free from pin holes which will cause uneven absorption over the samples area. Fluorescence measurements are also possible and may help achieve better experimental data, especially if the sample element is in low concentration.

XAS Data analysis

As stated above, EXAFS arises from the backscattered waves from neighbouring atoms interfering with the outgoing wave from the probed atom. A

typical EXAFS spectrum is given in Figure 2.14. We are interested in the energy-dependent oscillations in the absorption coefficient, $\mu(\mathrm{E})$, as these oscillations will give information regarding the neighbouring atoms. Thus the first step in data analysis is to describe the EXAFS as:

$$\chi(\mathrm{E}) = \frac{\mu(\mathrm{E}) - \mu_0(\mathrm{E})}{\Delta\mu_0(\mathrm{E}_0)} \tag{2.45}$$

The data is normalised by the edge step $\Delta\mu_0$ to allow the oscillations to be set to 1 absorption event and the background from all other absorbing material removed. The result is visually shown in Figure 2.15, with the curve $\mu_0(\mathrm{E})$ describing the smooth background which would occur for a single isolated atom. For convenience this normalised EXAFS, $\chi(\mathrm{E})$, is then expressed in terms of the photoelectron wavenumber (k) where:

$$\mathrm{k} = \sqrt{\frac{2\mathrm{m}(\mathrm{E} - \mathrm{E}_0)}{\hbar^2}} \tag{2.46}$$

where m is the electron mass and $\hbar$ is Plank's constant divided by 2. The EXAFS is then expressed as:

$$\chi(\mathrm{k}) = \chi(\mathrm{k}[\mathrm{E}]) \tag{2.47}$$

with this result shown in Figure 2.16. Often the data is weighted by multiplying $\chi(\mathrm{k})$ by k^2 or k^3, to amplify the oscillations at high wavenumbers (Figure 2.17).

In order to model the EXAFS data, the EXAFS equation is used:

$$\chi(\mathrm{k}) = \sum_{\mathrm{j}} \frac{\mathrm{N_j f_j(k)} e^{-2\mathrm{k}^2\sigma_\mathrm{j}^2}}{\mathrm{kR_j^2}} \sin[2\mathrm{kR_j} + \delta_\mathrm{j}(\mathrm{k})] \tag{2.48}$$

where f(k) and $\delta_\mathrm{j}(\mathrm{k})$ are the functions which describe the scattering amplitude and phase shift of the neighbouring or backscattering atoms. These functions depend on the atomic number of the scattering atoms. In the EXAFS equation, the distance to the neighbouring atoms (R) and the coordination number of the neighbouring atoms (N) can be found provided the

scattering properties of the neighbouring atoms are known. The mean-square disorder of the neighbouring atoms (σ^2) or Debye-Waller factor is also found, which describes the variation in R due to static or thermal disorder [44].

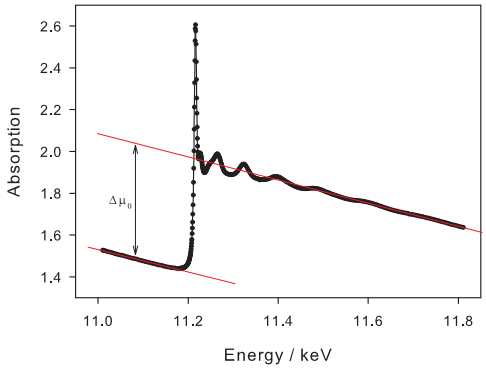

Figure 2.14: Raw EXAFS spectrum of $IrCl_3$

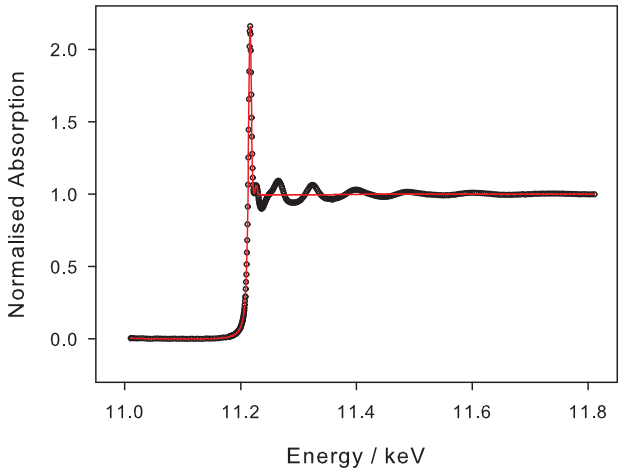

Figure 2.15: Normalised EXAFS spectrum of $IrCl_3$, ∘ - data, line - μ_0(E)

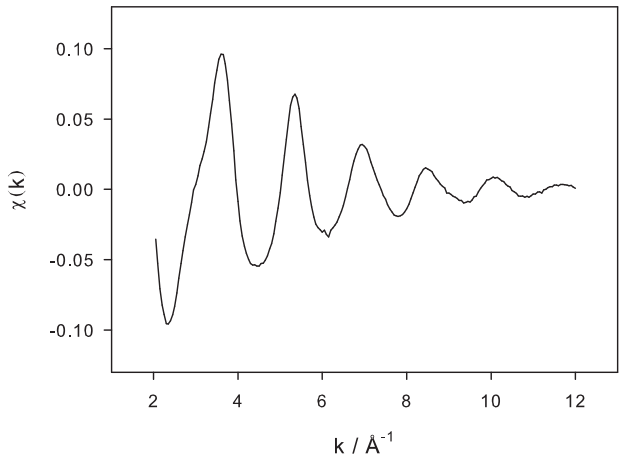

Figure 2.16: EXAFS spectrum of $IrCl_3$ - Wavenumber abscissa

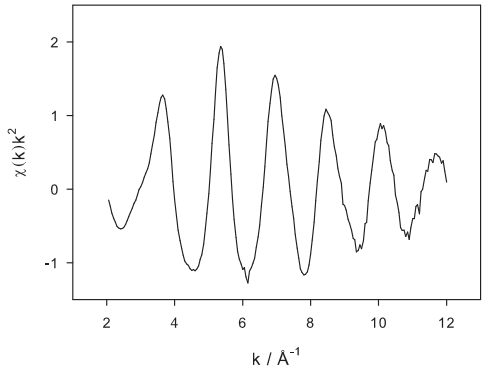

Figure 2.17: Weighted EXAFS spectrum of $IrCl_3$ - Wavenumber abscissa

2.6.5 BET surface area analysis

BET (Brunauer-Emmet-Teller) surface area is probably the most commonly used method to determine the surface area of materials such as catalysts. The method uses the BET isotherm, and the instrument measures the amount of N_2 adsorbed by the sample. The nitrogen is adsorbed by two ways, chemisorption and physical adsorption. Chemisorption involves the formation of chemical bonds, whereas only weak van der Waals forces are present in physical adsorption. The BET isothermal compensates for multi-layer adsorption, by assuming that the enthalpy of formation for the initial monolayer is larger than for the following layers. The BET equation relates the equilibrium pressure (P) with the volume of nitrogen (V_N) required to form a monolayer of adsorbed nitrogen over the surface of the sample.

$$\frac{\frac{P}{P_0}}{V_N(1-\frac{P}{P_0})} = \frac{1}{V_N c} + \frac{(c-1)(\frac{P}{P_0})}{V_N c} \tag{2.49}$$

where P_0 is the vapour pressure of nitrogen at standard conditions, and c is a term relating to the difference in enthalpy of formation between the initial monolayer and the following layers.

2.6.6 Temperature programmed techniques

Temperature programmed analysis encompasses several different techniques like Thermogravimetric analysis (TGA), Differential Scanning Calorimetry (DSC), and Temperature programmed reduction (TPR) and oxidation (TPO). These methods involve heating a sample with a programmed temperature profile (normally a linear sweep). For TGA, the samples mass is recorded with time, with the mass changes associated with reactions such as decompositions or oxidations. This technique is useful for following the decomposition of precursors to the final product (e.g. DSA electrodes [45]), thermal stability of materials or even the mass increase via the uptake of oxygen during an oxidation reaction. DSC is a similar method however the heat flow to or from the sample is measured. This can give information regarding glass transition temperatures, heat of reactions, heat of crystallisation etc. TPR and TPO are similar and are often used in combination when working

with catalyst samples. TPR involves the reduction of the sample in a flow of hydrogen gas and TPO involves the oxidation of the sample in oxygen. The reduction or oxidation reaction is often monitored by a thermal conductivity detector in the exit gas stream. These methods can be used to determine the degree of reduction or oxidation as well as the kinetics and mechanism of reduction and oxidation.

Chapter 3

Literature Review

3.1 PEM water electrolysis

Although PEM water electrolysis systems have been technologically feasible for many years, wide scale development and commercialisation has not been realised due to the expense of such systems [46]. The first PEM water electrolysers were developed by the General Electric Company during the 1960's [6].

A high current density SPE water electrolyser was investigated as a means of overcoming the disadvantage of the initial cost of these systems [3]. The cell consisted of a Nafion 117 electrolyte with a Pt cathode and a Pt-Ir anode. These metal electrocatalysts were deposited on the membrane by a chemical plating method (see section 3.4). The performance of the electrolyser was examined up to current densities of 13 A cm^{-2}, with free water circulation using gas-lift. The cell voltage at 13 A cm^{-2} was 5 V and corresponds to an energy efficiency $\epsilon_{\Delta G}$ of around 25%, whereas the cell voltage at 1 A cm^{-2} was approximately 1.9 V. It was shown that the IR drop contributed to about 90% of the cell voltage increase over the current density range of 1-5 A cm^{-2}. Water transport through the membrane was also examined and showed that the amount of water per proton did not change over the current density range of 1-10 A cm^{-2}.

Coatings of Pt and Ir were used in solid polymer electrolyte water electroly-

sers using a chemical reduction process [47]. The cell voltage using Pt as the anode and cathode (1.13 mg cm^{-2}) was measured to be around 2.15 V at 1 A cm^{-2} and 80 °C. By adding Ir to the anode at a loading of 0.2 mg cm^{-2}, the cell voltage was decreased to 1.75 V at the same operating conditions. This preparation method was tested for electrode areas up 150 cm^2 with the electrochemical performances maintained over 5000 hours. Further work showed that a Ru-Pt anode initially gave even better cell performance than the Pt-Ir anode, although the cell voltage quickly increase with time due to the dissolution of the Ru within the electrolyte [48].

Millet *et al* [4] discussed the design and performance of a PEM water electrolyser. The electrode materials were plated onto and slightly within the membrane by reducing a Pt precursor salt with sodium borohydride. This method is described further in section 3.4 and has been used to prepare MEA's with surface areas from 1 to 150 cm^2. Using a Pt / Nafion 117 / Pt cell the voltage was 2.2 V at 1 A cm^{-2} and 80 °C (cell area 10 cm^2). For larger cell areas of 50 cm^2 and 100 cm^2 the voltage was approximately 2.2 V and 5.5 V (two cell stack) respectively at 0.5 A cm^{-2}. High cell voltages was contributed to poor electrical connections which introduced an significant ohmic loss.

A similar plating method was used by others [49], and when the cell performance was tested using different anode catalysts and a Pt cathode catalyst, the anodic overvoltage was seen to increase in the order Ir < Rh < Rh-Pt < Pt-Ru < Pt < Pd. Ruthenium showed the greatest initial activity although was seen to corrode significantly during oxygen evolution. The best cell performance was obtained using an Ir anode and Pt cathode, resulting in a cell voltage of approximately 1.7 V at 1 A cm^{-2} and 90 °C.

Ruthenium dioxide was examined as the anode electrocatalysis in a solid polymer electrolyte water electrolyser [50]. The results showed that the RuO_2 used in this work was degraded quite quickly, corresponding to an increase in the cell voltage to 1.92 V from 1.73 V (at 1 A cm^{-2}, 82 °C) after 48 hours. The deterioration of the RuO_2 was thought to involve both electrical resistance and electrokinetic mechanism changes. A new Ru-based oxide anode was also tested and showed that even after 3000 hours of operation at 1 A cm^{-2} the cell voltage was comparable to a fresh RuO_2 anode at 1.76 V. Tafel behaviour was maintained after this operation time with the Tafel slope being approximately 112 mV dec^{-1} at current densities ranging from 20-2000

mA cm^{-2}. No further description was given regarding the preparation or nature of the anode catalyst. A Pt cathode and Nafion membrane was used in all experiments with cathode and anode catalyst loadings of 4 mg cm^{-2}.

Rasten [7] provided a study of various electrocatalysts for water electrolysis using proton exchange membranes. The bulk of the work concentrated on the oxygen evolution electrode where IrO_2, Ir-Ta mixed oxides, and Ir-Ru mixed oxides where used as the electrocatalysts. RuO_2 and Pt were also investigated as the catalysts for the hydrogen evolution reaction. The best performance for the anodic catalysts at current densities of 1 A cm^{-2} or below was observed using a Ir-Ta (85 mole% Ir) mixed oxide. At higher current densities the mixed Ir-Ru (60-80 mole%Ir) oxide electrocatalysts performed better. In terms of the hydrogen evolution reaction, Pt black was found to be most promising, with RuO_2 showing both low electrochemical activity and electrical conductivity. A cell voltage of 1.59 V was obtained at 1 A cm^{-2} and 90 °C using a noble metal loading of less than 2.4 mg cm^{-2} and a Nafion 115 membrane. It was thought by using a combination of the best electrodes found during this study, a cell voltage of less than 1.5 V is possible at the above conditions. A multi-disciplinary approach was suggested as the means forward in this area, particularly to understand the relationship between the electrochemical and physico-chemical properties of the oxide electrocatalysts.

A solid polymer electrolyser was developed using IrO_2 as the anode catalyst and Pt black as the cathode catalyst at a loading of 3 mg cm^{-2} [51]. The IrO_2 was prepared by the pyrolysis of Ir in oxygen at various temperatures, with the specific surface area of the IrO_2 decreasing with temperature. The cell voltage ranged from approximately 1.59 to 1.9 V at 1 A cm^{-2} and 80 °C for the prepared IrO_2 catalysts, with the IrO_2 prepared at 200 °C showing the best performance. The durability of the assemblies was shown by operating the cells for 5000 hr.

Since 1987 Mitsubishi Heavy Industries, Ltd. has been developing solid polymer water electrolyser technology [52]. A chemical plating technique was used to plate iridium metal onto each side of a Nafion membrane. Catalyst loading was varied between 0.5 and 2 mg cm^{-2} for cell areas of 50 cm^2 and showed that the cells could be operated at 3 A cm^{-2}. Cell voltages were measured to be 1.7 and 2.01 V for current densities of 1 and 3 A cm^{-2} respectively at 80 °C and an Ir loading of 1 mg cm^{-2}. Similar results were

found for cell areas of 200 cm^2.

A 50 cm^2 solid polymer electrolyte electrolyser was developed using a hot press method to adhere the catalyst film (catalyst + PTFE) to the membrane [53]. The thickness of the MEA decreased with the hot pressing temperature, resulting in a decrease in the cell voltage when using an anode catalyst of IrO_2 and a cathode catalyst of Pt black at loadings of 4 and 3 mg cm^{-2} respectively. The effect of anode catalyst type was also investigated over the current density range 0.5-4 A cm^{-2}. The results showed that the performance increased for the anode catalyst series RuO_2 (pyrolysed at 400 °C) > RuO_2 (pyrolysed at 600 °C) > Ir-Ru mixture (90 % Ir) > IrO_2 (pyrolysed at 200 °C) > Ir-Pt mixture (96.7 % Ir) > Ir black > Ir_2O_3 > Rh_2O_3 > Pt black. All these catalysts were loaded at 4 mg cm^{-2} with Pt black used as the cathode catalyst in all cases. The durability of the anode catalysts was investigated by monitoring the cell voltage over time. This showed the durability series as IrO_2 (pyrolysed at 200 °C) > Ir-Ru mixture (90 % Ir) = Ir-Pt mixture (96.7 % Ir) > RuO_2 (pyrolysed at 600 °C) > RuO_2 (pyrolysed at 400 °C). Membrane thickness and equivalent weight (EW) [1] was also examined and showed that thinner and lower EW membranes gave lower cell voltages, with this effect increased at higher current densities. Studies were also performed on the IrO_2 loading for the anode catalyst layer. The results showed that the increasing the loading beyond around 2.5 mg cm^{-2} gave little performance improvement with loadings of 3 mg cm^{-2} being suggested as adequate. Similar findings were found for the Pt black cathode catalyst with little changes observed above 0.5 mg cm^{-2}. Overall the best cell performance was found for the cell consisting of IrO_2 (pyrolysed at 200 °C, 3 mg cm^{-2}) and Pt black (0.5 mg cm^{-2}) as anode and cathode catalysts respectively. The membrane was 51 μm thick with a EW of 1000, and a hot pressing temperature of 140 °C was used. Cell voltages were 1.533 and 1.665 V for current densities of 1 and 3 A cm^{-2} respectively at 80 °C. The current supplier supports were Pt coated Ti sinter for the anode and gold plated stainless steel sinter for the cathode.

Based on the results above, a 2500 cm^2 solid polymer electrolyte electrolyser was developed [54]. The IrO_2 anode catalysts was prepared by reacting Na_2IrCl_6 with an aqueous NaOH solution. The resulting $Ir(OH)_4$ solution was purified, dried, and pyrolysed at 200 °C. The catalyst layer was prepared

[1] Membrane equivalent weight is defined as the weight of polymer per sulphonic group

by hot pressing the catalyst film (catalyst + PTFE) to the solid polymer electrolyte membrane with the catalyst loading being 3.6 and 3 mg cm^{-2} for the anode (IrO_2) and cathode (Pt black) respectively. At 80 °C the cell voltage was measured to be 1.54 and 1.74 V at 1 and 3 A cm^{-2} respectively. These high performance results were achieved despite the non-uniformity of the MEA thickness.

A high pressure solid polymer electrolyte water electrolyser was developed with Pt and Ir black serving as the anode catalyst and Pt black as the cathode catalyst [55]. The electrolyser showed a cell voltage of approximately 1.7 V at 1 A cm^{-2} and 90 °C at atmospheric pressure. At an elevated pressure of 2.5 MPa a slightly lower voltage was observed. The improvement in performance was contributed to the decrease in the anodic overvoltage.

The development of MEA's for a reversible solid polymer fuel cell was examined using Pt, Rh, Ir, and Ir-Ru mixed oxide, as the oxygen evolution electrocatalyst [56]. When operated as an electrolysis cell the anodic overvoltage increased in the order Ir-Ru mixed oxide < Ir < Rh < Pt. Due to Ir-Ru poor hydrogen oxidation activity, it was felt that Ir metal be used as a compromise between the oxygen evolution and hydrogen oxidation reactions. A cell voltage of approximately 1.52 V was achieved at a low current density of 0.1 A cm^{-2} when using Ir at the anode and Pt at the cathode for water electrolysis. During fuel cell operation a cell voltage of 0.8 V was measured at this same current density. High current densities (up to 25 A cm^{-2}) were also shown to be possible for the electrolysis cell although the ohmic losses meant that cell voltages were quite high (up to 6V).

Bifunctional electrocatalysts were examined for a regenerative PEM fuel cell [57]. The oxygen electrocatalyst was 50 wt% Pt black + 50 wt% IrO_2, and the hydrogen electrocatalyst was a Pt black layer. A transfer printing technique was used to apply the catalyst layer at a loading of 0.4 mg cm^{-2}. The platinum black was made by reducing H_2PtCl_6 and the IrO_2 made using the Adams fusion method. The water electrolysis performance was examined and showed a cell voltage of 1.71 V at 0.4 A cm^{-2} at a temperature of 80 °C.

Another regenerative PEM fuel cell was examined using a mixed Pt black + IrO_2 anode electrocatalyst, a Pt-black cathode at a loading of 8-10 mg cm^{-2}, and a Nafion 115 membrane [58]. The IrO_2 was prepared via a colloidal method whereby iridium hydroxide hydrate was prepared from

$H_2IrCl_6.xH_2O$, before being calcined at 200-700 °C to give IrO_2. The MEA was constructed by hot pressing the gas diffusion electrodes (porous catalyst-PTFE composite) to the Nafion membrane. The electrolysis performance was examined with the cell voltage around 1.74 V at 1 A cm^{-2}.

A review of PEM water electrolysis has also been conducted by Han *et al* [46] in which a range of issues such as membrane properties, electrocatalyst selection, and sensitivity to poisons was discussed.

3.1.1 Literature performance summary

Although there are many reports for PEM water electrolysis, the electrolysis conditions (e.g. temperature, membrane type) normally vary from group to group. In order to make some comparisons of performance, the available results have been tabulated 3.1, with the results normalised to 80 °C and a Nafion 115 membrane. The temperature correction was made using results obtained by Rasten [7] where a temperature coefficient of approximately 3.75 mV $°C^{-1}$ was found at a current density of 1 A cm^{-2}. This probably a conservative value compared with estimations from other results (5 [4], 4.8 [50], 3.05 [49], and 6 [57] mV $°C^{-1}$). To correct for the membrane type, the membrane IR-drop was first subtracted using a typical value found in literature (or the exact IR-drop when given) and then a typical ohmic resistance for Nafion 115 was added (150 mV at 1 A cm^{-2} and 80 °C).

Table 3.1: Summary of literature PEM water electrolysis performances

E_{cell}^{act} (V)	Anode/Cathode (mg cm^{-2})	E_{cell}^{est} V	Reference
1.590	Ir-Ru (70:30) oxide, 20% Pt/C (2.4)	1.623	[7]
1.645	Ir oxide, 10% Pt/C (2.4)	1.645	[7]
1.780	Ir-Ta oxide, 10% Pt/C (2.4)	1.572	[7]
1.533	Ir oxide, Pt black (3.5)	1.620	[53]
1.750	Pt-Ir, Pt (1)	1.750	[48]
1.725	Ru oxide, Pt (8)	1.675	[50]
1.720	Ir, Pt (3-6)	1.620	[49]
1.670	Ir-Ru oxide, 30% Pt/C (2.6)	1.708	[59]
1.590	Ir oxide, Pt black (3)	1.680	[51]

E_{cell}^{act} = Actual E_{cell} at 1 A cm^{-2}, E_{cell}^{est} = Estimated E_{cell} at 1 A cm^{-2},80 °C, Nafion115

As seen, the literature results are typically around 1.65-1.75 V at 1 A cm^{-2}, with only 2 results published with the cell potential below 1.6 V at any temperature and with any membrane. The excellent result from the WE-NET program [53] seems only possible due to the use of a thin membrane (52 μm) and therefore a low ohmic drop. When this value is corrected to give an estimate of the cell voltage if a Nafion 115 membrane was used, then the result is typical. This shows that reaching cell potentials less than 1.6 V at 1 A cm^{-2} and 80 °C using a Nafion 115 membrane is difficult although not impossible. Overall it is believed that the best published cell performance using Nafion 115 as the membrane and a temperature of 80 °C is 1.623 V at 1 A cm^{-2} which was reported by Rasten [7]. By careful development of the electrocatalyst, cell potentials less than 1.6 V could be possible.

3.2 Noble metal oxides as electrocatalysts

3.2.1 DSA vs. PEM water electrolysis electrodes

Since Beer first patented his work on dimensionally stabilised anodes (DSA) [60], almost all literature concerning noble metal oxides as electrocatalysts have been based on the DSA technology. For this reason the majority of literature reviewed in this section will be related to DSA layers. It is unclear exactly how much of this literature is applicable to this work, due to the differences between electrocatalytic particles and DSA layers. There is also a large variation in DSA electrodes prepared by different operators as shown by Trasatti [61].

Several distinct differences exist between electrocatalysts for DSA electrodes and PEM water electrolysis electrodes. These are outlined below:

- DSA electrocatalysts are generally formed “in-situ” on metallic substrates, whereas electrocatalysts for PEM water electrolysis electrodes are often synthesised first and then formed into the MEA.
- Many methods available for electrocatalyst particle synthesis, while DSA layers are almost solely limited to direct decomposition of precursors.
- The annealing conditions for a DSA electrode are limited to a small

temperature range. The temperature should be high enough to ensure complete decomposition of precursors and good mechanical adhesion to the substrate, but must not be too high in order to avoid the formation of a passivating metal oxide film between the substrate and the active layer.

- Nearly all DSA electrodes are prepared on titanium and therefore often contain significant levels of titanium in the oxide layer [62] even if this is not desired.
- DSA electrodes can be affected by the type of support material [63].

These points indicate that there will be significant differences between the properties of electrocatalyst prepared on DSA electrodes and PEM water electrolysis electrodes. Generally however, one can make observations based on a number of works, in order to suggest electrocatalyst compositions, annealing treatments, and expected outcomes or trends in the results.

3.2.2 Oxide powders as electrocatalysts

Other than the work conducted in PEM water electrolysers, very little attention has been paid to electrocatalysis on noble metal oxide powders due to the convenience of DSA type electrodes.

3.3 Preparation of oxide electrocatalysts

3.3.1 Thermal decomposition of noble metal precursors

DSA electrode layers are normally formed by direct decomposition of noble metal precursors onto metallic supports. Several investigations have been carried out to follow this process using temperature programmed analysis. The thermal decomposition of $IrCl_3.3H_2O$ in air was seen to occur via an overlapping two stage process, with the loss of crystal water at 100-200 °C and oxidation to IrO_2 above 600 °C [45]. Further decomposition to metallic iridium occurred just above 1000 °C. The decomposition of $RuCl_3.xH_2O$ showed a single continuous decomposition TGA profile, with RuO_2 found at around 400 °C [45]. The thermal decomposition of ruthenium (III) hydrate

was also investigated by DTA and TG analysis, and shown to yield Ru and $RuO_2.xH_2O$ at 100-150 °C [64]. The amorphous Ru metal is crystallised in nitrogen above 450 °C, and oxidised in air between 150 and 300 °C [64].

Normally chloride precursors are used to prepared DSA electrodes. This typically results in an oxide that contains significant levels of residual chlorine, which may have some effect on the properties of the electrode. To avoid this, nitrate salts [65] and organometallics [66] have also been investigated as precursors.

Thermal decomposition methods have been used for almost all possible mixed oxide films such as RuO_2-TiO_2 [67, 68], IrO_2-TiO_2 [67, 69], IrO_2-Ta_2O_5 [70], and IrO_2-SnO_2 [71], as well as IrO_2 [72]. Additives such as CeO_2 [73, 74], MnO_2 [75], Nb_2O_5 [74], Sb_2O_5 [76] and ZrO_2 [77] have also been added to standard DSA compositions via this method. Powders of RuO_2 have also been produced direct thermal decomposition [78, 79].

Role of the precursor and solution

An important aspect of DSA electrode preparation and in fact most preparation methods reviewed here, is the role of precursors and the solution, in the oxide formation process. Often this issue is neglected but will become increasingly significant when synthesising complex multi-element electrocatalysts.

A significant study of the role of precursors on the properties of Ir-Ta oxides has been carried out by Roginskaya *et al* [70]. The existence of Ir^{3+} and Ir^{4+} species in Ir-Ta chloride solutions (made from $IrCl_3$ and $TaCl_5$) was discussed and it was shown that increasing the Ta chloride content decreased the concentration of the $[IrCl_6]^{2-}$ complex. The concentration of the $[IrCl_6]^{2-}$ complex was seen to decrease with time and reached an equilibrium independent of the Ta concentration. It is believed that the $[IrCl_6]^{2-}$ complex may be reduced to the $[IrCl_6]^{3-}$ complex. A pure $H_2IrCl_6.4H_2O$ solution was shown to contain only $[IrCl_6]^{2-}$ and the EAS of this did not change with time. When pure $H_2IrCl_6.4H_2O$ was used to make a xIr^{4+} (100-x)Ta solution (x=10,30 mol%), the absorbance intensity was twice that of the pure $H_2IrCl_6.4H_2O$ solution. This was explained by the accumulation of the complex ions on the surface of the colloidal Ta species. Comparison of

the two Ir solutions (i.e. Ir^{3+}/Ir^{4+} and Ir^{4+}) revealed that in the Ir^{3+}/Ir^{4+} system the hydroxy and oxy forms of Ir are more rapidly produced due to the greater tendency for the Ir^{3+} to hydrolyse. The oxide films produced from these solutions were separated into two groups (x<30 and x≥30). The first group (x<30) showed that the predominate phase was β-Ta_2O_5 with two other rutile phases based on IrO_2. The predominate β-Ta_2O_5 phase was thought to be a solid solution containing small amounts of IrO_2 in the lattice. The two rutile phases were suggested to be pure IrO_2 and another solid solution of β-Ta_2O_5 and IrO_2. No differences were observed in the oxide properties based on the two different solutions when the iridium content was low. The second group of oxide films (x≥30) showed that the two systems (i.e. Ir^{3+}/Ir^{4+} and Ir^{4+}) can produce films with either 1 or 2 rutile phases from the Ir^{3+}/Ir^{4+} solution, or 3 rutile phases from the Ir^{4+} solution. These phases all have different crystallite size ranges. The crystallinity of the oxide films was also found to increase with iridium content and temperature. One phase was found to be IrO_2, and the other one or two solid solutions or mixed Ta+Ir oxide phases. These mixed phases were determined to be dispersed IrO_2 crystallites whose surfaces are modified by the Ta at the interface with Ta_2O_5, with the larger dispersion resulting in more modified IrO_2. The crystal growth of the IrO_2 was seen to be inhibited, a result of the crystals surface modification. These results suggest that the precursors in solution and the resulting intermediates can influence the morphology and structure of the oxide film. The dispersion of Ir complexes in the hydrated Ta oxide during the hydrolytic step of film formation is expected to be the cause of the films phase properties. The Ir^{3+} species interact more with the Ta complexes, so solutions containing more Ir^{3+} result in phases with more dispersed IrO_2 and therefore more surface modified IrO_2 with less IrO_2 crystal growth. The role hydrated precursors can also be mentioned in respect to the crystalline material distribution. The crystalline oxide formation begins from an amorphous phase, with the IrO_2 crystallising first. This results in an oxide film where the IrO_2 crystallites are held within a Ta_2O_5 phase or are coated by a Ta_2O_5 film.

In a precursor solution of Ti-Ir chloride the concentration of $[IrCl_6]^{2-}$ was found to increase with time [80]. This was contributed to the redox reaction of Ir^{3+} and Ti^{4+} to give Ir^{4+} (as $[IrCl_6]^{2-}$) and Ti^{3+}. This was supported by XPS analysis of the resulting oxide film, which showed that Ti was present in more than one oxidation state. Upon addition of $CeCl_3$ into the precursor

solution, the concentration of $[IrCl_6]^{2-}$ was observed to decrease with time, with the effect increasing with $CeCl_3$ concentration. This was suggested to be due to the reduction of the $[IrCl_6]^{2-}$ complex to $[IrCl_6]^{3-}$ by Ce^{3+}. Calculations suggested that the majority (79,7%) of the Ir was present as $[IrCl_6]^{3-}$. This is consistent with XPS analysis, which showed that the resulting oxide film contained Ir and Ce in +3 and +4 oxidation states.

Another study showed that the absorbance of the $[IrCl_6]^{2-}$ complex in a Ti-Ir chloride solution, increased with time and on heating [69]. The interaction of the Ir and Ti components only occurred at conditions at which polynuclear oxohydroxotitanium and colloidal forms of the hydrated titanium oxide were present. This interaction was considered to be a weak sorption between the $[IrCl_6]^{2-}$ complex and the surface of hydrated titanium oxide. This system is thought to differ from the Ru-Ti precursor system in that the Ir component exists as chloroiridate ion, and no aggregates of polymeric hydrate chloro-complexes are formed. The oxide layers prepared from the precursor solutions showed that 3 phases were formed. Two phases had a rutile structure and were suggested to be solid solutions of Ir and Ti oxides. The third phase was anatase (TiO_2) and only appeared in trace amounts when $IrO_2 > 30$ mol%. From IR analysis, one of the solid solution phases was thought to be based on partly hydrated IrO_2. The oxide films formed in this work were different in phase composition and morphology from Ru-Ti oxide films due to the interaction of the components in the precursor solutions.

For the precursor solutions of Ir-Ti oxide films the Ir complex reacts with the Ti species only when the conditions are such to form hydrated titanium oxides (HTO) [81]. As the $[IrCl_6]^{2-}$ complex has less tendency to hydrolyse compared to the Ru complexes, a significant amount of the $[IrCl_6]^{2-}$ stays isolated in solution. The final oxide films produced from these solutions shows two rutile phases. Analysis of these phases revealed that a true solid solution was produced unlike the RuO_2-TiO_2 films. The reason for this difference comes from the interaction of the Ir complex (unhydrolysed) with the HTO surface. This interaction leads to a finely dispersed Ir atoms in the titanium component and a solid solution phase of $(Ti,Ir)O_2$ with atomic substitution. The $[IrCl_6]^{2-}$ which does not interact with the HTO thermal decompose to IrO_2 leading to the observed second phase.

The effect of hydrated oxides in DSA-type oxide electrocatalysts was in-

vestigated [81]. Originally it was assumed that these DSA electrocatalysts consisted of crystalline material with stoichiometry close to RuO_2 and IrO_2, however it is shown that these electrode coatings contain significant levels of hydrated oxides [81]. This is contrary to the existing mechanism for chloride precursor decomposition where anhydrous oxides must be formed [45]. This suggests that the oxide formation may be a result of hydroxide decomposition as chlorides of Ir and Ru can be hydrolysed in the precursor solutions [81]. The degree of hydration of the chloride precursors was found to increase in the order Ir < Ru < Ti. The precursor solutions for RuO_2-TiO_2 films showed that the intensity of the Ru complexes increased with increasing Ti content. This was considered to be due to the polymerisation of the complexes or their sorption to the Ti colloids. The dried product formed from this solution revealed small clusters of hydrated RuO_2 on the surface of hydrated Ti oxide particles. Further thermal treatment results in aggregation of the Ru and Ti oxides into clusters linked by chloride ions, water and OH groups [81]. When the temperature was increased past 600 °C the OH^-, water, and chloride ions are removed and crystals start to grow based on the small clusters. Eventually two rutile phases are formed (TiO_2 and RuO_2).

A study was undertaken to investigate the properties of thermally prepared IrO_2 electrodes [72]. Ti supports were painted with $IrCl_3$ dissolved in either water or isopropanol. SEM showed no appreciable differences in the two layers formed from the two solvents, however the voltametric charge was significantly higher for the electrodes prepared form isopropanol. The dependence of the voltametric charge on the annealing temperature was similar for both solvents. This suggests that the solvent used in preparation of the precursor can contribute to the crystallinity and non-stoichiometry of the oxide layer [72].

The effect of the precursor on the electrocatalytic properties of thermally prepared RuO_2 was investigated [65]. In this work a comparison was made between an oxide electrode prepared from a chloride precursor and a nitrate precursor. The voltametric curves were practically identical in shape however the electrode prepared form the nitrate precursor had a voltametric charge approximately 17 times larger. This was assumed to be due to the surface roughness. Examination of Tafel slopes suggested that the lower crystallinity observed in the oxide formed from the nitrate, results in higher catalytic activity [65]. Overall the authors felt that the activity of RuO_x

arises from its specific chemical nature and defective structure, and not the possible residual presence of Cl in the oxides lattice.

Depth profiling of a RuO_2/TiO_2 coating was carried out and the effect of the Ru precursor salt was investigated [68]. The extent of surface enrichment was seen to be greater when the oxide is prepared using $RuCl_3.xH_2O$ compared to $Ru(NO)(NO_3)_3$ as the precursor. No study was performed to investigate the precursor interaction in this work. As shown, Ru/Ti oxides formed from the chloride precursor can show segregation of the Ti and Ru oxide components due to the interaction of the precursors in solution [81].

3.3.2 Preparation of electrocatalytic particles

This work is primarily concerned with the production of oxide powders, which then can be applied directly to a proton exchange membrane (PEM) or electrode support (e.g. porous titanium) to form a MEA. Several methods for preparing IrO_2 and RuO_2 based electrocatalysts powders will be discussed:

- Adams Fusion
- Sol-gel methods
- Polyol method
- Aqueous Hydrolysis

Adams Fusion method

Adams fusion method [82] is based on the oxidation of metal precursors with molten $NaNO_3$ as shown below.

$$H_2PtCl_6 + 6NaNO_3 \rightarrow 6NaCl + Pt(NO_3)_4 + 2HNO_3 \quad (3.1)$$

$$Pt(NO_3)_4 \rightarrow PtO_2 + 4NO_2 + O_2 \quad (3.2)$$

This method was later modified with a reported 25% reduction in preparation time of PtO_2 from spent catalyst [83]. It has also been used to produce IrO_2, IrO_2-Ta_2O_5 and RuO_2-IrO_2 [7] and SnO_2-RuO_2-IrO_2 powders [84] from their precursor salts for PEM water electrolysis applications.

Sol-Gel methods

Sol-gel chemistry has become a very important method in inorganic chemistry and material science. The method is based on the process of transforming a liquid based sol (normally colloidal) into a solid gel phase. This method can be used to make ultra-fine particles, dense solids, highly porous solids, and ceramic fibers.

Normally either inorganic metal salts (e.g. $IrCl_3$) or organic metal alkoxide or acetylacetonates (e.g. $Ir(OC_2H_5)_4$) are subjected to hydrolysis and polymerisation reactions. Often various catalysts (acetic acid, HCl, NH_3) are added to speed up or promote the hydrolysis step. The hydrolysis products can undergo condensation to form colloidal sols. These sols can be further polymerised to create 3-D matrix gels. Controlling the pH of the solution is the typical way of selecting either the polymerisation or hydrolysis processes, thus either synthesising small compact oxides or large inorganic polymer matrices. Upon drying the sols or gels, amorphous metal oxides form, which then can be further heat treated to crystallise the oxides. There are many references giving in-depth discussions regarding sol-gel chemistry [85, 86]. Noble metal oxides have been synthesised both as powders and as DSA type layers by sol-gel techniques.

A sol-gel method for producing RuO_2 based electrocatalysts was developed to avoid to complicated precursor chemistry, and resulting thermal processes of hydrolysis intermediates, which can form during the solvent evaporation / salt precipitation stage of DSA electrode manufacture [66]. The sol-gel method used here, tested three different Ru salt precursors added to the titanium isopropoxide solution. The resulting oxide was of the composition 30% RuO_2 and 70% TiO_2 and was deposited on a Ti or silica substrate as a thin film. The results showed that the method was reproducible in terms of the oxide properties. The effect of the Ru salt precursor on the morphology was clearly seen by SEM, with the annealing temperature having less effect. The authors suggested that the complex precursor chemistry seen in other preparation methods still exist in this method.

A mixed Ru/Ir oxide coating for the oxygen evolution reaction was prepared via an inorganic sol-gel method [87]. This was achieved by dissolving a mixture of Ru and Ir actylacetonates in solution of isopropanol and glacial acetic acid. The films were formed by painting on the sol from solution onto ti-

tanium plates. The films showed a very similar composition to the starting solution. The results also show that this method can produce highly homogeneous mixed oxides. The films formed via the inorganic sol-gel method showed a different surface morphology to films obtained from traditional thermal decomposition of the chloride precursors.

Ultrafine RuO_2-SnO_2 [88], RuO_2-TiO_2 [89], RuO_2-IrO_2-TiO_2 [90], IrO_2-SnO_2 [91], and IrO_2-Ta_2O_5 [92] oxide powders were produced using an inorganic sol-gel method. In this method the noble metal salt (i.e. $RuCl_3.3H_2O$) was dissolved in anhydrous ethanol. Sodium ethylate was added and the mixture refluxed at around 70-80 °C for 3-4 hours under N_2, forming the metal alkoxide. To this the second component was added as the metal tetraethoxide (e.g. $Sn(OC_2H_5)_4$). The mixture was hydrolysed by the addition of an ammonia-ethanol solution and then H_2O_2. The product was separated from the liquid, dried then calcined at high temperature. Several of these powders showed traces of metallic Ru [88, 89, 90] and Ir [92].

Ammonium hydrogen carbonate was added to a $RuCl_3.xH_2O$ solution containing polyethylene glycol, as a means of producing a ultrafine RuO_2 powder [93, 94]. The hydrolysis product (amorphous $RuO_2.xH_2O$) was separated from the solution, and can then be calcined to produce RuO_2 powder. The particle size can be controlled by the addition of polyethylene glycol, which partly inhibits the sol-gel reaction.

Another similar method to the sol-gel method is the polymeric precursor method or the Pechini method. This involves the polymerisation of organic monomers in the presence of metal ions and has been used to produce DSA type electrode layers. Once the polymer gel has formed the metal ions are homogeneously distributed through the polymer gel. The gel is calcined to form the metal oxide. The polymeric precursor method was investigated as a means of producing both RuO_2 films and powders [79]. Here the $RuCl_3.xH_2O$ was dissolved into a citric acid / ethylene glycol mixture. Films derived by the polymeric precursor method showed much higher anodic voltammetric charge and stability than a film derived from the thermal decomposition of chloride precursors.

This polymeric precursor method was compared with the inorganic sol-gel method and the traditional thermal decomposition method for the preparation of IrO_2 films on Ti [95]. The inorganic sol-gel coating solution was prepared from a solution of Ir actylacetonate, isopropanol, and acetic acid.

The PPM solution was prepared by dissolving $IrCl_3.3H_2O$ in a citric acid / ethylene glycol mixture. The morphology of the resulting films were all different as examined by SEM with the inorganic sol-gel method producing a homogeneous film with well-defined grains. The electrochemical behaviour of the electrodes of electrodes produced by the three methods was similar. The voltamograms of the three electrodes (performed in 0.5 H_2SO_4) showed that the electrode from the inorganic sol-gel method had redox peaks at 0.8 and 1.2 V which were much better defined, indicating that the film has a high degree of homogeneity and purity.

Polyol Method

The polyol method, has been widely used to prepare metallic particles by reducing the precursor salts in polyols such as ethylene glycol. In this process the polyol acts as the solvent and the reduction agent. It is thought that this process could be modified to produce metal oxide powders by thermally oxidising the metallic colloids/particles. The polyol method is a relatively simple way to synthesize nanosized noble metal colloids such as iridium or ruthenium well defined size distributions [96, 97]. Nanocrystalline alloys have also been successfully produced using this technique [97]. Often surfactants are added during this process to improve the properties of the resulting metallic colloids or particles [98]. The pH of the metallic colloid-polyol mixture has also been shown to affect the agglomeration process of the colloid [99]. Feldmann showed that by hydrolysis of polyol synthesised intermediates, nanoscale oxides could be prepared [100]. Currently it is believed that this process has not been extensively used to prepare intermediates suitable for thermally prepared oxides.

Aqueous hydrolysis

This method involves the hydrolysis of inorganic precursor salts in aqueous solutions. The resulting hydroxide, oxide, or hydrated oxide, and can further oxidised by chemical or thermal methods.

A method was discussed in which anhydrous RuO_2 was prepared by heating hydrous RuO_2 at various temperatures [101]. The hydrous RuO_2 was

precipitated from an aqueous solution containing Ru in the +7 oxidation state.

Pure IrO_2 was prepared by a chimie douce method process in which iridium (III) chloride was hydrolysed in a LiOH solution [102]. The effect of hydrolysis speed was examined by controlling the rate of pH change. It was observed that the first step to producing pure IrO_2 by this method was the hydrolysis of the hydrated iridium chloride resulting in $IrO_{1.45}(OH)_{1.10}$ $1.5H_2O$. The authors suggested that this method gave highly pure IrO_2 which unlike commercial IrO_2 powders was completely chlorine free. The structure was examined by EXAFS and shown to exhibit rutile structure with a perfectly ordered crystalline framework.

A ultrafine IrO_2 powder was synthesised from a colloidal precursor of iridium hydroxide hydrate [58] following a method for preparing $[Ir(OH_2)_6]^{3+}$ [103]. This hydrate precursor was prepared by dissolving $H_2IrCl_6.4H_2O$ in a NaOH solution. The Ir^{4+} chloride complex found in the solution was converted to the +3 complex, followed by the ligand and substitution reaction of Cl^- by OH^-. Upon addition of $HClO_4$ solution the iridium hydroxide hydrate was precipitated. This precipitate can be converted to IrO_2 through calcination. The IrO_2 was characterised by XRD, gas absorption, TGA, DTA, TEM and EPMA. TGA and DTA analysis showed that the precipitate was most likely $Ir(OH)_3(H_2O)_3$, and this dehydrated continously up to around 400 °C. A strong exothermal peak at 390-410 °C seen in the DTA was attributed to the final water loss and crystallisation into IrO_2. The surface area of the IrO_2 calcined at 400 °C was measured to be 38 m^2 g^{-1} and this area decreased with increasing temperatures. The IrO_2 particle size was approximately 30-50 nm compared with 10-20 nm for the Pt black, although the IrO_2 particles appeared to have much rougher surfaces.

A similar method was used to produce IrO_2 for a 2500 cm^2 solid polymer electrolyte membrane assembly [54]. This involved dissolving Na_2IrCl_6 in a NaOH solution to produced a $Ir(OH)_4$ solution. After purification and the removal of NaCl, the solution was dried and pyrolysed at 200 °C to give the IrO_2 catalyst.

3.4 Preparation of catalytic layers and MEA's

The preparation of catalytic layers on polymer electrolytes is widely discussed in PEM fuel cell and PEM water electrolysis literature. Generally there are several basic ways of preparing such layers.

- Electrocatalytic powders applied in an ink form to the membrane or the porous support material
- Electrocatalytic powders applied in a dry form to the membrane or the porous support material
- Electrocatalytic powders applied to a blank support (e.g. Teflon) and transferred to the membrane or the porous support material via hot pressing
- The electrocatalyst materials can be formed "in-situ" on the membrane by various plating methods

Each of these methods require their own set of optimised preparation conditions which probably also depended on the catalyst used (especially noble metal oxides vs. Carbon supported Pt)

The application of inks containing polymers and electrocatalytic particles has been widely used for both fuel cells and water electrolysers. These inks, which are typically either water or alcohol based, can be applied by brush, air-brush spraying, screening printing or by the "doctor-blade" technique. The ink composition is chosen to best suit each method and varies from laboratory to laboratory. Normally these inks are ultrasonically mixed prior to the application procedure. A simple automated spray method was developed at the Los Alamos National laboratory using a computer controlled X-Y recorder [23]. Rasten [7] used a mixture of electrocatalysts particles (typically 10 mg), 1-2 mg Nafion, 0.5 ml H_2O, 0.5 ml ethanol and 20 mg glycerol to spray electrodes of 5 cm^2.

A dry application method was recently developed for PEM fuel cells as a low cost method for large scale MEA production [104]. The method was based on a rolling procedure, in which a dry mixture of electrocatalyst powder and PTFE is blown onto the membrane or electrode backing. The active layer is fixed in place by hot-rolling the layer-assembly through a calender. Further layers can be added stepwise to achieve the desired loading. Layers as thin

as 5 μm were successfully obtained by this method. Electrochemical tests showed that electrodes prepared in this manner had performances similar to commercial fuel cell MEA's.

The transfer method has been described for PEM fuel cells [105]. Thin-film catalytic layers can be prepared by coating a clean PTFE film with a ink consisting of solubilised Nafion, electrocatalyst powder and water. Glycerol is added to improve the ink's "painting" properties. The PTFE film is first coated in a thin layer of fluorocarbon mold release spray. The catalyst ink is painted to this coated PTFE film and baked at 135 °C. Additional layers can then be added to achieve a desired loading. Overall it was suggested to minimise this baking time. This catalytic layer is then hot pressed to a polymer electrolyte membrane at 125-145 °C at 70-90 atm for 90 seconds. The MEA is cooled and the PTFE film peeled away from the thin film which is now bonded to the membrane.

The plating method or "in-situ" method has been developed for water electrolysis MEA's, in which the noble metal precursors were reduced using Na_2BH_4 solution [49]. The plating method used a continuous flow cell in which the reducing agent and metal salt solution were in contact with either side of the membrane. This method was found to give a good level of control in terms of the metal loading and plating adhesion. Various pre-treatments of the membrane, including hydrothermal treatment and surface etching by gas plasma, improved the characteristics of the Nafion membranes used, in respects to the resistivity and plating properties. Similar plating methods have also been used by others [4, 106, 48]

3.5 Characterisation of oxides

There are many properties, both electrochemical and physicochemical which are important for high performance electrocatalysts. It is important to separate some of the effects caused by these properties in order to understand and further develop the electrocatalyst (e.g. active surface area vs. specific activity). Trasatti has summarised a range of methods for the characterisation of electrocatalytic oxides [61] with this being slightly expanded upon to give Table 3.2. These methods may also help in understanding the preparation of the oxide materials (e.g. TGA/DSC gives information in regards to

annealing processes). In this section some literature examples of important findings using various characterisation methods are given.

Table 3.2: Important characterisation methods for electrocatalytic oxides

Method	Property / Information obtained
Temperature programmed analysis (TPA) e.g. TGA, DSC	Thermal decomposition Precursor/Intermediate interactions
X-ray diffraction	Lattice structure, Crystallinity Crystal size
BET surface area	Real surface area of material
Electrical resistance	Electronic structure
X-ray photoelectron spectroscopy	Surface composition Element interactions
Potentiometric titration / Electrophoretic mobility	Acid-base properties, PZC Surface charge
X-ray absorption spectroscopy (XANES, and EXAFS + in situ)	Valance, atomic structure Structure-potential relationship
Cyclic voltammetry	Electrochemical surface spectrum Electrochemical surface charge
Electrochemical impedance spectroscopy	Ohmic resistance, capacitance Morphology, Polarisation resistance
Steady state polarisation	Tafel slope (reaction mechanism) Exchange current Catalytic performance

3.5.1 TPA of electrocatalytic oxides

The use of temperature programmed techniques is often applied to heterogenous catalysts such as those for the water gas shift reaction [107]. However for oxide electrocatalysts, this method is normally used to follow the preparation of noble metal oxides, rather than the materials themselves.

The thermal decomposition of noble metal chlorides was followed in a variety of atmospheres by Newkirk and McKee [45]. The thermal decomposition of $IrCl_3.3H_2O$ in air was seen to occur via an overlapping two stage process, with the loss of crystal water at 100-200 °C and oxidation to IrO_2 above 600 °C [45]. Further decomposition to metallic iridium occurred just above 1000 °C. The decomposition of $RuCl_3.xH_2O$ showed a single continuous decomposition TGA profile, with RuO_2 found at around 400 °C [45]. The thermal decomposition of ruthenium (III) hydrate was also investigated by DTA and TG analysis, and shown to yield Ru and $RuO_2.xH_2O$ at 100-150 °C [64]. The amorphous Ru metal is crystallised in nitrogen above 450 °C, and oxidised in air between 150 and 300 °C [64].

TGA and DTA analysis has also been used to follow the thermal treatment of an intermediate prepared by the hydrolysis of iridium precursors in a basic solution [58]. This analysis showed that the precipitate was most likely $Ir(OH)_3(H_2O)_3$, and this dehydrated continously up to around 400 °C. A strong exothermal peak at 390-410 °C seen in the DTA was attributed to the final water loss and crystallisation into IrO_2. The hydrolysis of hexachloroiridate (IV) at pH 12 followed by addition of HNO_3 was suggested to give $Ir(OH)_4$ initially then $IrO_2.2H_2O$ after further heating [108].

3.5.2 XRD of electrocatalytic oxides

XRD is one of the most widely used methods for analysis of materials and electrocatalysts. The main uses of this technique is to determine the crystal size, crystallinity, and crystal lattice parameters of the material. As this work is primarily concerned with rutile type oxides this review will concentrate on these materials. Information regarding the theory of XRD can be seen in section 2.6.2.

The crystal size of the noble metals oxides normally increases with increasing

annealing temperature. Both RuO_2 and IrO_2 showed an increasing crystal size as a function of temperature [67]. Similar findings were found for IrO_2 by Lodi *et al*, who also showed that the temperature of the initial pyrolysis process had a stronger effect on crystallite size than the temperature of post preparation annealing [109].

Mixed Ir-Ti and Ru-Ti oxides have been examined by many groups, and De Battisti *et al* showed that the crystallite size increased with noble metal content for both Ir-Ti oxide and Ru-Ti oxides [67]. The Ru-Ti oxide was seen to show solid solution properties with the interplaner lattice spacing d_{110} decreasing linearly with Ru content. Ir-Ti oxides have seen to exhibit two rutile phases and one anatase phase [69]. It was suggested that the rutile phases were solid solutions between TiO_2 and IrO_2 with the lattice parameters varying linearly with composition. A somewhat higher than expected "a" parameter for pure IrO_2 was suggested to be due to high levels of OH in the oxide film.

Solution solutions between iridium and tin oxide have had some attention in the literature. Metastable iridium-tin oxide based solid solutions of the type (Sn, Ru, Ir)O_2, have been prepared via direct air oxidation and the Adams fusion method [84]. After heat treatment at 800 °C this metastable oxide was seen to decompose into (Ru, Ir)O_2 and SnO_2. DSA type Ti/IrO_x-Sb_2O_5-SnO_2 electrodes showed an IrO_x-Sb_2O_5-SnO_2 solid solution by XRD analysis, which was also decomposed into separate SnO_2 and Ir phases after high temperature annealing [76]. Ir-Sn oxide powders prepared via a sol-gel method revealed broad XRD patterns consistent with a solid solution between iridium and tin oxide with the lattice parameters of the solid solution phase showing a linear relationship over the entire composition range [91]. Ir-Sn oxide DSA electrodes showed a single rutile phase, with the d_{110} parameter showing a smooth variation with composition [110]. Others have found either no or very limited solubility of IrO_2 in SnO_2 [111, 112] at high temperatures, possibly confirming that only a metastable solution is possible. From a theoretical standing, by comparing the ionic radii of Ir^{4+} and Sn^{4+} (0.077 and 0.083 nm respectively) it is seen that the Hume-Rothery rule for solid solutions [42] is fulfilled.

The crystal properties of Ir-Ta oxide films has been comprehensively studied by Roginskaya *et al* [70]. These were separated into two groups ($x<30$ and $x\geq30$). The first group ($x<30$) showed that the predominate phase was

β-Ta_2O_5 with two other rutile phases based on IrO_2. The predominate β-Ta_2O_5 phase was thought to be a solid solution containing small amounts of IrO_2 in the lattice. The two rutile phases were suggested to be pure IrO_2 and another solid solution of β-Ta_2O_5 and IrO_2. The second group of oxide films (x$\geq$30) showed that the crystal properties of the films were dependent of the starting precursor solution, with either 1 or 2 rutile phases formed from an Ir^{3+}/Ir^{4+} solution, or 3 rutile phases from an Ir^{4+} solution. These phases all had different crystallite size ranges. The crystallinity of the oxide films was also found to increase with iridium content and temperature. One phase was found to be IrO_2, and the other one or two solid solutions or mixed Ta+Ir oxide phases. These mixed phases were determined to be dispersed IrO_2 crystallites whose surfaces are modified by the Ta at the interface with Ta_2O_5, with the larger dispersion resulting in more modified IrO_2. The crystal growth of the IrO_2 was seen to be inhibited, a result of the crystals surface modification. In contrast to the results above, Vercesi *et al* suggesting no solid solutions are present in Ir-Ta oxide DSA electrodes [63]. Likewise no solid solution phases between Ru and Ta oxides were found on Ru-Ta DSA oxides [62]. Structural analysis showed that the crystallisation processes of the two oxides in DSA Ir-Ta oxides, affect each other [113].

3.5.3 Electrical resistance of conductive rutile oxides

Normally, electronic conductivity is of little importance in DSA type layers as the thickness and conductivity of the oxide layers rarely causes a significant performance loss with the highest resistivity reported on the order of 10^{-2} Ω cm [61]. This is most likely due to the very compact nature and crystallinity of such layers. Single crystals of IrO_2 and RuO_2 show conductivities around 3-6 $\times$ 10^{-5} and 3-5 $\times$ 10^{-5} Ω cm respectively [25]. The mechanism or cause of the resistivity is suggested to occur primarily from the intergrain regions, and that the conductivity occurs via a "hopping" mechanism [61]. Clearly in a layer consisting of particles (as in a PEM water electrolyser), the resistance will be increased due to the large number of grain and particle boundaries. The contribution of the oxide layers resistivity to performance loss in PEM water electrolysers has been discussed previously [7].

Lodi *et al* showed that the electrical resistivity of IrO_2 supported on silica rods increased with temperature and that the resistivity was dependent

on the thermal history of the prepared oxides [109]. It was also suggested that an increase in crystal size did not necessary result in improved conductivity. This was explained by the accumulation of residue chloride at the boundary of the crystallites as the crystals undergo the growth process during heat treatments. Rasten suggested that IrO_2 with poor crystallinity can have semi-conducting properties with the conductivity increasing significantly with increased annealing temperature [7]. Rasten *et al* also showed using Mott-Schottky analysis that non-annealed IrO_2 can be considered as a n-type semi-conductor and that this switches to a p-type semi-conductor at high potentials [114].

DSA electrodes containing small levels of noble metals have considerable electrical resistivities as shown by Iwakura *et al* [115]. Doping SnO_2 electrodes with RuO_x, IrO_x, or PtO_x was shown to improve the conductivity in comparison with CrO_x, MnO_x or PdO_x-doped SnO_2 electrodes.

3.5.4 XPS of rutile oxide electrocatalysts

Several studies have concentrated on investigating oxides and oxide layers by XPS. Most of these studies use XPS to give a measure of the concentration of elements at the surface, and whether surface enrichment has occurred. Hutchings *et al* [84] showed that preferential surface segregation of iridium over ruthenium occured in both the binary oxide $Ir_{1-x}Ru_xO_2$ and the ternary oxide $Ir_xRu_xSn_{1-2x}O_2$, with the surface composition shifting closer to the bulk composition with increasing annealing temperature.

Ti was found in Ru-Ta oxide layers and was thought to be due to migration of Ti from the substrate used in this work [62]. The titanium content was seen to increase close to the surface of the layer by using a depth profiling technique. For coatings with high ruthenium contents, the maximum in ruthenium content occured at intermediate layer depths while the outer most surface showed strong Ta enrichment.

Depth profiling of a RuO_2/TiO_2 coating was carried out and the effect of the Ru precursor salt investigated [68]. The extent of Ru surface enrichment was seen to be greater when the oxide is prepared using $RuCl_3.xH_2O$ compared to $Ru(NO)(NO_3)_3$ as the precursor. It has been shown that Ru/Ti oxides formed from the chloride precursor can show segregation of the Ti and Ru

oxide components due to the interaction of the precursors in solution [81].

The iridium 4f region has been examined by several groups with Atanasoska *et al* [116], suggesting that determining the valence of iridium is very complex due to the overlapping of the multiple photoelectron lines normally found in IrO_2 samples. Rubel *et al* showed that the binding energies of Ir 4f and Sn 3d photoelectron lines did not vary when Sn was added to an oxide film prepared by thermal decomposition of the chloride precursors [117]. Likewise, Atanasoska *et al* did not find any evidence of binding energy peak shifts due to the addition of Ru to the oxide matrix [116].

Roginskaya *et al* examined the X-ray photoelectron spectra of Ir-Ta oxide films [70]. The Ir 4f region suggested that the Ir was present in only 1 valence state as was the tantalum. The oxygen region (O 1s) showed that two forms of oxygen were present at the surface. It was also suggested that the oxides have some semi-conducting properties due to the asymmetry of the photoelectron lines.

Ir-Ti oxide films examined by XPS showed that Ti was present in more than one oxidation state [80] due to the redox reaction between the Ir and Ti complexes in the precursor solution. Addition of Ce into this oxide layer also revealed that the resulting oxide film contained Ir and Ce in +3 and +4 oxidation states.

3.5.5 XAS of noble metal oxides

Both EXAFS and XANES have been used to examine the structure of noble metal oxides. The structure of pure IrO_2 was examined in transmission mode using finely ground powder [102]. The analysis showed that the structure was highly ordered and that the iridium was in an octahedral environment with approximately 6 oxygen atoms neighbouring each iridium atom.

The formation of RuO_2 and IrO_2 by the thermal decomposition of the chloride precursors was followed by EXAFS [118]. Changes in the structure were clearly seen, with the peak arising from the Ru-Cl bond decreasing and the Ru-Ru and Ru-O peaks increasing with increasing calcination temperature. The same behaviour for iridium oxide was observed. It was seen for Ru-Ir oxides, that the radial distribution function showed a continuous change

with the oxide composition. This lead the authors to suggest that a solid solution between IrO_2 and RuO_2 was formed.

As IrO_2 and RuO_2 electrodes undergo structural changes with potential, XAS can be used to follow these structural changes. Electrochemically deposited/oxidised ruthenium showed that the Ru-O bond lengths were reduced from 2.02 Å at 0.4 V to 1.94 Å at 1.2 V [119]. Similar bond length changes were observed for IrO_2 electrodes where the Ir-O bond length was found to be 2.02, 2.02 and 1.97 Å at 0.05, 0.37, and 0.8 V vs. SCE respectively in 0.5 M H_2SO_4 [120]. More pronounced bond length changes were observed in a 0.3 M Na_2CO_3 solution as a function of potential [120]. XANES spectra clearly showed the effect of potential on the valence of the iridium species in the electrode [120].

3.5.6 Cyclic voltammetry of noble metal oxides

Cyclic voltammetry of noble metal oxide electrodes, is a common method of evaluating the electrochemical surface properties of these oxides. The voltamograms of IrO_2 and RuO_2 have very characteristic shapes, with broad peaks resulting from the redox reaction of adsorbed oxygen species from solution and solid state redox transitions of the Ir and Ru. Normally the peaks found on the voltamograms of IrO_2 and RuO_2 in acid are too broad for any precise determination of the potentials at which these redox processes occur. RuO_2 electrodes have 3 redox peaks with a characteristic RuO_2 peak around 0.65 V [7, 121, 122].

The voltammetry of Ir-Ru oxide electrodes was carried out in both 0.5 M H_2SO_4 and KOH solutions as a way of determining the relative response of Ir and Ru present in the oxide [121]. The CV response of RuO_2 in KOH gives a small peak prior to oxygen evolution not present on IrO_2, and therefore can be used to measurement the relative electrochemical response of Ir and Ru species in mixed Ir-Ru oxide electrode.

The voltammetry of well define RuO_2 surfaces was carried out by Doubova *et al* [123]. It was seen that the voltamograms revealed much more structure than previously presentated. Also it was shown that the storage capacity of RuO_2 was crystal face dependent as was the relationship between charge and voltammetric sweep rate.

De Pauli and Trasatti followed the reversibility of the charging process on DSA type Ir-Sn oxide electrodes using cyclic voltammetry. It was found that the charge ratio of the anodic and cathodic sweep was approximately 1 except at low iridium contents (< 0.5 mol%) indicating that for DSA electrodes iridium strongly dominates the electrode response [71].

The voltamograms of noble metal oxides give vital information regarding the active area of these materials. It has been shown that the charge associated with the oxide region (normally 0.6-1.4 V) is directly proportional to the surface area or electrode roughness [124, 125, 126]. Furthermore measuring the anodic charge (Q) as a function of sweep rate (ν) can yield interesting information regarding the morphology of the active surface [35, 71]. By plotting 1/Q vs. $\nu^{0.5}$ and Q vs. $\nu^{-0.5}$ and extrapolating the linear sections to the origin, the charge values at $\nu = \infty$ and ν=0 are found. At high sweep rates only the outer surface of the oxide material takes part in the charging process, whereas at very low sweep rates the "inner" surface is also accessible due to diffusion of protons through pores, cracks and grain boundaries in the oxide material. The proton exchange between surface oxide-OH groups and the acid electrolyte is considered to be rapid at "easily accessible" regions, whereas this exchange has some diffusion limitations within the inner regions [127]. Thus at ν=0 the charge is said to be the total charge (Q_t) and at $\nu = \infty$ the charge gives the outer charge (Q_o). The total charge is the summation of the inner (Q_i) and outer charge.

$$Q_t = Q_o + Q_i \tag{3.3}$$

3.5.7 Steady state polarisation of noble metal oxides

Steady state polarisation analysis of noble metal oxide electrodes give a measure of overall performance and stability, as well as mechanistic information regarding the rate determining step and reaction pathway.

Matsumoto and Sato reviewed the electrocatalytic properties of transition metal oxides for the oxygen evolution reaction, and suggested that for practical use, only the potential at a certain current (or vice versa) should be used to compare electrocatalysts [12]. This was based on the fact that the electrocatalytic performance is governed by both the exchange current and Tafel

slope. Also it was suggested that mechanism analysis based on Tafel slopes should be treated carefully as the symmetry factor may not be the normally assumed value of 0.5. Conway has also shown in detail the variation which the symmetry factor and Tafel slope can have on various electrodes [20]. It was also shown that the electrochemical surface area does not necessary act only as a scaling factor with absorption process also being effect by geometric effects. De Pauli and Trasatti [128] showed that IrO_2-SnO_2 DSA electrodes showed the normal Bulter-Volmer relationship as the temperature varied indicating that the charge transfer coefficient is close to 0.5.

A wide range of Tafel slopes is seen for noble metal oxide electrodes as shown in a review [12]. RuO_2 Tafel slopes can range from 35 to 140 mV dec^{-1} and IrO_2 from 40-60 mV dec^{-1}. Single crystals of RuO_2 also can show variation in the Tafel slope depending on the crystal face expose to the electrolyte. Tafel slopes measured on Ir-Sn DSA electrodes were 55-60 mV dec^{-1} over the range 10-100 mol% IrO_2 and larger than 120 mV for iridium contents less than 10 mol% [128]. Others have found that the Tafel slope on Ir-Sn oxide DSA electrodes was 70 mV dec^{-1} for iridium contents of 50-100 mol%, and 100-170 for lower iridium contents [110]. Oxygen evolution also occurs on pure SnO_2 electrodes with a Tafel slope around 120 mV dec^{-1} [128]. The Tafel slope and electrochemical activity for oxygen evolution on doped SnO_2 in basic media has been shown to be related to the doping element [115]. Many other investigations on DSA electrodes, have shown that Tafel slopes of 60 mV dec^{-1} are typical for IrO_2 based electrodes [12, 95, 129]. Rasten showed that addition of tantalum to iridium oxide decreased the low current Tafel slope in a PEM water electrolyser [7]. Likewise the addition of ruthenium to DSA Ir-Ru oxide electrodes has shown to decrease the Tafel slopes from around 60 mV dec^{-1} for IrO_2 to 40 mV dec^{-1} for RuO_2 [87, 122] although the Tafel slope is not solely a composition effect with others showing a variation in the Tafel slope for RuO_2 electrodes as a function of crystallinity [65, 101]. Rasten has also showed that the Tafel slope for oxygen evolution on IrO_2 is a function of annealing temperature, most likely due to the change in the electrodes crystallinity [114].

Chapter 4

Preparation and Characterisation of $Ir_xSn_{1-x}O_2$ Electrocatalytic Powders

This chapter has been accepted for publication as:

A. Marshall, B. Børresen, G. Hagen, M. Tsypkin and R. Tunold
"Preparation and characterisation of nanocrystalline $Ir_xSn_{1-x}O_2$ electrocatalytic powders"
Materials Chemistry and Physics, accepted April 2005.

4.1 Abstract

Nanocrystalline oxide powders of the type $Ir_xSn_{1-x}O_2$ ($0.2 \leq x \leq 1$) have been produced and characterised. These oxides have been developed primarily as oxygen evolution electrocatalysts for proton exchange membrane (PEM) water electrolysers. Two methods were used to produce the oxide materials: the modified polyol method and the Adams fusion method. X-ray diffraction analysis suggests that an iridium-tin oxide solid solution with

a rutile structure can be produced using the modified polyol method, with a linear relationship between the lattice parameters and composition. The crystal size of the solid solution phase is below 15 nm for all compositions. The Adams fusion method results in at least two separate oxide phases, namely a tin rich oxide and an iridium rich oxide. XPS analysis revealed no significant difference between the bulk and surface compositions, and that the iridium was present in at least 2 valent states. The electrical resistivity of the powders was compared, and an exponential increase in resistivity with tin addition was found. Overall the resistivity measurements suggest that the limit for tin addition is around 50-60 mol% due to the high ohmic losses expected at higher tin contents in a PEM water electrolyser.

4.2 Introduction

Proton exchange membrane (PEM) water electrolysers have been shown to be a promising method of producing carbon free hydrogen [2]. Recently IrO_2 based materials have been examined as the anode or oxygen evolution electrode at our group [7, 130, 114, 131, 132]. In this work the preparation and structural characterisation of $Ir_xSn_{1-x}O_2$ ($0.2 \leq x \leq 1$) nanocrystalline powders is investigated. In particular, two methods for producing noble metal based oxides are compared based on X-ray diffraction (XRD) analysis and electrical conductivity measurements.

Noble metal oxides as electrocatalysts (particularly IrO_2 and RuO_2) are well established in many industrial electrochemical processes in the form of dimensionally stable anodes (DSA) as developed by Beer [60]. Most DSA electrodes are prepared by thermal decomposition of metal precursors onto titanium substrates. This method is thought to be unsuitable for PEM water electrolysers due to the difficulty in obtaining good contact between the electrocatalytic layer and the membrane electrolyte. Therefore to obtain an electrocatalytic layer on the membrane, either pre-prepared powders may be applied as an ink to the membrane [23, 105] or electrocatalytic particles can be synthesised directly on the surface or within the membrane [47, 49]. In our laboratory we normally use an ink-spray method, so have been concentrating on preparing noble metal based oxide powders.

Many methods are available for the synthesis of noble metal based oxides.

The Adams fusion method [82] has been widely used to produce fine noble metal oxide powders [7, 84, 114, 130, 131], and is based on the oxidation of metal precursors in a molten nitrate melt. Sol-gel methods have also proved useful in producing noble metal based oxides [88, 89, 91, 92, 133], however precursor type can effect the properties of the material [133] as can the solvent removal stage [134]. Preparation of metal oxides by thermal or chemical oxidation of metallic colloids is an interesting concept as there exists a wide range of methods to synthesize such colloids [135, 136]. The polyol method is a relatively simple way to synthesize nanosized noble metal colloids such as iridium or ruthenium [96, 97], by the reduction of metal precursors in ethylene glycol. Our additional steps include the separation of the metallic colloids from the ethylene glycol by centrifugation, followed by thermal oxidation at elevated temperatures in air.

Previously it has been shown that SnO_2 improves the stability of IrO_2-RuO_2 anodes in PEM water electrolysers [84]. It has also been suggested that SnO_2 does not reduce that activity of RuO_2 as much as TiO_2 [61, 137]. For these reasons, additions of SnO_2 to IrO_2 has been investigated.

4.3 Experimental

4.3.1 Oxide preparation

Modified polyol method

Metal precursors ($H_2IrCl_6.4H_2O$ [1] and $SnCl_2.2H_2O$ [2]) were added to ethylene glycol to achieve a total metal concentration of 1.67 x10^{-2} mol l^{-1}. The glycol–precursor solution was then heated under a nitrogen atmosphere to the refluxing temperature and magnetically stirred for 2 hours by which time a colloid had formed. The pH of this colloid–glycol mixture was then normally adjusted to pH 2.5 by the addition of 0.1 M NaOH solution and magnetically stirred for 10 minutes. This aided the separation process of the colloid from the glycol, which was achieved by centrifugation. The recovered colloid was washed in deionised water 3 times, before being ultrasonically

[1] OMG AG & Co. KG - 99.92 % metals basis
[2] Alfa Aesar - ACS grade

dispersed in acetone and dried in air at 60 °C. This dry colloid was then annealed in air at 500 °C for 30 minutes to oxidise the metallic material.

Adams fusion method

Metal precursors ($H_2IrCl_6.4H_2O$ and $SnCl_2.2H_2O$) were added to 10 ml of isopropanol to achieve a total metal concentration of 7-9 $x10^{-2}$ mol l^{-1}. This was magnetically stirred for 1-2 hours to ensure complete dissolution of the precursors, followed by the addition of 10 g of finely ground $NaNO_3$. This solution-$NaNO_3$ mixture was heated at 70 °C in air until completely dry. Using isopropanol as the precursor solvent appeared to give a more homogenous mixture than if water was used. The dry salt mixture was then placed into a preheated furnace at 500 °C for 30 minutes. The fused salt-oxide mixture was cooled slowly to room temperature then washed 3 times in deionised water to remove the remaining salts. The oxide was separated by centrifugation and the recovered oxide powder dried in air at 90 °C.

4.3.2 Characterisation

X-ray diffraction was performed on the dry electrocatalytic powders using a Siemens D5005 powder X-ray diffractometer, with a step size of 0.2 °, step time of 50 seconds, slit opening of 0.5 °, and a Cu-Kα X-ray source ($\lambda = 0.154$ nm). The diffraction patterns were fitted to a pseudo-Voigt profile and the crystal size distribution calculated using Warren-Auerbach analysis. XPS analysis was performed on the electrocatalysts, by preparing thin layers on aluminium foil, using a Nafion solution as a binder, with the layer normally containing 5 wt% Nafion. A VG ESCALAB MkII instrument was used with an Al Kα X-ray source, with the full spectrum collected with a band pass of 50 eV and the specific regions collected with a band pass of 20 eV. The surface ratio of iridium and tin was determined by comparison of the Ir 4f and Sn $3d_{5/2}$ photoelectron lines and the use of appropriate sensitivity factors [138]. Curve fitting was carried out using Gaussian-Lorentzian type profiles (XPSPeak 4.1) and the C 1s line (BE = 284.6 eV) was used as reference for the binding energy.

4.4 Results and discussion

4.4.1 Modified polyol method

On addition of the metal precursors to the ethylene glycol, the measured pH was seen to range from -0.15 to 0.2, with the pH increasing linearly with increasing tin content. The colour of the solution was observed as the glycol mixture was heated (Table 4.1). Similar observations have been made during ruthenium synthesis by this method [99].

Table 4.1: Observed colour changes during polyol reaction

Time (min)	Colour
0	Dark purple - Brown
1	Yellow - Brown
2	Clear yellow
3-4	Red - Brown
8-10	Brown - Black (colloid)

The colour changes are suggested to be due to the exchange or loss of ligands from the precursor complexes. After 2 hours of refluxing, the measured pH was 0.83 irrespective of the iridium:tin ratio. It has been shown that the pH of glycol - ruthenium colloid mixtures can determine the degree of agglomeration [99], an effect seen in most colloidal dispersions. In this work the colloid dispersion was seen to agglomerate between pH 1 and 2 when the colloid consisted of equal molar fractions of iridium and tin. For the majority of samples, the pH was adjusted to 2.5 prior to centrifugation to assist the separation process. It was observed however, that as the tin content decreased, the colloid exhibited less agglomeration at pH 2.5. Such an observation suggests that the iridium and tin species have a strong interaction during this procedure. This interaction is likely to be beneficial when solid solutions are desired. The observation is suggested to be due to the change in point of zero charge (pzc) with composition. On the Pauling scale, the electronegativities are 1.96 and 2.20 for Sn and Ir respectively, so the pzc for iridium rich species should be lower than Sn rich species. The pzc of iridium and tin oxides have been reviewed, and it is clear that the pzc of iridium oxide is lower than tin oxide [28]. It has been suggested that particles ag-

glomerate when the absolute zeta potential is lower than 50 mV [99]. XRD analysis was performed on annealed $Ir_{0.5}Sn_{0.5}O_2$ samples, where the colloids prior to oxidation were separated from the ethylene glycol at different pH values (Figure 4.1). Clear rutile oxide peaks are seen for all three samples, however the sample prepared at pH 1.5 also shows small peaks associated with metallic iridium (40.7 and 47.3 2θ).

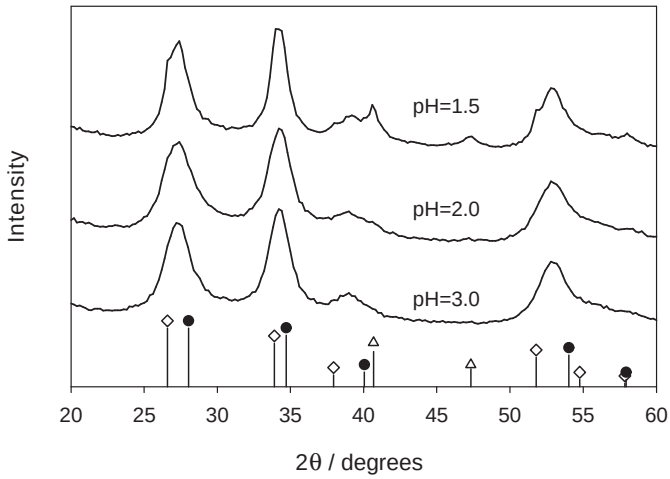

Figure 4.1: Effect of agglomeration pH on $Ir_{0.5}Sn_{0.5}O_2$, • - IrO_2, ◇ - SnO_2, △ - Ir

Upon close inspection it is also seen that the low pH sample contains multiple oxide phases as indicated by the shoulder to the left of the main oxide diffraction peaks. Profiling these peaks suggests that there is both a tin rich oxide and a iridium rich oxide. The main peak positions are listed in Table 4.2, and suggests that the tin rich oxide is almost pure SnO_2, and that the iridium containing phase is a solid solution between tin and iridium oxide (approximately 40 mol% IrO_2). Rubel *et al* has also reported that in IrO_2-SnO_2 thin films that there can be some non-homogeneity and surface enrichment by iridium [117].

The reason for the appearance of two separate oxide phases is not completely understood, however it is suggested that at lower pH values, preferential ag-

Table 4.2: Main XRD peak positions (2θ) for oxide when colloid agglomerated at pH 1.5

Sn rich oxide	Ir rich oxide	SnO_2	IrO_2
26.70	27.39	26.6	28.1
33.92	34.40	33.9	34.7
51.96	52.92	51.8	54.0

glomeration occurs, creating colloid agglomerates rich in metallic iridium. This may then lead to the heterogeneous oxide during the annealing stage. This is consistent with the observation that tin rich colloids show stronger agglomeration at pH 2.5 than iridium rich colloids (iridium rich colloids have a lower pzc and therefore will agglomerate at lower pH values than tin rich colloids). Therefore to ensure that a homogenous agglomerate is obtained, high pH values should be used to ensure all colloidal material is present in the agglomerate. Unfortunately, the diffraction patterns for the metallic colloids are very broad, and give no further conclusive information regarding this agglomeration stage. The crystal size distribution for the iridium containing oxide phase showed no significant difference as the agglomeration pH varied, with the average crystal size around 2-3 nm. It is suggested that the agglomeration process should be taken out at pH 2–3 to limit the observed separate phase formation.

The XRD patterns for $Ir_xSn_{1-x}O_2$ ($0.2 \leq x \leq 1$), annealed at 500 °C for 30 minutes with a initial agglomeration pH of 2.5, again show rutile type oxide peaks (Figure 4.2). It is suggested that this is a solid solution between iridium and tin oxide. It is observed that as the tin content decreases the peaks become broader, indicating that iridium rich oxides have smaller crystal sizes. The peak positions for this phase is seen to vary with composition, with both lattice parameters showing a linear relationship to the composition (Figure 4.3). The intercepts at x=1 and x=0 correspond closely with the typical values for pure IrO_2 (a = 0.4498, c = 0.3154) and SnO_2 (a = 0.4738, c = 0.3188).

The crystallinity of the oxide phase was estimated by comparing the area of the peaks associated with crystalline material and that associated with amorphous material [139]. The transition of amorphous to crystalline material is not well defined so this serves as an general indicator only. The

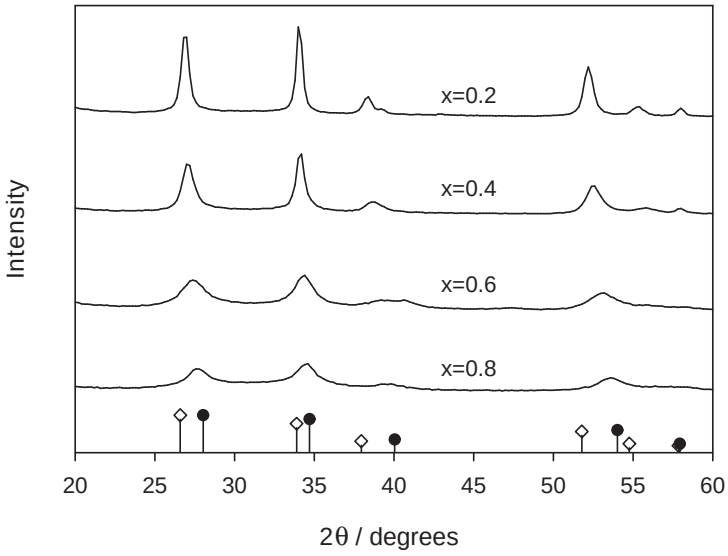

Figure 4.2: XRD of $Ir_xSn_{1-x}O_2$ (modified Polyol method), ● - IrO_2, ◇ - SnO_2

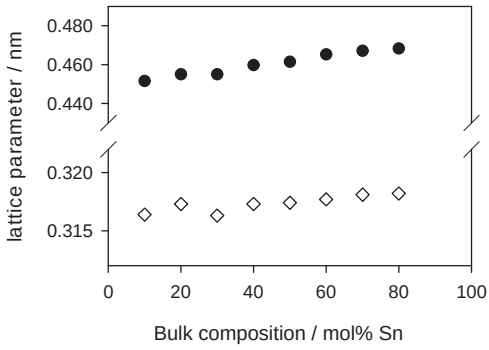

Figure 4.3: Lattice parameters of $Ir_xSn_{1-x}O_2$, ● - a, ◇ - c

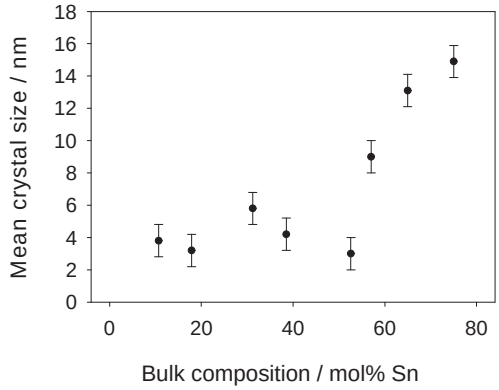

Figure 4.4: Mean crystal size of $Ir_xSn_{1-x}O_2$

results show that samples with higher tin contents (x < 0.5) are approximately 75-80 % crystalline whereas those containing more iridium (x > 0.5) are around 60 % crystalline. This is reflected in the mean crystal size with the crystal size increasing with increasing tin content (Figure 4.4).

Solution solutions between iridium and tin oxide have had some attention in previous literature. Metastable iridium-tin oxide based solid solutions of the type (Sn, Ru, Ir)O_2, have been prepared via direct air oxidation and Adams fusion method [84]. After heat treatment at 800 °C this metastable oxide was seen to decompose into (Ru, Ir)O_2 and SnO_2. DSA type Ti/IrO_x-Sb_2O_5-SnO_2 electrodes showed an IrO_x-Sb_2O_5-SnO_2 solid solution by XRD analysis, which was also decomposed into separate SnO_2 and Ir phases after high temperature annealing [76]. Ir-Sn oxide powders prepared via a sol-gel method gave broad XRD patterns consistent with a solid solution between iridium and tin oxide with the lattice parameters of the solid solution phase showing a linear relationship over the entire composition range [91]. Ir-Sn oxide DSA electrodes also showed a single rutile phase, with the d_{110} parameter showing a smooth variation with composition [110]. Previous work by us has indicated that Ir-Sn oxide solid solutions are only meta-stable and start to decompose into separate phases at 600–650 °C [132]. Others have found either no or very limited solubility of IrO_2 in SnO_2 [111, 112] at high temperatures, possibly confirming that only a metastable solution is

possible. From a theoretical standing, comparing the ionic radii of Ir^{4+} and Sn^{4+} (0.077 and 0.083 nm respectively) it is seen that the Hume-Rothery rule for solid solutions [42] is fulfilled. In this work, because strong interaction between the iridium and tin species occurs in the polyol stage, an highly mixed Ir-Sn material is probably produced prior to the annealing / oxidation stage increasing the likelihood of a stable or metastable solid solution forming. Interestingly, pure Sn colloids could not be formed using the method disclosed above. This indicates there must be an interaction between the precursors or intermediates during the colloid formation, rather than a simple co-formation pathway (i.e. iridium and tin colloids do not form independently from each other).

4.4.2 Adams fusion method

Adams fusion method [82] is based on the oxidation of metal precursors with molten $NaNO_3$ as shown below. The reaction is fast and has been shown to directly produce IrO_2 when the pyrolysis temperature is at least 460 °C for 30 minutes [131].

$$H_2IrCl_6 + 6NaNO_3 \rightarrow 6NaCl + Ir(NO_3)_4 + 2HNO_3 \tag{4.1}$$

$$Ir(NO_3)_4 \rightarrow IrO_2 + 4NO_2 + O_2 \tag{4.2}$$

In order to reduce differences caused by the heat treatment in each method, the pyrolysis of the iridium and tin precursors was carried out at 500 °C for 30 minutes. As expected the XRD patterns show that this produces a rutile type oxide (Figure 4.5), but unlike the modified polyol method, there is evidence to suggest that two separate phases are produced rather than a single solid solution phase. By profiling the obtained XRD pattern, it is seen that the pattern can be explained by a mixture of two highly dispersed rutile oxide phases (Figure 4.6). The peak positions of the proposed phases correspond closely with the peak positions for the pure oxides of iridium and tin, with the slight deviation in positions indicating that the separate phases probably are not completely pure, and may in fact be solid solutions with differing compositions. As the peaks are so broad, precise determination of the structure was not possible from this XRD analysis. EDX analysis showed that the bulk composition was very close to the desired composition,

as the pyrolysis process (Eqn 4.1 and 4.2) is a strong oxidising environment in which all precursors are oxidised with almost 100% yield. The crystal size of the oxide material also shows a different relationship to the oxides prepared by the modified polyol method. The Adams fusion oxides clearly show an increased broadening of the diffraction peaks as tin was added whereas the polyol oxide showed a clear decrease in the line broadening with tin content. This shows that although the preparation temperatures were identical, the mechanism of crystal formation is quite different, with a decrease in crystallinity observed for the Adams fusion oxides and an increase in crystal size observed for the Polyol oxide as tin was added.

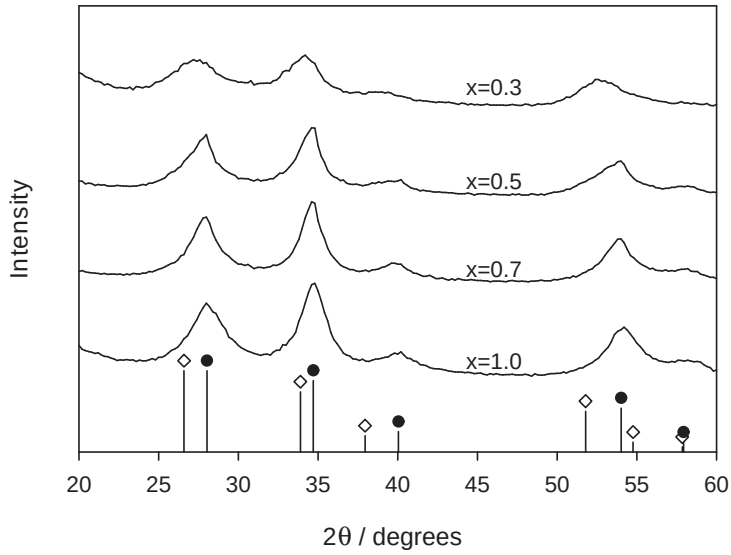

Figure 4.5: XRD of $Ir_xSn_{1-x}O_2$ (Adams fusion method), • - IrO_2, ◇ - SnO_2

The presence of multiple phases and apparent lack of a single solid solution phase is suggested to arise from the poor interaction between the precursors during the initial stages of the reaction. There is a significant difference in $\Delta G\ ^0_f$ for SnO_2 and IrO_2 (-510 kJ mol^{-1} [140] and -186.5 kJ mol^{-1} [25] respectively) indicating that SnO_2 will form first. Also the $SnCl_2.2H_2O$ used in this work has a low melting point (37-38 °C) which may result in a heterogenous mixture prior to the pyrolysis stage. This means that any

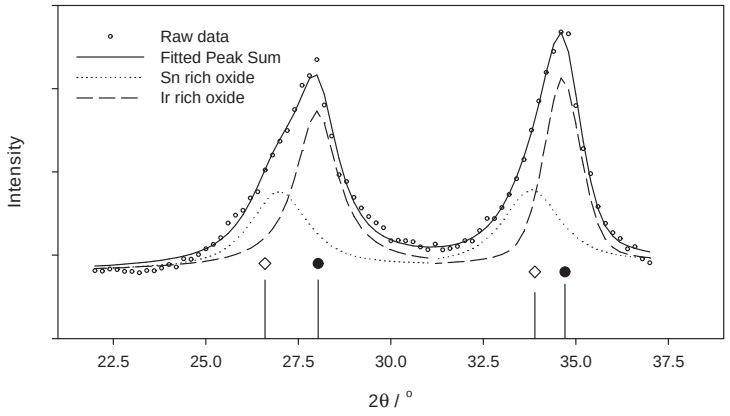

Figure 4.6: Profile fitting of $Ir_{0.5}Sn_{0.5}O_2$ (Adams fusion method) • - IrO_2, ◇ - SnO_2

changes in the oxide properties (from pure IrO_2) most likely would arise from a dispersion effect rather than an effect due to the different crystal parameters. As SnO_2 is believed to form first, it is thought that these non-conductive or semi-conducting crystals may be covered in IrO_2. This will likely improve the overall dispersion and usage of the active component.

4.4.3 X-ray photoelectron spectroscopy

A typical XPS survey spectrum is shown in Figure 4.7, along with the Ir 4f and Sn 3d regions (Figures 4.8 and 4.9) for oxides produce by the modified polyol method. The large F 1s peak is from the Nafion present in the sample, and this peak was always located at 688–689 eV. This served as a good reference when the C 1s peak was very small and difficult to accurately position, and in these cases the F 1s peak was set to 688.9 eV which is a typical value for F 1s in PTFE. As discussed previously [116], analysis of the Ir 4f region is very difficult with considerable disagreement in literature regarding the valence states in a normal IrO_2 DSA type electrode. What is certain however, is that the iridium is present in more than 1 valence state as shown by the two peak pairs in Figure 4.8. The fifth peak located around 67.5

eV is necessary to adequately fit the high energy side of this region. This has been previously discussed and was suggested to be a result of the final state screening [116]. Accurate binding energies for the Ir 4f region peaks could not be found due to an uncertainty of ± 0.20 eV and the added uncertainty caused by the multiple peak fitting. The low valent Ir $4f_{7/2}$ photoelectron line was found at binding energies between 61.1–62.1 eV and the high valent Ir $4f_{7/2}$ photoelectron line at 62.3-63.3 eV. The peak splitting was around 1.2-1.5 eV for both sets of peaks. These binding energies are higher than metallic iridium (BE Ir^0 $4f_{7/2}$= 60.8 eV) and therefore are attributed to oxidised iridium. Analysis of the Sn 3d photoelectron lines showed that the binding energy shifts to higher values as the tin content increased (Figure 4.10). This is in contrast with a previous investigation [117] and may show that there is an interaction at the atomic level between iridium and tin. The binding energy of the Sn $3d_{5/2}$ at high tin contents is similar to the binding energy found by others [117] and is consistent with Sn^{4+}. To confirm this apparent interaction, a detailed study should be carried out to accurately determine the binding energies of the Ir 4f photoelectrons. The ratio of iridium:tin at the surface showed a small deviation from the bulk ratio, with the surface showing a slight enrichment of tin (normally 5-10 mol%) in the case of the oxides prepared by the modified polyol method.

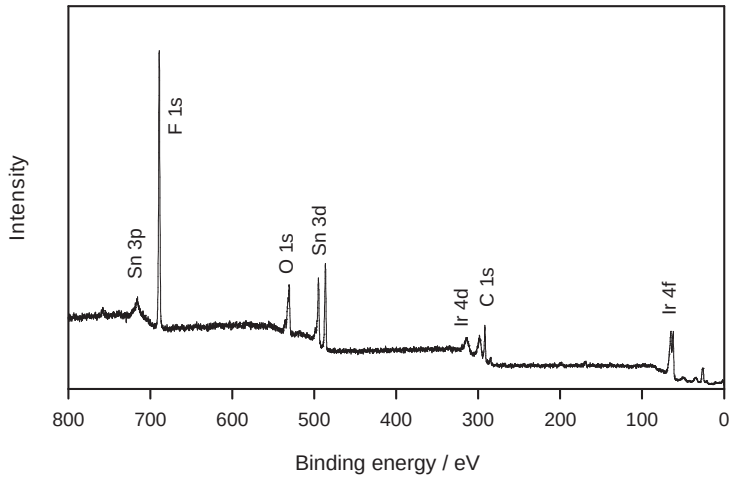

Figure 4.7: Typical XPS survey spectrum of $Ir_xSn_{1-x}O_2$

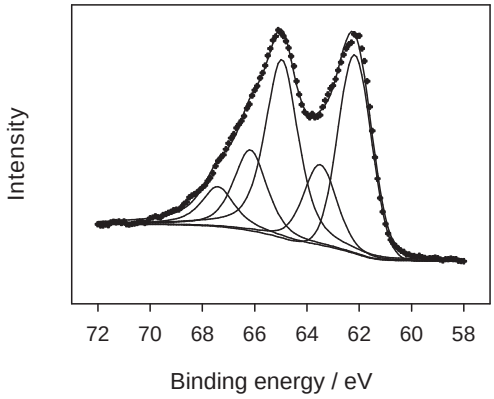

Figure 4.8: Typical Ir 4f region of $Ir_xSn_{1-x}O_2$

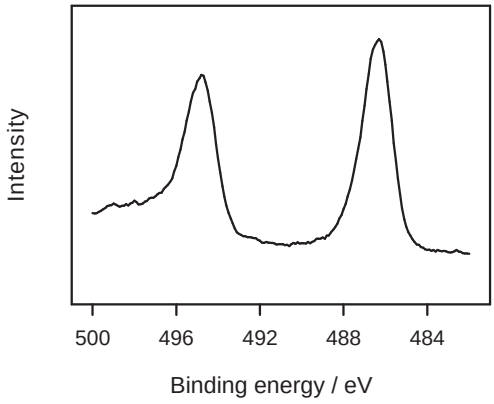

Figure 4.9: Typical Sn 3d region of $Ir_xSn_{1-x}O_2$

4.4.4 Electrical conductivity measurements

The electrical conductivity of the active layer in a PEM water electrolyser cell is very important [7]. In this work the electrical conductivity of the electrocatalytic powders was compared by pressing the oxide powder between

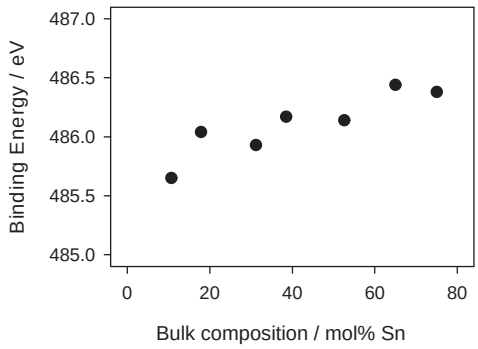

Figure 4.10: Binding energy of the Sn $3d_{5/2}$ photoelectron line

two pistons. The total resistance was measured between the two pistons as a function of pressed powder thickness. A standard micrometer gauge was used both to measure the thickness and provide a constant compression force. This enabled the resistivity to be estimated without including the piston – oxide contact resistance. A typical plot of resistance vs. pressed powder thickness shows that the relationship is linear allowing the resistivity to be found from the gradient (Figure 4.11). Normally values between 10 mΩ cm and 200 Ω cm can be measured by this method. Figure 4.12 shows the resistivity as function of tin content for oxides prepared by the modified polyol method and the Adams fusion method.

Overall, as tin is added to the oxide, the electrical resistivity increases as expected, with approximately 3 orders of magnitude difference between IrO_2 and $Ir_{0.25}Sn_{0.75}O_2$. There is also a small but significant difference between the materials produced by the two methods, with the oxides from Adams fusion method generally showing twice the electrical resistivity of the oxides produced by the modified polyol method. This is believed to arise from the difference in structure of the oxides. If a solid solution is present, lower resistivities could be expected due to a continuous electronic path through the oxide. In a two phase oxide powder, the insulating tin oxide phase will likely reduce the probability of an electronic pathway. Overall the electrical resistivity of the oxide particles will contribute to a performance loss in a PEM water electrolyser.

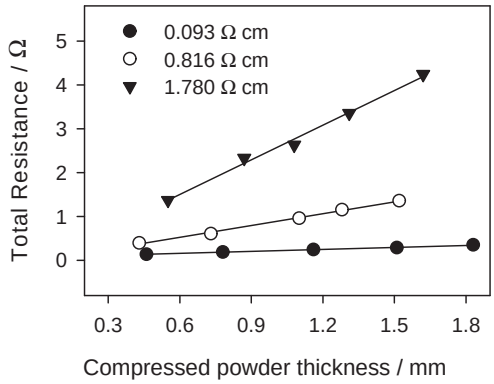

Figure 4.11: Resistance of pressed powders

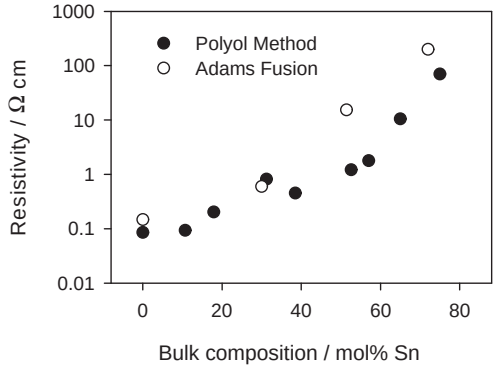

Figure 4.12: Resistivity of $Ir_xSn_{1-x}O_2$ powders

Electrical conductivity of DSA type oxide layers has had some attention in literature [61], and as discussed, the conductivity of the oxides rarely causes a significant performance loss as the highest resistivity reported is on the order of 10^{-2} Ω cm. The mechanism or cause of the resistivity is also suggested to occur primarily from the intergrain regions, and that the conductivity occurs with a "hopping" mechanism. Clearly in a layer consisting of particles (as in a PEM water electrolyser), the resistance will be increased due to the large number of grain and particle boundaries. The contribution of the oxide layers resistivity to performance loss in PEM water electrolysers has been discussed previously [7], however the ohmic drop of the polymer electrolyte membrane was included in these measurements so comparing these results is difficult. Some simple calculations can however be used to estimate the possible ohmic losses in a PEM water electrolyser. Of course the addition of a polymer electrolyte to the electrocatalytic layer will likely increase the total electrical resistivity of the layer and therefore these estimations represent the minimum expected electronic ohmic loss. The thickness of a catalytic layer would normally be 5–10 μm assuming an electrocatalyst loading of 1–3 mg cm^{-2}. Therefore the ohmic drop caused by the oxide will be approximately 0.05–0.1, 0.5–1, 5–10, and 50–100 mV at 1 A cm^{-2} for oxide resistivties of 0.1, 1, 10, and 100 Ω cm respectively. When we also consider that the lateral conductivity will increase this loss further due to the porous nature of the backing plate [114], we clearly see that only oxides with resistivities of 10 Ω cm or less will be suitable for PEM water electrolysis applications. In this case, the limit for tin addition to iridium oxide is around 50-60 mol%. Direct resistance measurements in PEM water electrolysers are now being carried out to assess whether this estimated ohmic loss actually appears in real MEA layers.

4.5 Conclusions

The crystal properties of $Ir_xSn_{1-x}O_2$ powders, depend on the method used to prepare such materials. Adams fusion method results in an oxide consisting of at least two separate oxide phases, with one of these containing mostly SnO_2. The modified polyol method is believed to form a solid solution between iridium and tin oxide, with the lattice parameters increasing linearly with tin content. Addition of tin also causes the average crystal size to

increase from around 3.5 to 15 nm. XPS clearly showed that iridium was present in at least 2 valence states while the tin was only present in a single valence state corresponding with the binding energy of Sn^{4+} at high tin contents. Comparing the electrical resistivity of these oxides shows that tin increases the resistivity and that oxides produced via Adams fusion method have higher resistivities. By making simple estimations of possible ohmic losses in a PEM water electrolyser, it is suggested that the limit for tin addition is around 50–60 mol%.

Acknowledgments

The authors would like to acknowledge the financial support from the Norwegian Research Council and Norsk Hydro ASA

Chapter 5

Effect of Annealing Temperature on $Ir_{0.6}Sn_{0.4}O_2$

This chapter can also be found published as:

A. Marshall, B. Børresen, G. Hagen, M. Tsypkin and R. Tunold
"Nanocrystalline $Ir_xSn_{1-x}O_2$ electrocatalysts for oxygen evolution in water electrolysis with polymer electrolyte - Effect of heat treatment"
Journal of New Materials for Electrochemical Systems, 7:197-204, 2004.

5.1 Abstract

Electrocatalysts for the oxygen evolution reaction in proton exchange membrane (PEM) water electrolysers have been produced and characterised. In particular the effect of the oxidising or annealing temperature on the properties of $Ir_{0.6}Sn_{0.4}O_2$ nanocrystalline powders has been examined. The synthesised powders were characterised by XRD and electrochemical methods such as cyclic voltammetry and AC impedance. It is believed that a solid solution between iridium and tin oxide has been synthesised. The results show that the annealing temperature influences the crystallinity, electrochemically active surface area, electrode capacity and particle porosity. The best performance overall at low current is achieved when the material has

been annealed at 450 ° C for 30 minutes. More tests need to be completed to find the performance and stability at high currents in PEM electrolysers.

5.2 Introduction

Water electrolysers with proton exchange membranes (PEM) have recently become interesting as a method for hydrogen production [2] and promising results have been achieved in the last years at our department [7]. The chemical and morphological properties of the anodic catalytic layer defines the most important properties of PEM water electrolysers, like lifetime, power efficiency and operating current density. A well developed three dimensional reaction zone is necessary for an optimal anode operation, where the polymer electrolyte is in a good contact with an electrocatalyst [141]. Also, this zone must be open for reactant supply and gaseous product removal.

It is well known that RuO_2 has the highest activity for oxygen evolution in acidic media, but is not stable [142]. The second most active material is IrO_2, which is essentially stable. Additives of non noble transition elements are used to reduce the cost of the catalyst, and Ta, Ti, and Sn have been shown to increase both active surface area and stability of noble metal oxides [110, 143, 144]. IrO_2 based materials have shown good performance as anode materials in PEM based water electrolysers [7].The electrochemical properties of metallic iridium have also be extensively investigated by Jaksic *et al* [145].

DSA-type electrodes have electrocatalytic noble metal oxide layers with large active surface areas [143], but sufficient contact between such coatings and a polymer electrolyte would not be possible. Also, such DSA-coatings are not homogenous [144].

Different methods can be used to create a three dimensional reaction zone, like: the application of an ink consisting of polymer electrolyte solution and electrocatalytic particles to a polymer electrolyte membrane [146], or particle formation directly in the volume or on the surface of the membrane by chemical or electrochemical reduction of various precursors [147, 148].

Electrocatalytic layer preparation from previously synthesized particles allows the verification and control of both the layer structure and its compo-

sition. Modern methods for nanoparticle synthesis gives the possibility to create electrocatalysts with the required properties [135]. The sol-gel method has been applied to Ir-Sn-oxide nanoparticle synthesis, with particle sizes less than 500 nm being obtained [91]. Although this method may produce layers with larger active surface areas than traditional thermal DSA-coatings, the precursor type strongly affects the particle formation and properties [133]. The polyol method uses glycols to reduce precursors to fine particles of noble metals (e.g. Ir with size of 3 nm) [96]. Bimetallic particles can also be produced by co-reduction of precursor chlorides by refluxing in water-alcohol mixture in the presence of poly-N-vinyl-2-pyrrolidone (e.g. Pt-Pd with size 1.5-3 nm [136]). These metallic particles may then be oxidised chemically or thermally to produce noble metal oxide powders. The polyol method looks as the most attractive method for synthesising single and bimetallic oxide nanoparticles with narrow particle size distributions and higher stability because an alloy may be formed (i.e. atomic mixing of metals) prior to any oxidation steps.

5.3 Experimental

5.3.1 Oxide preparation

Metal precursors ($H_2IrCl_6.4H_2O$ and $SnCl_2.2H_2O$) were added to 50 mL of ethylene glycol to achieve a total metal concentration of $1.54\,x10^{-5}$ mol ml^{-1}. The glycol-precursor solution was then heated under a nitrogen atmosphere to the refluxing temperature and held for 2 hours by which time the glycol was transparent and a black colloid had formed. The colloid was separated by centrifugation and washed in deionised water, before being ultrasonically dispersed in acetone and dried in air at 60 ° C. This dry colloid was then annealed in air at temperatures between 400 and 650 °C for 30 minutes to oxidise the metallic material.

5.3.2 Characterisation

X-ray diffraction was performed on the dry electrocatalytic powders using a Siemens D5005 powder X-ray diffractometer, with a step size of 0.2 °, step time of 50 seconds, slit opening of 0.5 °, and a Cu-K_α X-ray source ($\lambda = 0.154$

nm). A LaB_6 standard was used to calibrate the equipment. The diffraction patterns were fitted to a pseudo-Voigt profile and the crystal size distribution calculated using Warren-Averbach analysis. The crystalline content was estimated by comparing the area of the diffraction peaks associated with crystalline material to that associated with amorphous material [139].

A Hitatchi 3500 electron microscope with Oxford EDS system was used to examine the powder and subsequent electrode morphology and composition. Normally an acceleration voltage of 20 kV and working distance of 15 mm was used.

Electrochemical analysis of the electrocatalytic powders was conducted in a 0.5 M H_2SO_4 electrolyte at room temperature, by supporting the powders on titanium plates using a spraying technique. The electrocatalytic layer consisted of 95 wt% electrocatalyst and 5 wt% Nafion which acts as a binder/electrolyte. The loading was typically 1 mg cm^{-2}, and was determined gravimetrically. The electrodes were subjected to an initial polarisation at 0.5 mA cm^{-2} for 4 minutes, with a steady potential normally being reached within this time. Cyclic voltammetry, AC impedance, and polarisation measurements were performed using an IM6e electrochemical workstation from ZAHNER-elektrik GmbH & Co. KG. A $Hg/Hg_2SO_4,H_2SO_4$ reference electrode and a platinum foil counter electrode were used in the normal fashion. All potentials are quoted versus the reversible hydrogen electrode in the same electrolyte.

5.4 Results and discussion

To examine the effect of annealing temperature a large quantity of Ir-Sn colloid was synthesised and then divided into separate portions just prior to the annealing stage. This ensures that only the annealing temperature effect is observed. The nominal composition was set at 56 mole % iridium and 44 mole % tin. EDS measurements performed on the electrocatalyst showed that the bulk composition was actually 60 mole % iridium, which is in good comparison with the desired value.

5.4.1 XRD analysis

Powder X-ray diffraction patterns (Figure 5.1), show that all the annealed samples have broad diffraction peaks corresponding to a rutile oxide phase, and possibly traces of metallic iridium as indicated by the small peak at 41° (2θ).

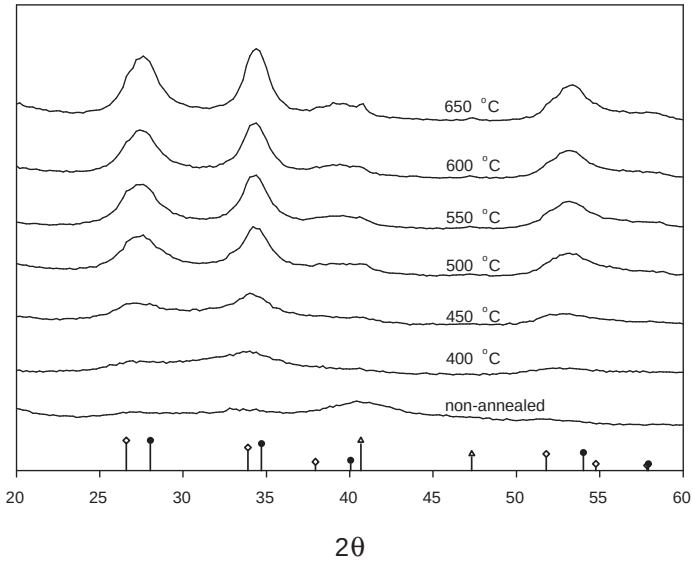

Figure 5.1: XRD patterns - vertical lines indicate peak positions for, • - IrO_2, ◇ - SnO_2, △ - Ir

Clearly there is a significant change upon annealing temperature with the rutile oxide peaks sharpening as the temperature increases. The non-annealed sample appears to be mostly amorphous iridium from the broad peak located around 41 ° (2θ). Development of a well ordered oxide structure (i.e. clear diffraction peaks) only occurs above 450 °C within the 30 minute period studied. The polycrystalline size distribution and the degree of crystallinity of the oxide phase are shown in Figures 5.2 and 5.3.

Figure 5.2 shows that after the initial crystal growth (i.e. oxidation of metallic colloid particles) the crystal size distribution is similar with the average

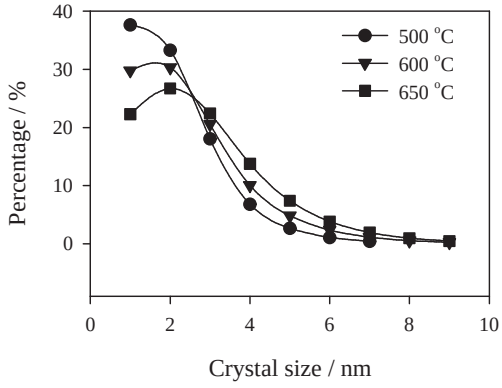

Figure 5.2: Effect of annealing temperature on the polycrystalline size distribution

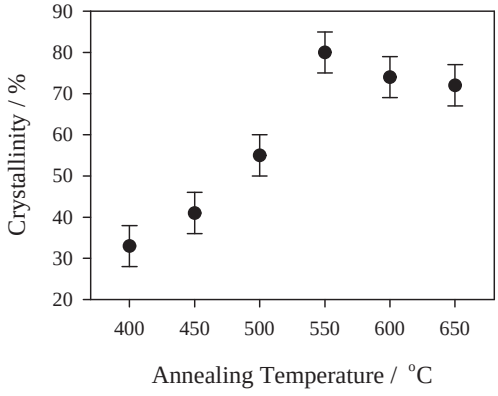

Figure 5.3: Effect of annealing temperature on the degree of crystallinity

crystal size around 1.5-2 nm. Unfortunately the samples prepared at 400 and 450 °C could not be accurately profiled in order to find their crystal size distribution due to their low crystallinity, but the average crystal size of these materials was similar to those prepared at higher temperatures. At temperatures around 550-600 °C it is seen that the crystallinity and crystal size distribution remains approximately constant, whereas at 650 °C there is a slight change in the crystal size distribution, most likely due to crystal growth. It is important to stress that the "crystallinity" value indicates the amount of material with a certain level of atomic ordering. So the increase in crystallinity from 400 to 550 °C indicates that more material has sufficient ordering to cross the amorphous-crystalline threshold (approximately 1 nm crystal size).

Table 5.1: Crystal Parameters - Solid solution phase

Annealing Temperature (°C)	a (nm)
450	0.454
500	0.459
550	0.459
600	0.459
650	0.457

The XRD analysis indicates that a solid solution between iridium and tin oxide is formed at all annealing temperatures, with broad diffraction peaks lying in-between those for pure IrO_2 and pure SnO_2. The lattice parameter, a, for this solid solution phase is shown in table 1, and indicates that the crystals may differ at 450 and 650 °C from those at 500-600 °C. The lattice parameter suggests that the crystal structure is more similar to IrO_2 at these two temperatures (a = 0.450 and 0.474 nm for IrO_2 and SnO_2 respectively). At 450 °C this difference is likely due to the high level of disorder and incomplete oxidation of the material. As the temperature increases, the material is ordered into crystals with a composition close to the bulk composition. At 650 °C this solid solution may become unstable, leading to tin segregation and a crystal with parameters closer to IrO_2. This may be supported by the presence of a tin rich oxide phase, indicated by the small shoulder appearing to the left of the oxide peaks. This is especially evident in materials that have been annealed at higher temperatures. This shoulder was included in

the peak profiling and it appears this phase is almost pure SnO_2. A surface sensitive technique such as XPS would greatly help in confirming the segregation of tin from the oxide lattice.

Iridium-tin oxide solid solutions have had some attention, with a metastable (Sn, Ru, Ir)O_2 powder being prepared via direct air oxidation and the Adams fusion method [84]. This metastable oxide was seen to decompose into (Ru, Ir)O_2 and SnO_2 after annealing at 800 °C. XRD data for thermally prepared Ti/IrO_x-Sb_2O_5-SnO_2 electrodes indicated an IrO_x-Sb_2O_5-SnO_2 solid solution was formed, which is decomposed into separate SnO_2 and Ir phases after high temperature annealing [76]. Another study examined Ir-Sn oxide powders prepared via a sol-gel method which revealed broad XRD patterns consistent with a solid solution between iridium and tin oxide [91]. The lattice parameters of the solid solution phase showed a linear relationship over the entire composition range. Others have found either no or very limited solubility of IrO_2 in SnO_2 [111, 112] at high temperatures, possibly confirming that only a metastable solution is possible. From a theoretical standing, comparing the ionic radii of Ir^{4+} and Sn^{4+} (0.077 and 0.083 nm respectively) it is seen that the Hume-Rothery rule for solid solutions [42] is fulfilled. Differences in preparation procedure could account for variation in oxide structure. In this work, because strong interaction between the iridium and tin species occurs in the polyol stage, an atomically mixed Ir-Sn material is probably produced prior to the annealing / oxidation stage increasing the likelihood of a stable or metastable solid solution forming.

5.4.2 SEM analysis

A SEM micrograph of a typical electrocatalytic layer is shown in Figure 5.4. At this magnification and resolution, no differences in the nanostructure can be concluded. It is obvious, however, that the electrocatalytic layer is highly porous and rough on the micrometer scale. No conclusive differences from SEM analysis could be established for the different samples prepared in this work. EDS analysis showed that the composition of the electrocatalytic layer was homogenous on the micrometer scale.

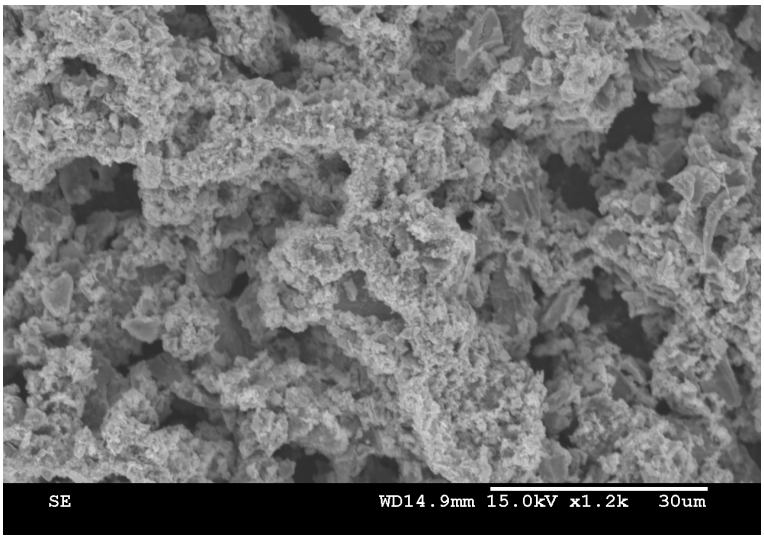

Figure 5.4: SEM micrograph of $Ir_{0.6}Sn_{0.4}O_2$ electrocatalytic layer

5.4.3 Cyclic voltammetry

Cyclic voltammograms were recorded at sweep rates between 5 and 200 mV s^{-1}. Voltammograms recorded at 20 mV s^{-1} show that overall the shape of the voltammograms resemble thermal iridium-based oxides, indicating that the surface electrochemistry is most likely dominated by the iridium species (Figure 5.5 - note the different current density scales).

At the lower annealing temperatures (400-450 °C), the shape of the voltammograms are different from the "normal" iridium dioxide shape seen in most literature. This difference is most likely due to the poorly defined crystal structure, imbalance of redox species, and non-stoichiometric nature of the oxide. Similar variations in shape are seen on DSA Ir-Sn electrodes prepared at low temperatures [71]. The samples annealed at higher temperature show the typical capacitance behaviour with the anodic:cathodic charge ratio close to 1. The redox peaks associated with iridium are unfortunately not very clear, although the broad peak at 0.90-0.95 V is probably related to the $Ir^{+3} \rightarrow Ir^{+4}$ transition. DSA type Ir-Sn oxide electrodes with high Sn contents showed a cathodic current at around 0.4 V which was suggested to be due to SnO_2 reduction [71]. Although there is a large cathodic current seen on

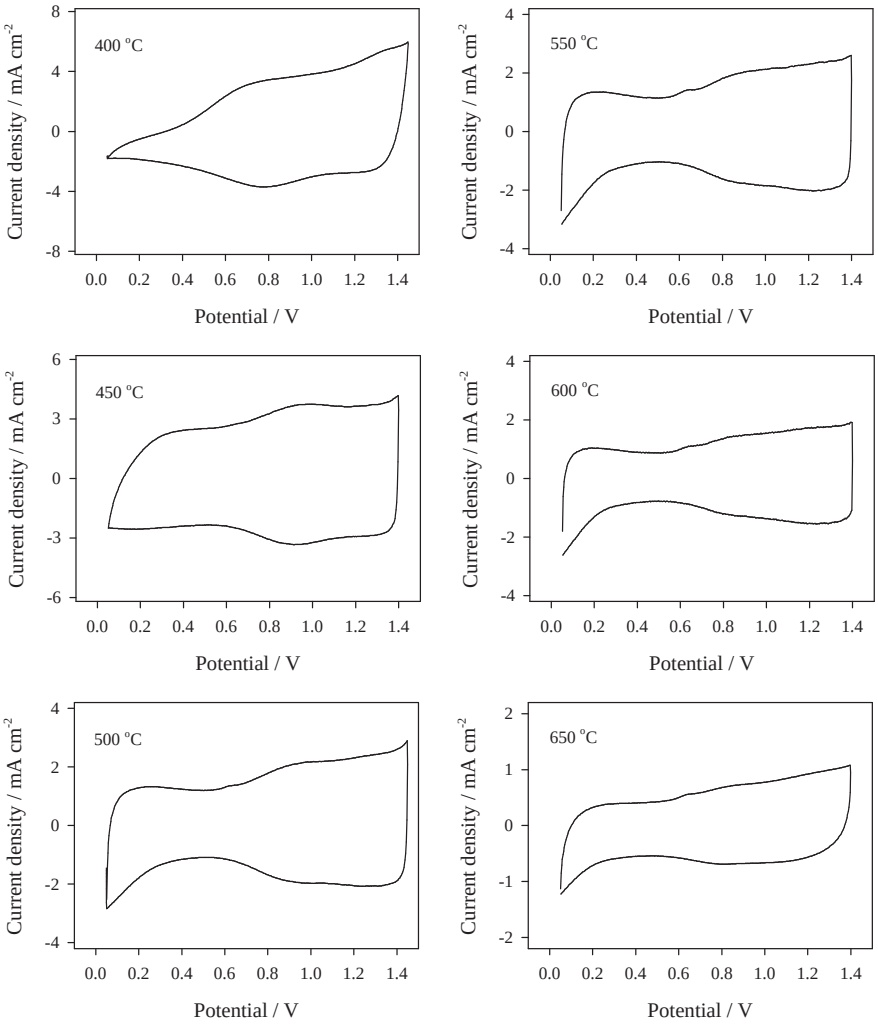

Figure 5.5: Cyclic voltammograms recorded 20 mV s^{-1} Annealing temperatures are indicated on the figures

the electrocatalysts with annealing temperatures above 500 °C this is similar to the hydrogen region seen on voltammograms of pure IrO_2 [7, 149, 114] which is suggested to be underpotential adsorption of hydrogen [7]. Also no change in the shape was observed upon cycling the potential between the hydrogen and oxygen evolution limits 20 times, indicating the material is at least stable for short periods within this potential window.

It is widely known that the anodic charge is a direct indication of the electrochemically active area for noble metal oxides like IrO_2 [61]. Furthermore measuring the anodic charge as a function of sweep rate can yield interesting information regarding the morphology of the active surface [71]. In this work the total and outer anodic charge was calculated for the potential range 0.6-1.4 V as described elsewhere [71]. At high sweep rates only the outer surface of the oxide material takes part in the charging process, whereas at very low sweep rates the "inner" surface is also accessible due to diffusion of protons through pores, cracks and grain boundaries in the oxide material. The proton exchange between surface oxide-OH groups and the acid electrolyte is considered to be rapid at "easily accessible" regions, whereas this exchange has some diffusion limitations within the inner regions [127].

Figure 5.6 shows both the total and inner anodic charge as a function of annealing temperature.

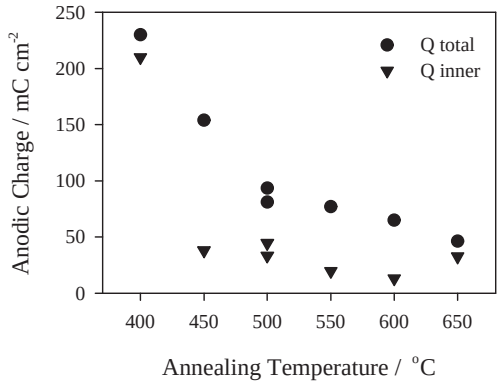

Figure 5.6: Anodic charge as a function of annealing temperature

The effect of annealing temperature on the total anodic charge is straightfor-

ward, showing a clear decrease with increasing temperature, which is typical for most noble metal oxides [61]. This is most likely due to an increase in crystal size and crystallinity, and a decrease in surface defects.

As the temperature is raised from 400 to 450 °C there is a large decrease in inner charge. This is understood by the initial development of crystals which sharply decreases the nanoporosity. This is confirmed by the change in the voltammogram shape towards the normal capacitive behaviour. Between 450 and 600 °C there is a steady decrease in the inner anodic charge due to the increased crystallinity and therefore reduced particle nanoporosity. The outer charge (difference between total and inner charge) is seen to significantly decrease between 450 and 500 °C due to the formation of well defined crystal surfaces, which are more stoichiometric with fewer defects. Indeed the voltammogram shape and XRD supports the idea of formation of well-defined IrO_2 like crystals at 500 °C.

At temperatures between 500 and 600 °C the outer charge is almost constant at around 50 mC cm^{-2}. This indicates that the crystal surfaces remain stable while the inner active area slightly decreases due to the development of less nanoporous particles. At 650 °C the inner area increases indicating more cracks and nanopores have been formed. The shape of the voltammogram for the sample prepared at 650 °C is also different from the others, in that the anodic:cathodic charge ratio deviates significantly from 1, indicating that the electrocatalyst-electrolyte interface is not that of a pure capacitor. This may be due to the instability of the crystal structure at this temperature, where tin segregation may create defects or cracks within the material and result in surface enrichment by tin.

5.4.4 Electrochemical impedance spectroscopy

AC impedance measurements were performed at 1.2 V and in the range 1.45-1.5 V with an amplitude of 5 mV over the frequency range of 40 kHz - 20 mHz. A Nyquist plot of the results obtained on a typical electrode over this potential range is shown in Figure 5.7.

As normally expected for a charge transfer reaction, the value of the charge transfer resistance (R_{ct}) as indicated by the size of the low frequency semicircle in the Nyquist plot, decreases with increasing potential. It is seen that

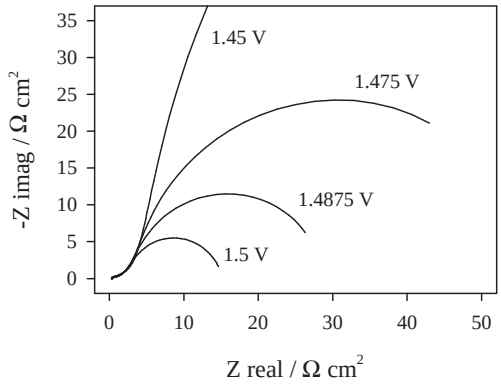

Figure 5.7: Impedance spectrum for a sample annealed at 500 °C

there is also another process occurring at high frequency, which is typical for noble metal oxide electrodes [127] (discussed later). This high frequency process was virtually potential independent in the range examined.

As with many impedance results, any number of complex equivalent circuits can be applied to the data obtained. However it is always important to be sure that the equivalent circuit has some physical relevance to the system under investigation. The electrodes used here are probably best described by a porous electrode model as discussed in some literature [150, 151]. DSA type electrodes are normally modeled using equivalent circuits, like $LR_{\Omega}(Q_1R_1)(Q_{dl}R_{ct})$ [73, 127] and $LR_{\Omega}(C_1R_1)(C_{dl}R_{ct})$ [152], where L is an inductor, R is a resistive element, Q is a constant phase element and C is a pure capacitive element. In these circuits the (Q_1R_1) or (C_1R_1) component normally used to describe the porous electrocatalytic layer, and the $(Q_{dl}R_{ct})$ or $(C_{dl}R_{ct})$ component describes the oxygen evolution reaction. The $LR_{\Omega}(Q_1R_1)(Q_{dl}R_{ct})$ circuit was fitted to the samples that had been annealed at 550 and 600 °C. These samples are believed to have lower nanoporosity and therefore the high frequency process is adequately described by the (Q_1R_1) term resulting in a satisfactory fit between the measured data and the model (Figure 5.8).

This circuit however could not be used for the other electrodes where the nanoporosity or defects are thought to have a greater influence on the elec-

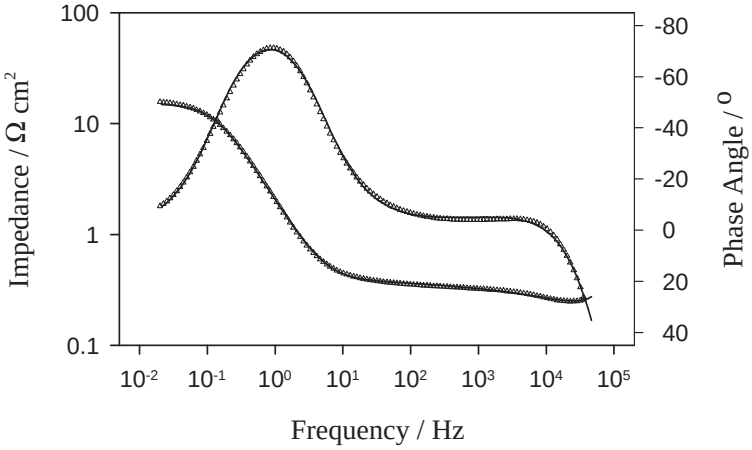

Figure 5.8: Measured and simulated impedance spectrum, 1.5 V - sample annealed at 600 °C, △ - measured data, line - fit results

trodes impedance response, especially at high frequency. To overcome this, the circuit was simplified further to $R_f(Q_{dl}R_{ct})$ and only fitted to the frequency range where the electrode reaction dominates (10Hz - 20mHz). In this circuit the R_f element is used to describe the ohmic resistance between the working electrode and reference electrode as well as the real term associated with the impedance response from the electrode porosity. The true capacitance, C_{dl}, was calculated from the constant phase element values using a previously described method [153]. Although the results should be treated carefully, the capacitance values closely matched those obtained at 1.2 V during voltammetry measurements where C = i / (dE/dt).

From the analysis we find that there is a general increase in R_{ct} with annealing temperature (Table 5.2) with this trend seen at all potentials between 1.45 and 1.5 V.

The increase in R_{ct} is attributed to the decrease in total active area as seen by cyclic voltammetry, although the change in area from charge measurements does not completely account for the large R_{ct} value measured for the oxide annealed at 650 °C. This indicates that at 650 °C there may also be a decrease in real activity of the material.

Table 5.2: Low frequency impedance parameters at 1.5 V

Annealing Temperature (°C)	R_{ct} (Ω cm^{-2})	C_{dl} (mF cm^{-2})	α_{ct}
450	6	150	0.9
500	11	83	0.9
550	10	93	0.93
600	15	82	0.99
650	64	25	0.78

The capacitance at all potentials follows a similar trend to the outer active area measured by voltammetry. There was also no significant potential dependence of the capacitance measurements. Often, due to the oxygen evolution reaction, gas blocking can lower the measured capacitance [73]. Although the nature of the active layer (i.e. a supported particle layer rather than a compact oxide film) is highly porous, the results observed indicate that gas blocking is not limiting the reaction at these potentials. This is probably due to the high macroporosity which allows the evolved gas to freely escape from the layer.

The exponent value, α_{ct}, of the CPE associated with the electrode reaction, indicates how close the electrocatalyst layer-electrolyte interface is to a pure capacitor. For a pure capacitor, α is equal to 1, and for a pure resistor α equals 0. When α equals 0.5 the CPE is said to be a Warburg type impedance. Normally a change in α is attributed to the layers morphology [127]. At 1.5 V a maximum in α_{ct} is found at an annealing temperature of 600 °C (Table 5.2). The increase in α_{ct} with annealing temperature is most likely due to more defined crystal surfaces and less nanoporosity (i.e. inner active area) within the material. The sudden decrease at 650 °C, is again likely due to changes within the crystal, where tin segregation from the lattice to the surface is suggested to occur.

The high frequency process is best examined in the Bode representation, in particular the phase angle (Figure 5.9). As stated above, this process is normally attributed to the porosity of the oxide layer or the contact between the conductive layer and the support (particularly if a doped titanium oxide layer has formed on the support) [127].

In this work a thermally formed titanium oxide layer is not possible, and any

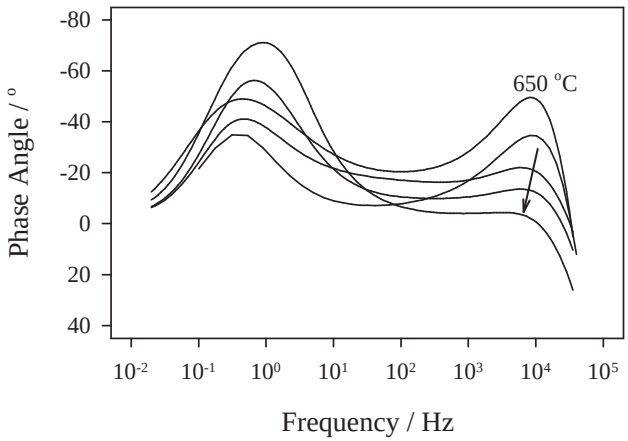

Figure 5.9: Phase angle of measured impedance spectrum at 1.5 V Arrow indicates increasing annealing temperature from 450-600 °C

electrochemically formed films between the support and active layer should be present in all electrodes due to the high micro porosity of the electrodes. Furthermore this process is unlikely to arise from a charge transfer reaction due to its potential independence. This suggests that the high frequency process is due to the particle porosity / morphology. In figure 5.9, it is seen that as the annealing temperature increases from 450 to 600 °C, the significance of the high frequency process decreases. This is in good agreement with other results, which indicate that crystal growth results in less nanoporous particles. The large change at 650 °C is difficult to explain, but is suggested to be due to the change in crystal properties. If instability of the solid solution at 650 °C causes cracks and defects within the material, the large increase in phase angle supports the hypothesis that the high frequency process arises from the transport processes within the cracks and pores of the oxide. Indeed a similar high frequency process has been attributed to diffusion of proton within the grains of thermally prepared IrO_2 [154].

5.4.5 Polarisation results

The steady state polarisation curves for all electrodes are shown in Figure 5.10. At low current densities the curves show Tafel behaviour, with the slope, b, indicated in Table 5.3

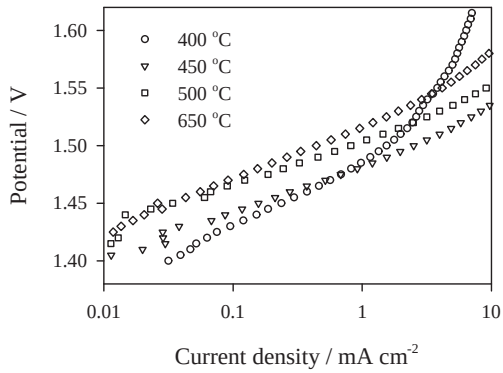

Figure 5.10: Steady state polarisation curves performed in 0.5 M H_2SO_4

Table 5.3: Results from steady state polarisation in 0.5 M H_2SO_4

Annealing Temperature (°C)	b (mV dec^{-1})	$E_{(1mAcm^{-2})}$ (V)	$E_{(0.002AC^{-1})}$ (V)
400	51	1.49	1.463
450	40	1.48	1.461
500	38	1.50	1.468
550	37	1.50	1.466
600	37	1.50	1.468
650	45	1.52	1.468

At 400 and 650 °C the electrodes shows different Tafel slopes to the samples prepared at intermediate temperatures. This is consistent with other measurements which suggests these materials have different crystal or particle properties. A Tafel slope of 40 mV dec^{-1} suggests that the second step in the Electrochemical Oxide Path mechanism [15] is the rate determining process at low current density. The slight decrease in Tafel slope as the an-

nealing temperature increases from 450 to 600 °C, may be due to a change in the relative rates of each step in the mechanism, especially if those steps have similar rates [7]. This may be resolved by investigating the reaction dependence on H^+ activity. The deviation in Tafel behaviour for the sample prepared at 400 °C is thought to be a result of catalyst loss due to the mechanical instability of this layer. Poor electrical conductivity may also play a role in this deviation [7]. Overall it is clear that the material prepared at 450 °C shows the best performance at 1 mA cm^{-2} (Table 5.3). When the currents are normalised by anodic charge (i.e. active surface area) the changes in performance appear to be solely due to surface area effects (Table 5.3).

As these materials have been developed for use in polymer electrolyte water electrolysers, some further work is needed to establish how these oxides behave in this environment. Such experiments are under way, in order to correlate the results obtained in aqueous electrolyte with results in polymer electrolytes.

5.5 Conclusions

Solid solutions of the type $Ir_xSn_{(1-x)}O_2$ have been produced by annealing metallic colloids produced by the polyol method, at elevated temperatures. In addition to the oxide solid solution, SnO_2, metallic iridium, and amorphous material are present in the powder. The properties of these materials vary within the temperature range examined, with the main differences ascribed to crystallisation and stability of the oxide. Polarisation analysis in 0.5 M H_2SO_4 suggests that $Ir_{0.6}Sn_{0.4}O_2$ should be heat treated at 450 °C to achieve a high active area, while maintaining well defined crystal surfaces. More analysis is necessary to confirm the stability and structure of these materials, and how these oxides perform in polymer electrolyte based systems.

5.6 PEM water electrolysis performance

Since the publication of the above results, some further analysis of the prepared materials was carried by testing the performance of a single PEM

water electrolysis cell using the $Ir_xSn_{(1-x)}O_2$ electrocatalysts as the anode. All measurements used a Nafion 115 membrane and 20% Pt/C cathode electrocatalyst. The anode loading was maintain at 2 mg cm^{-2} and the cathode loading 0.4 mg Pt cm^{-2}, with 5 wt% Nafion in the anode and 10 wt% Nafion in the cathode. The electrodes were prepared by spraying a dispersion of isopropanol, electrocatalytic particles, and Nafion ionomer directly to the membrane heated at 90 °C.

The cell polarisation curves at 80 °C is shown in Figure 5.11. The cell performance is seen to be approximately the same for the cells where the anode was annealed at 400-450 °C. At higher annealing temperatures, as expected based on the measurements in the aqueous electrolyte, the performance decreases and remains constant up to 550 °C. At higher annealing temperatures the cell voltage decreased further. The best result was obtained with an anode annealed at 450 °C, with a cell voltage of 1.655 V at 1 A cm^{-2} and 80 °C when using Nafion 115 as the electrolyte membrane. This equates to a cell efficiency of 72 % ($\varepsilon_{\Delta G}$) and an energy consumption of 3.96 kWhr Nm^{-3} H_2 at 1 A cm^{-2}. Comparing this cell potential with the best literature results, shows that even with additions of 40 mol% Sn, the cell performance is comparable with results obtained with higher noble metal loadings (see section 3.1.1).

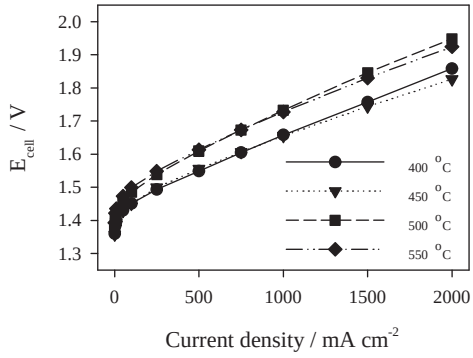

Figure 5.11: PEM water electrolysis cell polarisation

Chapter 6

Electrochemical Characterisation of $Ir_xSn_{1-x}O_2$ Powders as Oxygen Evolution Electrocatalysts[1]

This parts of this chapter have been submitted for publication as: A. Marshall, B. Børresen, G. Hagen, M. Tsypkin and R. Tunold
"Electrochemical characterisation of $Ir_xSn_{1-x}O_2$ powders as oxygen evolution electrocatalysts"
Electrochimica Acta, Feb 2005.

6.1 Abstract

The electrochemical properties and electrocatalytic performance of nanocrystalline oxide powders of the type $Ir_xSn_{1-x}O_2$ ($0.2 \leq x \leq 1$) have been examined. These oxides have been developed primarily as oxygen evolution

[1] A summary of this chapter was presented as a keynote lecture at the 55^{th} ISE meeting 19-24 September 2004 Thessaloniki, Greece

electrocatalysts for proton exchange membrane (PEM) water electrolysers. The modified polyol method was used to prepare these oxides, by reducing precursors in ethylene glycol followed by thermal oxidation at 500 °C. The materials were characterised in 0.5 M H_2SO_4 and PEM electrolytes by cyclic voltammetry, electrochemical impedance spectroscopy, and steady state polarisation measurements. Some comparisons were made between the electrocatalytic properties in the different electrolytes.

6.2 Introduction

Proton exchange membrane (PEM) water electrolysers can be used to produce carbon free hydrogen from water [2]. Recently IrO_2 based materials have been examined as the oxygen evolution electrode in our group [7, 130, 114, 131]. Previously it has been shown that SnO_2 improves the stability of IrO_2-RuO_2 anodes in PEM water electrolysers [84]. It has also been suggested that SnO_2 does not reduce that activity of RuO_2 as much as TiO_2 [61, 137]. For these reasons, additions of SnO_2 to IrO_2 has been investigated.

Noble metal oxides as electrocatalysts (particularly IrO_2 and RuO_2) are well established in many industrial electrochemical processes in the form of dimensionally stable anodes (DSA) as developed by Beer [60]. Most DSA electrodes are prepared by thermal decomposition of metal precursors (e.g. $RuCl_3$ and $IrCl_3$) on titanium substrates. This method is unsuitable for PEM water electrolysers due to the difficulty in obtaining good contact between the electrocatalytic layer and the membrane electrolyte. Therefore to obtain an electrocatalytic layer on the membrane, previously prepared powders may be applied as an ink to the membrane forming the membrane electrode assembly (MEA) [23, 105].

There are many methods available for the synthesis of noble metal based oxides. The polyol method is a relatively simple way to synthesise nanosized noble metal colloids such as iridium or ruthenium [96, 97] by the reduction of metal precursors in ethylene glycol. These metallic materials can then be thermally treated, forming the oxide material.

In this work, the electrochemical properties of $Ir_xSn_{1-x}O_2$ nanocrystalline powders are investigated by electrochemical measurements in 0.5 M H_2SO_4.

The performance of some of the oxides as anodes in a PEM water electrolysis cell is also examined. These materials have also been investigated by X-ray diffraction, X-ray photoelectron spectroscopy, and electrical resistivity measurements (Chapter 4).

6.3 Experimental

6.3.1 Oxide preparation

Metal precursors ($H_2IrCl_6.4H_2O$ [2] and $SnCl_2.2H_2O$ [3]) were added to 50 mL of ethylene glycol to achieve a total metal concentration of 1.67 x10^{-5} mol cm^{-3}. The glycol–precursor solution was then heated under a nitrogen atmosphere to the refluxing temperature and held for 2 hours, by which time the glycol was transparent and a black colloid had formed. The pH of this colloid–glycol mixture was measured and adjusted to pH 2.5 by the addition of 0.1 M NaOH solution. This aided the separation process of the colloid from the glycol, which was achieved by centrifugation. The recovered colloid was washed in deionised water 3 times, before being ultrasonically dispersed in acetone and dried in air at 60 °C. This dry colloid was then annealed in air at 500 °C for 30 minutes to oxidise the metallic material. Previously it has been seen that non-annealed Ir-Sn colloids have very broad diffraction patterns associated with metallic iridium and that a rutile oxide structure is formed above 450 °C [132].

6.3.2 Characterisation

Electrochemical analysis of the electrocatalytic powders was conducted in 0.5 M H_2SO_4 and PEM electrolytes. The aqueous electrolyte was used as this provides a simple model system in which to examine the synthesised electrocatalysts. It is quite common for PEM fuel cell electrocatalysts to be evaluated in this manner [155, 156]. The anode layers (both for the aqueous and PEM systems) were prepared by spraying an ink containing the

[2] OMG AG & Co. KG - 99.92 % metals basis
[3] Alfa Aesar - ACS grade

oxide particles and Nafion ionomer onto clean titanium plates for the aqueous electrolyte measurements and directly onto a Nafion 115 membrane for the PEM measurements. The anode layer consisted of 95 wt% electrocatalyst particles and 5 wt% Nafion which acts as a binder/electrolyte. The loading was 1 mg cm^{-2} for the titanium supported electrodes, and was determined gravimetrically. The loading for the PEM system was approximately 2 mg cm^{-2}. A more detailed discussion regarding the preparation of the membrane electrode assemblies for PEM water electrolysers has been given previously [114].

Within the PEM cell, a small reservoir was filled with 0.5 M H_2SO_4 and contacted perpendicularly to the polymer membrane approximately 5 mm from the electrode edge via a small capillary drilled into the polycarbonate cell housing. A Hg/Hg_2SO_4,H_2SO_4 reference electrode was then placed within the reservoir to measure the potential of each electrode separately. This electrode arrangement is shown in Figure 6.1. The cathode was prepared in a similar method to the anode, by spraying 20% Pt on Vulcan XC-72 R (E-TEK) directly to the opposite side of the membrane. This layer contained 10 wt% Nafion and the total Pt loading was 0.4 mg cm^{-2}. Porous titanium sinters were pressed against these catalytic layers to provide the electrical contact. Deionised water was circulated (300 l hr^{-1}) by small pumps through each electrode compartment.

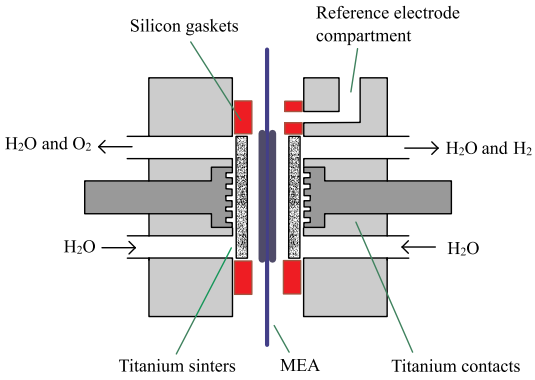

Figure 6.1: Schematic of the PEM water electrolysis cell

A Hg/Hg_2SO_4,H_2SO_4 reference electrode and a platinum foil counter electrode were used in the normal fashion for the aqueous electrolyte system.

This electrolyte was de-aerated with bubbling N_2 prior and during all measurements.

The electrodes in 0.5 M H_2SO_4 were subjected to an initial polarisation at 0.5 mA cm^{-2} for 4 minutes, with a steady potential normally being reached within this time. The PEM electrodes were galvanostatically polarised at 10 mA cm^{-2} for 10 minutes then 50 mA cm^{-2} for 20 minutes. Cyclic voltammetry, electrochemical impedance spectroscopy and polarisation measurements were performed using an IM6e electrochemical workstation from ZAHNER-elektrik GmbH & Co. KG. The impedance measurements were carried out with an offset of 20 mA cm^{-2} and an amplitude of 5 mV over the frequency range of 40 kHz - 20 mHz. The potential of the reference electrode was measured against a reversible hydrogen electrode (RHE) in the same electrolyte and all potentials are given versus RHE in 0.5 M H_2SO_4.

6.4 Results and discussion

6.4.1 Structural and electrical properties of $Ir_xSn_{1-x}O_2$

XRD analysis revealed that the produced oxides are nanocrystalline and consist of a single oxide phase with rutile structure. The lattice parameters showed a linear relationship to the bulk composition, with the two composition extremes (x= 0 and 1) corresponding to the lattice parameters of IrO_2 and SnO_2. The crystal size remained constant for $0.5 < x < 1$ at around 3–6 nm whereafter the crystallite size increased in a linear fashion to 15 nm for $x = 0.2$. The electrical resistivity of the oxide powders was also examined by pressing the oxide between two pistons and measuring the resistance as a function of the pressed oxide thickness. As tin is added to the oxide, the electrical resistivity increased as expected, with approximately 3 orders of magnitude difference between IrO_2 and $Ir_{0.25}Sn_{0.75}O_2$. XPS revealed that the Sn $3d_{5/2}$ photoelectron binding energy showed a linear increase as the iridium content decreased. At high tin contents the Sn $3d_{5/2}$ binding energy was consistent with Sn^{4+} in SnO_2. The changes in the Sn $3d_{5/2}$ binding energy is consistent with an electron pushing affect towards the tin surface atoms when the iridium content increased. The surface ratio of Ir and Sn showed a small difference to the bulk composition with a slight surface enrichment (5–10 mol%) of tin found for the majority of samples. A more

detailed analysis of the structural properties of these materials has submitted for publication elsewhere [157].

6.4.2 Cyclic voltammetry - Aqueous electrolyte

Typical voltammograms for $Ir_xSn_{1-x}O_2$ (x = 0.5, 1) are shown in Figure 6.2. The oxide electrodes have the normal iridium oxide shape, with the shape very similar to Ir-Sn oxide DSA electrodes examined by Balko and Nguyen [110]. Overall it can be seen that the anodic portion of the voltammograms are almost symmetrical around the zero current line, indicating that the oxides show capacitive behaviour in this potential window. The reversibility of the pseudo-capacitance process was examined by calculating the ratio of the charge between 0.6 and 1.4 V of the forward sweep and the reverse sweep (Qa/Qc). These calculations will give a measure of changes to the reversiblity of the charging process as well as the some idea of the relative difference in redox peak potentials during the anodic and cathodic scan. The result is shown for tin contents of 0, 40 and 80 mol% (Figure 6.3) with a change in the apparent reversibility occuring at 80 mol% Sn. De Pauli and Trasatti made similar calculations for DSA type Ir-Sn oxide electrodes, and found the Qa/Qc was approximately 1 except at low iridium contents (< 0.5 mol%) indicating that for DSA electrodes iridium strongly dominates the electrode response [71]. The change in reversibility may occur due to the differences in the metals electronegativity and acid–base properties of the two oxides. The electronegativity of Sn is lower than Ir, indicating that the SnO_2 will be less acidic than IrO_2. This has been shown by others using pzc measurements [28]. Therefore differences in the acid–base properties will perturb the charging process as the SnO_2 can act as an Brønsted base, accepting protons from the IrO_2 sites. It is proton exchange with the electrolyte which gives rise to the psuedo-capacitor behaviour of these oxides, and therefore if this process is altered by the presence of SnO_2, some irreversibility may occur.

Charge measurements are often used in DSA literature to compare the active area or number of active points of a noble metal oxide layer. By using the technique developed by others [35], the total charge and the outer charge for the oxides were calculated by measuring voltammograms at sweep rates of 5–200 mV s^{-1}. We believe that the outer charge (Q_{outer}) will best represent the

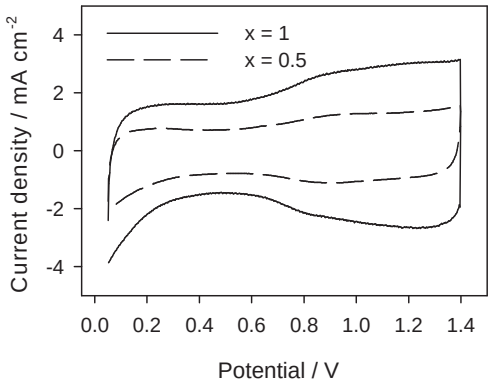

Figure 6.2: Cyclic voltammogram of $Ir_xSn_{1-x}O_2$ at 20 mV s^{-1}

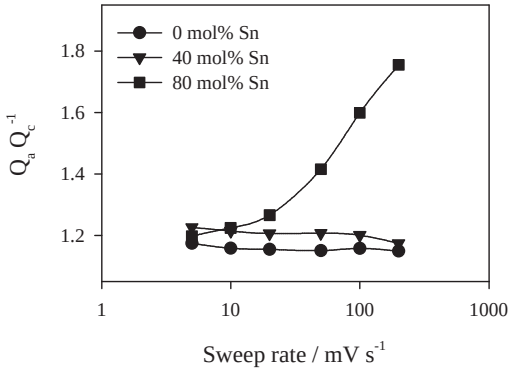

Figure 6.3: Reversibility of pseudo-capacitance process for $Ir_xSn_{1-x}O_2$

available active area during oxygen evolution. The results (Figure 6.4) show that as tin is added, both the total and outer charge decreases. This is clearly expected as tin oxide does not normally exhibit a large pseudo-capacitance compared to iridium oxide. Often, additions of a second or third non-active element gives rise to a large initial increase or some clear maximum in the active area due to more defects in the surface, reduced crystallinity, or favorable dispersion of the active species [71, 74, 129]. In this work we do not find clear evidence for this, as any dispersion will probably occur when the materials are heterogenous. The oxides here are very homogenous as seen by SEM/EDS and XRD. XRD showed that the crystallinity of the oxide increased as the tin content was increased, an affect which will contribute to the decrease in active area found here. Also XPS analysis revealed that the surface composition followed the bulk composition quite closely with only small derivations (5–10 mol%) cause by surface enrichment of tin. This indicates that the active surface area decreases upon tin addition due to both increased crystallinity and dilution of the active iridium sites by tin. Previous work with Ir-Sn oxide DSA electrodes showed considerably lower anodic charges (around 5 times lower) but a similar decrease in charge as tin replaced the iridium [128].

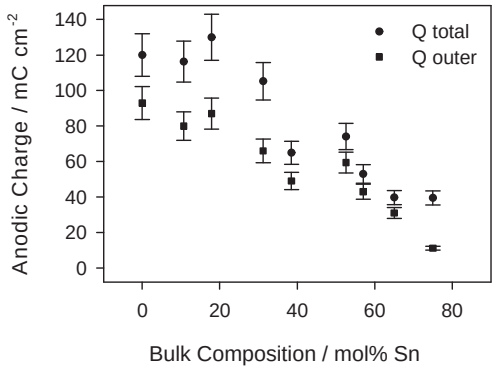

Figure 6.4: Total and Outer anodic charge of $Ir_xSn_{1-x}O_2$ calculated between 0.6–1.4 V using the method described by others [35]

6.4.3 Polarisation measurements - Aqueous electrolyte

After the cyclic voltammetry measurements, steady state polarisation curves were recorded by stepping the potential anodically in 5 mV steps from 1.4 V RHE, with a holding time of 1 minute by which time the current was seen to have stabilised. Due to the nature of the layer, normally current densities above 10 mA cm^{-2} caused the layer to become mechanically unstable. Typical polarisation curves of the oxides measured in 0.5 M H_2SO_4 are shown in Figure 6.5 with the data summarised in Table 6.1.

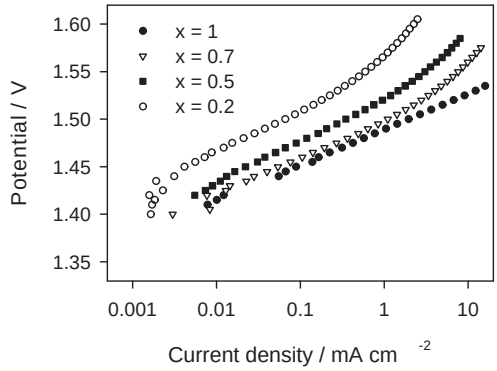

Figure 6.5: Polarisation curves of $Ir_xSn_{1-x}O_2$ in 0.5 M H_2SO_4

The Tafel slope for the oxides prepared by the polyol method appears to be approximately constant with values around 36 mV dec^{-1} except for the highest Sn content where the Tafel slope was measured to be 42 mV dec^{-1}. Tafel slopes measured on Ir-Sn DSA electrodes were 55-60 mV dec^{-1} over the range 10-100 mol% IrO_2 and larger than 120 mV for iridium contents less than 10 mol% [128]. Others found that the Tafel slope on Ir-Sn oxide DSA electrodes was 70 mV dec^{-1} for iridium contents of 50-100 mol% Ir, and 100-170 for lower iridium contents [110]. Oxygen evolution also occurs on pure SnO_2 electrodes with a Tafel slope around 120 mV dec^{-1} [128]. The Tafel slope and electrochemical activity for oxygen evolution on doped SnO_2 in basic media has been shown to be related to the doping element [115]. Many other investigations on DSA electrodes, have shown that Tafel slopes of 60 mV dec^{-1} are typical for IrO_2 based electrodes [12, 95, 129]. There is a clear

Table 6.1: Summary of polarisation measurements of $Ir_xSn_{1-x}O_2$ in 0.5 M H_2SO_4

x	b mV dec^{-1}	$E_{\ 1mAcm^{-2}}$ V vs. RHE
0.2	42	1.569
0.3	36	1.534
0.4	37	1.520
0.5	36	1.506
0.6	36	1.505
0.7	37	1.498
0.8	36	1.490
0.9	36	1.490
1.0	38	1.489

difference in the rate determining step for oxygen evolution on DSA and these composite electrodes, especially given that the Tafel slope remains relatively low over the entire composition range examined. There are several proposed mechanisms which can describe the oxygen evolution reaction in acidic media [12]. Tafel slopes of 30 and 40 mV dec^{-1} indicate that the second step in the "oxide path" and "electrochemical oxide path" respectively may be the rate determining steps. It is unclear in this case which mechanism is operating on these electrodes. As the oxides clearly consist of polycrystalline and amorphous materials, there is likely to be many different types of active sites, with oxygen evolution on each type of site possibly showing a different mechanism or rate determining step or both. This means that the measured response is some average of all the active points, and is therefore very difficult to decouple. Furthermore, the symmetry factor or charge transfer coefficient may not be 0.5, complicating the analysis of the mechanism from the Tafel slope.

The potential measured at 1 mA cm^{-2} shows that the overall performance of the materials decreases upon tin addition (Table 6.1). This is expected as SnO_2 is not as active towards oxygen evolution in comparison to IrO_2. The results therefore indicate that SnO_2 acts primarily to dilute the noble metal oxide. It is interesting however to note that addition of around 20 mol% Sn to the oxide does not increase the potential very much and therefore almost the same performance at low current densities is obtained with less noble

metal loading.

Normalising the current density by the outer charge found by voltammetry, enables a measure of the specific electrocatalytic activity to be estimated, assuming that the outer charge is directly proportional to the true active area. The potentials at a normalised current density of 0.02 A C^{-1} were used to compare the materials (Figure 6.6). It is clear that the initial decrease in overall performance for the oxides is solely due to a change in the active area rather than a reduction in the specific electrocatalytic activity, as the potential at the normalised current remains constant. At approximately 50–60 mol% Sn the activity is seen to decrease and perhaps reach a new level at 70–80 mol% Sn. The results are similar to the findings on Ir-Sn oxide DSA electrodes where the specific activity was approximately constant at low nominal tin contents [128]. In this DSA electrode investigation it was further shown that the activity decreased in a linear fashion as the tin content was increased above 60 mol% Sn. Generally the specific activity of the DSA type electrodes is higher (up to 1 order of magnitude in charge normalised current) compared with the present results, although exact comparison is difficult due to different Tafel slopes. The structure of Ir-Sn DSA electrodes is suggested to be heterogenous (i.e. multiple ultra-dispersed phases) [117], unlike the oxides examined here, which give only a single set of XRD peaks corresponding to a rutile oxide.

The reason for the apparent change in specific activity at high tin contents is not completely clear. Measurements made by XRD showed that there was a linear change in the lattice parameters, and a rapid increase in crystal size from 3–6 nm to 10–15 nm at approximately 50-60 mol% Sn. If the crystal parameters are responsible for this activity change it must mean there is a critical cell parameter/crystal size at which this step in activity occurs. Nanosized materials are often claimed to have superior properties to the equivalent bulk materials, and the rather rapid change in crystal size around the same tin content as the activity change could be therefore be responsible.

6.4.4 PEM water electrolysis results

The performance of the oxides were examined in a PEM water electrolysis cell. The reference electrode proved useful for making in-situ cyclic voltammetry measurements, however some further investigations must be carried

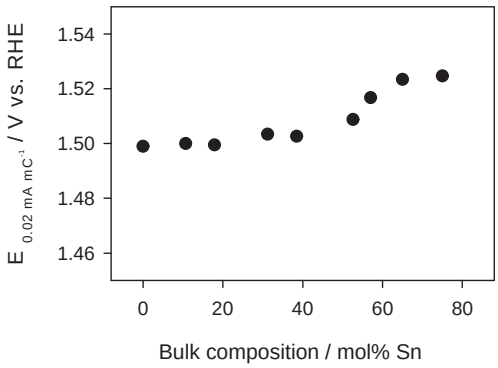

Figure 6.6: Specific activity of $Ir_xSn_{1-x}O_2$ in 0.5 M H_2SO_4 measured at a normalised current density of 0.02 mA mC^{-1}. The normalisation used Q_{outer} found from CV as the measure of active surface area

out to fully interpret the impedance measurements obtained when using the reference electrode.

The CV of $Ir_{0.4}Sn_{0.6}O_2$ in the PEM water electrolyser is compared to the CV performed in 0.5 M H_2SO_4 at 20 mV s^{-1} (Figure 6.7). It is clear that the overall shape is quite similar in both electrolytes and that the active area in the PEM system is larger than the aqueous electrolyte as expected due to the higher loading used in the PEM cell.

The outer anodic charge was also calculated from the voltammetry data and compared to the results from the aqueous electrolyte experiments (Figure 6.8). There is considerable differences found between the PEM and aqueous electrolyte environments as a function of the oxide composition. As the loading in the PEM cell is twice that in the aqueous cell, one would expect the anodic charge to be twice as high over the entire composition range, assuming a linear relationship between charge and loading. At high iridium contents the PEM Q_{outer} is slightly greatly than twice the aqueous Q_{outer}. At lower iridium contents the anodic charge is approximately equal for the PEM and aqueous environments despite the larger loading used in the PEM cell. This difference is suggested to be due to the resistivity of the oxides used in these experiments. From powder resistance measurements, it was seen that

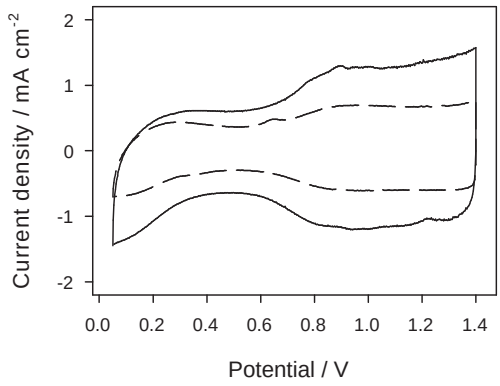

Figure 6.7: CV of $Ir_{0.4}Sn_{0.6}O_2$ in PEM (solid line) and 0.5 M H_2SO_4 (dashed line)

the resistivity increases almost exponentially with tin content. In the PEM layer, poor oxide conductivity will lead to the isolation of some portion of the electrocatalytic layer. This is because both perpendicular and lateral conductivity is required as the electrical contact to the layer is achieved through a porous support rather than a solid plate [7]. In the aqueous cell the layer requires little lateral conductivity as the electrical support plate is solid. Differences in the lateral and perpendicular conductivity will arise from the different particle-particle contact pressure in each direction. The porous titanium backings used here have porosities around 50%, and therefore a loss of 50% in active surface area may be reasonable, if the lateral conductivity is very low.

This increased resistivity in the MEA layer was confirmed by electrochemical impedance spectroscopy. From pressed powder resistance measurements it was expected that the resistivity difference between the low tin and high tin content oxides should correspond to 50-100 mV at 1 A cm^{-2} . The results from full cell impedance measurements show that there is an increase in the full cell resistance as the anode composition is varied (Figure 6.9). The maximum difference corresponds to 125 mV at 1 A cm^{-2} which is similar to that predicted by the pressed powder measurements. Clearly increasing the tin content to above 60 mol% causes unacceptable performance losses due

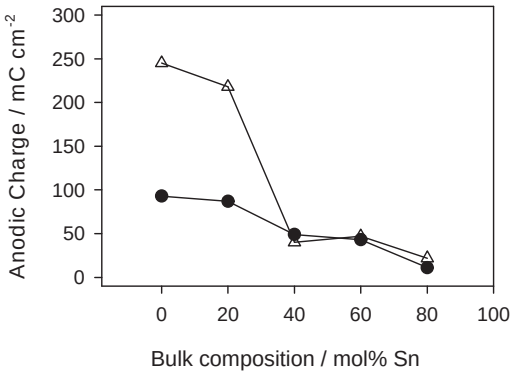

Figure 6.8: Q_{outer} of $Ir_xSn_{1-x}O_2$ in the PEM cell (△) and 0.5 M H_2SO_4 (•)

to considerably increased ohmic resistance.

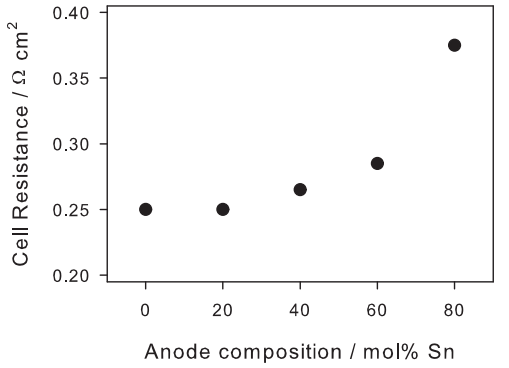

Figure 6.9: PEM water electrolysis cell resistance as a function of anode composition

Steady state polarisation measurements were also made in a PEM water electrolyser in order to establish the overall performance of the synthesised oxides towards the oxygen evolution reaction. The anode potential at 1 mA cm^{-2} ($E_{1mAcm^{-2}}$) was used to compare the electrocatalytic performance between the materials and their relative performance in the different elec-

trolytes. Figure 6.10 shows both $E_{1mAcm^{-2}}$ at 25 and 80 °C for the PEM cell and the data at 25 °C in 0.5 M H_2SO_4. At this low current density, the effect of composition on the anode potential is less significant at both 25 and 80 °C in the PEM cell compared with the results in 0.5 M H_2SO_4. This is somewhat surprising especially when the measured anodic charge in the PEM cell is much lower than expected for the tin rich oxides, implying that the difference should be more significant due to loss of active surface area. The Tafel slope in this low current range was similar to the aqueous electrolyte measurements, with the values typically between 35 and 40 mV dec^{-1}.

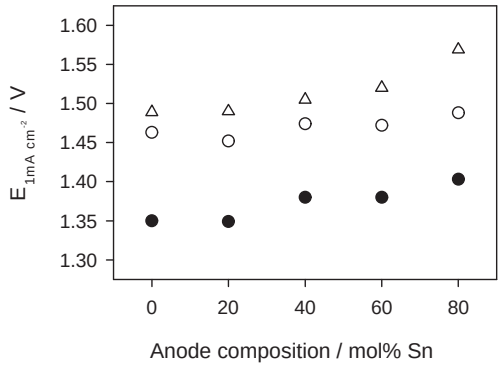

Figure 6.10: $E_{1mAcm^{-2}}$ of anodes in PEM water electrolysis cell (○ - 25 °C and ● - 80 °C) and 0.5 M H_2SO_4 (△)

The effect of temperature on the anodic Tafel slope in the low current range was also examined. Figure 6.11 shows a typical result as the cell was slowly heated, together with the response predicted by the Butler-Volmer relationship. Clearly the measured Tafel slope does not have the expected temperature dependence with the results between those for the "Electrochemical Oxide path" and "Oxide path" mechanisms. By following the Tafel slope while the cell was slowly cooled, it seems this is likely to be due to some activation process rather than a specific effect caused by the kinetics of the reaction as the measured Tafel slope approximately followed the relationship predicted by the "Oxide path" mechanism. Unfortunately only a few data points were collected during this cooling cycle, so it is unclear if the Tafel-temperature

relationship is linear, which would indicate that the charge transfer coefficient is temperature independent. De Pauli and Trasatti [128] showed that IrO_2-SnO_2 DSA electrodes showed the normal Butler-Volmer relationship as the temperature varied indicating that the charge transfer coefficient was close to 0.5 over the temperature range examined. Experiments showed this "activation" was not seen at room temperature after several hours under galvanostatic polarisation of 200 mA cm^{-2}. The heating rate was such that the Tafel-temperature relationship was collected within 5 hours, and indicates that this activation process is accelerated as the temperature increases. This may be due to thermally induced changes in the membrane-electrocatalyst interface structure, which enable a faster activation of the catalytic layer.

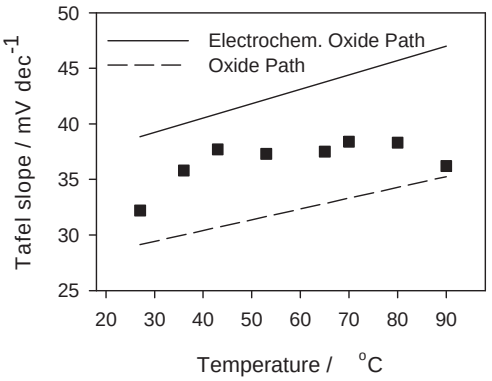

Figure 6.11: Anodic Tafel slope in PEM water electrolysis cell

High current polarisation was also carried out galvanostatically at 80 °C to examine the performance under normal electrolysis conditions (Figure 6.12). As expected the addition of tin causes the performance to decrease in the high current density range. The difference between pure IrO_2 and anodes containing 20, 40, 60 and 80 mol% Sn corresponded to 42, 55, 96, and 165 mV respectively at 1 A cm^{-2} and 80 °C. The best measured performance (1.61 V) was achieved with an pure IrO_2 anode at 1 A cm^{-2} and 90 °C. A IR-free plot of the cell voltage reveals not all the performance loss at high current is due to increased ohmic resistance (Figure 6.13). Although only data for the full cell is shown, the slope difference seen at high current between IrO_2 and tin containing oxides suggests that a change in the high

current rate determining step may also occur when SnO_2 is added to IrO_2. This may arise from the reduction in the density of active points as tin is added. As the density of active points decreases, the rearrangement step in the mechanism becomes more difficult and the Tafel slope increases.

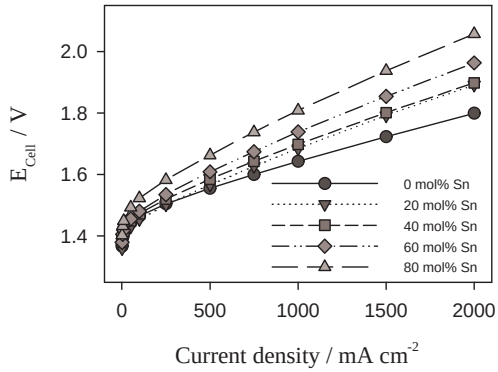

Figure 6.12: Voltage of PEM water electrolysis cell at 80 °C

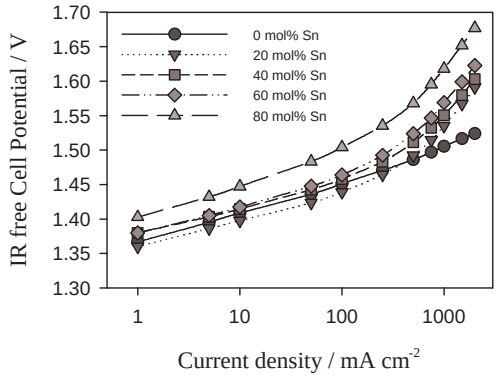

Figure 6.13: IR-free voltage of PEM water electrolysis cell at 80 °C

6.5 Conclusions

Addition of tin oxide to iridium oxide particles for oxygen evolution electrocatalysts shows no beneficial effect other than dilution of the more expensive iridium oxide at all the examined current densities. Cyclic voltammetry, shows that the active area or number of active points decreases as the tin content increases. Additions of up to 20 mol% tin may be acceptable as little change in the active area occurs at low tin contents, however there is still around 40 mV increase in cell voltage at 1 A cm^{-2} and 80 °C in a PEM water electrolyser. Normalising the current density by the active surface area, shows that the specific activity, remains constant until 50–60 mol% tin whereafter the activity decreases. Overall, the electrocatalytic properties in 0.5 M H_2SO_4 and a PEM cell are similar, however there is evidence to suggest different layer properties in the PEM cell due to the poor conductivity of some of the prepared oxides. The effect of anode composition on the PEM cell ohmic resistance confirmed that high tin contents cause high performance losses due to poor layer conductivity. The best PEM cell performance was achieved with a pure IrO_2 anode giving 1.61 V at 1 A cm^{-2} and 90 °C.

Acknowledgments

The authors would like to acknowledge the financial support from the Norwegian Research Council and Norsk Hydro ASA

Chapter 7

Nanocrystalline $Ir_xRu_ySn_zO_2$ Powders as Oxygen Evolution Electrocatalysts

7.1 Abstract

The addition of ruthenium to nanocrystalline oxide powders ($Ir_xRu_ySn_zO_2$) has been investigated, with the intent that these oxides be used as oxygen evolution electrocatalysts in proton exchange membrane (PEM) water electrolysers. The oxides have been synthesised using the modified polyol method, in which the chloride precursors are reduced to metallic colloids in ethylene glycol. These colloids are then annealed in air to obtain the desired oxide powders. X-ray diffraction analysis suggests that an iridium-tin-ruthenium oxide solid solution with a rutile structure can be produced using the modified polyol method at low ruthenium contents ($\leq$ 20 mol% Ru). At higher Ru contents, in addition to the oxide phase, metallic ruthenium is found, most likely due to the clustering of ruthenium colloids in the reduction stage. Electrochemical measurements in 0.5 M H_2SO_4 suggest that this metallic ruthenium is coated with an oxide layer which is probably a solid solution of iridium-tin-ruthenium oxide. It was found that replacing the iridium component with ruthenium caused the active area, as found from cyclic voltammetry, to decrease. Normalising the current by the

outer anodic charge showed that the specific activity of the surface elements increased with ruthenium content. The best overall performance at these preparation conditions exists at around 15–25 mol% Ru.

7.2 Introduction

Hydrogen can be efficiently produced using proton exchange membrane (PEM) water electrolysers [2]. Recently $Ir_xSn_{1-x}O_2$ nanocrystalline powders have been investigated as the anode or oxygen evolving electrode in our group [132, 157, 158]. To improve the performance and decrease the cost of these oxides, ruthenium has been added to replace the expensive iridium component of $Ir_{0.5}Sn_{0.5}O_2$ oxides.

Noble metal oxides as electrocatalysts are well established in many industrial electrochemical processes in the form of dimensionally stable anodes (DSA) as developed by Beer [60]. Ruthenium is known as the most active oxide for anodic oxygen evolution [10], however it suffers from instability and therefore should be stabilised with another oxide such as IrO_2 [122] or SnO_2 [84]. It has also been suggested that SnO_2 does not reduce the activity of RuO_2 as much as TiO_2 [61, 137].

Most DSA electrodes are prepared by thermal decomposition of metal precursors on titanium substrates. As PEM water electrolysis electrodes must be porous to allow the evolved gas to escape, the DSA approach to electrocatalyst preparation is unsuitable. Therefore to obtain an electrocatalytic layer on the membrane, pre-prepared powders are applied as an ink or transfer to the membrane [23, 105]. This also has the advantage of permitting the synthesis very high surface particles using a wide range of synthesis methods.

Here the replacement of iridium in $Ir_{0.5}Sn_{0.5}O_2$ by ruthenium is examined as a means to reduce the cost of this electrocatalyst while improving the overall performance of this oxide towards the oxygen evolution reaction.

7.3 Experimental

7.3.1 Oxide preparation

Metal precursors ($H_2IrCl_6.4H_2O$ [1], $SnCl_2.2H_2O$ [2], and $RuCl_3.xH_2O$ [3]) were added to 50 ml of ethylene glycol to achieve a total metal concentration of 1.67 x10^{-5} mol ml^{-1}. The glycol–precursor solution was then heated under a nitrogen atmosphere to the refluxing temperature and held for 2 hours, by which time a brown/black colloid had formed. The pH of this colloid–glycol mixture was then measured and adjusted to pH 2.5 by the addition of 0.1 M NaOH solution. This aided the separation process of the colloid from the glycol, which was achieved by centrifugation. The recovered colloid was washed in deionised water 3 times, before being ultrasonically dispersed in acetone and dried in air at 60 °C. This dry colloid was then annealed in air at 500 °C for 30 minutes to oxidise the metallic material.

7.3.2 Characterisation

X-ray diffraction (XRD) was performed on the dry electrocatalytic powders using a Siemens D5005 powder X-ray diffractometer, with a step size of 0.2 °, step time of 50 seconds, slit opening of 0.5 °, and a Cu-Kα X-ray source (λ = 0.154 nm). The diffraction patterns were fitted to a pseudo-Voigt profile and the crystal size distribution calculated using Warren-Auerbach analysis. A Hitatchi 3500 electron microscope with Oxford EDS system was used to examine the powder and subsequent electrode morphology and composition. X-ray photoelectron spectroscopy (XPS) was carried using a monochromatised Al Kα X-ray source from Gamma Data Scineta and a hemispherical SCIENTA SES 2002 electron analyser. The analysis was performed on the electrocatalysts, by preparing thin layers on titanium plates, using a Nafion solution as a binder, with the layer containing 5 wt% Nafion. The full survey spectrums and the specific regions were collected with a band pass of 500 eV. The surface ratio of iridium, tin, and ruthenium was determined by comparison of the Ir 4f, Sn $3d_{5/2}$, and Ru $3d_{5/2}$ photoelectron lines and

[1] OMG AG & Co. KG - 99.92 % metals basis
[2] Alfa Aesar - ACS grade
[3] Alfa Aesar - 99.9% PGM basis

the use of appropriate sensitivity factors [138]. Curve fitting was carried out using Gaussian-Lorentzian type profiles (XPSPeak 4.1) and the C 1s line (BE = 284.6 eV) was used as reference for the binding energy.

Electrochemical analysis of the electrocatalytic powders was conducted in 0.5 M H_2SO_4 (Merck, p.a) electrolyte at room temperature, by supporting the powders on titanium plates using a spraying technique. The electrocatalytic layer consisted of 95 wt% electrocatalyst and 5 wt% Nafion, with the total loading maintained at 1 mg cm^{-2}. The electrodes were subjected to an initial anodic polarisation at 0.5 mA cm^{-2} for 4 minutes, with a steady potential normally being reached within this time. Cyclic voltammetry and polarisation measurements were performed using an IM6e electrochemical workstation from ZAHNER-elektrik GmbH & Co. KG. A $Hg/Hg_2SO_4,H_2SO_4$ reference electrode and a platinum foil counter electrode were used in the normal fashion. All potentials are quoted versus the reversible hydrogen electrode in the same electrolyte.

7.4 Results and discussion

The bulk composition of the oxidised powder as measured by EDS is shown in Figure 7.1. In all these samples, the tin content was desired to remain constant at 50 mol%. These measurements indicate that the reduction reaction in the polyol medium is influenced by the composition of polyol-precursor mixture, with the level of tin found in the final oxide decreasing as the ruthenium content increases. This was not found in materials only containing iridium and tin, with the measured bulk composition close to the desired composition over the range 0–80 mol% Sn [157]. As the difference between the measured bulk composition and the desired composition is dependent on the ratio of precursors in the starting glycol mixture, some further optimisation of the reduction parameters may be necessary in order to obtain certain compositions. To simplify the following discussion, the desired composition will be quoted unless specifically stated.

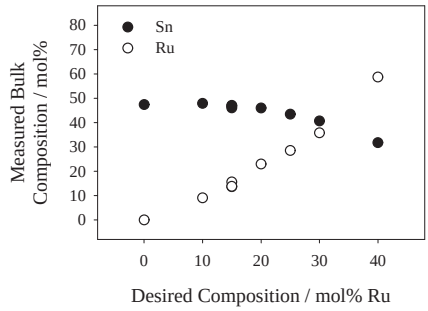

Figure 7.1: Composition of $Ir_xRu_{0.5-x}Sn_{0.5}O_2$

7.4.1 X-ray diffraction

Typical XRD patterns for the $Ir_xRu_{0.5-x}Sn_{0.5}O_2$ powders, are shown in Figure 7.2. For oxides containing no ruthenium (x=0.5), a typical rutile oxide pattern is obtained, with the peaks located between those for pure IrO_2 and SnO_2. This is suggested to be a solid solution of iridium and tin oxide, and it has been seen previously that the lattice parameters vary linearly with composition (Chapter **??**). Upon addition of ruthenium, no major change is observed until $x < 0.3$, where metallic ruthenium peaks become visible, with the intensity of these peaks increasing with the ruthenium content. The presence of metallic ruthenium is expected to arise from the clustering of metallic ruthenium colloids during the reduction of the precursors in ethylene glycol. It has been reported, that most noble metal colloids (except iridium) show significant clustering during this step if not protected with protective agent such as PVP [96]. Therefore it seems reasonable to suggest that during the preparation of the metallic colloids, ruthenium or ruthenium rich colloids cluster together strongly, and only the surface of these large colloid clusters is then oxidised during the thermal treatment.

The lattice parameters were calculated and compared to lattice parameters for pure IrO_2, SnO_2, RuO_2 (Table 7.1). The initial addition of Ru to $Ir_{0.5}Sn_{0.5}O_2$ shifts both lattice parameters towards the values for RuO_2, suggesting that the ruthenium enters the oxide matrix. As the ruthenium further replaces the iridium component, the lattice parameters increase to-

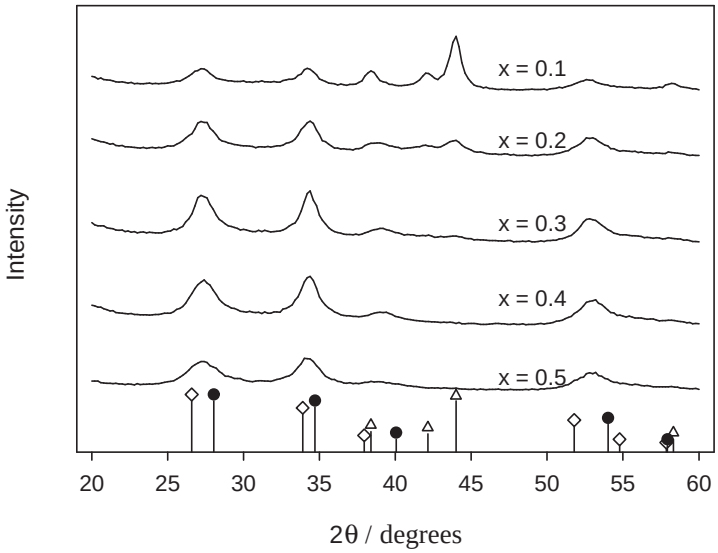

Figure 7.2: XRD patterns of $Ir_xRu_{0.5-x}Sn_{0.5}O_2$, • - IrO_2, ◇ - SnO_2, △ - Ru

wards the values typical for SnO_2. This indicates that the further additions of ruthenium do not completely replace the iridium, resulting in a decrease in the noble metal:tin ratio present in the oxide phase. This is supported by the increase in the metallic ruthenium phase at higher ruthenium contents. If it is assumed that only iridium and tin are present in the oxide phase and that the iridium:tin ratio in this oxide phase is that found by EDS measurements, we can estimate the expected lattice parameters based on previous analysis of a $Ir_xSn_{1-x}O_2$ solid solution [157]. This estimated parameter (a*), is shown along with the experimental 'a' lattice parameter as a function of the mole fraction of tin assuming that the oxide phase contains only tin and iridium (Figure 7.3). It is clearly seen that the assumption that the oxide crystals only contain iridium and tin in the ratio given by the EDS measurements is incorrect based on to the different lattice parameter values obtained from the XRD measurements.

The crystal size of the oxide phase was calculated and is shown in Table 7.1. Very little difference is seen in terms of the average crystal size with the

Table 7.1: XRD analysis of $Ir_xRu_{0.5-x}Sn_{0.5}O_2$

x	a	c	Crystal size
	nm	nm	nm
0.5	0.4613	0.3173	3.0
0.4	0.4600	0.3168	4.2
0.35	0.4604	0.3164	4.8
0.35	0.4606	0.3163	3.8
0.3	0.4610	0.3166	5.1
0.2	0.4611	0.3166	4.8
0.1	0.4631	0.3170	5.2
IrO_2	0.4498	0.3154	-
SnO_2	0.4738	0.3188	-
RuO_2	0.4491	0.3107	-

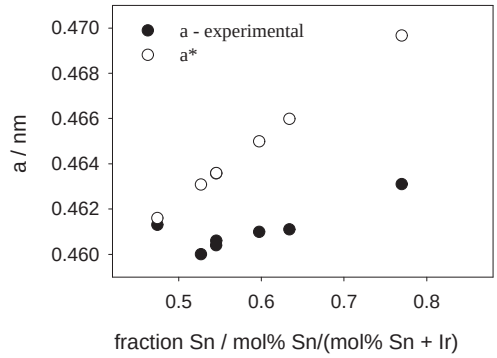

Figure 7.3: Lattice parameter analysis - see text for explanation

values calculated to be around 3–5 nm. The crystallinity of the samples was also estimated to be approximately constant at around 65 – 75 %. The composition of the amorphous material must also vary with bulk composition, based on elemental mass balances of the samples. Given that the tin content of the samples decreases while the tin content in the crystalline oxide phase increases as ruthenium is added, indicates that the amorphous material could become rich in noble metals as ruthenium is added to the system. This however is likely to be offset by the increase in the crystalline

Ru^0 phase. Currently the role of amorphous noble metal oxides or hydroxides in the electrocatalytic processes is unclear. Normally it is expected that amorphous oxides have very high surface area, due to the large number of defects and disorder. However these materials may have very low or no electrical conductivity [7], leading to electrically isolated regions, and therefore a low number of total active sites. This situation may be improved if the poorly conductive amorphous material is finely dispersed in or on a conductive material.

7.4.2 Electrical conductivity measurements

As alluded to above, a major criteria of these oxides is that they must possess high electrical conductivity. This is also true for the active layer in a PEM water electrolyser cell [7, 157, 158]. In this work the electrical conductivity of the electrocatalytic powders is compared by pressing the oxide between two pistons. The total resistance was measured between the two pistons as a function of pressed powder thickness, enabling the resistivity to be estimated without including the piston–oxide contact resistance [157]. Figure 7.4 shows the resistivity as a function of the ruthenium content.

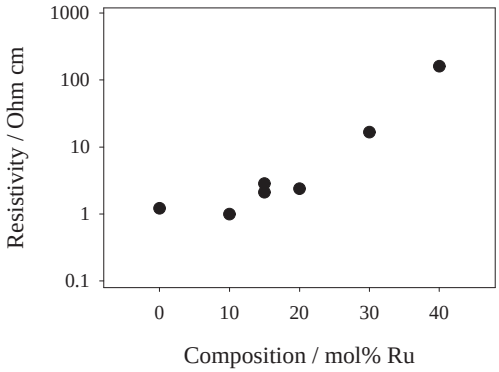

Figure 7.4: Resistivity of $Ir_xRu_{0.5-x}Sn_{0.5}O_2$

Clearly as the iridium is replaced by ruthenium, the resistivity of the powders increases significantly. Normally in DSA type oxide coatings, RuO_2

layers are more conductive than IrO_2 layers due to the larger crystallite size achieved when using RuO_2 [61]. In the materials examined here, the reason for increased resistivity lies in the tin content of the crystalline oxide phase. From the XRD analysis it is clear that although the total tin content of the powder decreased, the tin content of the crystalline oxide phase increases as the iridium is replaced by ruthenium. Therefore the resistivity change seen in Figure 7.4 is actually an artifact of ruthenium content changing the noble metal:tin ratio in the final rutile oxide phase. Similar results were seen for a solid solution of iridium-tin oxide, with the resistivity increasing exponentially with tin content [157]. The fact that the resistance is high (at 30-40 mol% Ru) even though there is significant levels of metallic ruthenium also suggests that this metallic phase must be coated by the poorly conductive oxide material, or dispersed within a poorly conductive material with a low degree of percolation through this phase.

7.4.3 X-ray photoelectron spectroscopy

XPS was carried out assuming that the sample layer was homogenous with no preferred orientation of certain particles towards the surface of the layer. A typical survey spectra is shown in Figure 7.5. The spectra reveals that all the metallic elements are present at the surface with the Sn 3d, Ru 3d and Ir 4f photoelectron lines found in the regions 496–486, 285–280, and 68–60 eV respectively. Additional peaks corresponding to oxygen (lattice oxygen, hydroxides and water), fluorine (Nafion), and carbon (Nafion and contamination) are also found.

Surprisingly the surface composition shows that the ruthenium is far below the bulk concentration and goes through a maximum for the sample $Ir_{0.3}Ru_{0.2}Sn_{0.5}O_2$ (Table 7.2). As mentioned above, metallic ruthenium colloids agglomerate quickly and therefore may get coated with a layer of iridium or tin particles during the polyol process. The structure of these intermediate particles may therefore be responsible for the low ruthenium content found at the surface of the final material. The increasing tin content and the decreasing noble metal content is consistent with the XRD finding concerning the composition of the oxide phase, suggesting that the surface measured by XPS is predominately an oxide, with the metallic ruthenium located within the core of the particles. The fact that the ruthenium content is very low,

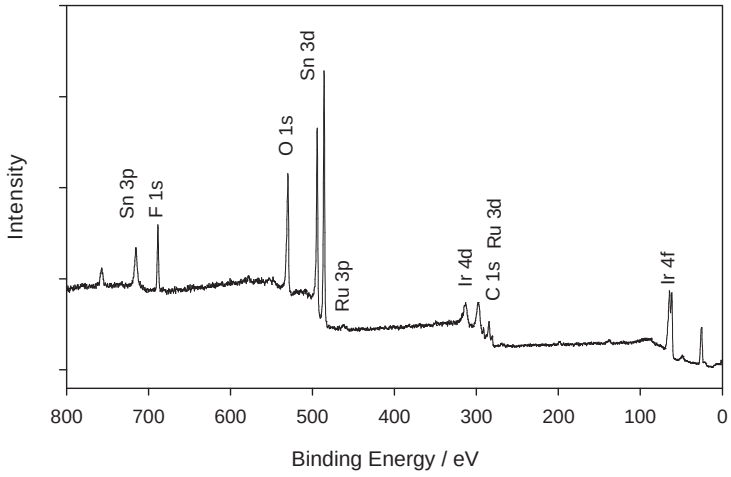

Figure 7.5: XPS survey spectra of $Ir_{0.4}Ru_{0.1}Sn_{0.5}O_2$

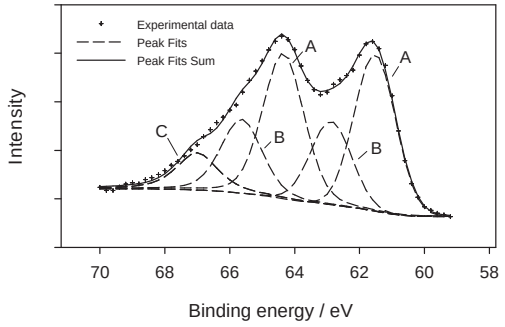

Figure 7.6: Iridium 4f spectra of $Ir_{0.4}Ru_{0.1}Sn_{0.5}O_2$

indicates that surface analysed by XPS is probably not the same composition as the bulk of the crystalline oxide phase. This is explained by either amorphous material with low ruthenium content coating the Ir-Ru-Sn oxide solid solution or enrichment/segregation of the non-ruthenium elements towards the surface of this solid solution. Hutchings et al [84] showed that preferential surface segregation of iridium over ruthenium occured in the ternary oxide $Ir_{0.25}Ru_{0.25}Sn_{0.5}O_2$, with the surface tin content increasing with annealing temperature. Here we also see that the surface is enriched by tin at x = 0.5.

Table 7.2: XPS analysis of $Ir_xRu_{0.5-x}Sn_{0.5}O_2$

x	Ir	Ru	Sn	Ir $4f_{7/2}$ peak-A	Ir $4f_{7/2}$ peak-B	Contribution of peak A	Sn $3d_{5/2}$
	mol%	mol%	mol%	eV	eV	%	eV
0.5	40.6	0	59.4	61.5	62.5	66	486.2
0.4	36.0	3.5	60.5	61.5	62.9	65	485.8
0.3	30.5	4.9	64.6	61.6	62.9	65	485.8
0.2	25.6	2.7	71.7	61.8	63.1	64	486.1
0.1	16.3	1.4	82.3	61.9	63.2	61	486.3

The Ir and Ru binding energies are consistent with an oxide state [115, 116], with the ruthenium $3d_{5/2}$ line located around 280.7–281 eV, which is approximately 1 eV higher than metallic ruthenium. As discussed by Atanasoska et al [116], determining the valence of iridium is very complex due to the overlapping of the multiple photoelectron lines normally found in IrO_2 samples. Similarly the Ru 3d photoelectron lines occur in the same region as C 1s so some overlapping also occurs here making exact analysis difficult, particularly at these low ruthenium contents.

In this work the regions were fitted and deconvoluted with Lorentzian-Gaussian profiles. The iridium region was characterised by two pairs of photoelectron lines (defined as A and B) which normally had Ir $4f_{7/2}$ binding energies of 61.5–61.9 and 62.5–63.2 eV with the spin-orbit splitting around 2.6–3.1 and 2.3–2.8 eV for the A and B peaks respectively. It is likely that the peak pairs A and B represent iridium atoms with different valence, with Atanasoska et al [116] suggesting that the second pair of peaks (B) must have a valence greater than +4. For fitting the Ir 4f region, the full width at half maximum (FWHM) was set to 1.5 and a fifth peak included following the method used in previous work [116]. Figure 7.6 shows both experimen-

tal data and the result from the fitting procedure for the Ir 4f photoelectron lines. Table 7.2 gives the Ir $4f_{7/2}$ binding energies for the two photoelectron lines. It appears that there is a shift towards higher binding energies and that the ratio of the two pairs of photoelectron lines changes, as the bulk ruthenium content increases. This may suggest an interaction occurs between the iridium and other elements present in the oxide material, and is consistent with an electron withdrawing effect by a more electronegative ligand. The binding energy of the Sn $3d_{5/2}$ photoelectron lines is also given in Table 7.2, and show that a shift in the Sn 3d binding energies occurs, with a minimum located around $Ir_{0.3}Ru_{0.2}Sn_{0.5}O_2$. This minimum corresponds to the maximum ruthenium surface content, and may confirm that there is some interaction between the tin and noble metals, supporting the suggestion from the XRD analysis that a very homogenous oxide has been synthesised. The binding energy of the Sn 3d photoelectrons are between 0.05 and 0.6 eV lower than given for SnO_2 [117]. Why the change in binding energy differs for the Ir $4f_{7/2}$ and the Sn $3d_{5/2}$ is not completely clear, however it is possible that the oxide material consists of more than one solid solution phase, leading to different interactions between the iridium and tin in each of these phases. It is also possible that the coating of metallic ruthenium particles by the oxide, has some electronic effect on the oxide elements.

7.4.4 Cyclic voltammetry

Typical voltammograms for $Ir_xRu_{0.5-x}Sn_{0.5}O_2$ (x = 0.25, 0.5) are shown in Figure 7.7. The voltammograms have the normal iridium oxide shape, with very broad waves located at potentials consistent with the redox couples Ir^{3+}/Ir^{4+} and Ir^{4+}/Ir^{6+}. This is similar to the findings on IrO_2-RuO_2 DSA electrodes [121] where little change in the voltammogram shape was found at intermediate compositions. RuO_2 electrodes are normally characterised by redox peaks around 0.64, 0.76, and 1.25 V vs. RHE [7]. These measurements correspond well with the XPS analysis in that the surface response is dominated by iridium oxide indicating low levels of surface ruthenium. Overall it can be seen that the anodic portion of the oxide voltammograms are almost symmetrical around the zero current line, showing that the oxides behave as capacitors. The current at a given potential was found to be linearly related to the sweep rate, which is another good indicator of capacitive behaviour. There is no obvious changes in the voltammogram shape as the iridium is

replaced by ruthenium, until 40 mol% Ru where the voltammogram began to resemble that for metallic ruthenium. This finding, combined with the XPS results showing a low surface ruthenium content and lack of surface metallic ruthenium, suggests that the electrode layer or particles are porous enough for electrolyte to penetrate through into the core of the particles, where the metallic ruthenium is located. A clear metallic response was only found at low sweep rates (ν <10 mV s^{-1}), when the slow electrolyte diffusion through the oxide outer surface into the core of the particle will not limit the electrochemical processes on the metallic ruthenium. This confirms the suggestion that oxide material is essentially agglomerates consisting of metallic ruthenium particles coated with a mixture of rutile oxide and amorphous oxides deficient in ruthenium.

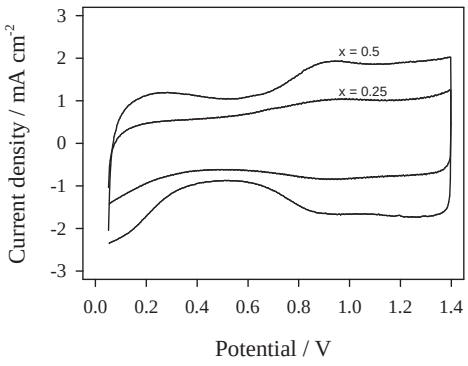

Figure 7.7: Cyclic voltammetry of $Ir_xRu_{0.5-x}Sn_{0.5}O_2$ in 0.5 M H_2SO_4 (ν = 20 mV s^{-1})

Charge measurements are often used in DSA literature to compare the active area or number of active points of a noble metal oxide layer. By using the technique developed by others [35], the total charge and the outer charge for the oxides was calculated by measuring voltammograms at sweep rates of 5–200 mV s^{-1}. We believe that the outer charge will best represent the available active area during oxygen evolution. The results show that as ruthenium is added to the oxide material outer charge decreases dramatically (Figure 7.8). This decrease is even more significant if the decrease in total tin content of the material and therefore higher noble metal load-

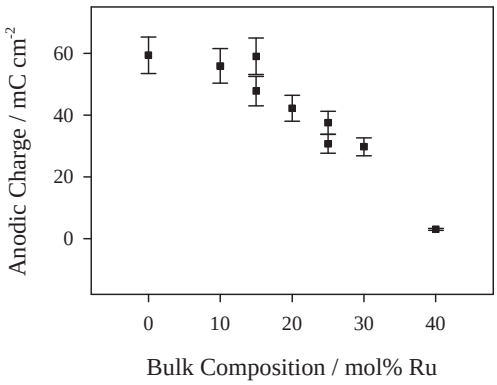

Figure 7.8: Outer anodic charge of $Ir_xRu_{0.5-x}Sn_{0.5}O_2$ in 0.5 M H_2SO_4

ing on the electrode is considered. Often in literature mixtures of iridium and ruthenium oxide give rise to a maximum in anodic charge at intermediate compositions [87, 121], however this charge–composition relationship can be strongly dependent on the preparation technique as pointed out by Trasatti [61]. Here, the charge–bulk composition relationship, can be simply explained in terms of the relative noble metal:tin ratio found at the surface. Clearly if the XPS analysis accurately reflects the electrochemically active surface during the voltammetry measurements, the low noble metal content at high bulk ruthenium compositions, is the reason for the large decrease in electrochemically active area.

7.4.5 Polarisation measurements

After the cyclic voltammetry measurements, steady state polarisation curves were recorded by stepping the potential anodically in 5 mV steps from 1.4 V, with a holding time of 1 minute. In this time the current was observed to have stabilised. Typical polarisation curves of the oxides measured in 0.5 M H_2SO_4 are shown in Figure 7.9 with the data summarised in Table 7.3.

The Tafel slope measured for the oxides containing ruthenium remains approximately constant at 43-45 mV dec^{-1}, except for the electrode which gave the metallic ruthenium response. The electrode containing no ruthe-

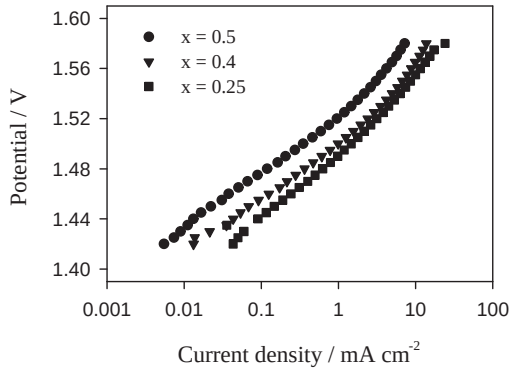

Figure 7.9: Polarisation of $Ir_xRu_{0.5-x}Sn_{0.5}O_2$ in 0.5 M H_2SO_4

Table 7.3: Summary of polarisation measurements of $Ir_xRu_{0.5-x}Sn_{0.5}O_2$ in 0.5 M H_2SO_4

x	b mV/dec	E $_{1mAcm^{-2}}$ V vs. RHE
0.5	36	1.522
0.4	43	1.500
0.35	45	1.496
0.3	45	1.496
0.25	44	1.493
0.2	43	1.500
0.1	83	—

nium gave a Tafel slope somewhat lower at 36 mV dec^{-1}. $Ir_xSn_{1-x}O_2$ solid solutions previously have shown Tafel slopes at this level independent of composition up to around 70-80 mol% Sn. Addition of ruthenium may therefore cause a change in the mechanism (e.g. Oxide path → Electrochemical oxide path) or a change in the rate determining step within a given mechanism. No strong conclusion can be made regarding the mechanism of oxygen evolution on the oxide electrodes containing ruthenium, however the Tafel slope is consistent with the second step of the Electrochemical oxide path [15].

The potential measured at 1 mA cm^{-2} shows that the overall performance

of the materials has a maximum around 15–25 mol% Ru. Clearly the initial addition of ruthenium to Ir-Sn oxides improves the low current performance. The addition of further ruthenium does not change the performance of the electrodes significantly, even though the active area clearly decreases. This indicates that the activity of the oxide must increase as the iridium is replaced by ruthenium. This is best seen by dividing the current density by the outer anodic charge found by the cyclic voltammetry measurements. This gives a measure of the specific electrocatalytic activity free from surface area effects. The potentials at a normalised current density of 0.02 mA mC^{-1} where used to compare the materials (Figure 7.10). It is very clear that the specific electrocatalytic activity increases (i.e. $E_{0.02 mA mC^{-1}}$ decreases) almost linearly with the ruthenium content. Therefore there exists an optimum in the electrocatalytic performance of these materials, based on the active area and the specific activity. Overall, we find that the low current performance of the Ir-Ru-Sn oxides is close to pure IrO_2 electrodes prepared by the same method, and slightly better than pure IrO_2 prepared by Adams fusion method [158]. This implies that an electrocatalyst with equal or better performance than pure IrO_2 can be produced with considerably less cost.

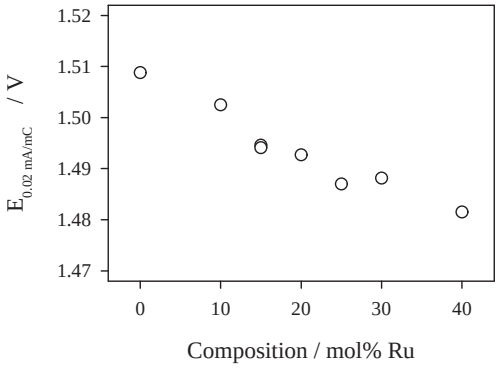

Figure 7.10: Specific activity of $Ir_xRu_{0.5-x}Sn_{0.5}O_2$ in 0.5 M H_2SO_4

The finding that the ruthenium does not directly contribute to the electrodes response indicates that the activity of the surface elements (mainly iridium) is affected by the bulk composition of the electrocatalyst. Indeed the XPS measurements showed some electronic changes in the state of the surface

elements as a function of bulk composition which may explain their enhanced electrocatalytic activity.

7.5 Conclusions

Addition of ruthenium to iridium-tin oxides has several effects, with the active area of the material decreasing and the specific activity increasing as the ruthenium replaces the iridium. Overall at low current densities in 0.5 M H_2SO_4, the best electrocatalytic performance is found at intermediate ruthenium contents (i.e. an optimum between active area and specific activity). The low current performance of the Ir-Ru-Sn oxides is similar to pure IrO_2 electrodes implying that an electrocatalyst with equal or better performance than pure IrO_2 can be produced at less cost. Cyclic voltammetry and XPS analysis both show that the surface is enriched in tin with very little ruthenium present. The XPS analysis also shows shifts in the Ir 4f and Sn 3d photoelectron binding energies as the composition changes. This suggests that there is some interaction between the elements / phases in the electrocatalyst, which results in enhanced electrocatalytic activity of the non–ruthenium elements present at the surface.

In terms of the preparation procedure, strong effects were observed as ruthenium is added to the system. Firstly the tin content in the final oxide decreases as ruthenium is added. This illustrates that the reduction process in the polyol medium is dependent on the concentration and type of precursor present. Also strong agglomeration of the ruthenium colloids leads to the formation of a metallic ruthenium phase in the final oxide. These factors suggest that some modification of the current preparation method or some other method should probably be used in future work.

Acknowledgments

The authors would like to thank Professor Steinar Raaen and Mari Juel of the Department of Physics, NTNU, for help with the XPS measurements. The financial support from the Research Council of Norway and Norsk Hydro ASA is also acknowledged.

Chapter 8

$Ir_xRu_yTa_zO_2$ Powders as Oxygen Evolution Electrocatalysts in PEM Water Electrolysers

8.1 Abstract

The addition of tantalum to nanocrystalline and amorphous $Ir_xRu_yO_2$ powders has been investigated. These oxides are applied as oxygen evolution electrocatalysts in proton exchange membrane (PEM) water electrolysers. The oxides have been synthesised using an aqueous hydrolysis method, followed by chemical and thermal oxidation. X-ray diffraction revealed that the oxide powders were mostly amorphous, with a small amount of a crystalline oxide. The lattice parameters of this crystalline phase was seen to vary only with the iridium:ruthenium ratio suggesting that this phase is a solid solution between IrO_2 and RuO_2. These oxides were examined electrochemically in 0.5 M H_2SO_4 by supporting the powders on titanium electrodes within a Nafion matrix. Cyclic voltammetry and steady state polarisation measurements were then used to evaluate the electrochemical active area, specific activity and performance towards the oxygen evolution reaction at low currents. The high current performance of a PEM water electrolysis cell

using these oxides as the anode electrocatalyst was examined by steady state polarisation measurements. Overall the best cell voltage was 1.567 V at 1 A cm^{-2} and 80 °C was achieved when using Nafion 115 as the electrolyte membrane.

8.2 Introduction

Hydrogen can be produced without the release of carbon dioxide using proton exchange membrane (PEM) water electrolysers [2]. Normally in these systems, the anode has the largest overpotential at typical operating current densities [7]. Recently $Ir_xSn_{1-x}O_2$ [132, 157, 158] and $Ir_xRu_{0.5-x}Sn_{0.5}O_2$ nanocrystalline powders have been investigated as oxygen evolution electrocatalysts in our group.

Noble metal oxides as electrocatalysts are well established in many industrial electrochemical processes in the form of dimensionally stable anodes (DSA) as developed by Beer [60]. Ruthenium is known as the most active oxide for oxygen evolution [10], however it suffers from instability and therefore should be stabilised with another oxide such as IrO_2 [122] or SnO_2 [84]. Tantalum is a well known addition to DSA electrodes, and Ir-Ta oxides have been suggested as the most efficient electrocatalysts for oxygen evolution in acidic electrolytes due to the high activity and corrosion stability [70]. Very comprehensive studies of the structural properties of Ir-Ta DSA oxides have been carried out. Roginskaya *et al* showed the presence of multiple rutile solid solutions [70], whereas Vercesi *et al* suggested no solid solutions are present [63]. Likewise, no solid solution phases between Ru and Ta oxides were found on Ru-Ta DSA oxides [62]. Yeo *et al* suggested that adding Ta^{+5} to ruthenium oxides stabilises the ruthenium by preventing the oxidation of the more stable Ru^{+3} to the less stable Ru^{+4} [159]. The ternary Ir-Ru-Ta oxide appeared to be more active than pure RuO_2 [159] however no structural study was conducted and the enhanced performance is most likely due to surface area improvements rather than an increase in specific activity. DSA Ir-Ta oxides electrodes have also shown that 30 mol% Ta improves the activity significantly [113] although other electrochemical results show very high variation in the properties such as anodic charge and double layer capacitance so such results need to be treated carefully. Structural analysis showed that the crystallisation processes of the two oxides affect each other

and that the open circuit potential (i.e. state of electrochemical surface) varied with both composition and pH.

Ir-Ta oxides have also been applied as the anode electrocatalysts in PEM water electrolysis cells [7]. It was suggested that additions of Ta species to IrO_2 enhanced the catalytic performance when the Ta content was low. The mechanism of enhancement was suggested to be due to the withdrawal of electrons from the Ir atoms, increasing the adsorption of oxygen species and lowering the Tafel slope. The maximum performance was achieved at 15 mol% Ta, which was due to a compromise between the exchange current density, Tafel slope, and resistivity.

It is well known that a wide range of preparation conditions affect the formation and properties of DSA type oxide layers [61] as will the presence of Ti originating from the substrate (see [62]), and therefore analysis of powder based oxides may facilitate further understand the specific nature of Ir-Ru-Ta oxides as electrocatalysts while providing a possible use in PEM water electrolysis applications.

In the present work we examine the structure and electrochemical properties of $Ir_xRu_yTa_zO_2$, as well as the overall performance of a PEM water electrolysis cell operating under real conditions when using these oxides as the anode electrocatalyst.

8.3 Experimental

8.3.1 Oxide preparation

Previous work in our group has used both the Adams fusion method [82] and a modified polyol method [157, 158] to produce nanocrystalline IrO_2 [114], $Ir_xSn_{1-x}O_2$ [157, 158] and $Ir_xRu_{0.5-x}Sn_{0.5}O_2$ powders. Initial results using these methods, showed that a new method was required for producing electrocatalysts containing tantalum, due to the strong surface enrichment by Ta in the case of the modified polyol method, and formation of sodium tantalate in the case of the Adams fusion method.

In the present work the oxide powders are prepared by adding metal pre-

cursors ($H_2IrCl_6.4H_2O$ [1], $RuCl_3.xH_2O$ [2], and $TaCl_5$ [3]) to deionised water followed by addition of 0.5 M NaOH solution. The $TaCl_5$ was added as a solution in isopropanol (15.4 mg $TaCl_5$ ml^{-1}) to prevent rapid oxidation. The total metal concentration (Ir+Ru+Ta) in this solution was set to 0.01 mol l^{-1} with a metal:NaOH molar ratio of 1:20. The large excess of NaOH ensured that no large pH changes occured during the hydrolysis process. The pH prior to NaOH addition was around 1-1.5 and immediately rose to 12.3 following the addition of NaOH. This solution was heated in a water bath at 80 °C while stirring for 1 hour. During this time the precursors had hydrolysed forming a dark blue-black complex. At high ruthenium or tantalum contents, a precipitate had also formed within this heating period, as ruthenium and tantalum are more easily hydrolysed and oxidised than iridium. This hydrolysed mixture was cooled to room temperature, and the complexes / precipitate oxidised by addition of 1 M HNO_3 solution until the pH reached 8. The mixture was again heated and stirred for a further 30 minutes at 80 °C. This oxidation caused a dark-blue precipitate to form while the remaining solution was transparent. The precipitate was separated by centrifugation, and washed in deionised water 2 times, before being ultrasonically dispersed in deionised water and dried in air at 90 °C. This dry precipitate was then annealed in air at 400 °C for 30 minutes to further oxidise and crystallise the material.

8.3.2 Characterisation

X-ray diffraction (XRD) was performed on the dry electrocatalytic powders using a Siemens D5005 powder X-ray diffractometer, with a Cu-Kα X-ray source. The lattice parameters were estimated using the peak positions of the [110] and [101] diffraction peaks. The crystalline content was estimated by comparing the area of the diffraction peaks associated with crystalline material to that associated with amorphous material [139]. A Hitachi S-4300SE FE-SEM electron microscope with Oxford EDS system was used to examine the powder morphology and composition. Thermal gravimetric analysis (TGA) and differential scanning calorimetry (DSC) of the hydrolysis precipitate was conducted using a Netzsch STA 449 C instrument.

[1] OMG AG & Co. KG - 99.92% metals basis
[2] Alfa Aesar - 99.9% PGM basis
[3] Merck - 99.8%

Electrochemical analysis of the electrocatalytic powders was conducted in 0.5 M H_2SO_4 (Merck, p.a) electrolyte at room temperature, by supporting the powders on titanium plates using a spraying technique. The electrocatalytic layer consisted of 95 wt% electrocatalyst and 5 wt% Nafion ionomer[4], with a total loading of 1 mg cm^{-2}. After preparing the electrodes, they were cleaned by repeated boiling in deionised water. The electrodes were then subjected to an initial polarisation at 0.5 mA cm^{-2} for 4 minutes, with a steady potential being reached within this time. Cyclic voltammetry and polarisation measurements were performed using an IM6e electrochemical workstation from ZAHNER-elektrik GmbH & Co. KG. A Hg/Hg_2SO_4,H_2SO_4 reference electrode and a platinum foil counter electrode were used in the normal fashion. All potentials are quoted versus the reversible hydrogen electrode in the same electrolyte. To improve the statistics, at least 3 electrodes were prepared and tested for each electrocatalyst composition.

A PEM water electrolysis cell was also used to evaluate the performance of the synthesised materials under real conditions by applying the oxide as the anode and 20% Pt/C[5] as the cathode. Details of the cell can be found elsewhere [158]. The membrane electrode assembly (MEA) was prepared by spraying the ink containing the electrocatalyst and Nafion ionomer directly to Nafion 115 membranes[6] at 90 °C using a custom built automated spray system. The electrode area was always 5 cm^2 and the Nafion content of the electrocatalytic layers was 5 and 10 wt% for the anode and cathode respectively. Once sprayed, the MEA was hot pressed at 20 kg cm^{-2} and 125 °C for 10 minutes. The complete MEA was then cleaned and protonated by boiling in 10 wt% HCl solution for 30 minutes, followed by repeated boiling in deionised water. The MEA was mounted into the cell between two porous titanium sinters[7], and preheated deionised water was supplied to both the anode and cathode compartments at 5 l min^{-1}. The electrodes were pretreated at 10 mA cm^{-2} for 10 minutes then 50 mA cm^{-2} for 20 minutes. Total cell polarisation curves were recorded by stepping the current between 1 and 2000 mA cm^{-2}.

[4]Dupont 1100 EW 5% Nafion solution, Ion Power Inc.
[5]20% Pt on Vulcan XC-72R, E-TEK Inc.
[6]N-115, Ion Power Inc.
[7]Applied Porous Technologies Inc, diameter 30mm, thickness 1.5mm, 50 % porosity

8.4 Results and discussion

The bulk composition of the oxidised powder was measured by EDS and seen to be identical to the desired composition. The yield of this synthesis method was typically greater than 98 wt% with the small losses attributed to the washing/separation stages.

8.4.1 TGA/DSC analysis

The TGA and DSC traces for the two dry precipitates containing 100 mol% Ir and 80-20 mol% Ir-Ta were conducted prior to any annealing stage (Figures 8.1 and 8.2). Both TGA curves reveal that a large mass change occurs at 80-150 °C, due to water loss from hydrated oxides. This is accompanied by a endothermal peak on the DSC trace at around 100 °C. A continuous mass change occurs as the temperature is increased until around 460-480 °C where a small step in the mass losses occurs with another endothermic peak at 520 °C. No further mass loss occurs and the total mass change corresponds to around 12-12.5 wt% for the dry precipitate containing 100 % iridium. This is close to the theoretical mass loss of 13.8 wt% assuming the process is given by:

$$Ir(OH)_4 \rightarrow IrO_2 + 2H_2O \tag{8.1}$$

This indicates that the iridium precipitate, formed by the hydrolysis and chemical oxidation process, is most likely $Ir(OH)_4$ or $IrO_2.2H_2O$. The hydrolysis of hexachloroiridate (IV) at pH 12 followed by addition of HNO_3 was also suggested to give $Ir(OH)_4$ initially then $IrO_2.2H_2O$ after further heating [108]. This is in contrast to the findings by Ioroi *et al* where $Ir(OH)_3(H_2O)_3$ was suggested to be the product of the hydrolysis/oxidation process [58].

The mass loss for the oxides containing tantalum were higher than those predicted for a precipitate containing only $Ir(OH)_4$ or $IrO_2.2H_2O$ and Ta_2O_5 or $Ta(OH)_5$. This indicates that the tantalum present in the precipitate is highly hydrated, is thought to be an amorphous hydrated oxide (e.g. $Ta_2O_5.xH_2O$).

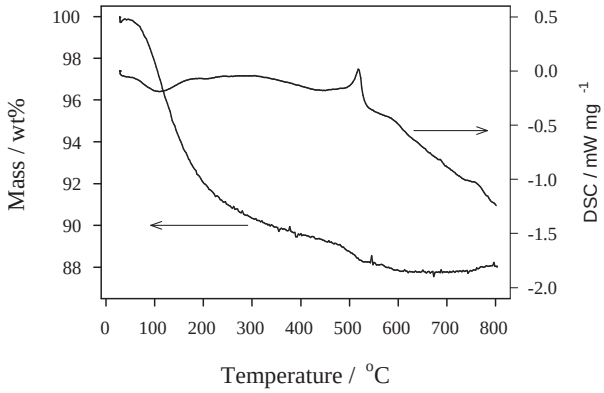

Figure 8.1: TGA/DSC trace of hydrolysis precipitate (100 mol% Ir)

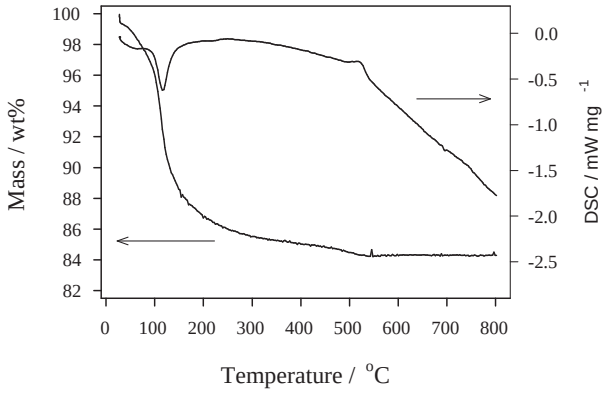

Figure 8.2: TGA/DSC trace of hydrolysis precipitate (80 mol% Ir, 20 mol% Ta)

The second clear peak on both DSC curves at 520 °C suggests that at this temperature the bulk of the oxide crystallises into a regular structure. This is consistent with previous work which showed that this second peak corresponded to the formation of crystalline IrO_2 as observed by XRD [58].

8.4.2 X-ray diffraction

Typical XRD patterns for the $Ir_xRu_yTa_zO_2$ powders, are shown in Figures 8.3, 8.4 and 8.5. It is immediately clear that the majority of synthesised oxides contain high levels of amorphous material as well as some crystalline phases corresponding to a rutile structure. Typically the amorphous content of the oxide samples was above 70 %. Figure 8.3 shows that very little changes in the oxide crystal properties occur as ruthenium is added, until 60 mol% Ru, at which the crystallinity of the material increases greatly. This is consistent with the findings of others who showed that RuO_2 crystallises at lower temperatures than IrO_2 [45, 67, 160]. Only a single rutile phase is found, with the lattice parameters for the crystal phase of the oxide $Ir_{0.4}Ru_{0.6}O_2$ (a=0.4493 nm, c=0.3125 nm) lying between those for pure IrO_2 (a=0.4498 nm, c=0.3154 nm) and RuO_2 (a=0.4491 nm, c=0.3107 nm). This suggests that a solid solution between IrO_2 and RuO_2 is formed.

Upon addition of tantalum to IrO_2 (Figure 8.4) it is observed that small crystal peaks are seen for oxides containing Ta, whereas pure IrO_2 are only amorphous. Normally in DSA literature Ta additions to IrO_2 are said to suppress the growth of IrO_2 [70], however it is also well known that the structure of DSA electrodes is strongly effected by the precursor chemistry [70, 81, 160]. IrO_2-Ta_2O_5 oxide powders produced by a sol-gel method also showed that Ta containing oxides were less crystalline than pure IrO_2 [92], although the pure iridium material also contained high levels of metallic iridium indicating that the formation mechanism is quite different from that used here. Although the crystal peaks seen for $Ir_{0.7}Ta_{0.3}O_2$ are very small, the estimated lattice parameters (a=0.4468 nm, c=0.3164 nm) are quite similar to the expected values for IrO_2 and show no significant changes as a function of Ta content.

Addition of ruthenium to replace iridium in samples containing tantalum reveals behaviour similar to that seen in the Ir-Ru oxide case, in that the crystallinity increases with ruthenium content. The addition of tantalum to

the Ir-Ru oxides implies that the ratio Ru:Ir, changes in these materials depending on the Ta content. This makes any trends in the lattice parameters difficult to assess. However if the lattice parameters are plotted as a function of the fraction of ruthenium on a noble metals basis ($f_{\mathrm{Ru_{NM}}}$ = mol% Ru / mol% Noble Metals), the lattice parameters, apart from some outliers, are consistent with a linear relationship to $f_{\mathrm{Ru_{NM}}}$ (Figure 8.6). This seems to indicate that tantalum has little affect on the crystal properties, although the positive increase in the "a" lattice parameter with $f_{\mathrm{Ru_{NM}}}$ is opposite to that expected for a solid solution only between IrO_2 and RuO_2 [160]. This indicates that the crystal structure of this oxide is quite complex, and unfortunately the data presented here is not suitable for any detailed analysis.

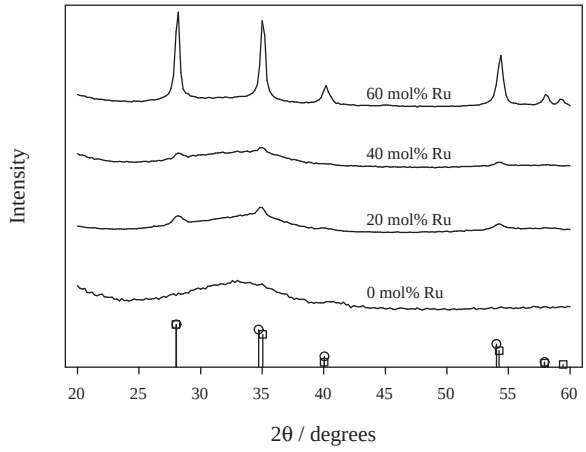

Figure 8.3: XRD patterns of $Ir_xRu_{1-x}O_2$, ∘ - IrO_2, □ - RuO_2

8.4.3 Particle morphology and size

Several electron micrographs were taken of the powder samples. The effect of tantalum content on the morphology is shown in Figure 8.7, and clearly shows that the particle / agglomerate size increases as the tantalum is added. No significant changes in morphology could be seen as iridium was replaced by ruthenium. This change in particle size does correspond with the small change in the crystalline content as tantalum is added to

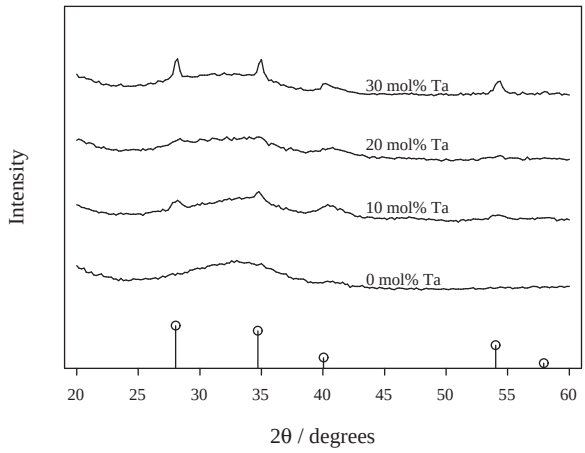

Figure 8.4: XRD patterns of $Ir_xTa_{1-x}O_2$, ∘ - IrO_2

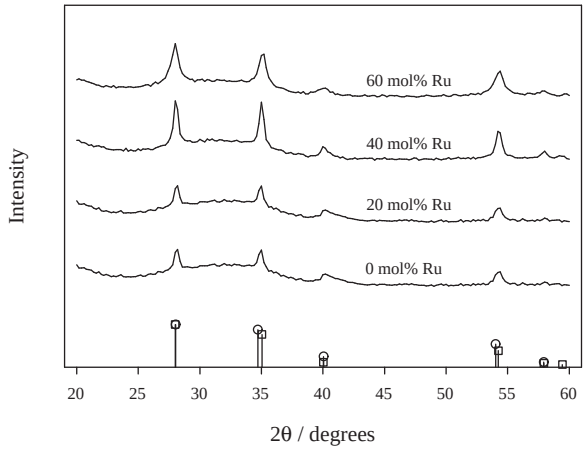

Figure 8.5: XRD patterns of $Ir_xRu_{0.7-x}Ta_{0.3}O_2$, ∘ - IrO_2, □ - RuO_2

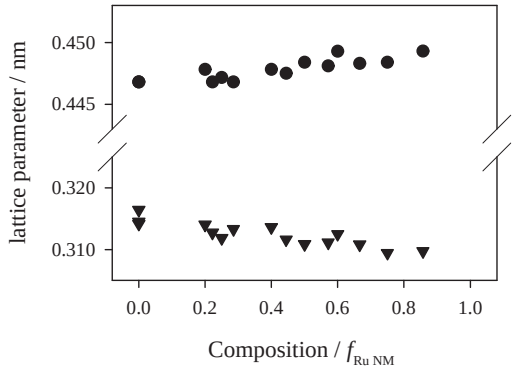

Figure 8.6: Lattice parameters of $Ir_xRu_yTa_zO_2$, ● - a, ▼ - c

IrO_2, although it is clear that the particles are agglomerates consisting of small crystals and amorphous material. Agglomerate size may have an influence on several important properties of these electrocatalysts. Normally an increase in agglomerate size would result in a reduction of the available surface area, depending of course on the porosity of the particles and the ability for electrolyte diffusion within the particle bulk. Agglomerate size may also influence the MEA layer properties such as electronic conductivity, catalyst utilisation, and gas/water transport, although no literature reports have studied this possible effect yet.

8.4.4 Electrical conductivity measurements

The electrical conductivity of the active layer in a PEM water electrolyser cell is very important. In this work the electrical conductivity of the electrocatalytic powders is compared by pressing the oxide powder between two pistons. The total resistance was measured between the two pistons as a function of pressed powder thickness. This enables the resistivity to be estimated without including the piston - oxide contact resistance. A typical plot of resistance vs. pressed powder thickness shows that the relationship is linear allowing the resistivity to be found from the gradient. Previously we have successfully examined the resistivity of $Ir_xSn_{1-x}O_2$ and $Ir_xRu_{1-x}Sn_{0.5}O_2$

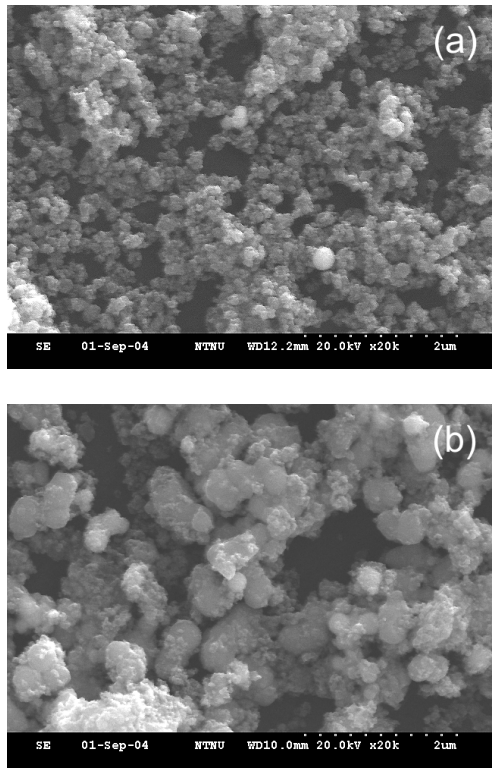

Figure 8.7: SEM micrographs of $Ir_xTa_{1-x}O_2$ electrocatalytic powders, (a) x=1, (b) x=0.7

powders in this manner [157]. Figure 8.8 shows the resistivity of $Ir_xRu_{1-x}O_2$, $Ir_xTa_{1-x}O_2$ and $Ir_xRu_{0.4}Ta_{1-x}O_2$ powders. Electrical conductivity of DSA type oxide layers has had some attention in literature [61], and as discussed in this review, the conductivity of the oxides rarely causes a significant performance loss as the highest resistivity reported is on the order of 10^{-2} Ω cm, with the resistivities around 3-6 x10^{-5} and 3-5 x10^{-5} Ω cm for crystalline IrO_2 and RuO_2 respectively [25]. The mechanism or cause of the resistivity is also suggested to occur primarily from the intergrain regions, and that the conductivity occurs with a "hopping" mechanism. Clearly in a layer consisting of particles, the resistance will be increased due to the large number of grain and particle boundaries. The contribution of the oxide layers resistivity to performance loss in PEM water electrolysers has been discussed

previously [7, 158].

Upon TaO_x addition to IrO_2 the resistivity clearly increases by two orders of magnitude by the time the composition reaches $Ir_{0.7}Ta_{0.3}O_2$. This is expected as tantalum oxides are normally electrically non-conductive. This increase is despite the increase in particle and crystal size, which implies there are less particle–particle and crystal grain boundaries present in the sample, indicating that the material itself becomes less conductive. A resistivity of 6 Ω cm will cause little problems in a PEM water electrolysis cell based on previous findings [157, 158]. Rasten showed that upon addition of tantalum to iridium oxide, the resistance of a PEM water electrolysis cell increased from around 0.05 Ω cm^2 for IrO_2 to 0.2 Ω cm^2 for 0.65 IrO_2 - 0.35 $TaO_{2.5}$ [7]. These measurements included some ionic resistance from the Nafion membrane, which was assumed to be half the full membrane resistance. Additions of RuO_2 to IrO_2 appear to have no significant effect on the measured resistivity, a finding which is expected due to the similar conductivities of both oxides. This was also the case for Ir-Ru oxides prepared by the Adams fusion method and tested in-situ in a PEM water electrolysis cell [7]. Oxides containing ruthenium showed a similar trend in resistivity to $Ir_xTa_{1-x}O_2$ as a function of tantalum content. The resistivities are only slightly lower at high Ta contents compared with Ir-Ta oxides, which is probably a result of the larger crystals in the ternary oxide.

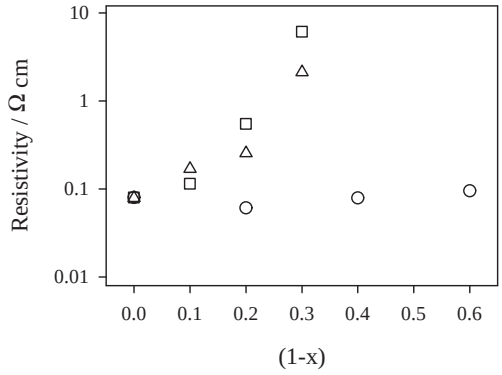

Figure 8.8: Resistivity of, ○ - $Ir_xRu_{1-x}O_2$, □ - $Ir_xTa_{1-x}O_2$, and △ - $Ir_xRu_{0.4}Ta_{0.6-x}O_2$

8.4.5 Cyclic voltammetry - 0.5 M H_2SO_4

Cyclic voltammograms of $Ir_xTa_{1-x}O_2$ are shown in Figure 8.9 and 8.10. At low sweep rate the pure IrO_2 has a typical shape with broad peaks located in the oxide region of the curve, corresponding to the solid state redox transitions which take place during the exchange of protons with the electrolyte. As tantalum is added to the oxide, the current densities during the sweep decreases. This is especially so in the double layer potential window (200-500 mV), with the initial sharp rise in anodic current shifting to higher potentials as the tantalum content increases. The redox peak at 800-900 mV also becomes more defined and shifts to lower potentials as tantalum is added. This indicates that tantalum effects the redox properties of the active iridium oxide phase as it is unlikely that the tantalum takes part in the redox processes directly. It is unclear at this stage whether the effect of tantalum is a specific effect during the electrode processes, or an artifact from the presence of tantalum during the synthesis of the electrocatalyst. The XRD analysis showed that at high tantalum contents the crystallinity of the oxide is higher, which can explain the more defined IrO_2 redox peaks. At higher sweep rates the general shape of most samples was similar to low sweep rates, with the main redox peak at located around 970 mV during the anodic sweep. However, on the cathodic sweep, the main peak was observed to shift to lower potentials as a function of tantalum content. The difference between the potential of this main peak during the anodic and cathodic sweep (ΔE_p), increased from 120 mV for the pure IrO_2 electrode, to 300 mV for $Ir_{0.7}Ta_{0.3}O_2$. A split of 300 mV in the peak potentials was also seen by Vercesi et al [63] who studied a DSA electrode with the same composition. This increase in peak splitting is probably a result of the stronger oxygen affinity of the material when the tantalum content increases, thus introducing some irreversible behaviour into the charging process.

The addition of RuO_2 to IrO_2 has no dramatic effect on the voltammogram shape, with the current densities first decreasing then going through a maximum at 40 mol% Ru before decreasing again. The low current densities seen for 60 mol% Ru is a result of decreased active area due to increased crystallinity. Normally RuO_2 electrodes have 3 redox peaks and there is some evidence that a new peak is present around 1.2 V for the electrodes containing 40 and 60 mol% Ru. The characteristic RuO_2 peak around 0.65 V [7, 121, 122] is not seen on any of the electrodes, which is most likely due

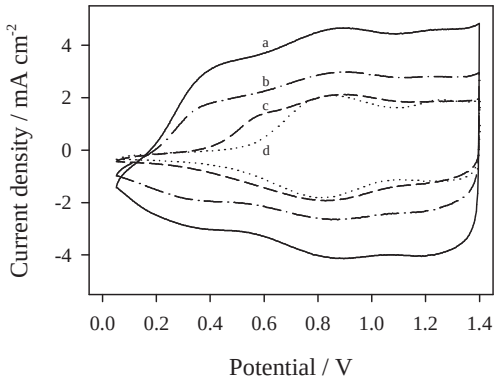

Figure 8.9: Cyclic voltammograms of $Ir_xTa_{1-x}O_2$ in 0.5 M H_2SO_4 at 10 mV s^{-1}. a - 0, b - 10, c - 20, d - 30 mol% Ta

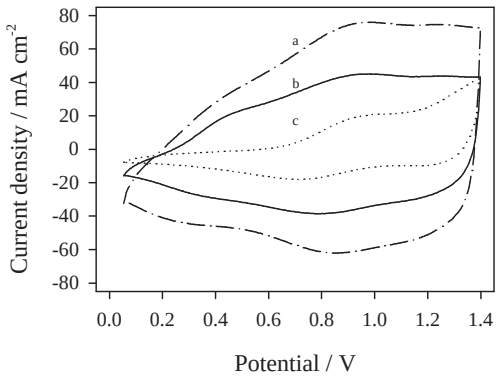

Figure 8.10: Cyclic voltammograms of $Ir_xTa_{1-x}O_2$ in 0.5 M H_2SO_4 at 200 mV s^{-1}. a - 0, b - 10, c - 30 mol% Ta

to the very large double layer current which masks this area of the sweep, although this peak was also absent on Ir-Ru oxide DSA electrodes [87].

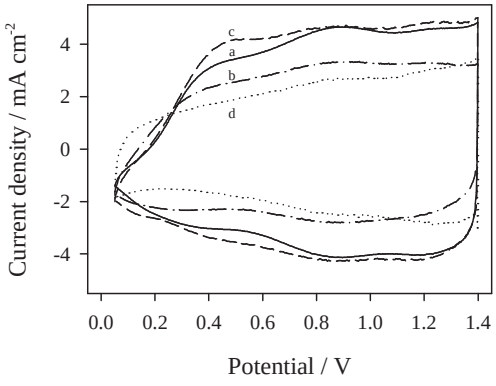

Figure 8.11: Cyclic voltammograms of $Ir_xRu_{1-x}O_2$ in 0.5 M H_2SO_4 at 10 mV s^{-1}. a - 0, b - 20, c - 40, d - 60 mol% Ru

The ternary oxide electrodes showed similar behaviour to that described above with the current density decreasing and the peak splitting increasing as tantalum was added.

Charge measurements are often used in DSA literature to compare the active area or number of active points of a noble metal oxide layer. Measuring the charge as a function of sweep rate, allows the total charge and the outer charge for the oxides to be calculated [35]. The outer charge represents the active area which is easily accessible, whereas the total charge includes active points within the particle structure, to which the electrolyte must diffuse, in order to be included in the electrode response. Often in literature, Ir-Ru oxides give rise to a maximum in anodic charge at intermediate compositions [87, 121], as do Ir-Ta oxides [7, 113], and Ru-Ta oxides [62]. The results obtained here are summarised in Figure 8.12 and show that as tantalum is added to the oxide material the total charge decreases. This is in agreement with the particle size analysis, which suggests that the active area should decrease as Ta is added, and the fact that the charging process will not occur to much degree on tantalum oxide, and thus any tantalum present will reduce the total number of available active points. For the Ir-

Ru oxides there is a maximum around 40 mol% Ru, whereas for the ternary electrodes the maximums are found around 20 mol% Ru. The lower charge for the electrodes containing high levels of Ru, is most likely due to the effect ruthenium has on the oxide crystallinity, with highly ordered oxide surfaces having less roughness and defects. Assuming that the charging process is similar, normally it should be expected that ruthenium oxide electrodes will have a larger anodic charge, as by weight, ruthenium oxide contains around 70 % more atoms than iridium oxide. The trend in the total anodic charge was similar for the outer charge measurements, and suggests that Ta additions reduces the available electrocatalytic surface area, as does high levels of Ru. The capacitance of these oxides was also calculated at 1.2 V using $C = i/\nu$. The i–ν plots were approximately linear, although some deviation did occur at high sweep rates for those oxides which showed irreversible charging behaviour. Generally the estimated electrode capacitance followed the same trend as the charge measurements, with the highest capacitance values found to be on the order of 200-300 F g^{-1}.

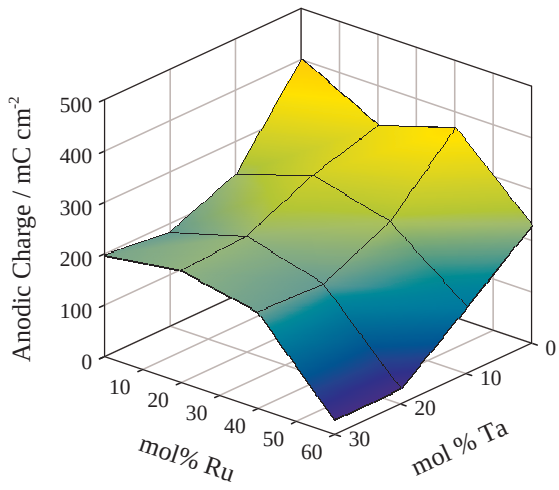

Figure 8.12: Total anodic charge of $Ir_xRu_yTa_zO_2$ in 0.5 M H_2SO_4

8.4.6 Steady state polarisation measurements - 0.5 M H_2SO_4

After the cyclic voltammetry measurements, steady state polarisation curves were recorded by stepping the potential anodically in 5 mV steps from 1.4

V, with a holding time of 1 minute, by which time the current was seen to have stabilised. Typical polarisation curves of the oxides measured in 0.5 M H_2SO_4 are shown in Figure 8.13 together with the a plot of the potential obtained at 1 mA cm^{-2} (Figure 8.14).

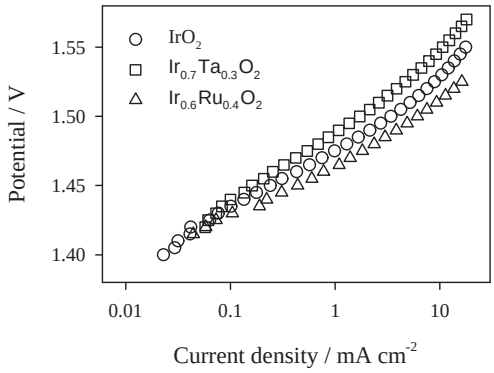

Figure 8.13: Polarisation curves of $Ir_xRu_yTa_zO_2$ in 0.5 M H_2SO_4

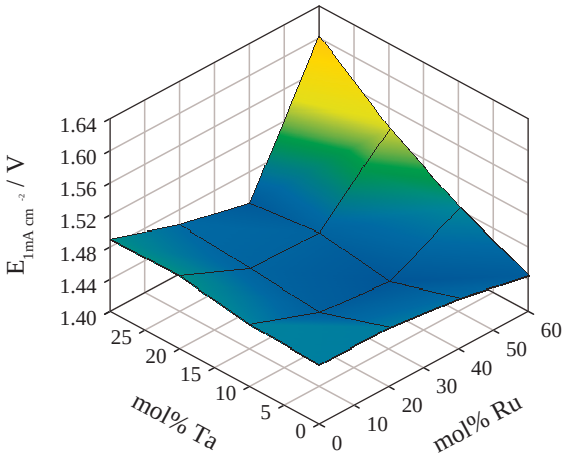

Figure 8.14: Potential at 1 mA cm^{-2} for $Ir_xRu_yTa_zO_2$ in 0.5 M H_2SO_4

It is clear that the performance of these electrodes is a function of the oxide composition. The general trend shows that additions of Ru up to 40 mol% are beneficial, with higher ruthenium contents causing a decrease in

the oxygen evolution performance. As RuO_2 is normally regarded as more active towards the oxygen evolution reaction in comparison with IrO_2, is not surprising that the performance increases upon Ru addition. The decrease in performance at high Ru contents is a result of decreased active surface area as found by cyclic voltammetry. Tantalum additions above 10 mol% also caused a decrease in the electrocatalytic performance, whereas slight improvement in performance can be seen when 10 mol% Ta is added to Ir-Ru oxides provided that the Ru content is less than 60 mol%. This improvement is most likely related to increased dispersion of the active material. Overall the best low current performance is seen for oxides containing 10 mol% Ta and 20-40 mol% Ru.

The Tafel slopes of the oxides typically ranged from 40-45 mV dec^{-1}, except for oxides containing 60 mol% Ru where the Tafel slope increased to 60 mV dec^{-1}. The oxide with the least iridium ($Ir_{0.1}Ru_{0.6}Ta_{0.3}O_2$) gave an even higher the Tafel slope of 116 mV dec^{-1}. Clearly the oxide composition can result in different mechanisms or rate determining steps for the oxygen evolution reaction. The Tafel slope of 116 mV dec^{-1} indicates that the slow adsorption and discharge of water probably limits the oxygen evolution reaction [7]. Tafel slopes of 40-45 mV dec^{-1} most likely indicates that the rate determining step is second electron transfer step of the Electrochemical Oxide pathway [15]. The increase towards 60 mV dec^{-1} is probably related to the increased crystallinity and reduced number of defects within the oxide lattice that these materials exhibited. Rasten showed that addition of tantalum to iridium oxide decreased the low current Tafel slope in a PEM water electrolyser [7]. DSA Ir-Ru oxide electrodes have shown Tafel slopes of close to 60 mV dec^{-1} for IrO_2 and decreasing to 40 mV dec^{-1} for RuO_2 [87, 122] although the Tafel slope is not solely a composition effect with others showing a variation in the Tafel slope for RuO_2 electrodes as a function of crystallinity [65, 101]. Rasten has also showed that the Tafel slope for oxygen evolution on IrO_2 increases with annealing temperature, most likely due to the change in the electrodes crystallinity [114].

As the cyclic voltammetry measurements showed a strong effect of composition on the electrochemically active area, it is interesting to determine whether the changes in low current performance is a result of an area effect or a result of changes in the specific electrocatalytic activity of the oxide. Specific activity is can be estimated by dividing the current density by the outer anodic charge as found by the cyclic voltammetry measurements, giv-

ing a measure of the specific electrocatalytic activity free from surface area effects. The potential at a normalised current density of 0.02 A C^{-1} where used to compare the materials, and, as tantalum oxide is expected to have zero activity towards oxygen evolution, the results are plotted as a function of $f_{Ru_{NM}}$ (Figure 8.15). Although there is several outliers, results indicate that the specific electrocatalytic activity increases (i.e. $E_{0.02AC^{-1}}$ decreases) in a linear fashion with the ruthenium content. This is expected due to the larger exchange current density of RuO_2 in comparison with IrO_2 [7]. Similar specific activity values were obtained by others for Ir-Ru oxide DSA electrodes in H_2SO_4, with the same trend as a function of composition [87]. At the stage there is little evidence to suggest that tantalum has an influence on the electrocatalytic activity. For the Ir-Ta oxide samples, there was no obvious systematic change in the specific activity as a function of tantalum content, with $E_{0.02AC^{-1}} = 1.499 \pm 0.016$ V (95% confidence). It has been shown that Ir-Ta oxides give complex multiple phase mixtures, in which the iridium is present in different $Ir_xTa_{1-x}O_2$ solid solutions and surface modified IrO_2 [70]. This structural complexity may explain the some of the scatter in these activity measurements and the lack of clear trend in the $Ir_xTa_{1-x}O_2$ specific activity. Previously for $Ir_xRu_ySn_zO_2$, a total change 0.03 V was found in $E_{0.02AC^{-1}}$ with the activity being clearly a linear function of ruthenium content. It is suggested that some further investigation of the specific electrocatalytic activity be carried out for Ir-Ta and Ru-Ta oxides.

8.4.7 PEM water electrolysis performance

The performance of the prepared $Ir_xRu_yTa_zO_2$ anode electrocatalysts were evaluated in a single PEM water electrolysis cell up to current densities of 2 A cm^{-2}. Typical polarisation curves at 80 °C are shown in Figure 8.16 (Anode composition indicated on Figure), and the results summarised in Table 8.1. The potential at 1 mA cm^{-2} ($E_{1mAcm^{-2}}$) is used to show the performance of the anode electrocatalysts without the influence of ohmic resistivity and high bubble formation, whereas the potential at 1 A cm^{-2} ($E_{1Acm^{-2}}$) will be affected by ohmic resistivity and bubble formation and thus gives a measure of the performance under real operating conditions.

With no exceptions, at all ruthenium contents the addition of tantalum

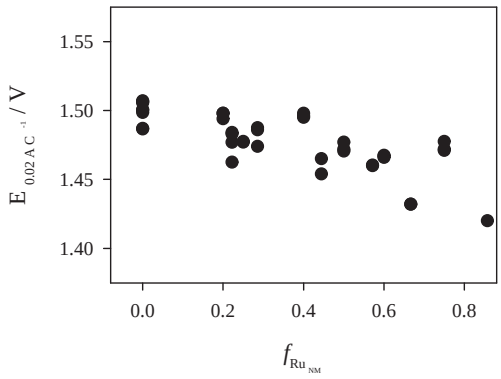

Figure 8.15: Specific electrocatalytic activity of $Ir_xRu_yTa_zO_2$ in 0.5 M H_2SO_4

cause the low current cell performance to decrease. A similar trend was seen in the aqueous system, although in 0.5 M H_2SO_4, additions of 10 mol% Ta caused a slight performance increase at low ruthenium contents. In the PEM cell, we expect there to be some variation in the performances caused by uncontrollable variations in MEA properties, which may account for the observed differences between the aqueous and PEM measurements. It was also assumed that the cathode performed equally well for each MEA, an assumption which is quite safe in the low current region, as the hydrogen evolution overpotential is small in this range [7]. It is also seen that the low current performance improves as the iridium is replaced with ruthenium up to 40 mol% Ru, a trend which was also observed in the aqueous electrolyte.

The high current measurements do not show the same trend in potential with composition as the low current measurements, most likely due to the influence of ohmic resistivity and bubble formation. At these high currents we expect the reproducibility of the cell voltage to be on the order of ± 20 mV. Clearly the cell potential is affected by the anode composition with good results obtained with the oxides containing 20-40 mol% Ru and 0-20 mol% Ta. Oxides containing low iridium contents show poor performance which is probably a result of the low active area of these oxides. Interestingly, in most cases, up to 20 mol% Ta can be added to Ir-Ru oxides without significantly

decreasing the cell performance. This is very important in terms of the possible lifetime of the prepared electrocatalysts, as it is likely that tantalum will increase the stability of the oxides. Unfortunately such stability tests could not be carried out here due to the passivation of the porous titanium backings, which occured within several hours under accelerated lifetime conditions (2 A cm^{-2}, 80 °C). Overall the best result was obtained with an $Ir_{0.6}Ru_{0.4}O_2$ anode and 20 wt% Pt/C cathode, with a cell voltage of 1.567 V at 1 A cm^{-2} and 80 °C when using Nafion 115 as the electrolyte membrane. This represents a cell efficiency of 76 % ($\varepsilon_{\Delta G}$) and an energy consumption of 3.75 kWhr Nm^{-3} H_2 at 1 A cm^{-2}.

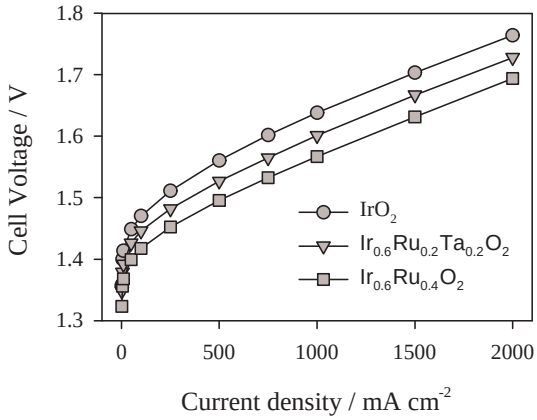

Figure 8.16: Polarisation curve of PEM water electrolysis cell at 80 °C

8.5 Conclusions

High performance $Ir_xRu_yTa_zO_2$ anode electrocatalysts were synthesised using a hydrolysis technique followed by thermal annealing. The resulting oxide powders were normally highly amorphous, with any crystalline material thought to be a solid solution between IrO_2 and RuO_2. No evidence was found to suggest tantalum is present within the crystal matrix. Voltammetry showed that the charging process was affected by the addition of tantalum, with less reversible behaviour occuring as the tantalum content increased.

Table 8.1: PEM water electrolysis results at 80 °C

Ir mol %	Ru mol %	Ta mol %	$E_{1mAcm^{-2}}$ V	$E_{1Acm^{-2}}$ V
100	0	0	1.357	1.638
90	0	10	1.360	1.688
80	0	20	1.366	1.624
70	0	30	1.369	1.637
80	20	0	1.335	1.596
70	20	10	1.337	1.588
60	20	20	1.348	1.601
50	20	30	1.352	1.682
60	40	0	1.323	1.567
50	40	10	1.332	1.586
30	40	20	1.337	1.588
20	40	30	1.358	1.654
40	60	0	1.330	1.575
30	60	10	1.344	1.594
20	60	20	1.346	1.709
10	60	30	1.358	1.905

The active surface area of the materials decreased at high ruthenium contents, which is most likely due to the increased crystallinity of these materials. Likewise the Tafel slope increased at high ruthenium contents, which again was contributed to the increase in crystallinity. Improvements in the specific activity (free from surface area effects) were found on addition of ruthenium, which is probably due to the larger exchange current density of RuO_2 in comparison with IrO_2. In the PEM water electrolysis cell, very high performance was obtained for anode materials containing 20-40 mol% Ru and 0-20 mol% Ta. The best result was obtained with an $Ir_{0.6}Ru_{0.4}O_2$ anode and 20 wt% Pt/C cathode, with a cell voltage of 1.567 V at 1 A cm^{-2} and 80 °C when using Nafion 115 as the electrolyte membrane. This equates to a cell efficiency of 76 % ($\varepsilon_{\Delta G}$) and an energy consumption of 3.75 kWhr Nm^{-3} H_2 at 1 A cm^{-2}.

Chapter 9

X-ray Absorption Spectroscopy of Anode Electrocatalysts

The background of XAS has been covered in Chapter 2, section 2.6.4. Some of this will be discussed further when dealing with cell design and the optimisation of samples. All the XAS measurements were carried out at the Swiss-Norwegian beamline (BM01B) at the European Synchrotron Radiation Facility, in Grenoble, France.

9.1 Objectives of XAS measurements

Structural analysis of the synthesised oxide materials has proved very useful in developing active anode electrocatalysts during this work. However many of the materials synthesised are highly amorphous making analysis based on X-ray diffraction difficult. The X-ray absorption process in XANES and EXAFS arise from local ordering of the analysed materials, allowing the structural analysis of the neighbouring environment around the probed element. This means that the structure of the amorphous or very small crystallites may be investigated and the results combined with analysis performed previously by XRD. A major advantage of XAS is the ease of making in-situ

measurements. This means that the structure of the materials may be examined as a function of applied electrode potential if the sample is prepared in the form of an electrode.

Therefore there are several objectives:

- Comparison of the structure of mixed oxides prepared by two methods (i.e. solid solutions vs. ultra-dispersed systems)
- Structural changes in mixed oxides as a function of electrode potential
- Following redox transitions as a function of potential
- Explore the use of XAS for analysis of electrochemical systems

9.2 In-situ cell design

In-situ XAS measurements require special consideration in order to collect data which reflects the process under investigation. A new electrochemical cell was required for the in-situ measurements, and therefore some time was used in order to develop a cell meeting the following requirements:

- Stable when filled with aqueous acid electrolyte
- Easy to fill and empty with electrolyte
- Easy and reproducible electrode placement
- Appropriate electrode geometries
- Suitable for XAS measurements
- Only polarised material is measured

The first three items are relatively straightforward to design for. The last three items however require some knowledge or assumption on how the XAS measurements will be made. XAS measurements can be recorded either in transmission or fluorescence mode. In transmission mode, the X-ray beam passes through the entire cell including the electrode of interest, the electrolyte, and the counter electrode if this is in the beam path. Fluorescence measurements are made by exposing the sample to the incoming beam, and measuring the resulting fluorescence signal coming from the radiated sample.

Normally the fluorescence signal is measured perpendicular to the incoming beam, with the sample-incoming beam angle set at 45 degrees. For the electrochemical measurements, ideally the electrode arrangement should be such that the working electrode is parallel to the counter electrode (which is normally larger than the working electrode) with a suitable thickness of electrolyte between these to ensure no changes to the working electrode's environment occur due to the changes in the electrolyte or from the reaction at the counter electrode. A relatively thick electrolyte (say 0.5–1 cm) also makes placement of the reference electrode simple. Measuring only polarised material is an important consideration due to the fact that the X-ray beam will penetrate the entire electrocatalytic layer. As the electrocatalytic layer is porous but at least 1-2 μm thick, it is critical that the particles within this layer are exposed to the identical environment such as electrolyte and potential etc. If the electrode layer is only partially exposed to the electrolyte, only that exposed section will be affected by the potential, and therefore the measured XAS signal will contain an average of both the polarised and un-polarised electrocatalyst. Such considerations have also been discussed in the review by Sharpe *et al* [161].

Several types of in-situ XAS electrochemical cells have been used in literature. A transmission cell for studying battery materials [162] and fuel cell Pt/C electrocatalysts [163] has been used with some success. This cell used a powder based nickel oxide or Pt/C working electrode and graphite foil counter electrode, with the electrolyte held within a porous separator. Others have examined fuel cell electrocatalyst in transmission cells [164] and fluorescence cells [165]. Electrochemically deposited IrO_2 and RuO_2 electrodes have been examined using fluorescence measurements [119, 120]. These electrodes were prepared by depositing the precursors onto Au-coated polymer films, however the required thinness of the Au coating to avoid excessive absorption of the X-ray beam, meant that the ohmic resistance of the electrodes were very high and had to be corrected for the IR-drop [120].

Reviews of XAS studies involving electrochemical processes and electrode materials are very useful in developing new in-situ cells. McBreen *et al* has reviewed the use of EXAFS to study fuel cell and battery materials [44] and Russell and Rose have reviewed the use of XAS to study low temperature fuel cell catalysts [166]. A review of EXAFS spectroelectrochemistry has also been given by Sharpe *et al* [161] and Deward has reviewed the use of EXAFS to probe electrode-solution interfaces [167].

A significant advantage of fluorescence measurements over transmission measurements is the ability to measure reliably on rough or uneven samples, as the fluorescence signal is less sensitive to thickness effects. Samples for transmission measurements must be completely pin-hole free, otherwise the measurements become distorted, due to the fact that the absorption coefficient is averaged over the entire sample, and therefore would include a "zero absorption" fraction from these pin-holes. This is normally overcome by mixing the active sample with a low absorption material and therefore the particles are more homogeneously distributed over the samples cross-section. This would make electrodes difficult to prepare as the extra inert material adds significant bulk to the electrode. This may prevent electrolyte penetration through the entire electrode layer, and thus only a portion of the electrode is active during the electrochemical polarisation and again the XAS is an averaged signal of polarised and un-polarised materials. These considerations has lead to the development of a fluorescence-based electrochemical cell, in which powders composites can be used as electrodes. This cell design is shown in Figure 9.1. The principle of this design is that the powder is applied to a graphite foil creating an electrode / electrocatalytic layer similar to that used in conventional PEM water electrolysis or PEM fuel cell electrochemical cells. This graphite foil acts as the X-ray window, electrical contact, and sealing mechanism of the electrolyte compartment. The active layer is placed in contact with the electrolyte and is parallel to a suitable counter electrode. The in-coming X-ray beam then travels through the thin graphite foil and is absorbed by the active electrode layer. The resulting fluorescence signal is then measured after returning back through the graphite foil. This process is schematically shown in Figure 9.2. The advantage of this design is the ability to measure on thin and uneven particle composite electrodes, while maintaining simple and "standard" electrochemical cell design and geometry. At the energies of interest in this work (11-23 keV) graphite foil 130 μm thick absorbs only around 1–5 % of the X-ray beam.

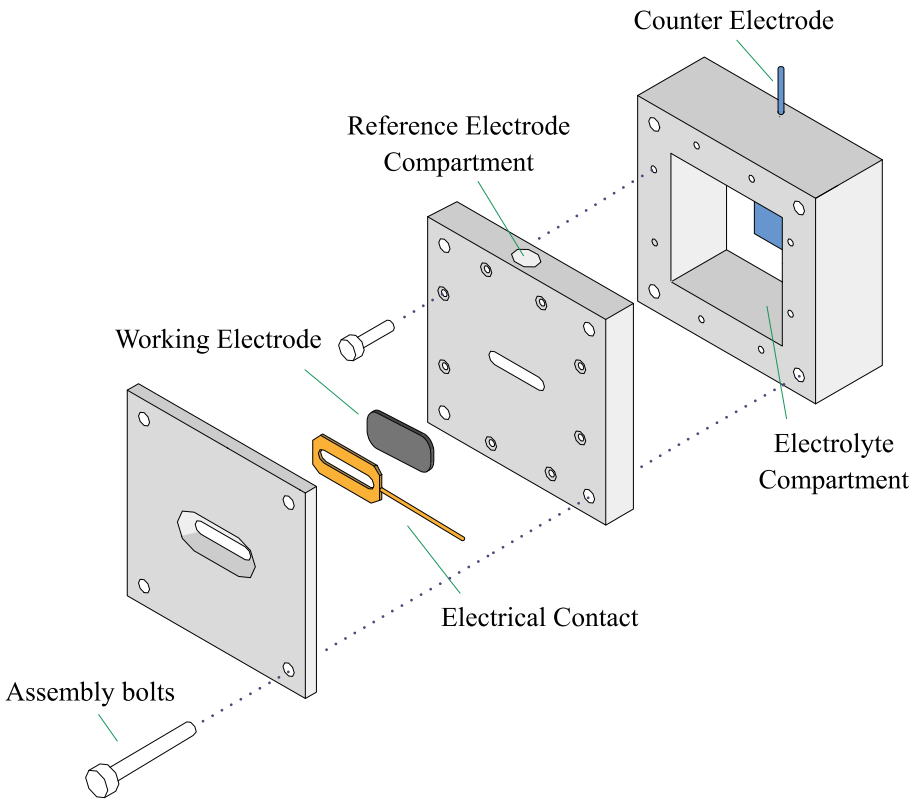

Figure 9.1: Schematic of XAS in-situ electrochemical cell

9.3 Experimental

9.3.1 Powder sample preparation

For dry oxide powders, the data was measured in transmission mode with the samples held in small aluminium holders sealed by Kapton adhesive tape. The oxide powders were first diluted with boron nitride powder by grinding the powders together in a mortar, in order to achieve the optimum X-ray absorption. This optimum was found by calculating the mass of material required (M) to give an absorption of $\Delta\mu x \sim 2$:

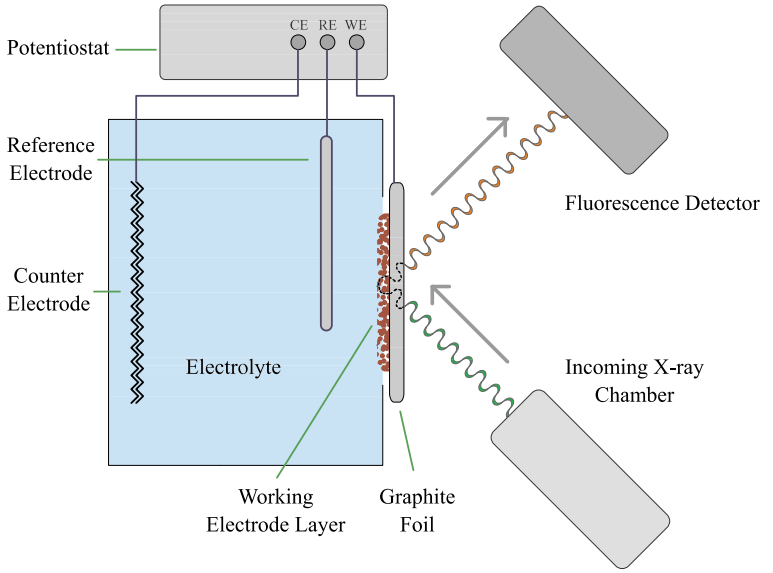

Figure 9.2: Principle of XAS in-situ electrochemical cell

$$M = \frac{A\Delta\mu x}{\Sigma f_i(\mu/\rho)_i} \tag{9.1}$$

where A is the sample area, f_i is the mass fraction of the ith element in the sample, and μ/ρ is the mass absorption coefficient of the ith element at the energy of interest. The mass absorption coefficients can be found tabulated in the *CRC Handbook of Chemistry and Physics* [168] and published on the Internet [169].

9.3.2 Electrode measurements

In-situ XAS measurements were also performed on electrodes polarised in an aqueous electrochemical cell. The electrodes were prepared by spraying a electrocatalytic ink (95 wt% oxide, 5 wt% Nafion ionomer[1]) to graphite foil[2] using the technique for preparing composite electrodes on titanium. The

[1]Dupont 1100 EW 5% Nafion solution, Ion Power Inc.
[2]Alfa Aesar, 99.8% metals basis, 130 μm thick

oxide loading was approximately 0.8 mg cm^{-2} and the geometric surface area of the electrode was 2.785 cm^2. The electrode was then loaded into the in-situ cell, and pretreated by cycling the potential between 0.4 and 1.4 V at 100 mV s^{-1} for 10 cycles followed by 3 cycles at 20 mV s^{-1} in the same potential window. The entire area of the electrode was exposed to the electrolyte to ensure that XAS measurements did not include "non-polarised" material. The electrode was polarised potentiostatically during all XAS measurements, with the potential held at the desired level for several minutes prior to starting the XAS measurements to ensure that the electrode had come to steady state. The cell was operated at room temperature for all in-situ measurements, with the potential controlled using a Radiometer Analytical PZG100 potentiostat. The electrolyte was 0.5 M H_2SO_4 (Merck, p.a.) with the working electrode potential measured against a reversible hydrogen electrode (RHE) in the same electrolyte. The electrochemical cell included a reference electrode chamber which enabled the potential of the working electrode to be sensed around 2 mm from the electrode surface, reducing the need for ohmic drop compensation.

9.3.3 XAS measurements

The XAS measurements were collected at the Ir LIII-edge (11 212 eV), and the Ru K-edge (22 119 eV). The X-ray monochromator was a Si-111 channel-cut type, and harmonic rejection was performed by a double-bounce gold (for the Ru K-edge) or chromium (for the Ir LIII-edge) coated mirror system. For the Ir LIII-edge tranmission measurements, a 95% N_2 - 5% Ar filled ion chamber (16 cm in length) was used before the sample and an Ar filled ion chamber (31 cm in length) was used after the sample. For the Ru K-edge measurements the first chamber was filled with 50% Ar and 50% Kr, and the second chamber filled with 80% N_2 and 20% Kr. A third ion chamber was also used to measure the XAS of a Ir or Ru metal reference which was located after the second chamber. This was used to ensure there were no changes in the monochromator position between experiments. The data were recorded at intervals of 5 eV before the edge, 0.5 eV over the edge and every 0.05 $Å^{-1}$ above the edge. For the in-situ measurements, the fluorescence from the electrocatalyst layer was measured using a 13 element solid state detector which was brought close (10-30 cm) to the electrode surface. Normally the cell was held at a 45° to the incoming beam with the

angle between the incoming beam and the fluorescence detector around 50°. Unfortunately the optimum of 90° could not be achieved due to the size and geometric constraints of the experimental stage, combined with the necessity of having the detector close to the electrode surface in order to achieve high fluorescence counts.

9.3.4 Data analysis

The XAS data analysis and fitting was performed using the ATHENA and ARTEMIS software packages. The ARTEMIS software provided a simple interface to the ab-initio multiple scattering XAS code FEFF6 by Rehr et al [170] which is widely used and has proven to be a reliable and user-friendly theoretical XAS code. The FEFF6 code was fitted to the data via the FEFFIT software [171] which is implemented in ARTEMIS. The FEFF6 code was generated from crystallographic data by using the ATOMS 3.0 software [172].

The initial XAS data reduction was carried out using the ATHENA software package. Firstly the background was removed using the AUTOBK algorithm developed by others [173]. This involved using the pre-edge data from 150 to 75 eV below the edge and fitting a spline over the wavenumber range of 2 to 14 $Å^{-1}$. The range of this spline was checked by examining the data in k-space to ensure that the background fit was sensible. The R-space cutoff value (R_{bkg}) was selected to be half of the first shell length without including the phase shift (typically set to 0.8 Å). The data were then normalised over the range 150-675 eV above the edge and the edge step found by comparing the pre-edge and normalisation. The EXAFS was then Fourier transformed into R-space by using k^3 weighted data over the range of 3-14 $Å^{-1}$ with Hanning window where the window sill (dk) was set to 1 $Å^{-1}$ to minimise the termination errors. The EXAFS function (χ(k)) was then fitted to the ab-initio multiple scattering XAS code FEFF using ARTEMIS. This fit was performed in R-space and a background function was also applied during this fit, with its contribution terminated at R_{bkg}. To reduce the number of fitting parameters and give more reliable results, the amplitude scaling factor (S_0^2) was set to that obtained by fitting the reference IrO_2 and RuO_2 materials.

9.4 Results - Powder measurements

Full XAS scans were recorded on a wide range of oxides containing iridium, tin and ruthenium. Generally two scans were measured to improve the statistics in later data analysis. For all samples the signal to noise ratio was good as the samples had been optimised prior to the measurements. Initial scans were performed on some iridium standard materials and the data processed (Figures 9.3 and 9.4). It is clear that both the XANES and EXAFS (plotted as the Radial distribution function, RDF) show significant differences as expected. XANES can often be used as a "fingerprint" of the structure in which the core element resides. From the XANES we find the expected result that the intensity of the white line[3] increases with increasing oxidation state [120, 174, 175] due to the greater number of 5d orbital vacancies to which the core electrons are excited (insert Figure 9.3). The RDF is similar to a radial atomic distribution in that the atomic distances of each shell which surround the core element (in this case iridium) are shown (uncorrected for phase shift[4]). The RDF shows that the first main peak for IrO_2 is situated around 1.6-1.7 Å and is associated to the first and second Ir-O shells [102, 176, 177]. Normally these Ir–O distances cannot be separated as they are very similar (within 0.06 Å) so most researchers choose to fit this peak to a single Ir–O distance with the iridium atom coordinated to 6 oxygen atoms [102, 118, 120]. The $IrCl_3$ RDF reveals that the first shell occurs around 2.0 Å which corresponds to the Ir–Cl distance [102, 118]. Similarly the first Ir–Ir distance for the metallic sample is seen around 2.7 Å which is typical for the Ir–Ir distance in a cubic close-packed structure. The first main peak for the reference IrO_2 material was fitted to the theoretical scattering model (Figure 9.5). In this fit, two sub-shells were used with the distances and coordination number set to the theoretical values. This fit enabled a good measure of the amplitude scaling factor (S_0^2), which was used in all other fits. The peak positions of the two sub shells were further refined and are tabulated in Table 9.1

The analysis of these standards shows that the edge energy [5] (E_0) or the

[3]The white line energy (E_w) is defined at the apex of the first sharp peak in the XANES profile. Its name comes from the use of photographic paper in early experimental setups

[4]Normally including the phase shift will add around 0.3–0.4 Å

[5]The edge energy is normally defined as the inflection point of the initial steep increase in X-ray absorption

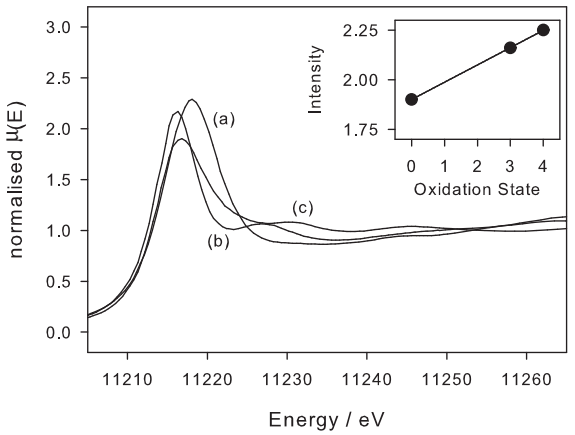

Figure 9.3: XANES profile of (a) IrO_2 - prepared following [102], (b) $IrCl_3.3H_2O$ - Alfa Aesar 99.9%, (c) Iridium black - Alfa Aesar 99.9%, Insert - Intensity of the white line vs. formal oxidation state

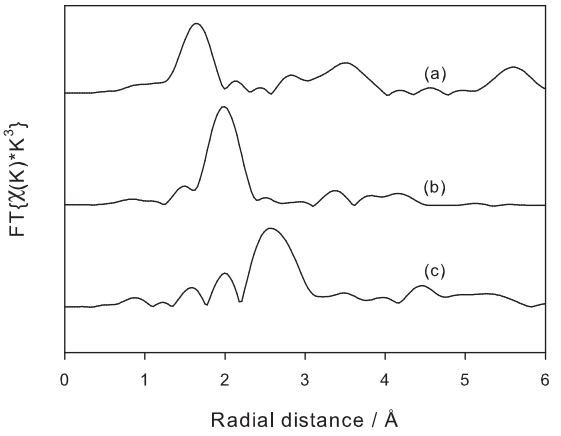

Figure 9.4: Radial Distribution function of (a) IrO_2- prepared following [102], (b) $IrCl_3.3H_2O$ - Alfa Aesar 99.9%, (c) Iridium black - Alfa Aesar 99.9%

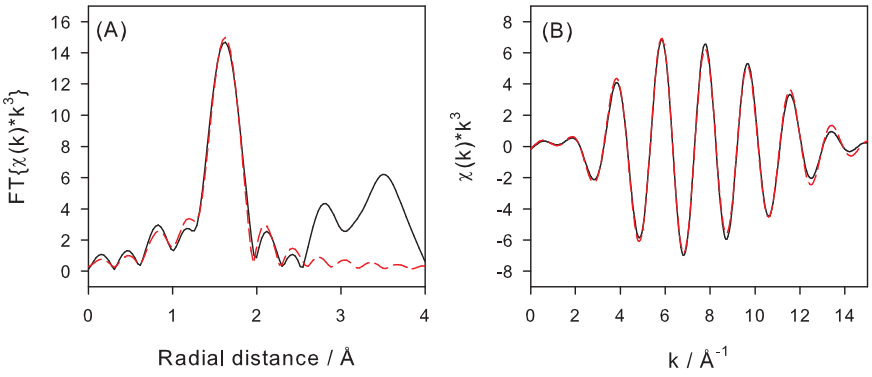

Figure 9.5: Curve fitting the Ir-O shells of IrO_2 standard, Solid line - data, Dotted line - Fit result, (A) FT EXAFS space (B) Back Transform space

Table 9.1: EXAFS fit results for IrO_2 standard material

Bond	N	S_0^2	R (Å)	σ^2 (Å)	ΔE_0 (eV)
IrO_2 standard					
Ir-O	2	0.735	1.96	0.001	14.8
Ir-O	4	0.735	1.99	0.002	14.8
IrO_2 theoretical					
Ir-O	2	-	1.959	-	0
Ir-O	4	-	1.995	-	0

white line energy does not show a clear trend with oxidation state as others have shown [120, 175, 178]. Mo *et al* revealed that electrochemically induced oxidation resulted in a positive shift in E_w of around 1 eV in going from Ir^{3+} to Ir^{4+} [120]. A positive shift of 0.7 eV was also seen for a range of iridium perovskite materials in which the iridium changed from Ir^{4+} to Ir^{6+} [175]. In our measurements, E_w shifted from 11216.1 to 11217.9 eV and E_0 from 11213.3 to 11214.5 eV on going from Ir^{3+} to Ir^{4+}. The difference between our Ir^0 and Ir^{4+} is smaller, with a change of 1.55 eV in E_w and 1 eV in E_0. The E_w of the iridium metal reference, which was recorded simultaneously during the sample measurements, revealed a small variance

between each measurement of around ± 0.2 eV, but this cannot explain the results found here. Unfortunately the absolute values of E_w and E_0 are not comparable with literature results, there exists a wide range of these values between various works (see [120, 175]). The reason that our Ir^{3+} has a E_w and E_0 lower than Ir^0 maybe because the XANES or in particular the E_0 and E_w are effected by more than just oxidation state. Clearly ligand and chemical environment play a significant role in the XANES regions [175, 178]. Unfortunately standards consisting of only iridium and oxygen with variable oxidation state do not exist. Another explanation could be the presence of higher valent iridium in the Ir^0 reference material. Surface oxidation of the metal may be possible due to the use of fine powder as the reference material. From the EXAFS analysis, we see small peaks on the RDF consistent with Ir–O and Ir–Ir distances in iridium oxide. This oxidation could occur at room temperature due to the small size of the powder grains (evidenced by the lack of strong long range order in the RDF). However this fact cannot completely account for the inconsistency in E_w and E_0 as the measured oxidation state is an average over the entire sample and it seems unlikely that surface oxidation would cause such a large increase in the apparent oxidation. Based on LC XANES, approximately 75 % of the iridium in the iridium metal standard would be have to be in a +4 oxidation state in order to give an apparent valance of +3, a level which would be very obvious in both the XANES profile shape and in RDF from the EXAFS. Clearly in this case such a level of oxidation is not possible and therefore, the inconsistency in E_w and E_0 with oxidation is assigned to the influence of ligand and chemical environment. Therefore to properly interpret any E_w and E_0 changes, the structural and chemical environment of the element must also be taken into consideration.

9.4.1 XAS of Ir-Sn oxides

The XANES profile and the RDF of the EXAFS data of IrO_2-SnO_2 prepared by Adams fusion and the modified Polyol method are shown in Figures 9.6 and 9.7. The aim of these measurements was to confirm the previous suggestion that the polyol method produces a homogenous single phase solid solution of the type $Ir_xSn_{1-x}O_2$, whereas the Adams fusion method produces a heterogenous oxide with at least two phases.

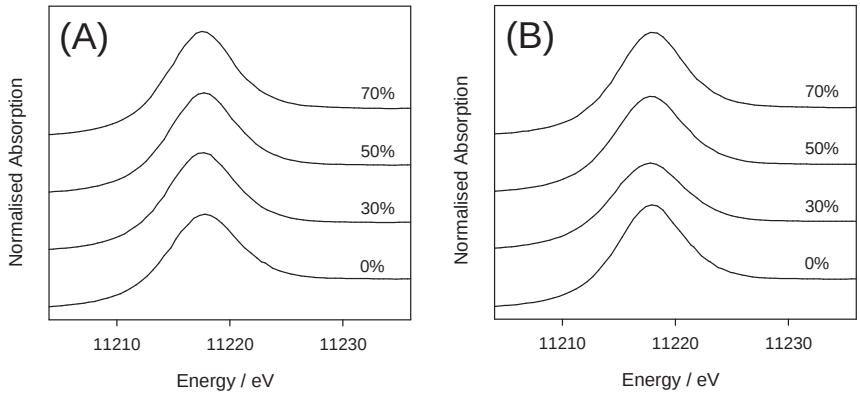

Figure 9.6: XANES of IrO_2-SnO_2 powders, (A) Polyol method, (B) Adams fusion method

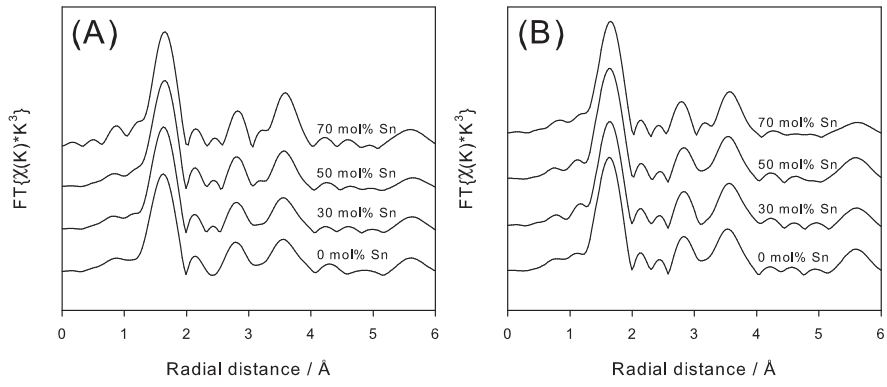

Figure 9.7: Fourier Transform of EXAFS for IrO_2-SnO_2 powders produced by the (A) Polyol method, (B) Adams fusion method.

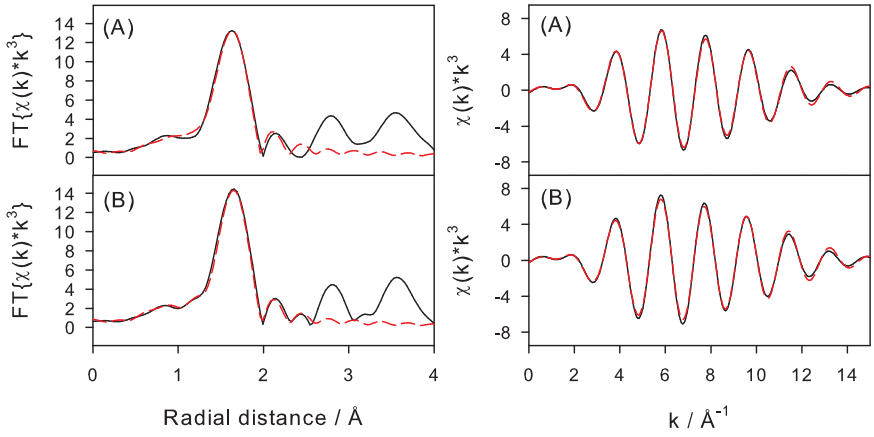

Figure 9.8: Curve fitting of IrO_2-SnO_2 powders produced by the Polyol method. (A) 100 mol% Ir, (B) 50 mol% Ir - 50 mol% Sn

Initial comparison of the XANES and EXAFS data reveals only small differences in the oxide samples as a function of the tin content. The Ir–O interatomic distance was estimated by fitting the first peak in the RDF to a single scattering path found from the theoretical scattering model (Figure 9.8). For this fitting, the two sub-shells distances were combined to a single peak with the coordination number set to 6. The results (Table 9.2) show that the Ir–O distance was found to be slightly increased at high tin content for both methods. In SnO_2 the Sn–O distance should be close to 2.05 Å, and therefore it is may be concluded that at high tin contents the Ir–O distance is not strongly affected by the SnO_2 lattice.

In order to evaluate the structure more closely, the iridium–metal distances should be evaluated. We find that the next group of peaks (those at 2.8 and 3.5 Å) in the RDF, which correspond to the Ir–metal distances, are very similar. A theoretical scattering model for $Ir_{0.5}Sn_{0.5}O_2$ was generated assuming that the tin atoms replace half the iridium atoms in the lattice. Two separate models were made with the difference between these models in the interatomic distances of iridium and tin. Model IrSn-1 assumed that the Ir–Sn distance was equal to Ir–Ir whereas model IrSn-2 assumed that the distance was an average between the Ir–Ir distance and the Sn–Sn distance

Table 9.2: EXAFS fit results for IrO_2-SnO_2 powder samples

Composition mol% Sn	M-O distance Å	σ^2 Å	ΔE_0 eV
Polyol method			
0	1.98	0.003	15.3
30	1.99	0.002	15.3
50	2.00	0.002	16.2
70	2.00	0.002	16.5
Adams fusion method			
0	1.99	0.002	16.2
30	1.99	0.002	16.3
50	1.99	0.002	16.4
70	2.00	0.002	16.9

in the pure oxides. The models were used to calculate a sum of all single scattering paths up to 4 Å from the core iridium atom. Figure 9.9 shows although the general shape of the Fourier transform magnitude is similar for each calculation, the peak position and relative intensity of the iridium–metal contributions are different tin is present in the iridium oxide lattice.

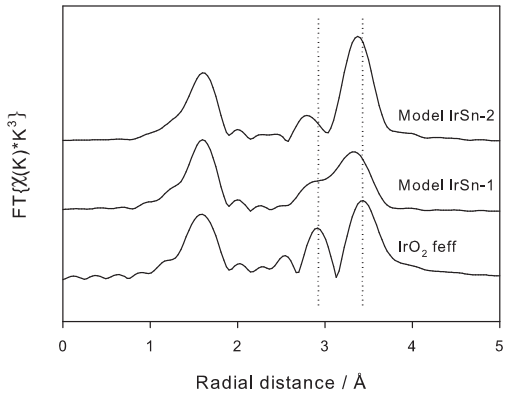

Figure 9.9: Fourier Transform of calculated EXAFS spectrum of IrO_2 and $Ir_{0.5}Sn_{0.5}O_2$ (refer to text for model descriptions)

This analysis leads us to believe that tin is not substituted into the iridium oxide unit cell in significant levels. This can then be used to suggest that previous conclusions based solely on XRD analysis, which suggested that the oxide prepared by the polyol method was a true solid solution (Chapter 4), are not likely to be correct. The previous XRD analysis was based on peak profiling, in which a single pseudo-Voigt profile was used to fit each diffraction peaks. This method of analysis is complex for broad diffraction patterns, as a number of peak combinations or even a single peak can fit the experimental data satisfactory. The EXAFS shows that the structure of the mixed iridium-tin oxides is not based on atomically mixed IrO_6^{2-} and SnO_6^{2-} octahedron, but rather show some preferential ordering in which like octahedra are bonded together. It is interesting however to note that the Ir–O bond length still shows a small increase as SnO_2 is added to the material, leading us to conclude that the presence of SnO_2 does affect the structure of IrO_2. As the polyol oxide shows clear increases in crystallinity and ordering as the tin content increases (Chapter 4 and the current EXAFS analysis), it is believed that this increase in bond length is due to the composition of the oxide rather than an effect caused by stoichiometry or disorder. This conclusion is reached based on that it is expected that as the oxide becomes more ordered or stoichiometric, the Ir–O bond lengths will tend towards the theoretical bond lengths.

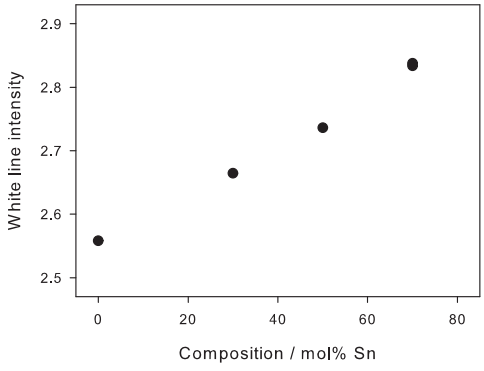

Figure 9.10: White line intensity of IrO_2–SnO_2

Analysis of the white line intensity reveals that the addition of tin also has some affect on the electronic state of the iridium, with a clear increase the

white line intensity as a function of the tin content (Figure 9.10). The white line occurs from transitions of $2p_{3/2}$ electrons to the unoccupied 5d states [6]. Therefore it seems reasonable to suggest that the presence of SnO_2 causes more holes in the Ir 5d5 orbital and thus a more intense white line is found.

An explanation of this finding could arise from a support effect (i.e. IrO_2 supported on SnO_2) as seen in other catalyst systems. For Pt supported materials, it has been shown that acidic supports cause the Pt to be electron deficient compared with neutral supports, which increases the white line intensity [179]. As we know that these oxides will contain significant levels of surface hydration, hydroxide species, as well as protons within the bulk [28, 180], it makes sense to discuss the acid/base properties of these oxides. Metal ions with high electronegativity withdraw electrons from these OH groups and therefore cause protons to be released. This implies that the acidity of metal oxide increases as the electronegativity of the metal increases. Using the Pauling scale [7], it is clear that SnO_2 will be more basic than IrO_2 and indeed the pzc and iep reveal this to be true [28]. Therefore the support effect (if it is present here) is different in nature than that described by Vaarkamp *et al* [179], which should probably be expected due to the differences between Pt metal and IrO_2.

For mixed oxides the total pzc or acidity will lie somewhere between that for the pure oxides [30, 31]. As these oxides contain water, it is likely that there may be some proton exchange between these oxides even if two separate oxide phases exist. As IrO_2 is more acidic than SnO_2, protons could be lost from the iridium oxide phase in a similar manner to the redox processes which occur during cyclic voltammetry [34]. Unlike this electrochemical exchange process, in which the white line energy increases [120, 181] due to valence change, the white line energy of these samples does not increase with tin content. Therefore it seems unlikely that the iridium valence increases, however the tin oxide may accept these protons from the hydrated iridium oxide (i.e. Ir oxy species acts as a Brønsted acid and the Sn species acts as a Brønsted base). As the oxy–hydroxide ligands bonded to iridium lose protons, the oxygen becomes more electronegative, thus causing the electron withdrawing effect seen in the XANES measurements. XPS measurements showed that the binding energy of Sn $3d_{5/2}$ increased as the content of SnO_2

[6] This 5d5 orbital can be described by two sub shells; t_{2g} and e_g. These sub shells can be either in the low spin state, $t_{2g}{}^5e_g{}^0$ (S = 1/2), or the high spin state, $t_{2g}{}^3e_g{}^2$ (S = 5/2).

[7] Electronegativity of Sn = 1.96, Ir = 2.20, O = 3.44 on the Pauling scaling

in a IrO_2–SnO_2 mixture increased (Chapter 4). At high tin contents the binding energy was consistent with Sn^{4+} in pure SnO_2. This indicated that iridium oxide causes an electron pushing effect towards the Sn species (i.e. At high iridium oxide contents the photoelectrons in the Sn $3d_{5/2}$ shell are more easily ejected). Although the XPS measurements only probe the surface of this oxide, some similarities with the present XANES measurements exist. At low tin contents there may be a lot of protons arising from the exchange with iridium oxy species and therefore the Sn 3d binding energy is reduced as the oxy-hydroxide ligands are more electropositive. From the EXAFS analysis, it was found that the average Ir–O bond length increased as the tin content increased. Given that the O^{2-} ion is larger than the OH^- ion [182], this bond length change is consistent with the proton exchange hypothesis described here. This result is also consistent with the findings by others who showed that the Ru–O bond length was decreased as the water content (and therefore presumably Ru–OH bonding) decreased [183].

This analysis, although somewhat speculative, points to the importance of acid-base properties in determining the electronic state of the elements in mixed oxides. For a long period, discussions by Trasatti have stressed the importance of pzc as a direct measurement of the specific surface state of oxide electrocatalysts without introducing the typical complications caused by surface area [28, 29, 9].

9.4.2 XAS of Ir-Ru oxides

XAS measurements were also carried out on IrO_2-RuO_2 prepared by a hydrolysis method. This oxides were largely amorphous oxides when rich in IrO_2 and crystalline when rich in RuO_2. From XRD analysis it was suggested that these oxides were a solid solution of the type $Ir_xRu_{1-x}O_2$. To confirm this, EXAFS was measured on the powder samples at the Ir LIII-edge (11 212 eV) and Ru K-edge (22 199 eV) in transmission mode.

Ir LIII-edge measurements

Figures 9.11 and 9.12 give the XANES profile and the Fourier Transform of the EXAFS spectrum, found from the measurements at the Ir LIII-edge. There are no significant differences in the XANES profiles indicating that

the valence and electronic state of the iridium remains constant as a function of composition. Unlike the IrO_2-SnO_2 samples, the white line intensity remains constant over the whole composition range. The EXAFS radial distribution function however shows that the structure of the shells immediately surrounding the central iridium atom change as ruthenium is added to the oxide. As the crystallinity of the oxide increases as ruthenium is added, the metal–metal radial distances become more prominent at high ruthenium contents due to the decrease in the variation in these interatomic distances as expected. Comparing the RuO_2 rich samples with the crystalline IrO_2 standard, shows that the changes in RDF are not only due to crystallinity or stoichiometry but also composition. It is clear that the main Ir–metal distance in the ruthenium rich samples is less than the Ir–Ir distance in IrO_2 This indicates that a true solid solution between IrO_2 and RuO_2 is formed. This analysis is consistent with Arikawa *et al* who also showed by EXAFS analysis of the Ir LIII-edge, that IrO_2–RuO_2 mixtures form solid solutions [118]. In their measurements, the first and second Ir–metal distance in RuO_2(80%)–IrO_2(20%) were around 0.3 and 0.2 Å shorter than the first and second Ir–Ir distances in their IrO_2 standard. In our analysis we find the main two Ir–metal distances in $Ir_{0.2}Ru_{0.8}O_2$ are both approximately 0.15–0.2 Å shorter than the Ir–Ir distances in our IrO_2 standard.

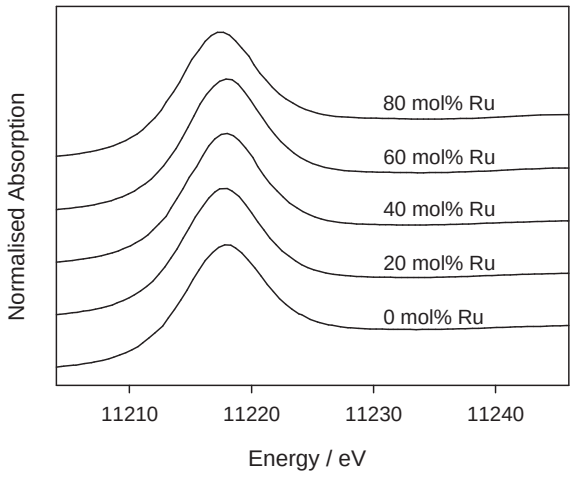

Figure 9.11: Ir LIII XANES of IrO_2-RuO_2 powders

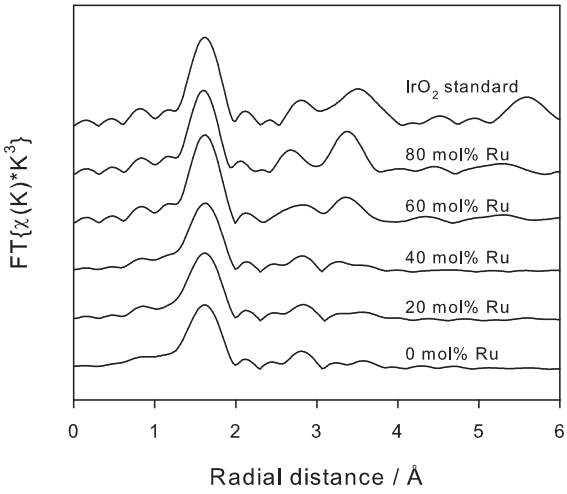

Figure 9.12: Fourier Transform of EXAFS for IrO_2-RuO_2 powders - Ir LIII-edge

The first shell in the EXAFS results was fitted to a single Ir–O bond with the oxygen coordination fixed at 6 (Figure 9.13). The results suggest that the bond length and disorder remain constant until 60 mol% Ru, after which the disorder decreases (Table 9.3). This is consistent with the sharp increase in crystallinity of the oxide phase at 60 mol% Ru. Understandablely, the bond length does not show any large change as M–O in both IrO_2 and RuO_2 are similar. The average Ru–O bond length should be around 1.97 for RuO_2 [183, 25].

Table 9.3: EXAFS fit results for IrO_2-RuO_2 powder samples - Ir LIII-edge

Composition mol% Ru	M-O distance Å	σ^2 Å	ΔE_0 eV
0	1.98	0.005	15.7
20	1.98	0.004	15.3
40	1.98	0.004	15.9
60	1.98	0.002	16.0
80	1.97	0.003	14.1

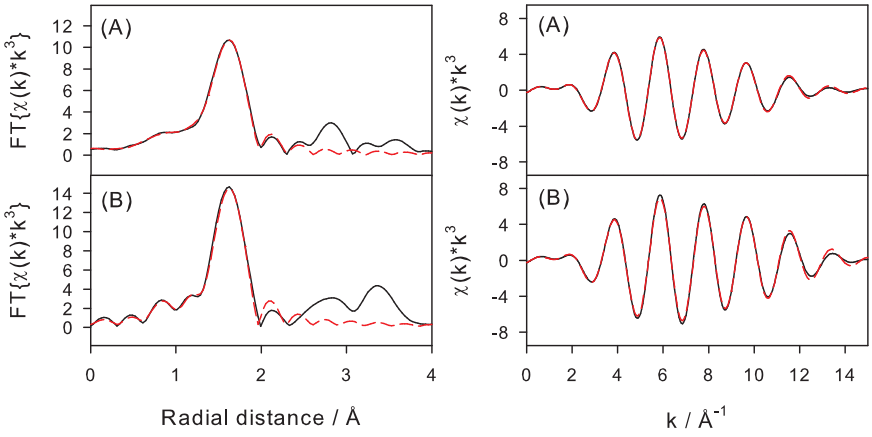

Figure 9.13: Curve fitting of IrO_2-RuO_2 powders (A) 100 mol% Ir, (B) 40 mol% Ir - 60 mol% Ru

Ru K-edge measurements

As with the iridium edge measurements, several ruthenium reference materials were measured and analysed. The data for anhydrous RuO_2 (Alfa Aesar 99.9%) and the fit results to the Ru–O shells are shown in Figure 9.14 with the parameters of the fit given in Table 9.4.

Table 9.4: EXAFS fit results for anhydrous RuO_2 standard material

Bond	N	S_0^2	R (Å)	σ^2 (Å)	ΔE_0 (eV)
RuO_2 standard					
Ru-O	2	0.813	1.94	0.003	1.8
Ru-O	4	0.813	1.98	0.003	1.8
RuO_2 theoretical					
Ru-O	2	-	1.942	-	0
Ru-O	4	-	1.984	-	0

Figures 9.15 and 9.16 show the XANES profile and the Fourier Transform of the EXAFS spectrum, found from the measurements at the Ru K-edge. Un-

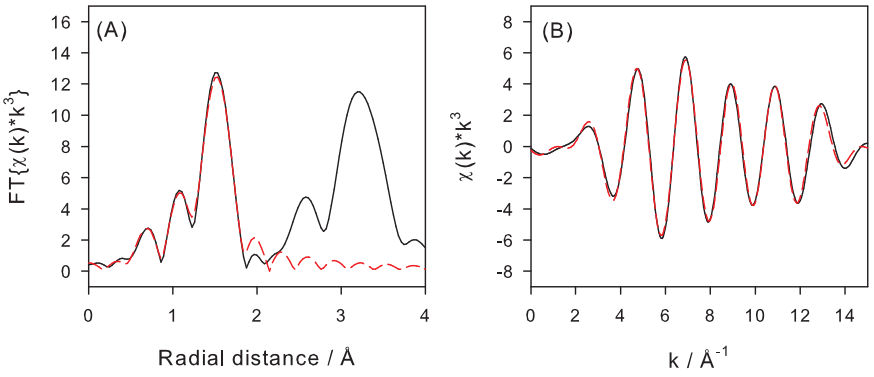

Figure 9.14: Curve fitting the Ru-O shells of anhydrous RuO_2 standard, Solid line - data, Dotted line - Fit result, (A) FT EXAFS space (B) Back Transform space

like the Ir LIII-edge measurements, it is difficult to see significant changes in the metal–metal atomic distances. This is mainly due to the fact that the high iridium content samples, which should reveal the most significant differences, are highly amorphous and therefore the samples have very poor Ru–metal peaks which cannot be used confidentially to show that there are iridium atoms neighbouring the probed Ru atoms. In truly amorphous materials there is a large degree of static disorder which hampers the XAS data analysis. In these cases it shows that even EXAFS analysis cannot be used to analyse structural details which are not within the first coordination shell. Ideally, to confirm that these IrO_2-RuO_2 powders are true solid solutions, the samples should be carefully heat treated to achieve sufficient long range ordering over the entire composition range. This would enable analysis of the structure from both the Ir LIII and Ru K edge, to show that RuO_2 is within the IrO_2 matrix and that IrO_2 is also within the RuO_2 matrix.

The Ru–O shell was fitted in a similar manner to the Ir LIII-edge measurements with the results tabulated in Table 9.5. At high RuO_2 contents the Ru–O bond length is close to the theortical value for pure RuO_2, and at high IrO_2 contents, the Ru–O bond length is slightly extended. Although this could be explained by the influence of IrO_2, others have shown that the

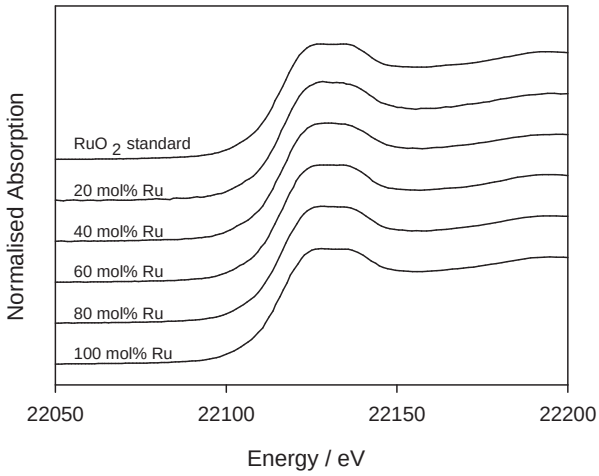

Figure 9.15: XANES of IrO_2-RuO_2 powders - Ru K-edge

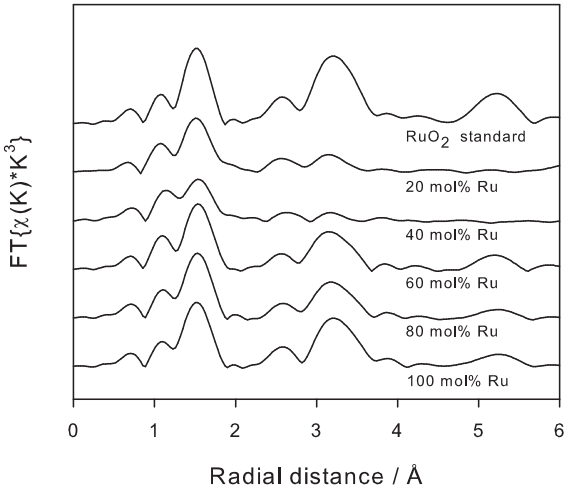

Figure 9.16: FT EXAFS of IrO_2-RuO_2 powders - Ru K-edge

Ru–O bond length can increase when the oxide is hydrated [183]. As the oxides rich in iridium are largely amorphous, it is expected that these oxides contain significant levels of hydration.

Table 9.5: Fit results for IrO_2-RuO_2 powder samples - Ru K-edge

Composition mol% Ru	M-O distance Å	σ^2 Å	ΔE_0 eV
100	1.98	0.004	3.3
80	1.98	0.004	4.0
60	1.99	0.004	5.5
40	1.99	0.004	5.4
20	1.99	0.006	5.1

9.5 Results - In-situ measurements

9.5.1 XAS of polarised amorphous IrO_2

An amorphous IrO_2 sample was prepared into an electrode and mounted into the in-situ cell. Cyclic voltammetry was performed between 400 and 1400 mV at 20 mV s^{-1} and as expected, the curve is quite featureless (Figure 9.17). After the cyclic voltammetry, the potential was fixed at potentials between 400 and 1400 mV while the full XAS data was recorded. The XAS measurements took approximately 45 minutes at each potential. Between some potentials, cyclic voltammetry was used to ensure no changes in the electrochemical surface occurred during the experiment period. At potentials above 1400 mV, excessive gas evolution caused some mechanical instability of the layer, making measurements at these potentials difficult. An example of the data recorded at the Ir LIII-edge while under potential control is shown in Figure 9.18 revealing that the data has a good signal to noise ratio up to around 10 $Å^{-1}$ even when weighted by k^3.

XANES of polarised amorphous IrO_2

As a major feature of noble metal oxide electrodes is the solid state redox transitions which arise through proton exchange with the electrolyte [61], it

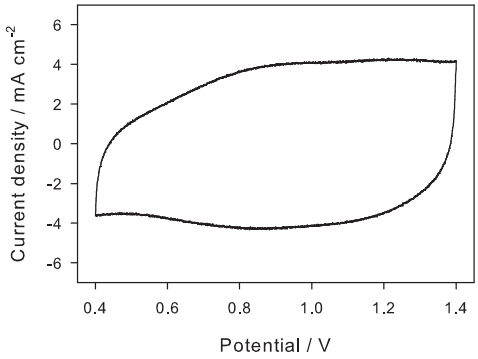

Figure 9.17: Cyclic voltammetry of amorphous IrO_2 at 20 mV s^{-1} in 0.5 M H_2SO_4

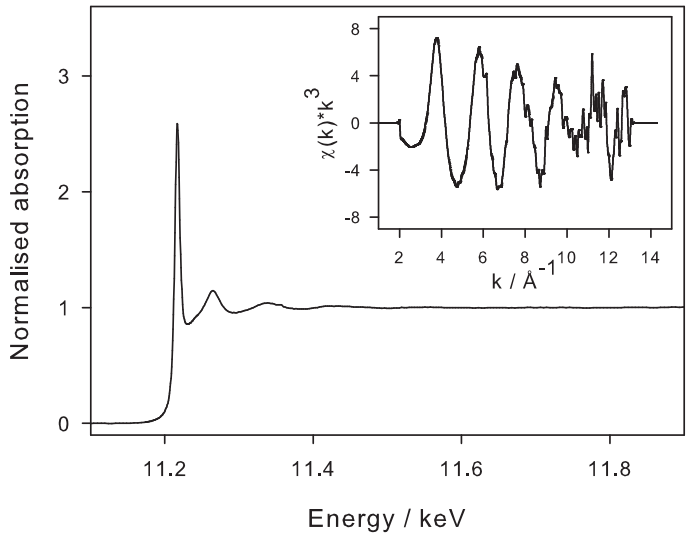

Figure 9.18: Experimental data of in-situ XAS of amorphous IrO_2 at 1.1 V, Insert: EXAFS in k-space

makes sense to firstly examine the XANES region as a function of electrode potential (Figure 9.19). No major shape changes over this potential range occur, indicating that the iridium is still coordinated to oxygen in a similar way to an un-polarised dry sample which was not exposed to electrolyte. There is however a difference in the E_0 and E_w of the polarised electrode and the "dry electrode". Clearly in the case of iridium oxide, the properties of the oxide electrode in the electrolyte are quite different from the "dry" oxide, indicating that the properties of the electrode surface[8] undergo significant changes depending on the environment (i.e. electrolyte and electrode potential) in which the oxide exists. Therefore to properly understand the oxygen evolution reaction and the electrocatalysis processes from an electrode structure point of view, one must also understand how the structure of the electrode changes with environment. This indicates that in-situ measurements are critical in any comprehensive study of electrocatalysts.

Few papers have examined the XANES of electrochemically polarised "iridium oxide", and it is believed that structure of the oxides used in these previous works are quite different from rutile structured IrO_2. In one of these previous papers, IrO_2 was electrochemically deposited onto Au coated polymer films from an iridium chloride electrolyte [120]. It is likely that the structure of that oxide will differ from the thermally prepared IrO_2 used in this work, as this oxide will be highly hydrated and have virtually no ordering beyond the first Ir–O shell [120]. The other works used anodically oxidised iridium films [184] and thin oxide films prepared by reactive RF sputtering [185], both of which will contain variable amounts of metallic iridium [120]. The dry oxide films prepared by reactive sputtering gave an average iridium valency of +3.3 [185] which is inconsistent with a pure IrO_2 structure even before any electrochemical processes occurred.

For electrodeposited IrO_x films, it was revealed that there was a linear increase of 1 eV in the E_w on going from 0.74 to 1.14 V vs RHE [120]. It was concluded that in 0.5 M H_2SO_4 the total valence change corresponded to around +1.2 for the potential window of 0.05–1 V vs. SCE [120]. In basic electrolyte, it was suggested that the iridium valence increased from +3 at -0.5 V vs. SCE to +5 at 0.4 V vs. SCE [120]. Hüppauff and Lengeler used a linear extrapolation based on iridium standard materials, to suggest that

[8] which is a large proportion of the total material in the case of these oxides, and therefore gives a significant XANES response

at 1.2 V vs. Ag/AgCl in 1 M H_2SO_4 the valence of iridium in an electrochemically oxidised Ir metallic film was +4.8 [184]. These two investigations represent hydrous oxides and from the discussions by Conway it is reasonable to expect a significant Ir valence change due to the pseudocapacitance which occurs in hydrous oxides of this nature [186]. In the work by Pauporte *et al*, there was no evidence to suggest that the sputtered iridium oxide films (which are less hydrous) contained iridium with oxidation states higher than +4 at similar potentials [185]. Similarly Stefan *et al* found no evidence to suggest RuO_2 films polarised at 1.05 V vs. RHE contained any Ru with an oxidation state greater than +4 [181].

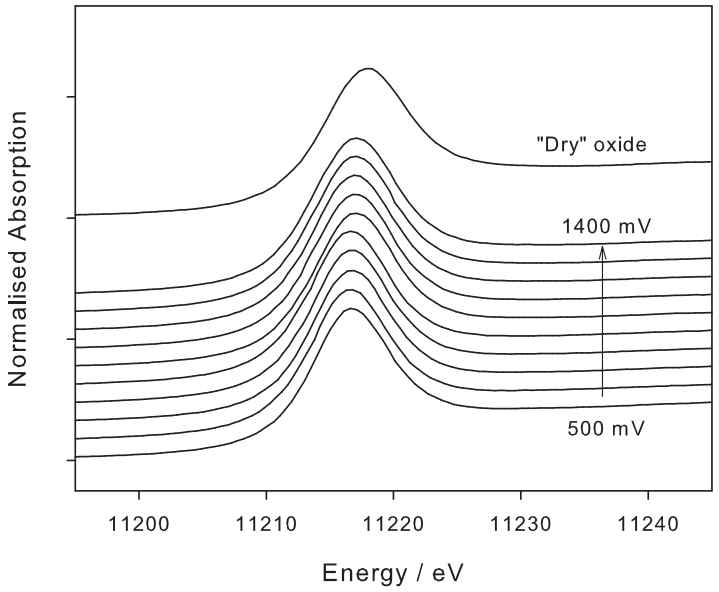

Figure 9.19: In-situ XANES of polarised amorphous IrO_2, 500-1400 mV at 100 mV intervals. Un-polarised "dry" IrO_2 XANES is also shown for reference

As others [120, 184, 185] have given the E_w (or valence) as a function of electrode potential, for comparison the E_w of the polarised IrO_2 electrodes used here have been given along with the anodic sweep portion of the cyclic voltammogram (Figure 9.20). Unlike the others who showed continuous

changes in E_w with potential [120, 184], the results here show that it is most likely that two distinct E_w levels exist (11216.6 eV for potentials 0.5–0.9 V and 11216.85 eV for potentials 1.0–1.4 V, thus ΔE_w= 0.25 eV). This suggests that between 0.9 and 1.0 V a change in the oxidation state of iridium occurs (probably $Ir^{3+} \rightarrow Ir^{4+}$). Although comparative analysis with the iridium standards should be treated carefully, based on the Ir^0 and the IrO_2 standard, ΔE_w for a single valence change is estimated to be around 0.39 eV. This would suggest that around 64 % of the iridium in the electrode undergoes valence change (and therefore is electrochemically active). From previously electrochemical measurements it is known that the capacitance of this oxide is on the order of 300 F g^{-1}. Using a capacitance–area constant for compact rutile surfaces of 60–80 μFcm^{-2} [127], the real surface area is estimated to be around 375–500 m^2g^{-1}. This value is not unreasonable and implies that the apparent active particle size is around 1–2 nm. Considering that protons have been detected at depths of 50 nm [180] it is feasible that the particle size can be much larger without any corresponding change in the iridium usage. From SEM analysis, the particle or agglomerate size of this oxide was estimated to be around 100 nm (Figure 8.7).

Another explanation for the change in E_w is that the white line profile actually consists two separate transitions[9] which are very close together, and that the relative intensity change of these transitions gives the E_w change. This may be resolved experimentally by using XANES measurements with less distance between the measured data points.

The white line intensity is also shown as a function of electrode potential (Figure 9.21). The white line intensity, which should reflect the average occupancy in the 5d electron orbital, shows an increase with potential over the entire potential range. Comparing the white line intensity change of the electrodes as a function of potential (ΔWLI = 0.11) and the change as a function of formal oxidation state from the iridium standards (ΔWLI = 0.088 / valence state), it is found that there appears to be some inconsistencies between the white line intensity and E_w. If the change in the white line intensity only occurred from the formal oxidation state of iridium, the total intensity change should be closer to 0.06 (i.e. 64 % of 0.088). This shows that there is a difference between the potential effect on the probability of 5d-orbital occupancy and the valence of the iridium. We know that as the

[9] e.g. Transitions from the $2p_{3/2}$ orbital to the t_{2g} and e_g orbitals

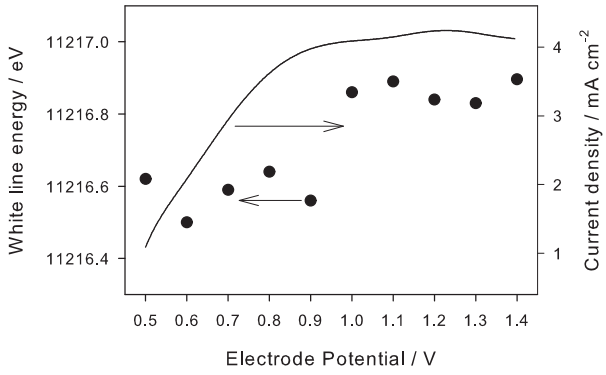

Figure 9.20: White line energy (•) and voltammetric anodic sweep at 20 mV s^{-1} (line) of polarised amorphous IrO_2

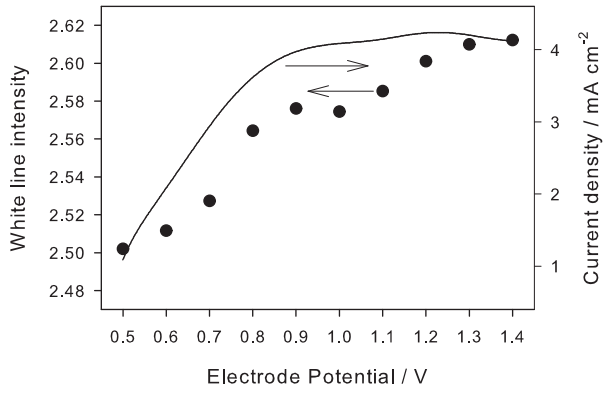

Figure 9.21: White line intensity (•) and voltammetric anodic sweep at 20 mV s^{-1} (line) of polarised amorphous IrO_2

potential is made more positive, there should be a greater positive charge on the oxide at the oxide–electrolyte interface. It is this charge which may account for the larger than expected change in the white line intensity.

Trasatti has reviewed the surface charging and adsorption process and concluded that the local charge on the oxide does not change significantly with potential due to the electrochemical uptake or release of protons [9]:

$$\mathrm{IrO_a(OH)_b} \rightleftharpoons \mathrm{IrO_{a+\delta}(OH)_{b-\delta}} + \delta\mathrm{H^+} + \delta\mathrm{e^-} \tag{9.2}$$

This is quite different from the effect of pH, where the surface charge is strongly effected by pH, as the oxide acts as a Brøsted acid or base [9]:

$$\mathrm{IrO_xO^-} + 2\mathrm{H^+} \rightleftharpoons \mathrm{IrO_xOH} + \mathrm{H^+} \rightleftharpoons \mathrm{IrO_xOH_2^+} \tag{9.3}$$

On thermally prepared RuO_x electrodes, it was shown that at 0.84 V vs. RHE the Cl^- adsorption decreased [187] indicating that the electrochemical transfer of protons does not fully compensate the charge increase caused by potential. It should be pointed out that ionic adsorption experiments on polarised electrodes are problematic due to the size of the electrode required in order to detect the small changes in the ion concentration as a function of electrode potential, and therefore such experiments have not been widely studied.

Here, the effective charge of the iridium atoms has been directly measured by the white line intensity, with more 5d occupancies as the potential is made more anodic, indicating that there is accumulation of positive charge. The fact that E_w remains constant may suggest that the valence of the iridium remains constant until 0.9–1.0 V at which an oxidation of the iridium occurs. The metal atoms in thermally prepared oxides should have quite similar properties, indicating that they should have a well defined oxidation potential. Thus, at low sweep rates or under potentiostatic control the iridium atoms should be oxidised within a narrow potential window. At higher sweep rates, we can expect a widening of this potential window due to diffusion related restrictions of the protons involved. The potential at which this valence change occurs based on our work (0.9–1.0 V) coincides closely with the redox potential for the Ir^{3+}/Ir^{4+} chloride couple (1.02 V [168]),

the IrO_2/Ir_2O_3 couple (0.926 V [188]) and anodic peak found on most IrO_2 voltammograms [7, 122, 129, 189, 152].

Therefore it appears that potential does cause an accumulation of charge on the oxide. This change in charge is suggested to be compensated by the chemical proton transfer or rearrangement of water in the double layer (i.e. only double layer capacitance), with the electrochemical discharge of protons and electrons (and therefore valence change) only occuring at a fixed and well defined potential. This brings into question whether the charging current seen during cyclic voltammetry of these thermally prepared oxides contains a significant level of pseudocapacitance or if it is nearly all derived from "normal" double layer capacitance. Conway has suggested that there maybe some differences between thermally and electrochemically produced oxides in terms of this question, and has suggested that pseudocapacitance becomes dominant when the oxides are highly hydrated [186].

EXAFS of polarised amorphous IrO_2

The Fourier Transform of the EXAFS measured on the polarised amorphous IrO_2 electrode is shown in Figure 9.22. As expected compared to the well ordered IrO_2 standard, the IrO_2 electrode only has weak peaks after the first Ir–O shell, indicating that the electrode materials is not well ordered beyond the first coordination sphere. Comparing the electrode measurements with the un-polarised sample, which is the identical material measured in tranmission mode without any electrolyte, it is interesting to see that the spectrum of the un-polarised sample (particularly the Ir–O bond) most resembles that of the electrode polarised at 1400 mV. As the "dry" powder will be close to the most stable form of iridium oxide (i.e. IrO_2), this comparison confirms that iridium in the electrode at 1400 mV will be primarily in the +4 oxidation state. The same is true for the IrO_2 standard.

It is also clear from this analysis that potential does affect the structure of the polarised electrode, with the Ir–O bond length decreasing continously as the potential is made more anodic. Also the intensity of the higher shells increases as the potential is increased, although even at 1400 mV the intensity of these peaks is still too low for any detailed discussion.

The first shell of the EXAFS data was fitted to the FEFF path for Ir–O with

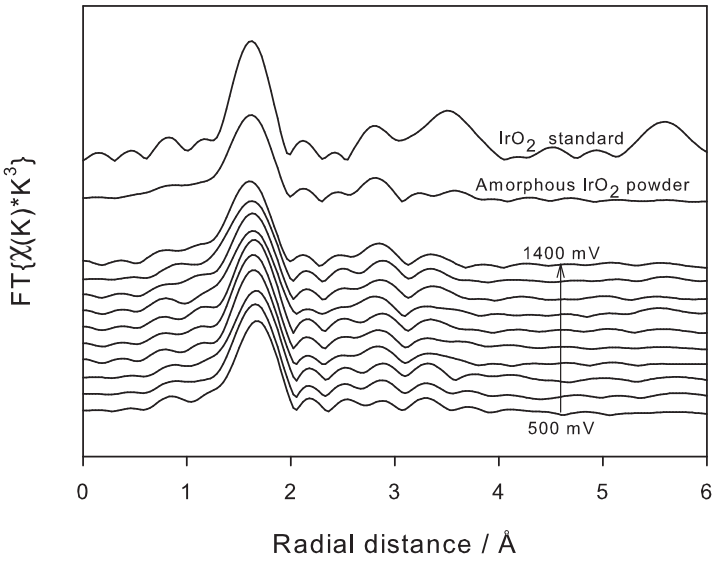

Figure 9.22: In-situ EXAFS of polarised amorphous IrO_2, 500-1400 mV at 100 mV intervals. The EXAFS of un-polarised amorphous IrO_2 and IrO_2 reference material is also shown

the coordination number set to 6. The fitting procedure was as described above. The results are tabulated in Table 9.6 and examples of the fit are given in Figure 9.23. From the fitting results, it is found that the Ir–O bond length decreases from around 2.03 to 1.98 Å on increasing the potential from 0.5 to 1.4 V (Figure 9.24). From the XANES measurements, it seems that the valence of the iridium increases from +3 (or really a mix of +3 and +4) to +4 between 0.9 and 1.0 V and that the electron vacancy increases continuously over the entire potential range examined. Thus the size of the iridium ion will decrease as the potential is made more positive and therefore the Ir–O bond length will also decrease.

Mo *et al* showed that for electrodeposited iridium oxide films the Ir–O bond decreased by 0.05 Å on going from 0.05 to 0.8 V vs. SCE [120]. Others have observed a maximum bond length decrease of 0.012 [184] and 0.05 [185] Å over a similar potential range. The size the iridium ions in the oxide

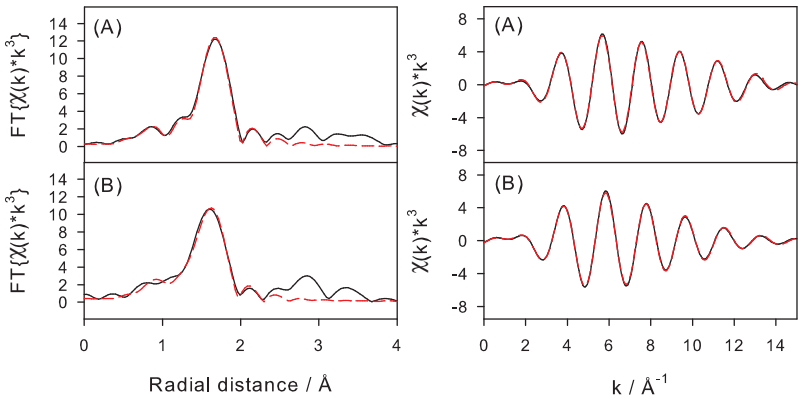

Figure 9.23: Fit results of the Ir–O shell of polarised IrO_2 in FT and BT space, Solid line - data, Dotted line - Fit result, (A) 500 mV (B) 1400 mV

Table 9.6: Fit results for polarised amorphous IrO_2 - Ir LIII-edge

Potential V vs RHE	M-O distance Å	σ^2 Å	ΔE_0 eV
0.5	2.03	0.003	15.41
0.6	2.02	0.003	14.59
0.7	2.02	0.004	15.57
0.8	2.01	0.003	15.22
0.9	2.01	0.003	15.10
1.0	2.01	0.004	16.21
1.1	2.01	0.004	16.18
1.2	2.00	0.004	15.77
1.3	1.99	0.004	15.98
1.4	1.98	0.005	15.08

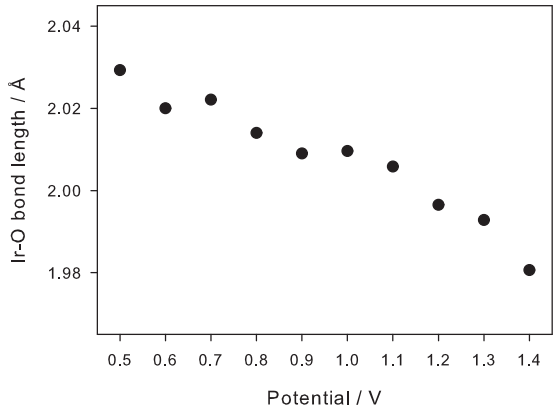

Figure 9.24: Ir–O bond length of polarised IrO_2

environment have been calculated to be 0.645–0.671 Å (for Ir^{3+}) and 0.575–0.624 Å (for Ir^{4+}) [185, 184]. Shannon has also given the ionic radius of Ir^{3+} and Ir^{4+} as 0.68-0.73 and 0.625-0.63 Å respectively [190, 182]. More recently the ionic radii of various ions have been calculated and suggests that the change in theoretical ionic radius (for $Ir^{3+} \rightarrow Ir^{4+}$) is a lot smaller (0.014 Å) than that estimated from experimental results [191]. The size of the oxide ion (O^{2-}) is given as 1.38 Å and the hydroxide ion (OH^{-}) as 1.35 Å [182].

Overall as the valence of the iridium increases from +3 to +4, the reduction in cation size corresponds to a Ir–O bond decrease of between 0.05 and 0.1 Å, and if only 64 % of the iridium undergoes this valence change the observed bond length change will be 0.032–0.064 Å. In the results presented here, the total bond length change is 0.05 Å which shows that the usage and bond length findings are in good agreement with the expected results. From the work of Mo *et al*, the change of 0.05 Å measured here would indicate that 100 % of the iridium is involved in the redox processes [120]. It seems unlikely that 100 % of the iridium is electrochemically active, and the analysis and conclusions of Mo *et al* were based on the assumption that at the 0.05 V vs. SCE, 100 % of the iridium in their electrodes was in the +3 state.

It is interesting to check the oxygen coordination number based on these radii

with the Pauling's rule 1 of coordination polyhedron[10]. For an octahedral coordination the limiting radius ratios are $0.732 > r+/r- > 0.414$, where r+ and r- are the ion radii of the cation and anion respectively. From these guidelines it seems reasonable to assume that both the Ir^{3+} and Ir^{4+} ions will be coordinated by 6 oxygen atoms.

9.5.2 Final comments and suggestions

The results presented here show without doubt that there is a bond length and probably an iridium valence change as a function of electrode potential. These results are in quite good agreement with the other works in this field and indicate that such measurements can be made successfully on powder based iridium oxide electrodes prepared by wet chemical methods.

The study of oxide electrodes where the oxide has different levels of crystallinity are expected to reveal two important aspects of these electrocatalysts. Firstly it is clear that in amorphous oxides, a large portion of the oxide is electrochemically active and therefore surface structure changes due to potential are detectable. For oxides with larger crystals, one will determine whether the observed changes are solely surface effects or also involve some of the bulk. Such analysis should be combined with electrochemical charge analysis (using CV) to determine what proportion of the oxide is really involved in the electrochemical reactions. This may also give insights into the pseudocapacitance phenomenon which are suggested to occur on these oxides.

XAS analysis of the potential effect on the mixed oxides, particularly those with "inert" components may reveal important features which relate to the interaction of the cations present in the oxides. By analysis of the "inert" component, it may be possible to determine whether both metals are electrochemically active or if only the active oxide takes place in the electrochemical processes. This relates directly to electrocatalytic synergy which is an important and interesting aspects of electrocatalysis. Also by comparing the structural and electronic properties of mixed oxides during O_2

[10] Pauling's rule 1 of coordination polyhedron: *"The coordination polyhedron of anions formed around every cation will only be stable if the cation is in contact with each of its neighbours"*

evolution with the specific electrocatalytic activity of these oxides, empirical structural–activity relationships may be derived.

9.6 Conclusions

The structural and electronic properties of various oxygen evolution electrocatalysts have been examined using X-ray absorption spectroscopy. Ex-situ results revealed that for the IrO_2-SnO_2 there was no evidence to suggest that Sn was closely coordinated to the Ir. However additions of tin did result in changes to the electronic structure of the iridium atoms. In the IrO_2-RuO_2 there was some evidence for "atomic" mixing of the two metals with changes in the Ir–metal coordination shells most likely arising from Ir–Ru coordination.

A new in-situ XAS cell was developed during this work, and in-situ XAS measurements were successfully recorded in fluorescence mode on electrocatalysts under potential control in aqueous 0.5 M H_2SO_4 electrolyte. The preliminary results from this work confirmed the importance of in-situ structural characterisation, with the electronic properties of IrO_2 as measured by XANES, showing differences depending on whether the oxide was dry or emersed in aqueous electrolyte. The effect of potential on the XANES region was also clearly seen, with an increase in the d-orbital vacancies found as the potential was made more anodic. Evidence was also found to suggest that the iridium atoms undergo an oxidation between 0.9 and 1.0 V vs. RHE. The Ir–O bond length was found to decrease by around 0.05 Å as the potential increased from 0.5 to 1.4 V vs RHE. Overall it is believed that XAS can provide useful information regarding electrocatalyst development and it is strongly suggested that in-situ XAS measurements become part of regular electrocatalyst structural analysis.

Acknowledgments

Associate Professor Magnus Rønning at the Department of Chemical Engineering, NTNU, contributed a great deal to the work discussed in this chapter. His help with organising and running the experiments is very much

appreciated. Discussions with Magnus were also useful in the design of the in-situ XAS electrochemical cell. Nina Hammer, Dr Sten Egil Johnsen, and Dr Mikhail Tsypkin are also thanked for helping with the measurements while in Grenoble and for discussions while processing data in the afterwards. The staff at the Swiss-Norwegian beamline are also acknowledged for their support of these experiments and their willingness to try out the "unproven" electrochemical cell. The financial support of this work from the Norwegian Research Council and Norsk Hydro ASA is also acknowledged.

Chapter 10

Conclusions

The following will give a summary of the conclusions from this work. This is intended to give an overall view of the results from the aspect of electrocatalyst development and characterisation.

10.1 Preparation of electrocatalysts

The preparation of electrocatalyst for PEM applications is a complex and demanding task. Although there exists many synthesis methods and a lot of literature discussion, without understanding the structural implications of the synthesis method, misleading conclusions can be made. From the experience gained during this work, some conclusions can be made regarding electrocatalyst synthesis and development:

- Synthesis method should be applicable to a range of electrocatalyst compositions
- A range of controllable synthesis variables are helpful
- Highly reproducible results are important
- High level of electrocatalyst homogeneity is beneficial

It was found that to understand how the structure and other properties of the electrocatalyst were affected by the synthesis method, it was often best

to examine how a trend in a measured property varied with electrocatalyst composition. This implies that the synthesis method should be suitable for a range of compositions so that these trends can be followed easily. An example of this, was that the addition of SnO_2 to IrO_2 caused the crystallinity of the material to increase, resulting in a reduction in the active surface area. Without this trend one could assign the loss in active area with only the dilution effect of SnO_2 addition and not a combination of the dilution and crystal size effects.

The addition of tantalum when using the polyol method, was found to extremely reduce the active area of the synthesised electrocatalyst due to strong surface segregation of tantalum. This meant that effect of tantalum on iridium oxide based materials could not be examined when using this method as the electrocatalysts were effectively non-active even at very low tantalum contents. This was solely due to the synthesis method (and its affect on structure) and not directly related to the actual composition as the hydrolysis method showed that tantalum could be added to iridium oxide without causing large performance losses in a PEM water electrolysis cell. This result clearly shows that importance of the electrocatalysts structure and how this affected by the synthesis method. Another conclusion which can be made from this example is the importance of controllable variables. As the method clearly affects the structural properties of the electrocatalyst, by controlling a range of synthesis variables it should be possible to tailor the structure of the prepared materials. This however leads to another important conclusion, in that the synthesis method must give reproducible results. Without reproducibility, the structural and electrocatalytic properties will not give a true representation of the effect of the variable under investigation.

The last conclusion regarding the preparation of electrocatalyst is one which simplifies the characterisation of the prepared materials. A high level of homogeneity will ensure that the measured electrocatalytic properties is a response which is specific to one structure and not some average of multiple structures. This enables the relationship between various properties to be understood more precisely.

10.2 Characterisation of $Ir_xSn_{(1-x)}O_2$ electrocatalysts

$Ir_xSn_{(1-x)}O_2$ electrocatalysts were investigated to evaluate how SnO_2 additions affect the electrocatalytic and structural properties of the electrocatalyst powders. It was found that the crystal properties of $Ir_xSn_{1-x}O_2$ powders, depend on the method used to prepare such materials. Adams fusion method results in an oxide consisting of at least two separate oxide phases, with one of these containing mostly SnO_2. From XRD analysis it was concluded that the modified polyol method enables the formation a solid solution between iridium and tin oxide, with the lattice parameters increasing linearly with tin content. Addition of tin also causes the average crystal size to increase from around 3.5 to 15 nm. XPS clearly showed that iridium was present in at least 2 valence states while the tin was only present in a single valence state corresponding with the binding energy of Sn^{4+} at high tin contents. The properties of these materials vary with the annealing temperature range examined, with the main differences ascribed to crystallisation and stability of the oxide. At 650 °C there was evidence that the proposed solid solution phase is only metastable, with segregation of at least two separate oxide phases and a metallic iridium phase occuring at this temperature. As expected the electrical resistivity of these oxides increased significantly as tin was added. Overall, $Ir_{0.25}Sn_{0.75}O_2$ powders exhibited a resistivity around 3 orders higher than IrO_2. By making simple estimations of possible ohmic losses in a PEM water electrolyser, it is suggested that the limit for tin addition is 50–60 mol%. EXAFS analysis revealed that the presence of tin caused the Ir–O bond length to increase, although there was no evidence to suggest that tin was located within the immediate coordination shells around iridium. The XANES analysis suggested that as SnO_2 was added to IrO_2, there was more d-orbital vacancies in the iridium atoms.

The electrochemical properties of the oxides prepared by the polyol method, showed that the addition of SnO_2 to IrO_2 particles had no beneficial effect other than dilution of the more expensive iridium oxide at all the examined current densities. Cyclic voltammetry, shows that the active area decreases as the tin content increases. Additions of up to 20 mol% tin may be acceptable as little change in the active area occurs at low tin contents, however there was still a 40 mV increase in cell voltage at 1 A cm^{-2} and 80 °C in

a PEM water electrolyser. The specific activity of the oxides prepared by the polyol method remains constant until 50–60 mol% tin whereafter the activity decreases. Overall, the electrocatalytic properties in 0.5 M H_2SO_4 and a PEM cell are similar, however there is evidence to suggest that there are extra resistance issues in the PEM cell due to the poor conductivity of some of the prepared oxides. The effect of anode composition on the PEM cell ohmic resistance confirmed that high tin contents causes high performance losses due to poor layer conductivity. Polarisation analysis in 0.5 M H_2SO_4 showed that the increasing the annealing temperature of $Ir_{0.6}Sn_{0.4}O_2$ decreased the active surface area. There was no evidence to suggest that the specific activity of this oxide is affected by the annealing temperature over the range examined. The best PEM cell performance was achieved with a pure IrO_2 anode giving 1.61 V at 1 A cm^{-2} and 90 °C.

10.3 Characterisation of $Ir_xRu_ySn_zO_2$ electrocatalysts

Addition of ruthenium to iridium-tin oxides for oxygen evolution electrocatalysts was examined using the modified polyol method. Firstly the addition of ruthenium causes less tin to be present in the final oxide, indicating that ruthenium somehow adversely effects the reaction of the tin precursor in polyol. Strong agglomeration of the ruthenium colloids was also observed, leading to the formation of a metallic ruthenium phase in the final oxide. Cyclic voltammetry and XPS analysis show that the surface is enriched in tin with very little ruthenium present at the surface of the particles. This meant that the active area decreased considerably as the iridium was replaced by ruthenium and was approximately proportional to the surface concentration of noble metals. The specific electrocatalytic activity, free from the effect of surface area, increased as ruthenium replaced the iridium. As there was little ruthenium at the surface of the electrocatalyst powders, it is believed that this finding indicates that the activity of the non–ruthenium surface elements is enhanced. XPS revealed that the electronic properties of the surface iridium was seen to change as a function of the bulk ruthenium content. These electronic changes may explain the enhanced electrocatalytic activity found during the electrochemical measurements. Overall at low current densities in 0.5 M H_2SO_4, the best electrocatalytic performance is found at interme-

diate ruthenium contents (i.e. an optimum between active area and specific activity), with the low current performance of the Ir-Ru-Sn oxides similar to pure IrO_2 electrodes. Therefore an electrocatalyst with equal or better performance than pure IrO_2 can be produced with considerably less cost.

10.4 Characterisation of $Ir_xRu_yTa_zO_2$ electrocatalysts

Additions of tantalum to noble metal oxide electrodes is common in the DSA industry, and therefore such additions were also examined here. The $Ir_xRu_yTa_zO_2$ powders for these measurements were prepared via an aqueous hydrolysis route, as both the polyol and Adams method were found to be unsuitable. The resulting oxide powders were normally highly amorphous, with any crystalline material thought to be a solid solution between IrO_2 and RuO_2. EXAFS analysis showed that for the Ir-Ru oxides, ruthenium was closely coordinated to iridium, which is consistent with the conclusions found from XRD. Both XRD and EXAFS revealed that oxides with high levels of ruthenium contained well ordered crystals. The active surface area of the materials decreased at high ruthenium contents, which is most likely due to the increased crystallinity of these materials. Likewise the Tafel slope increased at high ruthenium contents, which again was contributed to the increase in crystallinity. The specific activity showed that tantalum played little role in the oxygen evolution reaction, and that the presence of ruthenium improved the specific activity probably due to the larger exchange current density of RuO_2 in comparison with IrO_2. In a PEM water electrolysis cell, high performance was obtained for anode materials containing 20-40 mol% Ru and 0-20 mol% Ta. The best result was obtained with an $Ir_{0.6}Ru_{0.4}O_2$ anode and 20 wt% Pt/C cathode, with a cell voltage of 1.567 V at 1 A cm^{-2} and 80 °C when using Nafion 115 as the electrolyte membrane. This equates to a cell efficiency of 76 % ($\varepsilon_{\Delta G}$) and an energy consumption of 3.75 kWhr Nm^{-3} H_2 at 1 A cm^{-2}.

10.5 Characterisation of electrocatalysts using X-ray Absorption Spectroscopy

The structural and electronic properties of various oxygen evolution electrocatalysts was examined using x-ray absorption spectroscopy. Ex-situ results revealed that there are changes in the Ir–O bond length occured with IrO_2 was mixed with other oxides. For IrO_2-SnO_2 there was no evidence to suggest that Sn was closely coordinated to the Ir. In the IrO_2-RuO_2 there was some evidence for "atomic" mixing of the two metals with changes in the Ir–metal coordination shells most likely arising from Ir–Ru coordination.

The main aim of this work was to make in-situ structural measurements while the electrocatalysts were under potential control in aqueous 0.5 M H_2SO_4 electrolyte. A new in-situ XAS cell was developed for this work, and in-situ XAS measurements were successfully recorded in fluorescence mode. The preliminarily results from this work confirmed the importance of in-situ structural characterisation, with the electronic properties of IrO_2 as measured by XANES, showing differences depending on whether the oxide was dry or immersed in aqueous electrolyte. The effect of potential on the XANES region was also clearly seen, with an increase in the d-orbital vacancies found as the potential was made more anodic. Evidence was also found to suggest that the iridium atoms undergo a one-electron oxidation between 0.9 and 1.0 V vs. RHE. The Ir–O bond length was found to decrease by around 0.05 Å as the potential increased from 0.5 to 1.4 V vs RHE. Overall it is believed that XAS can provide useful information regarding electrocatalyst development. Investigations using in-situ XAS is strongly recommended for future electrocatalysis development and characterisation.

Chapter 11

Suggestions for further work

11.1 Electrocatalyst development

Noble metal oxide electrocatalysts are clearly active for the oxygen evolution reaction. To further develop these electrocatalysts several approaches can be suggested. Two main goals should be defined: to increase the specific activity of the oxide particles and to increase the surface area of the active phase. These might be achieved by:

- Supporting active oxides on inert materials in a similar fashion to Pt/C fuel cell electrocatalysts
- Doping the oxides with a range of transition metals
- Using sol-gel technology to control particle growth
- Using a combinatorial approach to screen many compositions

It seems sensible to continue work on the oxygen evolution electrocatalyst, but it may also be useful to examine the development of some new hydrogen evolving electrocatalyst especially those based on non-platinum materials.

11.2 Electrochemical measurements

A major aspect of this work was the separation of the specific electrocatalytic activity and active area of the prepared electrocatalysts. This approach should be continued so that the "cause" of electrocatalytic activity can be elucidated. A combinatorial approach to electrocatalyst screening would be useful, as there is currently few ways to develop electrocatalysts without the use of "trial and error" which results in a large number of electrocatalyst compositions. Electrochemical impedance spectroscopy may prove to be a valuable method for future work, particular in understanding the properties of electrocatalytic layers and the pseudocapacitance process on noble metal oxides. Rotating disc and ring-disc measurements may be useful for analysis of the oxygen evolution reaction on new electrocatalytic materials. In particular the identification / analysis of reaction intermediates could help in areas such as the understanding of the oxygen evolution mechanism on new materials and possible cause of problems connected with electrocatalyst and cell instability.

11.3 Spectroscopic and other measurements

Combining spectroscopic measurements (e.g. XRD, XPS, XAS, Raman) with electrochemical measurements is strongly suggested as a valuable way of improving the knowledge of electrocatalysis. In particular in-situ spectroelectrochemical measurement can give information of the electrocatalyst structure and reaction intermediates under conditions similar or even identical to the real operating conditions of a water electrolysis cell. In-situ XAS may enable the cause of oxygen evolution electrocatalysis to be found by following electronic and structural changes as a function of electrode potential and electrocatalyst composition, and comparing this to measures of specific electrocatalytic activity. The electrical conductivity properties of these oxides have been accessed from a basic comparative perspective, but a more comprehensive study including the use of methods in which semi-conducting properties can be determined would be beneficial in further studies. Methods such as point of zero charge measurements and agglomerate size analysis would be very interesting and important when considering the surface nature of new electrocatalysts.

11.4 PEM water electrolysis cell testing and development

Although the majority of the work in this thesis was concerned with electrocatalyst development and characterisation, some suggestions related to PEM water electrolysis cells and PEM catalytic layers can be made. The effect which the catalyst layer composition has on the layer structure is unknown. The importance of various layer properties are also unknown from a quantitive point of view. As these layers normally are prepared via ink dispersions, by studying these dispersions, advances in catalytic layer preparation and understanding may be made. A related issue is the interface between the titanium sinter and the catalytic layer and how this affects aspects such as mass transport and electronic resistance. Currently little is known regarding the electronic pathways in the catalytic layer and how the structure of the catalytic layer influences this.

A more technological suggestion is to study the stability and performance of cells and stacks under real operating conditions. This may highlight new areas of research which are important for the development of commercial PEM water electrolysis technology.

Bibliography

[1] M. Peavey. *Fuel from water energy independence with hydrogen.* Merit Products, 2003.

[2] R. Oberlin and M. Fischer. Status of the membral process for water electrolysis. In T. Veziroglu, N. Getoff, and P. Weinzierl, editors, *Hydrogen Energy Progress VI, Proceedings of the 6th World Hydrogen Energy Conference*, pages 333–340. Pergamon Press, 1986.

[3] Y. Nishimura, K. Yasuda, Z. Siroma, and K. Asaka. High current density solid polymer electrolyte water electrolysis. *Denki kagaku oyobi kogyo butsuri kagaku*, 65:1122–1123, 1997.

[4] P. Millet, F. Andolfatto, and R. Durand. Design and performance of a solid polymer electrolyte water electrolyzer. *Int. J. Hydrogen Energy*, 21:87–93, 1996.

[5] M. Tsypkin, E. Lyutikova, V. Fateev, and V. Rusanov. Catalytic layers in a reversible system comprising an electrolyzing cell and a fuel cell based on solid polymer electrolyte. *Russ. J. Electrochem.*, 36:545–548, 2000.

[6] J. Divisek. Water electrolysis in a low- and medium-temperature regime. In H. Wendt, editor, *Electrochemical Hydrogen Technologies*, pages 137–. Elsevier Publishing Company, 1990.

[7] E. Rasten. *Electrocatalysis in Water Electrolysis with Solid Polymer Electrolyte.* PhD thesis, NTNU, Trondheim, Norway, 2001.

[8] D. Ohms, V. Plzak, S. Trasatti, K. Wiesener, and H. Wendt. Electrode kinetics and electrocatalysis of hydrogen and oxygen electrode

reactions. In H. Wendt, editor, *Electrochemical Hydrogen Technologies*, pages 1–12. Elsevier Publishing Company, 1990.

[9] S. Trasatti. The oxygen evolution reaction. In H. Wendt, editor, *Electrochemical Hydrogen Technologies*, pages 104–135. Elsevier Publishing Company, 1990.

[10] S. Trasatti. Electrocatalysis in the anodic evolution of oxygen and chlorine. *Electrochim. Acta*, 29:1503–1512, 1984.

[11] P. Rasiyah and A. Tseung. The role of the lower metal oxide/higher metal oxide couple in the oxygen evolution reactions. *J. Electrochem. Soc.*, 131:803–808, 1984.

[12] Y. Matsumoto and E. Sato. Electrocatalytic properties of transition metal oxides for oxygen evolution reaction. *Mater. Chem. Phys.*, 14:397–426, 1986.

[13] M. Gattrell and B. MacDougal. Reaction mechanisms of the O_2 reduction/evolution reaction. In W. Vielstich, H. Gasteiger, and A. Lamm, editors, *Handbook of Fuel Cells: Fundamentals, Technology and Applications*, volume 2, pages 443–464. John Wiley and Sons Ltd., 2003.

[14] S. Mukerjee, S. Srinivasan, M. Soriaga, and J. McBreen. Role of structural and electronic properties of Pt and Pt alloys on electrocatalysis of oxygen reduction. An in situ XANES and EXAFS investigation. *J. Electrochem. Soc.*, 142:1409–1422, 1995.

[15] J. Bockris. Kinetics of activation-controlled consecutive electrochemical reactions: anodic evolution of oxygen. *J. Chem. Phys.*, 24:817–827, 1956.

[16] S. Trasatti and G. Lodi. Oxygen and chlorine evolution reactions on conductive metallic oxide anodes. In S. Trasatti, editor, *Electrodes of Conductive Metallic Oxides Part B*, page 521. Elsevier scientific publishing company, 1980.

[17] A. Riddiford. Mechanisms for the evolution and ionization of oxygen at platinum electrodes. *Electrochim. Acta*, 4:170–178, 1961.

[18] A. Damjanovic, A. Dey, and J. Bockris. Kinetics of oxygen evolution and dissolution on platinum electrodes. *Electrochim. Acta*, 11:791–814, 1966.

[19] B. Conway and M. Salomon. Electrochemical reaction orders: Applications to the hydrogen- and oxygen-evolution reactions. *Electrochim. Acta*, 9:1599–1615, 1964.

[20] B. Conway. The temperature and potential dependence of the electrochemical reaction rates, and the real form of the Tafel equation. In B. Conway, R. White, and J. Bockris, editors, *Modern Aspects of Electrochemistry*, volume 16, pages 103–185. Springer, 1986.

[21] A. Bell. The impact of nanoscience on heterogeneous catalysis. *Science*, 299:1688–1691, 2003.

[22] G. Blyholder. Metal-support interaction: A theoretical approach. *J. Mol. Catal. A: Chem.*, 119:11–17, 1997.

[23] S. Gottesfeld and T. Zawodzinski. Polymer electrolyte fuel cells. In R. Alkire, H. Gerischer, D. Kolb, and C. Tobias, editors, *Advances in Electrochemical Science and Engineering*, volume 5, pages 197–298. John Wiley and Sons Ltd, 1997.

[24] J. Honig. Electronic band structure of oxides with metallic or semiconducting characteristics. In S. Trasatti, editor, *Electrodes of Conductive Metallic Oxides*, pages 1–96. Elsevier scientific publishing company, 1980.

[25] S. Trasatti and G. Lodi. Properties of conductive transition metal oxides with rutile-type structure. In S. Trasatti, editor, *Electrodes of Conductive Metallic Oxides*, pages 301–358. Elsevier scientific publishing company, 1980.

[26] D. Rogers, R. Shannon, A. Sleight, and J. Gillson. Crystal chemistry of metal dioxides with rutile-related structures. *Inorg. Chem.*, 8:841–849, 1969.

[27] J. Goodenough. Metallic oxides. *Prog. Solid State Chem.*, 5:145–399, 1971.

[28] S. Ardizzone and S. Trasatti. Interfacial properties of oxides with technological impact in electrochemistry. *Adv. Colloid Interface Sci.*, 64:173–251, 1996.

[29] A. Daghetti, G. Lodi, and S. Trasatti. Interfacial properties of oxides used as anodes in the electrochemical technology. *Mater. Chem. Phys.*, 8:1–90, 1983.

[30] R. Vigano, J. Taraszewska, A. Daghetti, and S. Trasatti. The point of zero charge of RuO_2 + IrO_2 mixed oxides. *J. Electroanal. Chem.*, 182:203–209, 1985.

[31] L. De Faria and S. Trasatti. Effect of composition on the point of zero charge of RuO_2 + TiO_2 mixed oxides. *J. Electroanal. Chem.*, 340:145–152, 1992.

[32] D. Pletcher, R. Greef, R. Peat, L. Peter, and J. Robinson. *Instrumental Methods in Electrochemistry*, chapter Potential sweep techniques and cyclic voltammetry, pages 178–228. Horwood Publishing, 2001.

[33] L. Burke. Oxide growth and oxygen evolution on noble metals. In S. Trasatti, editor, *Electrodes of conductive metallic oxides Part A*, page 144. Elsevier Publishing Company, 1980.

[34] D. Michell, D. Rand, and R. Woods. A study of ruthenium electrodes by cyclic voltammetry and X-ray emission spectroscopy. *J. Electroanal. Chem.*, 89:11–27, 1978.

[35] S. Ardizzone, G. Fregonara, and S. Trasatti. "Inner" and "outer" active surface of RuO_2 electrodes. *Electrochim. Acta*, 35:263–267, 1990.

[36] D. Pletcher, R. Greef, R. Peat, L. Peter, and J. Robinson. *Instrumental Methods in Electrochemistry*, chapter A.C. techniques, pages 251–282. Horwood Publishing, 2001.

[37] U. Rammelt and G. Reinhard. On the applicability of a constant phase element (CPE) to the estimation of roughness of solid metal electrodes. *Electrochim. Acta*, 35:1045–1049, 1990.

[38] J. Goldstein, D. Newbury, P. Echlin, D. Joy, C. Lyman, E. Lifshin, L. Sawyer, and J. Michael. *Scanning Electron Microscopy and X-Ray Microanalysis*. Kluwer Academic Publishers, 2003.

[39] D. Williams and C. Carter. *Transmission Electron Microscopy*. Plenum Press, 1996.

[40] J. Liu. High-resolution and low-voltage FE-SEM imaging and microanalysis in materials characterization. *Mater. Charact.*, 44:353–363, 2000.

[41] B. Warren. X-ray studies of deformed metals. In B. Chalmers and R. King, editors, *Progress in Metal Physics*, volume 8, pages 147–202. Pergamon Press, 1959.

[42] W. Hume-Rothery and G. Raynor. *The Structure of Metals and Alloys*. Institute of Metals, London, 1954.

[43] P. Behrens. X-ray absorption spectroscopy in chemistry. *Trends Anal. Chem.*, 11:218–222, 1992.

[44] J. McBreen, W. O'Grady, and K. Pandya. Exafs: A new tool for the study of battery and fuel cell materials. *J. Power Sources*, 22:323–340, 1988.

[45] A. Newkirk and D. McKee. Thermal decomposition of rhodium, iridium, and ruthenium chlorides. *J. Catal.*, 11:370–377, 1968.

[46] S. Han, K. Park, R. Rana, and K. Singh. Developments of water electrolysis technology by solid polymer electrolyte. *Indian J. Chem.*, 41:245–253, 2002.

[47] P. Millet, M. Pineri, and R. Durand. New solid polymer electrolyte composites for water electrolysis. *J. Appl. Electrochem.*, 19:162–166, 1989.

[48] P. Millet, R. Durand, and M. Pineri. Preparation of new solid polymer electrolyte composities for water electrolysis. *Int. J. Hydrogen Energy*, 15:245–253, 1990.

[49] H. Takenaka, E. Torikai, Y. Kawami, and N. Wakabayashi. Solid polymer electrolyte water electrolysis. *Int. J. Hydrogen Energy*, 7:397–403, 1982.

[50] J. Sedlak, R. Lawrence, and J. Enos. Advances in oxygen evolution catalysis in solid polymer electrolyte water electrolysis. *Int. J. Hydrogen Energy*, 6:159–165, 1981.

[51] M. Yamaguchi, K. Yagiuchi, and K. Okisawa. R&D of high performance solid polymer electrolyte water electrolyzer in WE-NET. *Hydrogen Energy Progress*, 11:781–786, 1996.

[52] M. Nagai, H. Tazima, A. Sakanishi, N. Hisatome, and S. Ohkura. Development on solid polymer electrolyte water electrolysis technology for high current density and energy efficiency. *Hydrogen Energy Progress*, 11:825–830, 1996.

[53] M. Yamaguchi, K. Okisawa, and T. Nakanori. Development of high performance solid polymer electrolyte water electrolyzer in WE-NET. In *Proc. 32nd Intersociety Energy Conversion Engineering Conference*, pages 1958–1965, 1997.

[54] M. Yamaguchi, T. Shinohara, H. Taniguchi, T. Nakanori, and K. Okisawa. Development of 2500 cm^2 solid polymer electrolyte water electrolyzer in WE-NET. *Hydrogen Energy Progress*, 12:747–755, 1998.

[55] S. Grigor'ev, M. Khaliullin, N. Kuleshov, and V. Fateev. Electrolysis of water in a system with a solid polymer electrolyte at elevated pressure. *Russ. J. Electrochem.*, 37:819–822, 1998.

[56] K. Ledjeff, F. Mahlendorf, V. Peinecke, and A. Heinzel. Development of electrode membrane units for the reversible polymer fuel cell (RSPFC). *Electrochim. Acta*, 40:315–319, 1998.

[57] S. Zhigang, Y. Baolian, and H. Ming. Bifunctional electrodes with a thin catalyst layer for 'unitized' proton exchange membrane regenerative fuel cell. *J. Power Sources*, 79:82–85, 1999.

[58] T. Ioroi, N. Kitazawa, K. Yasuda, Y. Yamamoto, and H. Takenaka. Iridium oxide/platium electrocatalysts for utilized regenerative polymer electrolyte fuel cells. *J. Electrochem. Soc.*, 147:2018–2022, 2000.

[59] V. Fateev, E. Lyutikova, S. Grigoriev, V. Porembsky, A. Kalinnikov, and F. Pekhota. Electrocatalytic layers for pem electrolysis. *55th ISE meeting, 19-24 Sept. Thessaloniki, Greece*, page 791, 2004.

[60] H. Beer. Improvements in or relating to electrodes for electrolysis. *British Patent 1,147,442*, 1969.

[61] S. Trasatti. Physical electrochemistry of ceramic oxides. *Electrochim. Acta*, 36:225–241, 1991.

[62] A. De Battisti, R. Brina, G. Gavelli, A. Benedetti, and G. Fagherazzi. Influence of the valve metal oxide on the properties of ruthenium based mixed oxide electrodes : Part I. Titanium supported RuO_2/Ta_2O_5 layers. *J. Electroanal. Chem.*, 200:93–104, 1985.

[63] G. Vercesi, J. Salamin, and C. Comminellis. Morphological and microstructural study of the titanium/iridium oxide (IrO_2)-tantalum oxide (Ta_2O_5) electrode: effect of the preparation temperature. *Electrochim. Acta*, 36:991–998, 1991.

[64] P. Duvigneaud and D. Reinhard-Derie. DTA study of RuO_2 formation from the thermal decomposition of ruthenium (III) hydrate. *Thermochim. Acta*, 51:307–314, 1981.

[65] S. Ardizzone, M. Falciola, and S. Trasatti. Effect of the nature of the precursor on the electrocatalytic properties of thermally prepared ruthenium oxide. *J. Electrochem. Soc.*, 136:1545–1550, 1989.

[66] M. Guglielmi, P. Colombo, V. Rigato, G. Battaglin, and A. Boscolo-Boscoletto A. De Battisti. Composition and microstructural charaterization of RuO_2-TiO_2 catalysts synthesized by the sol-gel method. *J. Electrochem. Soc.*, 139:1655–1661, 1992.

[67] A. De Battisti, G. Lodi, L. Nanni, G. Battaglin, and A. Benedetti. Preparation and characterization of oxide film electrodes. *Can. J. Chem.*, 75:1759–1765, 1997.

[68] A. De Battisti, G. Lodi, M. Cappadonia, G. Battaglin, and R. Koetz. Influence of the valve metal oxide on the properties of ruthenium based mixed oxide electrodes. II. Ruthenium dioxide/titanium dioxide coatings. *J. Electrochem. Soc.*, 136:2596–2598, 1997.

[69] T. Varlamova, I. Belova, R. Shifrina, B. Galyamov, Yu. Roginskaya, and Yu. Venevtsev. The composition, structure, and electronic properties of iridium titanium oxide films. *Russ. J. Phys. Chem.*, 64:202–206, 1990.

[70] Yu. Roginskaya, O. Morozova, E. Loubnin, A. Popov, Yu. Ulitina, V. Zhurov, S. Ivanov, and S. Trasatti. X-ray diffraction, transmission electron microscopy and x-ray photoelectron spectroscopic charaization of iridium dioxide + tantalum oxide (Ta_2O_5) films. *J. Chem. Soc., Faraday Transactions*, 89:1707–1715, 1993.

[71] C. De Pauli and S. Trasatti. Electrochemical surafce characterization of IrO_2 + SnO_2 mixed oxide electrodes. *J. Electroanal. Chem.*, 396:161–168, 1995.

[72] S. Ardizzone, A. Carugati, and S. Trasatti. Properties of thermally prepared iridium dioxide electrodes. *J. Electroanal. Chem.*, 126:287–292, 1981.

[73] V. Alves, L. da Silva, and J. Boodts. Surface characterization of $IrO_2/TiO_2/CeO_2$ oxide electrodes and faradaic impedance investigation of oxygen evolution reaction from aklaline solution. *Electrochim. Acta*, 44:1525–1534, 1998.

[74] M. Santana, L. Da Silva, and L. De Faria. Investigation of surface properties of Ru-based oxide electrodes containing Ti, Ce and Nb. *Electrochim. Acta*, 48:1885–1891, 2003.

[75] J. Fernandez, M. Gennero De Chialvo, and A. Chialvo. Preparation and electrochemical characterization of $Ti/Ru_xMn_{1-x}O_2$ electrodes. *J. Appl. Electrochem.*, 32:513–520, 2002.

[76] X. Chen, G. Chen, and P. Yue. Stable Ti/IrO_x-Sb_2O_5-SnO_2 anode for O_2 evolution with low Ir content. *J. Phys. Chem. B*, 105:4623–4628, 2001.

[77] O. Camara and S. Trasatti. Surface electrochemical properties of $Ti/(RuO_2 + ZrO_2)$ electrodes. *Electrochim. Acta*, 41:419–427, 1996.

[78] T. Arikado, C. Iwakura, and H. Tamura. Some oxide catalysts for the anodic evolution of chlorine: reaction mechanism and catalytic activity. *Electrochim. Acta*, 23:9–15, 1978.

[79] A. Terezo and E. Pereira. Preparation and charaterisation of Ti/RuO_2 anodes obtained by sol-gel and conventional routes. *Mater. Lett.*, 53:339–345, 2002.

[80] V. Alves, L. da Siliva, S. de Castro, and J. Boodts. Surface characterization by UHV techniques and cyclic voltammetry of thermal IrO_2-based electrocatalysts containing TiO_2 and CeO_2. *J. Chem. Soc., Faraday Transactions*, 94:711–717, 1998.

[81] Yu. Roginskaya and O. Morozova. The role of hydrated oxides in formation and structure of DSA-type oxide electrocatalysts. *Electrochim. Acta*, 40:817–822, 1995.

[82] R. Adams and R. Shriner. Platinum oxide as a catalyst in the reduction of organic compounds. ii Preparation and properties of the oxide of platinum obtained by the fusion of chloroplatinic acid with sodium nitrate. *J. Am. Chem. Soc.*, 45(9):2171–2179, 1923.

[83] W. Bruce. Preparation of platinum oxide for catalytic hydrogenations. *J. Am. Chem. Soc.*, 58:687–688, 1936.

[84] R. Hutchings, K. Müller, and S. Stucki. A structural investigation of stabilized oxygen evolution catalysts. *J. Mater. Sci.*, 19:3987–3994, 1984.

[85] C. Brinker and G. Scherer. *Sol-gel science : the physics and chemistry of sol-gel processing*. Academic Press, 1990.

[86] J. Wright and N. Sommerdijk. *Sol-gel materials : chemistry and applications*. Gordon and Breach, 2003.

[87] F. Mattos-Costa, P. de Lima-Neto, S. Machado, and L. Avaca. Characterisation of surfaces modified by sol-gel $Ru_xIr_{1-x}O_2$ coatings for oxygen evolution in acid medium. *Electrochim. Acta*, 44:1515–1523, 1998.

[88] M. Ito, Y. Murakami, H. Kaji, H. Ohawauchi, K. Yahikozawa, and Y. Takasu. Preparation of ultrafine RuO_2-SnO_2 binary oxide particles by a sol-gel process. *J. Electrochem. Soc.*, 141:1243–1245, 1994.

[89] K. Kameyama, S. Shohji, S. Onoue, K. Nishimura, K. Yahikozawa, and Y. Takasu. Preparation of ultrafine RuO_2-TiO_2 binary oxide particles by a sol-gel process. *J. Electrochem. Soc.*, 140:1034–1037, 1993.

[90] Y. Takasu, S. Onoue, K. Kameyama, Y. Murikami, and K. Yahikozawa. Preparation of ultrafine RuO_2-IrO_2-TiO_2 oxide particles by a sol-gel process. *Electrochim. Acta*, 39:1993–1997, 1994.

[91] Y. Murakami, H. Ohkawauchi, M. Ito, K. Yahikozawa, and Y. Takasu. Preparation of ultrafine IrO_2-SnO_2 binary oxide particles by a sol-gel process. *Electrochim. Acta*, 39:2551–2554, 1994.

[92] Y. Murakami, S. Tsuchiya, K. Yahikozawa, and Y. Takasu. Preparation of ultrafine IrO_2-Ta_2O_5 binary oxide particles by a sol-gel process. *Electrochim. Acta*, 39:651–654, 1994.

[93] Y. Takasu and Y. Murakami. Design of oxide electrodes with large surface area. *Electrochim. Acta*, 45:4135–4141, 2000.

[94] Y. Murakami, S. Ichikawa, and Y. Takasu. Preparation of ultrafine ruthenium oxide particles with ammonium hydrogencarbonate. *Denki kagaku oyobi kogyo butsuri kagaku*, 65:992–996, 1997.

[95] A. de Oliveira-Sousa, M. de Siliva, S. Machado, L. Avaca, and P. de Lima-Neto. Influence of the preparation method on the morphological and electrochemical properties of Ti/IrO_2-coated electrodes. *Electrochim. Acta*, 45:4467–4473, 2000.

[96] F. Bonet, V. Delmas, S. Grugeon, R. Herrera-Urbina, P. Silvert, and K. Tekaia-Elhsissen. Synthesis of monodisperse Au, Pt Pd, Ru and Ir nanoparticles in ethylene glycol. *NanoStructured Mater.*, 11:1277–1284, 1999.

[97] L. Kurihara, G. Chow, and P. Schoen. Nanocrystalline metallic powders and flims produced by the polyol method. *NanoStructured Mater.*, 5:607–613, 1995.

[98] F. Bonet, K. Tekaia-Elhsissen, and K. Sarathy. Study of the interaction of ethylene glycol/PVP phase on noble metal powders prepared by polyol process. *Bull. Mater. Sci.*, 23:165–168, 2000.

[99] A. Miyazaki, K. Takeshita, K. Aika, and Y. Nakano. Formation of ruthenium colloid in ethylene glycol. *Chem. Lett.*, pages 361–362, 1998.

[100] C. Feldmann. Preparation of nanoscale pigment particles. *Adv. Mater.*, 13:1301–1303, 2001.

[101] C. Iwakura, K. Hirao, and H. Tamura. Preparation of ruthenium dioxide electrodes and their anodic polarization characteristics in acidic solutions. *Electrochim. Acta*, 22:335–340, 1977.

[102] N. Bestaoui and E. Prouze. A chimie douce route to pure iridium dioxide. *Chem. Mater.*, 9:1036–1041, 1997.

[103] P. Beutler and H. Gamsjager. Preparation and ultraviolet-visible spectrum of hexa-aquairidium(III). *J. Chem. Soc., Chem. Comm.*, 14:554–555, 1976.

[104] E. Gulzow, M. Schulze, N. Wagner, T. Kaz, R. Reissner, G. Steinhilber, and A. Schneider. Dry layer prepartion and characterization of polymer electrolyte fuel cell components. *J. Power Sources*, 86:352–362, 2000.

[105] M. Wilson and S. Gottesfeld. Thin-fim catalyst layers for polymer electrolyte fuel cell electrodes. *J. Appl. Electrochem.*, 22:1–7, 1992.

[106] P. Millet, T. Alleau, and R. Durand. Charaterization of membrane-electride assemblies for solid polymer water electrolysis. *J. Appl. Electrochem.*, 23:322–331, 1993.

[107] A. Venugopal and M. Scurrell. Low temperature reductive pretreatment of Au/Fe_2O_3 catalysts, TPR/TPO studies and behaviour in the water-gas shift reaction. *Appl. Catal., A*, 258:241–249, 2004.

[108] A. Harriman and J. Thomas. Catalytic and structural properties of iridium-iridium dioxide colloids. *New J. Chem.*, 11:757–762, 1987.

[109] G. Lodi, A. De Battisti, G. Bordin, C. De Asmundis, and A. Benedetti. Microstructure and electrical properties of iridium dioxide prepared by thermal decomposition of iridium trichloride hydrate. Role played by the conditions of thermal treatment. *J. Electroanal. Chem.*, 277:139–150, 1990.

[110] E. Balko and P. Nguyen. Iridium-tin mixed oxide anode coatings. *J. Appl. Electrochem.*, 21:678–682, 1991.

[111] C. McDaniel and S. Schneider. Phase relations in the systems titanium(IV) oxide-iridium(IV) oxide and tin(IV) oxide-iridium(IV) oxide in air. *J. Res. NBS A Phys. Ch.*, 71:119–123, 1967.

[112] F. Reames. Growth of iridium dioxide, tin dioxide, and tin dioxide:iridium dioxide crystals. *Mater. Res. Bull.*, 11:1091–1095, 1976.

[113] J. Hu, J. Zhang, H. Meng, and C. Cao. Effect of crystallite orientation of the IrO_2 rutile on the corrosion characteristics of IrO_2+Ta_2O_5. *J. Mater. Sci.*, 38:705–712, 2003.

[114] E. Rasten, G. Hagen, and R. Tunold. Electrocatalysis in water electrolysis with solid polymer electrolyte. *Electrochim. Acta*, 48:3945–3952, 2003.

[115] C. Iwakura, M. Inai, T. Uemura, and H. Tamura. The anodic evolution of oxygen and chlorine on foreign metal-doped SnO_2 film electrodes. *Electrochim. Acta*, 26:579–584, 1981.

[116] Lj. Atanasoska, R. Atanasoska, and S. Trasatti. XPS and AES study of mixed layers of RuO_2 and IrO_2. *Vacuum*, 40:91–94, 1990.

[117] M. Rubel, R. Haasch, P-Mrozek, A. Wieckowski, C. De Pauli, and S. Trasatti. Characterization of IrO_2-SnO_2 thin layers by electron and ion spectroscopies. *Vacuum*, 45:423–427, 1994.

[118] T. Arikawa, Y. Takasu, Y. Murakami, K. Askura, and Y. Iwasawa. Characterization of the structure of RuO_2-IrO_2/Ti electrodes by EXAFS. *J. Phys. Chem. B*, 102:3736–3741, 1998.

[119] Y. Mo, M. Antonio, and D. Scherson. In situ Ru K-edge x-ray adsorption fine structure studies of electroprecipitated ruthenium dioxide films with relevance to supercapacitor applications. *J. Phys. Chem. B*, 104:9777–9779, 2000.

[120] Y. Mo, I. Stefan, W. Cai, J. Dong, P. Carey, and D. Scherson. In situ iridium LIII-edge x-ray absorption and surface enhanced raman spectroscopy of electrodeposited iridium dioxide films in aqueous electrolytes. *J. Phys. Chem. B*, 106:3681–3686, 2002.

[121] C. Angelinetta, L. Atanasoska, R. Atanasoski, and S. Trasatti. Surface properties of RuO_2 + IrO_2 mixed oxide electrodes. *J. Electroanal. Chem.*, 214:535–546, 1986.

[122] R. Kötz and S. Stucki. Stabilization of RuO_2 by IrO_2 for anodic oxygen evolution in acid media. *Electrochim. Acta*, 31:1311–1316, 1986.

[123] L. Doubova, A. De Battisti, and S. Trasatti. Surface reactivity and charge storage mechanism of well defined RuO_2 surfaces. *55th ISE meeting, 19-24 Sept. Thessaloniki, Greece*, page 731, 2004.

[124] R. Savinell, R. Zeller, and J. Adams. Electrochemical active surface area. *J. Electrochem. Soc.*, 137:489–494, 1990.

[125] B. Aurian-Biajeni, A. Kimball, L. Robblee, G. Kahanda, and C. Tomkiewicz. Correlation between charge storage capacity and morphology. *J. Electrochem. Soc.*, 134:2637–2638, 1987.

[126] L. Burke and O. Murphy. Cyclic voltammetry as a technique for determining the surface area of RuO_2 electrodes. *J. Electroanal. Chem.*, 96:19–27, 1979.

[127] T. Lassali, J. Boodts, and L. Bulhoes. Charging processes and electrocatalytic properties of $IrO_2/TiO_2/SnO_2$ oxide films investigated by in situ AC impedance measurements. *Electrochim. Acta*, 44:4203–4216, 1999.

[128] C. De Pauli and S. Trasatti. Composite materials for electrocatalysis of O_2 evolution: $IrO_2 + SnO_2$ in acid solution. *J. Electroanal. Chem.*, 538-539:145–151, 2002.

[129] K. Endo, Y. Katayama, T. Miura, and T. Kishi. Composition dependence of the oxygen-evolution reaction rate on $Ir_xTi_{1-x}O_2$ mixed-oxide electrodes. *J. Appl. Electrochem.*, 32:173–178, 2002.

[130] E. Rasten, G. Hagen, and R. Tunold. Effect of thermal treatment of IrO_2 anode catalysts for pem water electrolysis. *Proc. - Electrochem. Soc.*, 2001-23:151–164, 2001.

[131] A. Marshall, B. Børresen, G. Hagen, M. Tsypkin, and R. Tunold. Development of Oxygen Evolution Electrocatalysts for Proton Exchange Membrane Water Electrolysis. In *1st European Hydrogen Energy Conference, 2-5 September, Grenoble, France*, September 2003.

[132] A. Marshall, B. Børresen, G. Hagen, M. Typskin, and R. Tunold. Nanocrystalline $Ir_xSn_{(1-x)}O_2$ electrocatalysts for oxygen evolution in water electrolysis with polymer electrolyte - Effect of heat treatment. *J. New Mater. Electrochem. Sys.*, 7:197–204, 2004.

[133] T. Lassali, J. Boodts, and L. Bulhoes. Effect of Sn precursor on the morphology and composition of $Ir_{0.3}Sn_{0.7}O_2$ oxide films prepared by the sol-gel process. *J. Non-Cryst. Solids*, 273:129–134, 2000.

[134] T. Boiadjieva, G. Cappelletti, S. Ardizzone, S. Rondinini, and A. Vertova. Nanocrystalline titanium oxide by sol-gel method. the role of the solvent removal step. *Phys. Chem. Chem. Phys.*, 5:1689–1694, 2003.

[135] H. Bönnemann and R. Richards. Nanoscopic metal particles - synthetic methods and potential applications. *Eur. J. Inorg. Chem.*, pages 2455–2480, 2001.

[136] N. Toshima and T. Yonezawa. Bimetallic Nanoparticles - Novel Materials for Chemical and Physical Applications. *New J. Chem.*, pages 1179–1201, 1998.

[137] J. Boodts and S. Trasatti. Effect of composition on the electrocatalytic activity of the ternary oxide ruthenium titanium tin oxide $Ru_{0.3}Ti_{(0.7-x)}Sn_xO_2$. I. Oxygen evolution from perchloric acid solutions. *Electrochim. Acta*, 137:3784–3789, 1990.

[138] J. Moulder, W. Stickle, P. Sobol, and K. Bomben. *Handbook of X-ray Photoelectron Spectroscopy.* Perkin-Elmer Corp, 1992.

[139] S. Krimm and A. Tobolsky. Quantitative x-ray studies of order in amorphous and crystalline polymers. Quantitative x-ray determination of crystallinity in polyethylene. *J. Polym. Sci.*, 7:57, 1951.

[140] C. Mallika, A. Edwin Suresh Raj, K. Nagaraja, and O. Sreedharan. Use of SnO for the determination of standard gibbs energy of formation of SnO_2 by oxide electrolyte E.M.F. measurements. *Thermochim. Acta*, 371:95–101, 2001.

[141] P. Millet, R. Durand, E. Dartyge, and G. Tourillon. Precipitation of metallic platinum into Nafion ionomer membranes. I. Experimental results. *J. Electrochem. Soc.*, 140:1373–1380, 1993.

[142] J. Ahn and R. Holze. Bifunctional electrodes for an integrated water-electrolysis and hydrogen-oxygen fuel cell with a solid polymer electrolyte. *J. Appl. Electrochem.*, 22:1167–1174, 1992.

[143] C. Comninellis and G. Vercesi. Characterization of DSA-type oxygen evolving electrodes: choice of a coating. *J. Appl. Electrochem.*, 21:335–345, 1991.

[144] K. Kameyana, K. Tsukada, K. Yahikoshima, and Y. Takasu. The application of scanning auger microscopy to the surface characterization of ruthenium dioxide-titanium dioxide coated titanium electrodes. *J. Electrochem. Soc.*, 140:996–999, 1993.

[145] M. Jaksic, B. Johansen, and R. Tunold. Electrochemical behaviour of iridium in alkaline and acidic solutions of heavy and regular water. *Int. J. Hydrogen Energy*, 19:321–335, 1994.

[146] M. Wilson and S. Gottesfeld. High Performance Catalyzed Membranes of Ultra-Low Platinum Loadings for Polymer Electrolyte Fuel Cells. *J. Electrochem. Soc.*, 139:L–28, 1992.

[147] P. Fedkiw and W. Her. An Impregnation-Reduction Method to Prepare Electrodes on Nafion SPE. *J. Electrochem. Soc.*, 136:L–889, 1992.

[148] Z. Ogumia, K. Inatomi, J. Hinatsu, and Z. Takehara. Application of the SPE method to organic electrochemistry XIII. Oxidation of geraniol on Mn,Pt-Nafion. *Electrochim. Acta*, 37:1295, 1992.

[149] Y. Roginskaya, M. Gol'dshtein, O. Morozova, and L. Glazunova. Charge accumulation in nanoheterogenous iridium oxide films. *Russ. J. Electrochem.*, 37:1065–1071, 2001.

[150] O. Barcia, E. D'Elia, O. Mattos, N. Pebere, and B. Tribollet. Application of the impedance of de levie for the characterization of porous electrodes. *Electrochim. Acta*, 47:2109–2116, 2002.

[151] A. Terezo, J. Bisquert, G. Garcia-Belmonte, and E. Pereira. Separation of transport, charge storage and reaction processes of porous electrocatalytic $IrO_2$and IrO_2/Nb_2O_5 electrodes. *J. Electroanal. Chem.*, 508:59–69, 2000.

[152] L. da Silva, V. Alves, M. da Silva, S. Trasatti, and J. Boodts. Oxygen evolution in acid solution on IrO_2 + TiO_2 ceramic films. A study by impedance, voltammetry and SEM. *Electrochim. Acta*, 42:271–281, 1997.

[153] C. Hsu and F. Mansfeld. Technical note: concerning the conversion of the constant phase element parameter Y_0 into a capacitance. *Corrosion*, 57:747–748, 2001.

[154] S. Glarum and J. Marshall. The A-C response of iridium oxide films. *J. Electrochem. Soc.*, 127:1467–1474, 1980.

[155] S. Guerin, B. Hayden, C. Lee, C. Mormiche, J. Owen, A. Russel, B. Theobald, and D. Thompsett. Combinatorial electrochemical

screening of fuel cell electrocatalysts. *J. Comb. Chem.*, 6:149–158, 2004.

[156] G. TamizhMani, J. Dodelet, D. Guay, and L. Dignard-Bailey. A rapid half-cell technique for the pre-screening of polymer fuel cell catalysts. *J. Electroanal. Chem.*, 444:121–125, 1998.

[157] A. Marshall, B. Børresen, G. Hagen, M. Tsypkin, and R. Tunold. Preparation and characterisation of nanocrystalline $Ir_xSn_{1-x}O_2$ electrocatalytic powders. *submitted to Mater. Chem. Phys.*, 2005.

[158] A. Marshall, B. Børresen, G. Hagen, M. Tsypkin, and R. Tunold. Electrochemical characterisation of $Ir_xSn_{1-x}O_2$ powders as oxygen evolution electrocatalysts. *submitted to Electrochim. Acta*, 2005.

[159] R. Yeo, J.Orehotsky, W. Visscher, and S. Srinivasan. Ruthenium-based mixed oxides as electrocatalysts for oxygen evolution in acid electrolytes. *J. Electrochem. Soc.*, 128:1900–1904, 1981.

[160] Y. Roginskaya, T. Varlamova, M. Goldshtein, T. Belova, B. Galyamov, R. Shifrina, V. Shepelin, and V. Fateev. Formation, structure and electrochemical properties of IrO_2-RuO_2 oxide electrodes. *Mater. Chem. Phys.*, 30:101–113, 1991.

[161] L. Sharpe, W. Heineman, and R. Elder. EXAFS spectroelectrochemistry. *Chem. Rev.*, 90:705–722, 2004.

[162] J. McBreen, W. O'Grady, K. Pandya, R. Hoffman, and D. Sayers. EXAFS study of the nickel oxide electrode. *Langmuir*, 3:428–433, 1987.

[163] W. O'Grady and D. Ramaker. Atomic x-ray absorption fine structure: a new tool for examining electrochemical interfaces. *Electrochim. Acta*, 44:1283–1287, 1998.

[164] S. Maniguet, R. Mathew, and A. Russell. EXAFS of carbon monoxide oxidation on supported Pt fuel cell electrocatalysts. *J. Phys. Chem. B*, 104:1998–2004, 2000.

[165] R. Wiltshire, M. Hogarth, D. Thompsett, and A. Russell. A PEM fuel cell for XAS studies. *55th ISE meeting, 19-24 Sept. Thessaloniki, Greece*, page 761, 2004.

[166] A. Russell and A. Rose. X-ray absorption spectroscopy of low temperature fuel cell catalysts. *Chem. Rev.*, 104:4613–4635, 2004.

[167] H. Dewald. Use of EXAFS to probe electrode-solution interfaces. *Electroanalysis*, 3:145–155, 1991.

[168] R. Weast, editor. *Handbook of Chemistry and Physics - 57th Edition.* CRC Press, 1976.

[169] Center for X-ray Optics Lawrence Berkeley National Laboratory. Internet address – $http://www-cxro.lbl.gov/$.

[170] J. Rehr, R. Albers, and S. Zabinsky. High-order multiple-scattering calculations of x-ray-absorption fine structure. *Phys. Rev. Lett.*, 69:3397–3400, 1992.

[171] M. Newville, B. Ravel, D. Haskel, J. Rehr, E. Stern, and Y. Yacoby. Analysis of multiple-scattering XAFS data using theoretical standards. *Physica B (Amsterdam, Neth.)*, 208:154–156, 1995.

[172] B. Ravel. ATOMS: Crystallography for the x-ray absorption spectroscopist. *J. Synchro. Radiat.*, 8:314–316, 2001.

[173] M. Newville, P. Livins, Y. Yacoby, E. Stern, and J. Rehr. Near-edge x-ray-absorption fine structure of Pb: A comparison of theory and experiment. *Phys. Rev. B: Condens. Matter Mater. Phys.*, 47:14126–14131, 1993.

[174] A. Balerna, E. Bernieri, E. Burattini, A. Kuzmin, A. Lusis, J. Purans, and P. Cikmach. XANES studies of MeO_{3-x} (Me = W, Re, Ir) crystalline and amorphous oxides. *Nucl. Instrum. Methods Phys. Res., Sect. A*, 308:240–242, 1991.

[175] J. Choy, D. Kim, G. Demazeau, and D. Jung. XANES studies of MeO_{3-x} (Me = W, Re, Ir) crystalline and amorphous oxides. *J. Phys. Chem.*, 98:6258–6262, 1994.

[176] A. Balerna, E. Bernieri, E. Burattini, A. Kuzmin, A. Lusis, J. Purans, and P. Cikmach. EXAFS studies of MeO_{3-x} (Me = W, Mo, Re, Ir) crystalline and amorphous oxides. *Nucl. Instrum. Methods Phys. Res., Sect. A*, 308:234–239, 1991.

[177] E Prouzet. Multiple-sctattering contribution in extended x-ray absorption fine structure for iridium oxide IrO_2. *J. Phys.: Condens. Matter*, 7:8027–8033, 1995.

[178] J. Choy, S. Hwang, J. Yoon, C. Chin, M. Oh, and H. Lee. x-ray absorption spectroscopic studies on the iridium(III) complexes. *Mater. Lett.*, 37:168–175, 1998.

[179] M. Vaarkamp, J. Miller, F. Modica, G. Lane, and D. Koningsberger. The relation between catalytic and electronic properties of supported platinum catalysts: the local density of states as determined by x-ray absorption spectroscopy. *Stud. Surf. Sci. Catal.*, 75:809–820, 1993.

[180] G. Lodi, G. Zucchini, A. De Battisti, A. Giatti, G. Battaglin, and G. Della Mea. Proton exchange in group VIII metal-oxide film. *Surf. Sci.*, 252:836–840, 1991.

[181] I. Stefan, Y. Mo, M. Antonio, and D. Scherson. In situ Ru L_{II} and L_{III} edge x-ray absorption near edge structure of electrodeposited ruthenium dioxide films. *J. Phys. Chem. B*, 106:12373–12375, 2002.

[182] R. Shannon. Revised Effective Ionic Radii and Systematic Studies of Interatomic Distances in Halides and Chaleogenides. *Acta Crystallogr., Sect. A: Found. Crystallogr.*, 32:751–767, 1976.

[183] D. McKeown, P. Hagens, L. Carette, A. Russell, K. Swider, and D. Rolison. Structure of hydrous Ruthenium Oxides: Implications for Charge Storage. *J. Phys. Chem. B*, 103:4825–4832, 1999.

[184] M. Hüppauff and B. Lengeler. Valency and structure of iridium in anodic iridium oxide films. *J. Electrochem. Soc.*, 140:598–602, 1993.

[185] T. Pauprte, D. Aberdam, J. Hazemann, R. Faure, and R. Durand. X-ray absorption in relation valency of iridium in sputtered iridium oxide films. *J. Electroanal. Chem.*, 465:88–95, 1999.

[186] B. Conway. *Electrochemical Supercapacitors: Scientific Fundamentals and Technological Applications.* Kluwer Academic, 1999.

[187] V. Andreev, K. Heckner, M. Glas, and V. Kazarinov. Study of anion adsorption on ruthenium oxide and iridium oxide electrodes by the radioactive indicator method. *Elektrokhimiya*, 19:1558–1561, 1983.

[188] M. Pourbaix. *Atlas of Electrochemical Equilibria in Aqueous Solutions*. Pergamon Press, 1966.

[189] I. Belova, T. Varlamova, B. Galyamov, Y. Roginskaya, R. Shifrina, S. Pruchenko, G. Kaplan, and M. Sevostyanov. The composition, structure and electronic properties of thermally prepared iridium dioxide films. *Mater. Chem. Phys.*, 20:39–64, 1988.

[190] R. Shannon and C. Prewitt. Effective Ionic Radii in Oxides and Fluorides. *Acta Crystallogr., Sect. B: Struct. Sci.*, 25:925–946, 1969.

[191] D. Ghosh and R. Biswas. Theoretical Calculation of Absolute Radii of Atoms and Ions. Part 2. The Ionic Radii. *Int. J. Mol. Sci.*, 4:379–407, 2003.